

## Preface

### Special Issue on Platforms for Medical Robotics Research

Medical robotics have been around us for 3 decades, yet today there is an unprecedented rise in applications and systems. Surgical robotics is entering new domains such as single site surgeries and advanced decision making support, requiring highly sophisticated manipulation capabilities. The coming generations of medical and surgical robots may not only function as an agile extension of the human eyes and hands, but will also become a skillful and coordinated partner for their human counterpart. In the last couple of years, outreach and community formation activities are gradually following the individual technical developments, striving to establish an R&D ecosystem.

Shared hardware and software platforms for robotic systems can foster collaboration between groups and accelerate the progress of technology development. In the medical robotics community, a variety of common research platforms and software frameworks have emerged, such as the RAVEN-II, the da Vinci Research Kit (DVRK) and the KUKA Lightweight Arm. The goals of this Special Issue are to more broadly engage the medical/surgical robotics community, present the latest developments, and to define the road map for future enhancements to these platforms. Some of these initiatives are supported by government initiatives as well, such as the U.S. National Science Foundation (NSF) National Robotics Initiative (NRI) grant “Collaborative Research: Software Framework for Research in Semi-Autonomous Teleoperation”, and social media initiatives, such as the SurgRob blog (<http://surgrab.blogspot.com>).

Probably the largest such existing group, the DVRK community, uses hardware from the da Vinci classic surgical robot with separately developed DVRK controllers (<https://github.com/jhu-dvrk/sawIntuitiveResearchKit/wiki>) to facilitate research uses. Its history started 15 years ago, with the first efforts at Johns Hopkins University, to create/re-create a da Vinci research version. In 2012, the first key sites were added to the group (WPI, Stanford, UBC), and the first non-American groups joined in 2014. The PIs regularly meet at IEEE ICRA, IROS conferences, at the Hamlyn Symposium and other key international forums. Today, there are over 35 research labs across the globe taking advantage of the open controllers that provide access to the first generation da Vinci. Research projects range from novel, intelligent tool development to deep learning based endoscope stream segmentation and processing. Key topics addressed in this issue include the kinematic modeling of the da Vinci, where the WPI group proposed a modeling method of the closed-loop kinematics, using the existing da Vinci kinematics and an optical motion capture link length calibration. The Johns Hopkins group developed a compliance model that relates displacement of the

first two joints of the da Vinci Patient Side Manipulator to lateral forces applied to the instrument shaft, which enables compensation for the position errors based on the measured joint efforts, which are derived from the measured motor currents. The Università degli Studi di Napoli Federico II researchers present the Portable DVRK, which is based on a V-REP simulator (from Coppelia Robotics) of the DVRK patient side and endoscopic camera manipulators which are controlled through two haptic interfaces and a 3D viewer. The team at Óbuda University developed a software framework to ease and hasten the automation of surgical subtasks implementation, based on the Robot Operating System (ROS).

The other popular platform is the Raven (<http://applieddexterity.com/community/raven-sites>). The Raven I and the Raven II surgical robots, as open research platforms, have been serving the robotic surgery research community since 2002. The related article in this issue briefly presents the Raven I and the Raven II robots, and reviews recent publications describing research performed with the Raven robots, research on improvements to the Raven robots, or research directly compared with the Raven robots, and uses the Raven robots as a case study to discuss the popular research problems in the research community and the trend of robotic surgery study.

Other contributions to this volume describe systems and surgical techniques, such as the article from the group at Queens University, presenting two open-source technologies based on electromagnetic tracking: a navigation system to help target needles using a tracked needle guide, and software for electromagnetic reconstruction of catheter paths.

The overall accuracy assessment methods of image-guided systems are discussed and a stochastic approach is provided by the article from Óbuda University. In another paper from UniÓbuda, a review of the manual and automated Robot-Assisted Minimally Invasive Surgery (RAMIS) skill assessment techniques is provided, focusing on their general applicability, robustness and clinical relevance.

All advanced development projects relate in some way to engineering standards. A new standard, IEC 80601-2-77, was recently issued to establish safety requirements for surgical robots under regulatory control, and is reported on in the paper by a senior researcher at the Japanese National Institute of Advanced Industrial Science and Technology (AIST).

The contributions in this book are evidence that this community will continue to grow and strive for many more years, providing significant R&D results to feed the innovation chain in medical robotics towards the goal of better outcomes for surgical patients.

Budapest/Baltimore/Seattle  
August 2019

Tamás Haidegger  
Peter Kazanzides  
Blake Hannaford

# The Raven Open Surgical Robotic Platforms: A Review and Prospect

Yangming Li<sup>1</sup>, Blake Hannaford<sup>2</sup>, and Jacob Rosen<sup>3</sup>

<sup>1</sup>Department of Electrical Computer and Telecommunications Engineering  
Technology, Rochester Institute of Technology, Rochester, NY, USA 14623,  
yangming.li@rit.edu

<sup>2</sup>Departments of Electrical Engineering, University of Washington, Seattle, WA,  
USA 98195, blake@uw.edu

<sup>3</sup>Department of Mechanical and Aerospace Engineering, University of California,  
Los Angeles, CA, USA 90095, jacobrosen@ucla.edu

---

*Abstract:* The Raven I and the Raven II surgical robots, as open research platforms, have been serving the robotic surgery research community for ten years. The paper 1) briefly presents the Raven I and the Raven II robots, 2) reviews the recent publications that are built upon the Raven robots, aim to be applied to the Raven robots, or are directly compared with the Raven robots, and 3) uses the Raven robots as a case study to discuss the popular research problems in the research community and the trend of robotic surgery study. Instead of being a thorough literature review, this work only reviews the works formally published in the past three years and uses these recent publications to analyze the research interests, the popular open research problems, and opportunities in the topic of robotic surgery.

*Keywords:* the Raven Robots, Robotic Surgery, Open Platform

---

## 1 Introduction

In the past two decades, research on surgical robotics has made impressive progress. Surgical robots successfully transferred from research labs to operating rooms and even became the standard care for a number of surgeries.

Because of the high value of surgical tasks, the robotic surgery research has focused on the development and the validation of the devices and the techniques that are clinically practical from the very beginning. On one hand, realistically validating the robotic system promotes surgical robotics research, on the other hand, such validation raises the difficulty of surgical robot research as developing surgical robots often requires a significant amount of resources and technical accumulation.

The Raven I [1] and II [2] surgical robotic platforms were created to serve the robotic surgery research community as open platforms, designed for the study of robotic assisted Minimally Invasive Surgeries (MISs). The Raven robots are also compact in size, and low cost, making them widely adopted by 18 research institutes worldwide.

The Raven I and II surgical robots are designed to provide both hardware (mechanics and electronics) and software to support open research innovations. The Raven software is fully open-source [3] and is made ROS compatible, in order to support research in both the high-level robotic functional development and the low-level position and velocity control. In order to further promote the open robotic surgery research, Raven simulator and the online Raven access interface are under development.

This paper will assess the impact of Raven I and II by surveying the Raven related literature published in the past three years. Through reviewing the Raven literature, we attempt to summarize some of the recent progress in the research field and identify unmet needs and challenges.

This rest of this paper is organized as follows: Section II briefly describes the Raven I and II platforms. Section III quantifies Raven citations and analyzes the trends. Section IV analyzes and summarizes the Raven citations according to the research topics and contributions. Based on the analysis, discussions are made in the last section to conclude this work.

## 2 Surgical Robotics and Raven I and II Platforms

### 2.1 Overview

The introduction of surgical robotics into the operating room offers a significant breakthrough to potentially improve the quality and outcome of surgery. In robotic surgeries, two human-machine interfaces are established: the surgeon-robot interface (S-R) and the patient-robot interface (R-P). These two interfaces may be used to classify the various surgical robotic systems described as of the end of 2018 (Fig. 1). From the figure we can also see the development of surgical robotics and the shift of research interests. The detailed introduction to the surgical robots listed in Fig. 1 can be found in [4].

The Raven I and II surgical robots were first presented as full surgical platforms in [1] and [2] respectively (Figure 2). The Raven II evolved from the Raven I with improved mechanical design and software. This section summarizes some important features they have in common. From the hardware perspective, the Raven robots provide seven Degrees of Freedom (DoF) in manual Minimally Invasive Surgeries (MISs) (x, y, and z positions, three axes of rotation, and grasper open/close), through a seven DoF cable-driven robotic manipulator. The platform was specifically designed and optimized for MIS, as the remote center was built in with a spherical mechanism, and neither physical constraints nor control algorithms are needed to prevent tangential motions and forces, which could injure the patient at the insertion site in the abdominal wall. From the software perspective, the Raven



## 2.2 Raven Hardware

The Raven robot hardware consists of the master console (the surgeon site) and the slave robotic arms (the patient site).

The master console consists of devices that teleoperate the slave robots' movements, and a foot pedal that couples/decouples the master/slave motion synchronization. The Raven I robots used PHANTOM Omni devices to control the motion, and the Raven II robots can work with various control devices.

The slave robot arms and instruments contain the core of Raven mechanical design effort. Each Raven arm contains one rotational shoulder joint, one rotational elbow joint, one transnational insertion/retraction link, two grasper tip (finger) rotational links (one for rotation, the other one for open/close grasping), and two rotational wrist links (for the two different wrist rotational motions). The Raven II and the Raven I share the same fundamental mechanical design, such as having built-in remote centers, and 7 DoFs. The differences between the two platforms are: 1) the Raven II has the more compact mechanical design, 2) the Raven II improves the tool interface design.

The detailed hardware designs, including the mechanics, the DH parameters, the kinematics, and the electronics can be found in [1] and [2].

## 2.3 Raven Software

The Raven software design started from the safety requirements. The control system was built upon real-time Linux, and works at 1000 Hz. In order to achieve the software system reliability, the Raven software contains four states: initialization, pedal up, pedal down and an emergency stop. The software failures in the first three states are constantly monitored with a watchdog timer and a separate hardware PLC guarantees the failures are reliably caught and the system immediately switches to the emergency stop once failures are caught.

Both the Raven I and the Raven II software contain modules for hardware control and monitoring, forward and inverse kinematics, gravity compensation, and closed-loop control. The main differences between the two are: 1) the Raven I software is based on RTAI and the Raven II uses RT-Linux, 2) the Raven II software provides the ROS compatibility and contains more modules such as dynamics, state estimation, interactive force estimation, and autonomous motion planning. The latest Raven software can be found: <https://github.com/uw-biorobotics/raven2>.

In order to facilitate the robotic surgery research, an ongoing project is underway to unify the programming environment between the Raven platforms and another prominent research platform the da Vinci Research Kit [5] through 1) open APIs, 2) remote access, 3) simulators. The latest open-sourced APIs and simulators can be found here: <https://github.com/collaborative-robotics>.

### 3 Raven: An Open Platform for Robotic Surgery Study

The Raven platforms attract robotic surgery researchers through its open source software stack and flexible hardware interfaces. This section studies selected publications which cite the Raven I [1] and the Raven II [2] introduction papers. Only the publications in the last 3 years (Jan. 2016 Oct. 2018) are reviewed. According to Google Scholar (scholar.google.com), the two Raven papers [1,2] were cited 197 times since Jan. 2016. Only *research papers* that are formally published are included, which leads to 69 publications.

According to the relevance, the Raven citations are categorized into two groups: 1) the research described does not use the Raven platforms, 2) the research describes ones use the Raven platforms in their researches, we refer the later as “Direct”. In the former category, we further divide these publications into two groups, the ones related to robotic surgeries (referred as “Benchmark”) and the ones out of the scope of robotic surgeries (referred as “General”). The percentages of the three categories are shown in Fig. 3. The figure shows that it is reasonable to use the Raven platforms as a sample to study the prospect of robotic surgery study because it shows the Raven platforms have a broader impact on robotic surgery research and general robotic research.

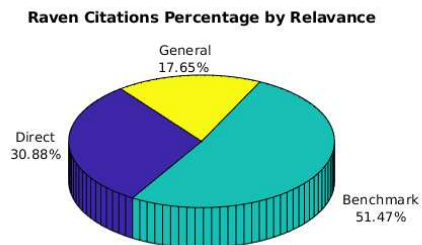


Figure 3

Percentage of Raven Citations by Relevance. The Raven citations are divided into three groups: 1) the ones that directly used Raven (indicated by “Direct”), 2) the ones not used Raven but related to robotic surgeries (referred as “Benchmark”), and 3) the ones not used Raven and out of the scope of robotic surgeries (referred as “General”).

We also summarize the Raven citations over the past three years to show the popularity of Raven related researches, as shown in Fig.4. The categorized publications based on the relevance to the Raven platforms is also compared with respect to time, as shown in Fig.5, to show the popularity and the trend of the related research.

It is interesting to see how the publications in each of the relevant categories vary with time (Fig. 5). From the figure we can see that the quantities of the surgical related Raven citations (the green line indicates the citations in the category

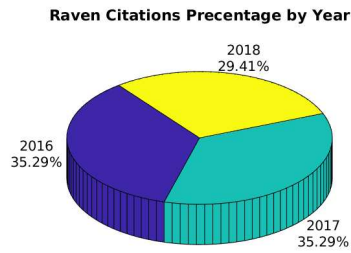


Figure 4

Raven Citations Distribution over Years. The figure shows the total number of the formally published Raven citations in 2016, 2017 and 2018. From the figure we can see that the Raven related research is stable in the number of publications.

“Benchmark”, the red line indicates the citations in the category “Direct”, the blue line indicates the citations in the category “General”, we can see that the Raven Platforms have bigger impact in the robotic surgery research community than in the general robotic research community, and the publications that use Raven .

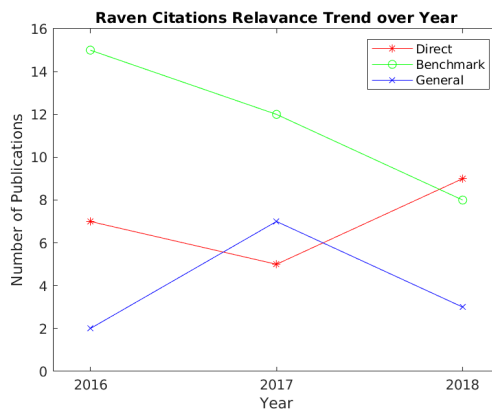


Figure 5

Raven Citations Relevance by Years. It categories the Raven citations by relevance and shows the numbers of citations in the three categories changed over years. From the figure we can see the total number of direct Raven research papers climbs up and matches the number of the publications used the Raven robots as a benchmark.

### 3.1 Research Citing Raven but Not Using Raven

As the Raven platforms are widely used in the robotic surgery research, many works have cited the Raven system but not used it in the research they describe. It may be instructive to analyze these papers to the extent they portray directions and frontiers of surgical robotics research today.

Several groups citing the Raven system have developed complete or nearly complete *surgical robotic systems* [6–12]. These systems often address new surgical procedures (such as pediatric cases or needle guidance) [6,9,10] novel delivery modes [8] or integration of industrial manipulators into surgery [12]

Numerous groups have developed *new hardware* influenced by the Raven design [12–22] or focused on numerical optimization of mechanisms [23]. Key aspects of these designs are minimally invasive character, often making a contribution such as novel mechanisms for decoupling motion at the laparoscopic entry port [13], decoupling drive axes [16], or reducing weight and size [19].

Novel mechanical design directions include integration with soft robotics [14], elbowed instrument design [20], mechanical decoupling design [13], and mechanical integration of novel force/torque sensors [19].

Other works focus on kinematic issues related to surgical robotics [12, 24–26], which are often approached from the point of view of improved motion control or teleoperation. Specific issues include manipulability index [24], singularity avoiding trajectory planning [12], and inverse kinematics algorithms for the particular requirements of surgical teleoperation [26].

### 3.2 Research Using Raven

The Raven platform users form a research community applying the system as a common experimental research platform. Much of this work has focused on issues related to *control, sensing, and software*. A challenging frontier for surgical robotic control software, drawing increasing study, is augmenting teleoperation with autonomous functions [27–32]. Such functions may trade control authority back and forth between computer and surgeon, or may share control of different degrees of freedom simultaneously with the surgeon [33].

Other work has used the Raven to study factors affecting *teleoperation performance* [34,35]. For example, experimental study focusing on effects of control parameters (in this case motion scale for the tool gripping axis) on a notion of human-centered transparency [36].

Several groups have used Raven in experiments studying *measurement or acquisition or updating of surgical skills* in robotic surgeons [37–39]. For example, [37] quantized robotic gestures into strings which were shown statistically able to discriminate skill level. Another skill assessment study [38] compared performance and learning of trainees between a hands-on user interface device and a contactless control interface based on a low cost (compared to haptic devices) depth sensing

camera and hand gestures. They concluded that such contactless sensing has utility in training applications. The metric used to assess the interfaces was based on an unsupervised gesture recognition system [39].

## 4 Problems and Trends in Robotic Surgeries: A Raven Perspective

The robotic surgery techniques have made impressive progress in the past two decades. Meanwhile, with the maturation of robotic surgical techniques, the research interests shift in order to expand the application of robotic surgeries and to improve surgical outcomes. In this section, we use the Raven platform as a sample to reveal the research problems that attract attention and to discuss the open problems and the trends in the community.

Raven citations reviewed above were categorized into 5 research topics: 1) simulation and training, 2) mechanical design, 3) modeling and control, 4) teleoperation, and 5) autonomy (Fig. 6). From the figure, it is clear that the modeling and control papers and the mechanical design papers are the two largest group of studies. Most of the mechanical design papers modeled the system so such papers are considered to belong to both of the two categories. We also visualized the number of citations in each of the 5 categories with respect to years (Fig. 7).

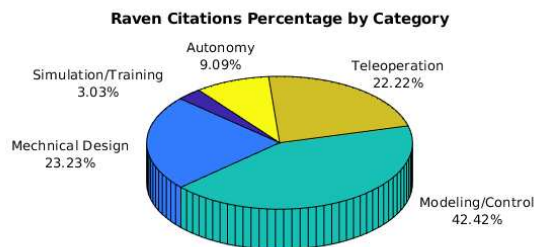


Figure 6

Raven Citations Percentage Distribution over Research Categories. It categorizes the Raven citations into five categories: 1) simulation and training, 2) mechanical design, 3) modeling and control, 4) teleoperation, 5) autonomy. The figure shows the modeling and the control is the biggest research area for the Raven related research.

Under the five categories, we further divide the citations into 10 sub-categories, as shown in Table 1, and show the numbers of citations in each of the subcategories. In the rest of this section, we analyze the publications in the 10 sub-categories to reveal the challenge problems and the trend in the research field.

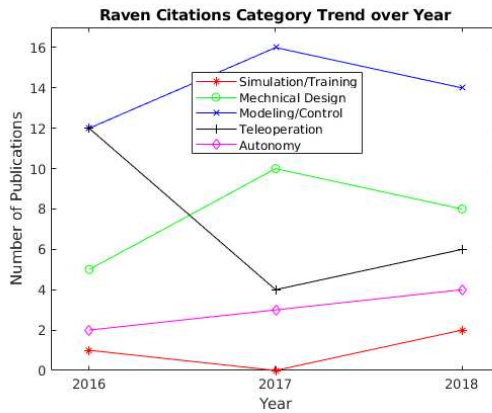


Figure 7

Categories of Raven Related Researches Trend Over Years. The mechanical design and the modeling/controlling research are dominant in raven related research. The two categories also share similar trends as the majority of the mechanical design publications also establishes the system (kinematic) models.

Year	Simulation Training		Mechanical Design		Modeling & Control		Teleoperation			Autonomy
	Simulation	Training	Rigid	Soft	Modeling	Learning	Master	System	Communication	
2016	1	0	5	0	12	0	3	3	6	2
2017	0	0	10	0	15	1	2	1	1	3
2018	0	2	7	1	14	0	4	1	1	4

Table 1

Publications Categorized by Topics over Years.

## 4.1 Modeling and Control

Reflecting researchers' interests, most of the Raven citations discussed the modeling and the control of surgical robots [6, 7, 9, 11–17, 19, 20, 23, 25–28, 33, 38–46, 46–62]. Most of the mechanical design publications also describe the corresponding system models and pointed out the suitable control methods.

Many of publications in this category focus on remaining challenges in modeling and control. For example, to model the control errors introduced by the driven tendons a Dahl friction model was proposed to predict cable tension for parallel robots in [51]. Some efforts were made from the hardware perspective such as the new surgical robot design and the corresponding model described in [15].

There are also papers on the new challenges in the robotic surgeries. For example, a new surgical robot that delivers improved dexterity in paediatric congenital esophageal atresia surgeries [6], and a control architecture that addresses the communication, the obstacle avoidance problems in surgeon/robot collaboration [54].

## 4.2 Mechanical Design

While the broader robotic community focuses on the robotic learning and the robotic vision problems, many of the efforts in the robotic surgery community were made in the area of mechanical design [6, 7, 10, 11, 13–20, 22, 23, 25, 38, 49, 50, 58, 63–66]. This is partially because the surgical robots are quickly expanded into new surgical disciplines, in which new designs are required to meet different requirements, for example, a percutaneous surgical robot [10]. More efforts are made to improve the dexterity, the stability and the control precision of surgical robots. For example, a new surgical instrument, featuring polymer based force sensors integrated into the instrument wrist and jaws [65], and a novel low-cost contactless optical sensor, designed to decrease the device costs and the human resource costs on training the operation of teleoperated surgical robotic systems [38].

## 4.3 Simulation and Evaluation

Simulation is a significant topic in robotic surgery as teleoperated robotic surgeries become more common and drive the need for a cost-efficient way to improve surgeons' skills in operating surgical robots. However, there is only one Raven citation that studies the simulation [61], and only two raven citations are about evaluation [37, 67].

## 4.4 Teleoperated Robotic Surgeries

As teleoperation is still the dominant way to control surgical robots, there are many Raven citations in this topic [8, 12, 24, 26, 34, 38, 39, 44, 63, 64, 66, 68–78]. While much research focuses on the classical teleoperation problems, such as the system architecture, the master controller and the communication problems, etc., we do see some new research problems attracting attention. A very important issue in a surgical robotic system is security from online adversaries. [71, 73, 74] studied cybersecurity issues *specific to telesurgery systems* using the Raven system.

## 4.5 Autonomous Robotic Surgeries

In a major contrast with the broader robotics community, there is only limited research on autonomy in robotic surgeries [27–29, 40, 43, 53, 70, 75]. Among these works, many focus on autonomizing surgical tasks, such as needle insertion [27] and suturing [28]. There are also some works on motion planning, either motion pattern planning [40, 53], or the planning of the motion trajectories [43, 70].

## 5 Discussion and Conclusion

In the past two decades, surgical robotics has made notable progress and attract more roboticists worldwide. The Raven platforms, designed to enable various exploratory

research through the open source software and the flexible hardware interfaces, have been serving the research community for more than 10 years. This paper used the Raven citations as a case study to review popular research problems and discusses the trends in robotic surgery study. In the literature review, we do notice some interesting phenomenon.

The surgical robot mechanical design and modeling is still the most popular research topic, according to the total number of Raven citations. More and more novel designs are proposed and developed to increase the robotic dexterity, the manipulability, the reliability, and to extend the application to new surgical procedures and address new challenges.

In contrast to the broader robotics field, machine learning, especially the deep learning, is not as popular in the surgical robotic research community. This may be due to: 1) the surgical data are often expensive so it is challenging to collect a big amount of data for training deep neural networks [79, 80], 2) the known challenging problems, such as environmental perception and dynamic planning, are not solved and can not reach desired reliability in the robotic surgery context [81–84], 3) the focus of the research community still lies on designing new robots, rather than improving robots' performance based on learning algorithms, 4) comparing with deep learning, the classical modeling methods are easier to interpolate and the performances are easier to predict, thus it is easier to predict the robot reliability.

The soft robot research in robotic surgeries is also not as popular as what we noticed in the general robotics. This may be because the Raven platforms are rigid robots and it is not straightforward to apply the soft robots on the Raven platforms or compare soft robots with the Raven.

## Acknowledgment

This work was partially supported by NSF grant IIS-1637444 and NIH grant 5R21EB016122-02.

## References

- [1] M. J. Lum, D. C. Friedman, G. Sankaranarayanan, H. King, K. Fodero, R. Leuschke, B. Hannaford, J. Rosen, and M. N. Sinanan, "The raven: Design and validation of a telesurgery system," *The International Journal of Robotics Research*, vol. 28, no. 9, pp. 1183–1197, 2009.
- [2] B. Hannaford, J. Rosen, D. W. Friedman, H. King, P. Roan, L. Cheng, D. Glozman, J. Ma, S. N. Kosari, and L. White, "Raven-ii: an open platform for surgical robotics research," *IEEE Transactions on Biomedical Engineering*, vol. 60, no. 4, pp. 954–959, 2013.
- [3] B. Lab., "Raven II Software." <https://github.com/uw-biorobotics>, 2018.

- 
- [4] J. Rosen, B. Hannaford, and R. M. Satava, *Surgical robotics: systems applications and visions*. Springer Science & Business Media, 2011.
- [5] P. Kazanzides, Z. Chen, A. Deguet, G. S. Fischer, R. H. Taylor, and S. P. DiMaio, "An open-source research kit for the da vinci® surgical system," in *Robotics and Automation (ICRA), 2014 IEEE International Conference on*, pp. 6434–6439, IEEE, 2014.
- [6] M. Kim, C. Lee, N. Hong, Y. J. Kim, and S. Kim, "Development of stereo endoscope system with its innovative master interface for continuous surgical operation," *Biomedical engineering online*, vol. 16, no. 1, p. 81, 2017.
- [7] Y. Ai, B. Pan, Y. Fu, and S. Wang, "Design of a novel robotic system for minimally invasive surgery," *Industrial Robot: An International Journal*, vol. 44, no. 3, pp. 288–298, 2017.
- [8] M. Reichenbach, T. Frederick, L. Cubrich, W. Bircher, N. Bills, M. Morien, S. Farritor, and D. Oleynikov, "Telesurgery with miniature robots to leverage surgical expertise in distributed expeditionary environments," *Military medicine*, vol. 182, no. suppl\_1, pp. 316–321, 2017.
- [9] Q. Liu, C. Shi, B. Zhang, C. Wang, L. Duan, T. Sun, X. Zhang, W. Li, Z. Wu, and M. G. Fujie, "Development of a novel paediatric surgical assist robot for tissue manipulation in a narrow workspace," *Assembly Automation*, vol. 37, no. 3, pp. 335–348, 2017.
- [10] C. Zhou, H. Wu, X. Xu, Y. Liu, Q. Zhu, and S. Pan, "Development and control of a robotic arm for percutaneous surgery," *Assembly Automation*, vol. 37, no. 3, pp. 314–321, 2017.
- [11] M. Kim, C. Lee, W. J. Park, Y. S. Suh, H. K. Yang, H. J. Kim, and S. Kim, "A development of assistant surgical robot system based on surgical-operation-by-wire and hands-on-throttle-and-stick," *Biomedical engineering online*, vol. 15, no. 1, p. 58, 2016.
- [12] M. M. Marinho, M. C. Bernardes, and A. P. Bo, "Using general-purpose serial-link manipulators for laparoscopic surgery with moving remote center of motion," *Journal of Medical Robotics Research*, vol. 1, no. 04, p. 1650007, 2016.
- [13] G. Niu, B. Pan, F. Zhang, H. Feng, and Y. Fu, "Improved surgical instruments without coupled motion used in minimally invasive surgery," *The International Journal of Medical Robotics and Computer Assisted Surgery*, p. e1942, 2018.
- [14] A. Diodato, M. Brancadoro, G. De Rossi, H. Abidi, D. Dall'Alba, R. Muradore, G. Ciuti, P. Fiorini, A. Menciassi, and M. Cianchetti, "Soft robotic manipulator for improving dexterity in minimally invasive surgery," *Surgical innovation*, vol. 25, no. 1, pp. 69–76, 2018.
- [15] G. Niu, B. Pan, F. Zhang, H. Feng, W. Gao, and Y. Fu, "Dimensional synthesis and concept design of a novel minimally invasive surgical robot," *Robotica*, vol. 36, no. 5, pp. 715–737, 2018.

- [16] W. Xu, Y. Wang, S. Jiang, J. Yao, and B. Chen, "Kinematic analysis of a newly designed cable-driven manipulator," *Transactions of the Canadian Society for Mechanical Engineering*, vol. 42, no. 2, pp. 125–135, 2018.
- [17] M. Bazman, N. Yilmaz, and U. Tumerdem, "Dexterous and back-drivable parallel robotic forceps wrist for robotic surgery," in *Advanced Motion Control (AMC), 2018 IEEE 15th International Workshop on*, pp. 153–159, IEEE, 2018.
- [18] S. Nisar, T. Endo, and F. Matsuno, "Design and kinematic optimization of a two degrees-of-freedom planar remote center of motion mechanism for minimally invasive surgery manipulators," *Journal of Mechanisms and Robotics*, vol. 9, no. 3, p. 031013, 2017.
- [19] U. Kim, D.-H. Lee, Y. B. Kim, D.-Y. Seok, J. So, and H. R. Choi, "S-surge: Novel portable surgical robot with multiaxis force-sensing capability for minimally invasive surgery," *IEEE/ASME Transactions on Mechatronics*, vol. 22, no. 4, pp. 1717–1727, 2017.
- [20] M. Hwang, U.-J. Yang, D. Kong, D. G. Chung, J.-g. Lim, D.-H. Lee, D. H. Kim, D. Shin, T. Jang, J.-W. Kim, *et al.*, "A single port surgical robot system with novel elbow joint mechanism for high force transmission," *The International Journal of Medical Robotics and Computer Assisted Surgery*, vol. 13, no. 4, p. e1808, 2017.
- [21] J. Rosen, L. N. Sekhar, D. Glozman, M. Miyasaka, J. Doshier, B. Dellon, K. S. Moe, A. Kim, L. J. Kim, T. Lendvay, *et al.*, "Roboscope: A flexible and bendable surgical robot for single portal minimally invasive surgery," in *Robotics and Automation (ICRA), 2017 IEEE International Conference on*, pp. 2364–2370, IEEE, 2017.
- [22] L. Cubrich, M. A. Reichenbach, J. D. Carlson, A. Pracht, B. Terry, D. Oleynikov, and S. Farritor, "A four-dof laparo-endoscopic single site platform for rapidly-developing next-generation surgical robotics," *Journal of Medical Robotics Research*, vol. 1, no. 04, p. 1650006, 2016.
- [23] G.-j. Niu, B. Pan, F.-h. Zhang, H.-b. Feng, and Y.-l. Fu, "Multi-optimization of a spherical mechanism for minimally invasive surgery," *Journal of Central South University*, vol. 24, no. 6, pp. 1406–1417, 2017.
- [24] A. Torabi, M. Khadem, K. Zareinia, G. R. Sutherland, and M. Tavakoli, "Manipulability of teleoperated surgical robots with application in design of master/slave manipulators," in *Medical Robotics (ISMR), 2018 International Symposium on*, pp. 1–6, IEEE, 2018.
- [25] S. Singh, A. Singla, and E. Singla, "Modular manipulators for cluttered environments: A task-based configuration design approach," *Journal of Mechanisms and Robotics*, vol. 10, no. 5, p. 051010, 2018.
- [26] D. Yang, L. Wang, and Y. Li, "Kinematic analysis and simulation of a mistr system using bimanual manipulator," in *Robotics and Biomimetics (ROBIO), 2016 IEEE International Conference on*, pp. 271–276, IEEE, 2016.

- [27] H. Dehghani, S. Farritor, D. Oleynikov, and B. Terry, "Automation of suturing path generation for da vinci-like surgical robotic systems," in *2018 Design of Medical Devices Conference*, pp. V001T07A008–V001T07A008, American Society of Mechanical Engineers, 2018.
- [28] S. A. Pedram, P. Ferguson, J. Ma, E. Dutson, and J. Rosen, "Autonomous suturing via surgical robot: An algorithm for optimal selection of needle diameter, shape, and path," in *Robotics and Automation (ICRA), 2017 IEEE International Conference on*, pp. 2391–2398, IEEE, 2017.
- [29] S. McKinley, A. Garg, S. Sen, D. V. Gealy, J. P. McKinley, Y. Jen, and K. Goldberg, "Autonomous multilateral surgical tumor resection with interchangeable instrument mounts and fluid injection device," in *2016 IEEE International Conference on Robotics and Automation (ICRA)*, 2016.
- [30] D. Hu, Y. Gong, B. Hannaford, and E. J. Seibel, "Semi-autonomous simulated brain tumor ablation with ravenii surgical robot using behavior tree," in *2015 IEEE International Conference on Robotics and Automation (ICRA)*, pp. 3868–3875, IEEE, 2015.
- [31] D. Hu, Y. Gong, E. J. Seibel, L. N. Sekhar, and B. Hannaford, "Semi-autonomous image-guided brain tumour resection using an integrated robotic system: A bench-top study," *The International Journal of Medical Robotics and Computer Assisted Surgery*, 2017.
- [32] D. Hu, Y. Gong, B. Hannaford, and E. J. Seibel, "Path planning for semi-automated simulated robotic neurosurgery," in *2015 IEEE/RSJ International Conference on Intelligent Robots and Systems (IROS)*, September 2015.
- [33] R. J. Varghese, P. Berthet-Rayne, P. Giataganas, V. Vitiello, and G.-Z. Yang, "A framework for sensorless and autonomous probe-tissue contact management in robotic endomicroscopic scanning," in *Robotics and Automation (ICRA), 2017 IEEE International Conference on*, pp. 1738–1745, IEEE, 2017.
- [34] A. Milstein, T. Ganel, S. Berman, and I. Nisky, "Human-centered transparency of grasping via a robot-assisted minimally invasive surgery system," *IEEE Transactions on Human-Machine Systems*, vol. 48, no. 4, pp. 349–358, 2018.
- [35] A. Milstein, T. Ganel, S. Berman, and I. Nisky, "The scaling of the gripper affects the action and perception in teleoperated grasping via a robot-assisted minimally invasive surgery system," *arXiv preprint arXiv:1710.05319*, 2017.
- [36] I. Nisky, F. A. Mussa-Ivaldi, and A. Karniel, "Analytical study of perceptual and motor transparency in bilateral teleoperation," *IEEE Transactions on Human-Machine Systems*, vol. 43, no. 6, pp. 570–582, 2013.
- [37] G. Forestier, F. Petitjean, P. Senin, F. Despinoy, A. Huaultmé, H. I. Fawaz, J. Weber, L. Idoumghar, P.-A. Muller, and P. Jannin, "Surgical motion analysis using discriminative interpretable patterns," *Artificial intelligence in medicine*, 2018.

- [38] F. Despinoy, N. Zemiti, G. Forestier, A. Sánchez, P. Jannin, and P. Poignet, “Evaluation of contactless human–machine interface for robotic surgical training,” *International journal of computer assisted radiology and surgery*, vol. 13, no. 1, pp. 13–24, 2018.
- [39] F. Despinoy, D. Bouget, G. Forestier, C. Penet, N. Zemiti, P. Poignet, and P. Jannin, “Unsupervised trajectory segmentation for surgical gesture recognition in robotic training,” *IEEE Transactions on Biomedical Engineering*, vol. 63, no. 6, pp. 1280–1291, 2016.
- [40] Y. Li, S. Li, and B. Hannaford, “A model based recurrent neural network with randomness for efficient control with applications,” *IEEE Transactions on Industrial Informatics*, 2018.
- [41] W. Yu, *PID Control with Intelligent Compensation for Exoskeleton Robots*. Academic Press, 2018.
- [42] S.-H. Choi and K.-S. Park, “Integrated and nonlinear dynamic model of a polymer cable for low-speed cable-driven parallel robots,” *Microsystem Technologies*, pp. 1–11, 2018.
- [43] Y. Li, S. Li, and B. Hannaford, “A novel recurrent neural network control scheme for improving redundant manipulator motion planning completeness,” in *Robotics and Automation (ICRA), 2018 IEEE International Conference on*, p. 1 6, IEEE, 2018.
- [44] C. Bergeles, “Toward intracorporeally navigated untethered microsurgions,”
- [45] Y. Li, R. A. Bly, R. A. Harbison, I. M. Humphreys, M. E. Whipple, B. Hannaford, and K. S. Moe, “Anatomical region segmentation for objective surgical skill assessment with operating room motion data,” *Journal of Neurological Surgery Part B: Skull Base*, vol. 369, no. 15, pp. 1434–1442, 2017.
- [46] S.-H. Choi and K.-S. Park, “Advanced numerical modeling of nonlinear elastic cable with recovery characteristics,” in *ASME 2017 Conference on Information Storage and Processing Systems collocated with the ASME 2017 Conference on Information Storage and Processing Systems*, pp. V001T07A009–V001T07A009, American Society of Mechanical Engineers, 2017.
- [47] Y. Li, S. Li, M. Miyasaka, A. Lewis, and B. Hannaford, “Improving control precision and motion adaptiveness for surgical robot with recurrent neural network,” in *Intelligent Robots and Systems (IROS), 2017 IEEE/RSJ International Conference on*, pp. 1–6, IEEE, 2017.
- [48] Y. Li and B. Hannaford, “Gaussian process regression for sensorless grip force estimation of cable-driven elongated surgical instruments,” *IEEE Robotics and Automation Letters*, vol. 2, no. 3, pp. 1312–1319, 2017.
- [49] V. Megaro, E. Knoop, A. Spielberg, D. I. Levin, W. Matusik, M. Gross, B. Thomaszewski, and M. Bächer, “Designing cable-driven actuation networks for kinematic chains and trees,” in *Proceedings of the ACM SIG-*

- GRAPH/Eurographics Symposium on Computer Animation*, p. 15, ACM, 2017.
- [50] F. Anooshahpour, P. Yadmellat, I. G. Polushin, and R. V. Patel, “Modeling of tendon-pulley transmission systems with application to surgical robots: A preliminary experimental validation,” in *Advanced Intelligent Mechatronics (AIM), 2017 IEEE International Conference on*, pp. 761–766, IEEE, 2017.
- [51] S.-H. Choi, J.-O. Park, and K.-S. Park, “Tension analysis of a 6-degree-of-freedom cable-driven parallel robot considering dynamic pulley bearing friction,” *Advances in Mechanical Engineering*, vol. 9, no. 8, p. 1687814017714981, 2017.
- [52] S.-H. Choi and K.-S. Park, “The integrated elasto-plastic cable modeling for cable driven parallel robots (cdprs),” in *Control, Automation and Systems (IC-CAS), 2017 17th International Conference on*, pp. 420–422, IEEE, 2017.
- [53] Y. Li and B. Hannaford, “Soft-obstacle avoidance for redundant manipulators with recurrent neural network,” in *Intelligent Robots and Systems (IROS), 2018 IEEE/RSJ International Conference on*, pp. 1–6, IEEE, 2018.
- [54] E. Bauzano, B. Estebanez, I. Garcia-Morales, and V. F. Muñoz, “Collaborative human–robot system for hals suture procedures,” *IEEE Systems Journal*, vol. 10, no. 3, pp. 957–966, 2016.
- [55] B. Hannaford, D. Hu, D. Zhang, and Y. Li, “Simulation results on selector adaptation in behavior trees,” 2016.
- [56] T. Beyl, P. Nicolai, M. D. Comparetti, J. Raczkowski, E. De Momi, and H. Wörn, “Time-of-flight-assisted kinect camera-based people detection for intuitive human robot cooperation in the surgical operating room,” *International journal of computer assisted radiology and surgery*, vol. 11, no. 7, pp. 1329–1345, 2016.
- [57] M. Haghhighipناه, M. Miyasaka, Y. Li, and B. Hannaford, “Unscented kalman filter and 3d vision to improve cable driven surgical robot joint angle estimation,” in *Robotics and Automation (ICRA), 2016 IEEE International Conference on*, pp. 4135–4142, IEEE, 2016.
- [58] Y. Ai, B. Pan, Y. Fu, and S. Wang, “Control system design for a novel minimally invasive surgical robot,” *Computer Assisted Surgery*, vol. 21, no. sup1, pp. 45–53, 2016.
- [59] Y. Li, M. Miyasaka, M. Haghhighipناه, L. Cheng, and B. Hannaford, “Dynamic modeling of cable driven elongated surgical instruments for sensorless grip force estimation,” in *Robotics and Automation (ICRA), 2016 IEEE International Conference on*, pp. 4128–4134, IEEE, 2016.
- [60] M. Miyasaka, M. Haghhighipناه, Y. Li, and B. Hannaford, “Hysteresis model of longitudinally loaded cable for cable driven robots and identification of the parameters,” in *Robotics and Automation (ICRA), 2016 IEEE International Conference on*, pp. 4051–4057, IEEE, 2016.

- [61] A. Bhardwaj, A. Jain, and V. Agarwal, “Preoperative planning simulator with haptic feedback for raven-ii surgical robotics platform,” in *Computing for Sustainable Global Development (INDIACom), 2016 3rd International Conference on*, pp. 2443–2448, IEEE, 2016.
- [62] M. Haghhighipanah, Y. Li, M. Miyasaka, and B. Hannaford, “Improving position precision of a servo-controlled elastic cable driven surgical robot using unscented kalman filter,” in *Intelligent Robots and Systems (IROS), 2015 IEEE/RSJ International Conference on*, pp. 2030–2036, IEEE, 2015.
- [63] H. Lee, B. Cheon, M. Hwang, D. Kang, and D.-S. Kwon, “A master manipulator with a remote-center-of-motion kinematic structure for a minimally invasive robotic surgical system,” *The International Journal of Medical Robotics and Computer Assisted Surgery*, vol. 14, no. 1, p. e1865, 2018.
- [64] T. Wang, B. Pan, Y. Fu, S. Wang, and Y. Ai, “Design of a new haptic device and experiments in minimally invasive surgical robot,” *Computer Assisted Surgery*, vol. 22, no. sup1, pp. 240–250, 2017.
- [65] D.-H. Lee, U. Kim, T. Gulrez, W. J. Yoon, B. Hannaford, and H. R. Choi, “A laparoscopic grasping tool with force sensing capability,” *IEEE/ASME Transactions on Mechatronics*, vol. 21, no. 1, pp. 130–141, 2016.
- [66] A. Tzemanaki, L. Fracczak, D. Gillatt, A. Koupparis, C. Melhuish, R. Persad, E. Rowe, A. G. Pipe, and S. Dogramadzi, “Design of a multi-dof cable-driven mechanism of a miniature serial manipulator for robot-assisted minimally invasive surgery,” in *Biomedical Robotics and Biomechanics (BioRob), 2016 6th IEEE International Conference on*, pp. 55–60, IEEE, 2016.
- [67] K. Liang, Y. Xing, J. Li, S. Wang, A. Li, and J. Li, “Motion control skill assessment based on kinematic analysis of robotic end-effector movements,” *The International Journal of Medical Robotics and Computer Assisted Surgery*, vol. 14, no. 1, p. e1845, 2018.
- [68] A. Munteanu, R. Muradore, M. Merro, and P. Fiorini, “On cyber-physical attacks in bilateral teleoperation systems: An experimental analysis,” in *2018 IEEE Industrial Cyber-Physical Systems (ICPS)*, pp. 159–166, IEEE, 2018.
- [69] T. Frank, A. Krieger, S. Leonard, N. A. Patel, and J. Tokuda, “Ros-igtl-bridge: an open network interface for image-guided therapy using the ros environment,” *International journal of computer assisted radiology and surgery*, vol. 12, no. 8, pp. 1451–1460, 2017.
- [70] T. Matsunaga, T. Okano, X. Sun, T. Mizoguchi, and K. Ohnishi, “Motion reproduction system using multi dof haptic forceps robots for ligation task,” in *Industrial Electronics Society, IECON 2017-43rd Annual Conference of the IEEE*, pp. 2888–2893, IEEE, 2017.
- [71] H. Alemzadeh, J. Raman, N. Leveson, Z. Kalbarczyk, and R. K. Iyer, “Adverse events in robotic surgery: a retrospective study of 14 years of fda data,” *PloS one*, vol. 11, no. 4, p. e0151470, 2016.

- [72] H. Wei, Z. Shao, Z. Huang, R. Chen, Y. Guan, J. Tan, and Z. Shao, "Rt-ros: A real-time ros architecture on multi-core processors," *Future Generation Computer Systems*, vol. 56, pp. 171–178, 2016.
- [73] H. Alemzadeh, D. Chen, X. Li, T. Kesavadas, Z. T. Kalbarczyk, and R. K. Iyer, "Targeted attacks on teleoperated surgical robots: Dynamic model-based detection and mitigation," in *Dependable Systems and Networks (DSN), 2016 46th Annual IEEE/IFIP International Conference on*, pp. 395–406, IEEE, 2016.
- [74] H. Lin, H. Alemzadeh, D. Chen, Z. Kalbarczyk, and R. K. Iyer, "Safety-critical cyber-physical attacks: Analysis, detection, and mitigation," in *Proceedings of the Symposium and Bootcamp on the Science of Security*, pp. 82–89, ACM, 2016.
- [75] N. Preda, F. Ferraguti, G. De Rossi, C. Secchi, R. Muradore, P. Fiorini, and M. Bonfè, "A cognitive robot control architecture for autonomous execution of surgical tasks," *Journal of Medical Robotics Research*, vol. 1, no. 04, p. 1650008, 2016.
- [76] G. Niu, B. Pan, Y. Ai, and Y. Fu, "Intuitive control algorithm of a novel minimally invasive surgical robot," *Computer Assisted Surgery*, vol. 21, no. sup1, pp. 92–101, 2016.
- [77] X. Da, Q. Cao, P. Chen, and M. Adachi, "Architecture design for a mis robot control system,"
- [78] S. Sundarapandian, S. Ferris-Francis, H. Michko, C. Charters, J. Miller, and N. Prabakar, "A novel communication architecture and control system for telebot: A multi-modal telepresence robot for disabled officers.," *International Journal of Next-Generation Computing*, vol. 7, no. 3, 2016.
- [79] Y. Li, R. Bly, M. Whipple, I. Humphreys, B. Hannaford, and K. Moe, "Use endoscope and instrument and pathway relative motion as metric for automated objective surgical skill assessment in skull base and sinus surgery," in *Journal of Neurological Surgery Part B: Skull Base*, vol. 79, p. A194, Georg Thieme Verlag KG, 2018.
- [80] R. A. Harbison, Y. Li, A. M. Berens, R. A. Bly, B. Hannaford, and K. S. Moe, "An automated methodology for assessing anatomy-specific instrument motion during endoscopic endonasal skull base surgery," *Journal of Neurological Surgery Part B: Skull Base*, vol. 38, no. 03, pp. 222–226, 2017.
- [81] Y. Li, J. Zhang, and S. Li, "STMVO: biologically inspired monocular visual odometry," *Neural Computing and Applications*, vol. 29, no. 6, pp. 215–225, 2018.
- [82] F. Qin, Y. Li, Y.-H. Su, D. Xu, and B. Hannaford, "Surgical instrument segmentation for endoscopic vision with data fusion of cnn prediction and kinematic pose," in *Robotics and Automation (ICRA), 2019 IEEE International Conference on*, pp. 1–6, IEEE, 2019.

- 
- [83] Y. Li, S. Li, Q. Song, H. Liu, and M. Q.-H. Meng, “Fast and robust data association using posterior based approximate joint compatibility test,” *IEEE Transactions on Industrial Informatics*, vol. 10, no. 1, pp. 331–339, 2014.
- [84] B. Thananjeyan, A. Garg, S. Krishnan, C. Chen, L. Miller, and K. Goldberg, “Multilateral surgical pattern cutting in 2d orthotropic gauze with deep reinforcement learning policies for tensioning,” in *2017 IEEE International Conference on Robotics and Automation (ICRA)*, pp. 2371–2378, IEEE, 2017.

# An Approach to Modeling Closed-Loop Kinematic Chain Mechanisms, Applied to Simulations of the da Vinci Surgical System

**Radian A Gondokaryono<sup>1†</sup>, Ankur Agrawal<sup>1†</sup>, Adnan Munawar<sup>1</sup>, Christopher J Nycz<sup>1</sup>, and Gregory S Fischer<sup>1</sup>**

<sup>1</sup>Robotics Engineering Department, 85 Prescott St, Worcester, MA, USA, 01609

<sup>†</sup>These authors contributed equally to this work

ragondokaryono@wpi.edu, asagrawal@wpi.edu, amunawar@wpi.edu,  
cjnycz@wpi.edu, gfischer@wpi.edu

---

*Abstract: Open-sourced kinematic models of the da Vinci Surgical System have previously been developed using serial chains for forward and inverse kinematics. However, these models do not describe the motion of every link in the closed-loop mechanism of the da Vinci manipulators; knowing the kinematics of all components in motion is essential for the foundation of modeling the system dynamics and implementing representative simulations. This paper proposes a modeling method of the closed-loop kinematics, using the existing da Vinci kinematics and an optical motion capture link length calibration. Resulting link lengths and DH parameters are presented and used as the basis for ROS-based simulation models. The models were simulated in RViz visualization simulation and Gazebo dynamics simulation. Additionally, the closed-loop kinematic chain was verified by comparing the remote center of motion location of simulation with the hardware. Furthermore, the dynamic simulation resulted in satisfactory joint stability and performance. All models and simulations are provided as an open-source package.*

*Keywords: Surgical Robots; Closed Chain Model; Kinematic Calibration; ROS Simulations*

---

## 1 Introduction

Advances in the field of medical robotics have enabled the commercial success of tele-operated surgical robots in medical practice. Among these robots, the Intuitive Surgical's da Vinci is the most recognized system in the market [1]. Although there are a number of different models and configurations, the da Vinci, Figure 1, typically comprises of three slave Patient Side Manipulators (PSMs), one slave Endoscope Camera Manipulator (ECM), a passive Setup Joint (SUJ)

Cart and two Master Tool Manipulators (MTMs). The SUJ Cart is used to position the PSM and ECM manipulators in the desired configuration with respect to the patient before the surgical procedure [2]. The manipulators' tool is inserted through a trocar which is placed through the incision of the patient. The surgeon then controls the movement of these tools using the MTMs.

The success of the da Vinci in clinical practice has sparked significant research efforts worldwide to augment the currently available functionality. For example, adding haptic sensing to restore tactile feel [3], automating camera control to reduce the effort of operation [4], and adding an assistive control to increase the safety of the system [5]. Robot-assisted surgery using da Vinci involves many challenging subtasks. One of the more challenging subtasks is suturing and is an active research topic in terms of automation [6].

To accommodate this expanding research related to novel algorithms, John Hopkins University and Worcester Polytechnic Institute have developed software and firmware in conjunction with hardware [7] [8] to access low-level control data of the PSMs, ECM, and MTMs. The da Vinci robot, the open-source hardware robot controllers, and the open-source software/firmware is called the da Vinci Research Kit (dVRK).

Among the open-source applications, the dVRK community has also provided kinematic models of the PSMs, ECM, and MTMs (<https://github.com/WPI-AIM/dvrk-ros>) which visualizes the hardware components. These models correspond to the dVRK forward kinematics used for position control which represents each manipulator as a serial chain. This is done by simplification of the remote center of motion (RCM) in Figure 2 where the double four-bar linkage (yellow, orange, and pink lines) is represented as one joint with an axis of rotation at the RCM. An RCM is a fixed virtual point in space constructed by two intersecting rotation axis of the first and second joints.

While suited for real-time kinematic applications, this simplification does not accurately describe the motion of every link which is used as a foundation for describing the dynamics of the manipulators. Essentially, dynamics are necessary for a variety of applications including model-based control [9], gravity compensation [10] and representative simulations [11].

Most da Vinci simulations such as dV-Trainer [12] and Robotic Surgery Simulator (RoSS) [13] are used for training surgeons [14]. Research on the objective criteria of these simulations has been done, for example, on the force/torque evaluation of surgical skills in minimally invasive surgery [15]. Many research examples on haptics and force feedback [16] of the System suggests that accurate kinematics and dynamics should be an essential feature of a simulation. Such a simulation of the da Vinci has been developed in V-REP for research of novel control algorithms in [11].

This paper presents the procedure to obtain closed-loop kinematic chain models of the da Vinci Surgical System. Models were first developed using the dVRK forward kinematics. Next, a motion capture system with least squares axis calibration method is used for obtaining the missing data of the double four-bar linkage. To provide a useful application, the models are simulated in Robot Operating Systems [17] (ROS) visualization tool namely RViz [18], and Gazebo. Gazebo uses physics engines to simulate dynamics [19]. While RViz currently only supports serial chains, it is possible to add closed-loop kinematic chains in Gazebo [20]. The simulated RCM of the models is then verified with the physical RCM of the hardware using a least squares calibration of the tool-tip obtained via motion capture system. The presented models and the simulations are available as an open-source package at [https://github.com/WPI-AIM/dvrk\\_env](https://github.com/WPI-AIM/dvrk_env).

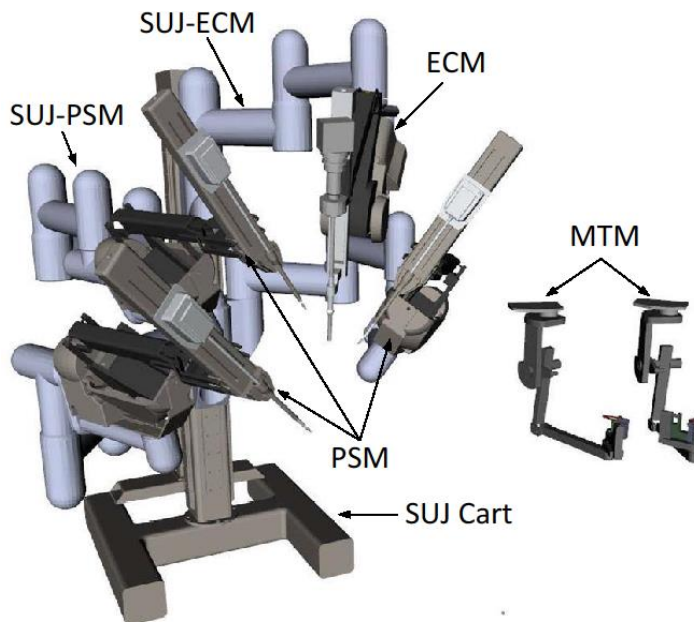


Figure 1

The da Vinci Surgical System simulated in RViz

## 2 Kinematic Modeling

Figure 1 shows the daVinci surgical system divided into main components: a Setup Joint (SUJ) Cart, three passive SUJ-PSM 6 degree-of-freedom (DOF) arms, one passive SUJ-ECM 4 DOF arm, three PSMs, one ECM, and two MTMs.

The kinematics of the SUJ Cart, SUJ-PSM, and SUJ-ECM were readily available in the dVRK repository [6] and are explained here for an understanding of the

CAD/Simulation model development in Section 3. The serial chain kinematics of the PSM, and ECM in the dVRK repository are used for manipulator Cartesian position control of the dVRK. Therefore, our close-loop kinematic chain models correspond to the dVRK repository serial chain kinematic models. The missing closed-loop kinematic chain parameters are obtained with an optical motion capture axis distance calibration method explained in Section 2.4. The following sub-sections explain the developed kinematic models utilizing modified Denavit-Hartenberg (DH) convention.

## 2.1 Setup Joint Cart

The SUJ-PSM arms have 6 DOF each described by a vertical prismatic joint, four vertical revolute joints, and a horizontal revolute joint. Table 1 describes the modified DH parameters for the identical SUJ-PSM1 and SUJ-PSM2 arms. Table 2 describes the SUJ-PSM3 arm which has similar kinematics to SUJ-PSM1, 2, but different lengths. Table 3 describes the SUJ-ECM which is similar to SUJ-PSM until the last vertical revolute joint at which the ECM is mounted at a 45-degree angle.

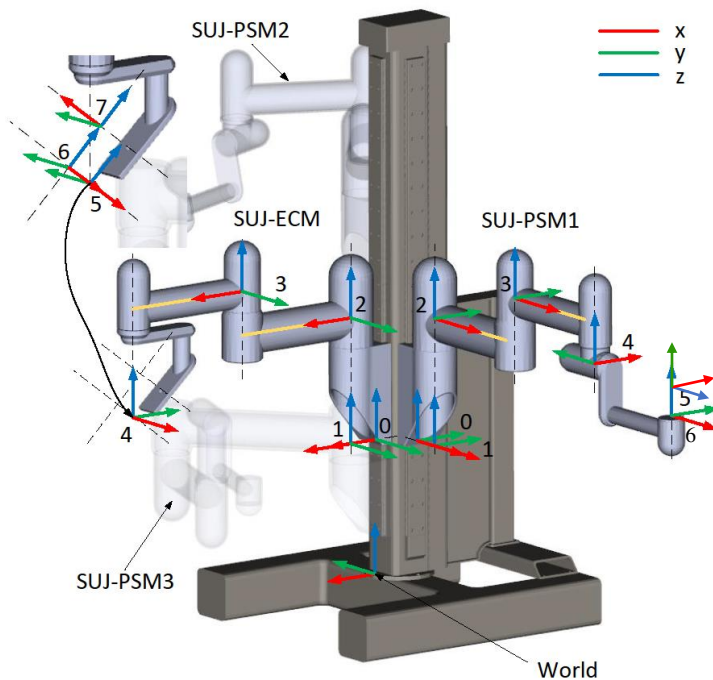


Figure 2

Set Up Joint (SUJ) Cart kinematics and frame definitions shown in Rviz

Table 1  
SUJ-PSM1, 2 modified DH parameters

Link	Joint	$a_i [m]$	$\alpha_i [rad]$	$d_i [m]$	$\theta_i [rad]$
1	P	0.0896	0	$q_1$	0
2	R	0	0	0.4166	$q_2$
3	R	0.4318	0	0.1429	$q_3$
4	R	0.4318	0	-0.1302	$q_4 + \pi/2$
5	R	0	$\pi/2$	0.4089	$q_5$
6	R	0	$-\pi/2$	-0.1029	$q_6 - \pi/2$

Table 2  
SUJ-PSM3 modified DH parameters

Link	Joint	$a_i [m]$	$\alpha_i [rad]$	$d_i [m]$	$\theta_i [rad]$
1	P	0.0896	0	$q_1$	0
2	R	0	0	0.3404	$q_2$
3	R	0.5842	0	0.1429	$q_3$
4	R	0.4318	0	0.2571	$q_4 + \pi/2$
5	R	0	$\pi/2$	0.4089	$q_5$
6	R	0	$-\pi/2$	-0.1029	$q_6 - \pi/2$

Table 3  
SUJ-ECM modified DH parameters

Link	Joint	$a_i [m]$	$\alpha_i [rad]$	$d_i [m]$	$\theta_i [rad]$
1	P	0.0896	0	$q_1$	0
2	R	0	0	0.4166	$q_2$
3	R	0.4318	0	0.1429	$q_3$
4	R	0.4318	0	-0.3459	$q_4 + \pi/2$
5	R	0	-0.7853	0	$\pi/2$
6	R	-0.0667	0	0	0
7	R	0	0	0.1029	$\pi/2$

## 2.2 Patient Side Manipulator

The PSM kinematics and associated frame definitions are described in Figure 3. Following the modified DH convention, the axis of rotation (translation for prismatic joints),  $q_i$ , of each frame corresponds to the z-axis (blue). Positive rotation is counterclockwise.

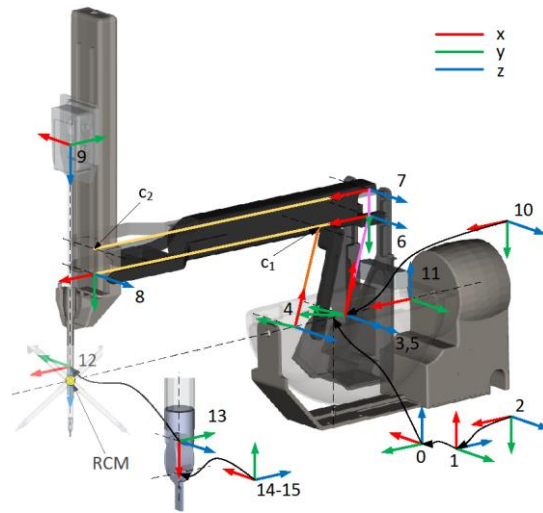


Figure 3

Patient Side Manipulator (PSM) kinematics and frame definitions shown in RViz. Pink, orange, and yellow lines show separate parts of the four-bar linkage (Frames 3-8). RCM: Remote Center of Motion

Frame 0 of the PSM is attached to frame 6 of the SUJ-PSM. Frame 1 describes a yaw motion actuated by the first joint,  $q_1$ . Frames 2-8 describe the double four-bar linkage closed-loop kinematic chain (yellow, orange, and pink lines) all actuated by joint  $q_2$ . Due to parallel links, frames 6 and 7 have a constant orientation throughout the motion of  $q_2$  and frames 8 and 9 rotate about the RCM.

Frame 2 is an intermediate frame with three child links frame 3, frame 4, and frame 5. Frame 9 is a prismatic joint, actuated by  $q_3$ , that describes the insertion axis of the tool. A counterweight, frame 11, is added to frame 3 that is actuated by a prismatic motion,  $\mu q_3$ . This frame moves opposite to the tool insertion with a scaling factor  $\mu$ . Frames 12-15 describe a standard manipulator wrist motion with end effector grippers.  $q_4$  actuates the tools' roll motion which is parallel to the insertion axis and  $q_5$  actuates the tools' pitch motion. The left and right gripper frames are shown as individual frames actuated by  $q_6$  and  $q_7$ . Yaw rotation and gripper motion of the hardware is a coupled motion of  $q_6$  and  $q_7$ .

Table 4 describes the resulting modified DH parameters. *Succ* in the table refers to the successor or child frames of the current frame. Blue highlighted text are parameters obtained from axis distance calibration in Section 2.4.

The axis distance calibration outputs the location of the axes,  $\mathbf{g}$ , in camera frame at the home/zero joint position of the PSM. By using the distances, for example, of frames 4-6 and 5-6, it is possible to find the DH parameter  $\beta_1$  angle. Additionally, intuition about the double four-bar linkage constructing the RCM, the location of the RCM from the dVRK kinematics, and the distances between axes, provides sufficient information to construct the required modified DH parameters. The

double-four bar linkage requires that the origin of frame 3, 4, and 5 must be intersecting the z-axis of frame 1. Frames 6 and 8 are always relatively horizontal to each other throughout the motion of joint  $q_2$ . Finally, the z-axis of frame 9 must intersect the RCM. Note again that the RCM location is already provided by the dVRK repository. The same method is also used for deriving the modified DH of the ECM in Section 2.3.

Table 4

PSM modified DH parameters. Blue highlighted text are parameters obtained from link length calibration of section 2.4  $\beta_1 = 0.2908s$  [rad],  $B_2 = 0.3675$  [rad],  $\mu = 0.6025$

Frame	Succ	Joint	$a_i$ [m]	$\alpha_i$ [rad]	$d_i$ [m]	$\theta_i$ [rad]
1	2	R	0	$\pi/2$	0	$q_1 + \pi/2$
2	3, 4, 5	-	0	$\pi/2$	0	$\pi/2$
3	6, 10	R	-0.0296	0	0	$q_2 - \beta_1 - \pi/2$
4	-	R	0.0664	0	0	$q_2 - \beta_1 - \pi/2$
5	7	R	-0.0296	0	0	$q_2 - \beta_2 - \pi/2$
6	8	R	0.150	0	0	$-q_2 + \beta_1 + \pi/2$
7	-	R	0.1842	0	0	$-q_2 + \beta_2 + \pi/2$
8	9	R	0.516	0	0	$q_2$
9	12	P	0.043	$-\pi/2$	$q_3 - 0.2881$	$\pi/2$
10	11	-	0	0	0	$\beta_1 + \pi/2$
11	-	P	-0.1	$\pi/2$	$\mu q_3$	0
12	13	R	0	0	0.4162	$-\pi/2 + q_4$
13	14, 15	R	0	$\pi/2$	0	$-\pi/2 + q_5$
14	-	R	-0.0091	$\pi/2$	0	$-\pi/2 + q_6$
15	-	R	-0.0091	$\pi/2$	0	$-\pi/2 + q_7$

## 2.3 Endoscope Camera Manipulator

The ECM kinematics, shown in Figure 4, has similar kinematics to the PSM but which ends at frame 10 (frame 12 PSM). Frame 0 of the ECM is attached to frame 7 of the SUJ-ECM. The ECM also rotates about an RCM point used as the insertion point of the camera. Table 5 describes the resulting modified DH parameters.

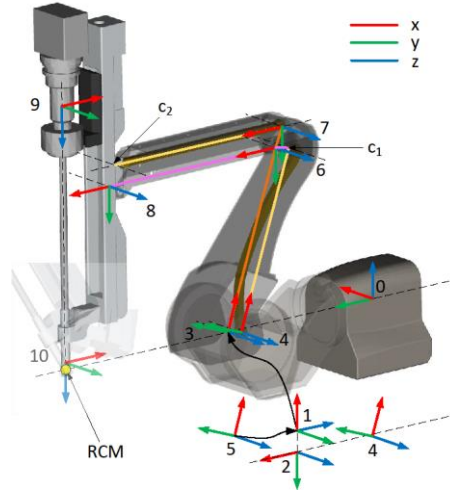


Figure 4

Endoscope Camera Manipulator (ECM) kinematics and frame definitions shown in RViz. Pink, orange, and yellow lines show separate parts of the four-bar linkage (Frames 3-8).

Table 5

ECM modified DH parameters. Blue highlighted text are parameters obtained from link length calibration of section 2.4.  $\beta_1 = 0.3448$  [rad].  $\beta_2 = 0.3229$  [rad].

Frame	Succ	Joint	$a_i$ [m]	$\alpha_i$ [rad]	$d_i$ [m]	$\theta_i$ [rad]
1	2, 3, 5	R	0	$\pi/2$	0.2722	$q_1 + \pi/2$
2	4	-	-0.0098	$-\pi/2$	0	$\pi/2$
3	6	R	0	$-\pi/2$	0	$q_2 - \beta_1$
4	-	R	0.03657	0	0	$q_2 - \beta_1 - \pi/2$
5	7	R	0	$-\pi/2$	0	$q_2 - \beta_2$
6	8	R	0.3047	0	0	$-q_2 + \beta_1 + \pi/2$
7	-	R	0.3419	0	0	$-q_2 + \beta_2 + \pi/2$
8	9	R	0.3404	0	0	$q_2$
9	10	P	0.103	$-\pi/2$	$q_3 - 0.0953$	$\pi$
10	-	R	0	0	0.3829	$q_4$

## 2.4 Axis Distance Calibration using Motion Capture Setup

The method used to obtain the axis distances of the closed-loop kinematic chain uses an optical motion tracking system and a least squares axis location calculation [21]. To identify all axes during a range of motion, a modification of the previous method [22] has been used. The experimental setup is shown in Figure 5. Three optical markers are placed on each link  $i$  of the closed-loop chain for 5 links.

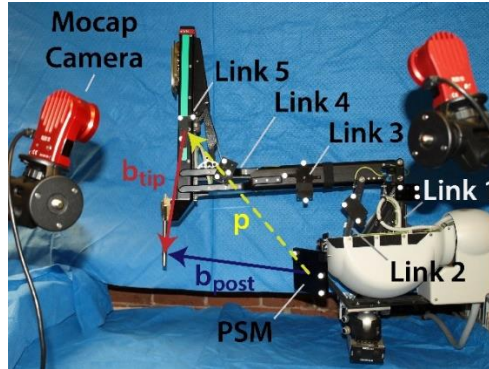


Figure 5

Motion tracking setup for calculating the link lengths and remote center of motion of the Patient Side Manipulator. Three Markers are placed on each link to represent a coordinate frame. The global coordinate frame is named PSM on the bottom of the picure.

We will assign  $z$  as the number of axes to be identified. In this case, there 7 axes locations to be identified. These optical markers describe the rigid body position,  $p \in R^3$ , and orientation,  $R \in SO^3$ , of each link  $i$  with respect to the optical trackers camera frame  $c$ . We use a transformation matrix  $T \in SE^3$  to describe the position and rotation of a marker frame  $i$

$$T_i^o = \begin{bmatrix} R_i & p_i \\ 0 & 0 & 0 & 1 \end{bmatrix}$$

where  $o$  is the reference frame of the target frame  $i$ . Consider the identification of axis  $a$ - $b$ , Figure 6, where link  $b$  is rotated about link  $a$ . The data obtained from the optical camera system is the transformation of link  $a$ ,  $T_a^c$ , and link  $b$ ,  $T_b^c$ , in camera frame  $c$ . To solve the relative rotation of link  $b$  about link  $a$ , use

$$T_b^a = T_c^a \cdot T_b^c \#(1)$$

where  $c$  denotes the camera frame. Actuating the robot joint,  $q_2$ , along a trajectory for  $w$  data points and using (2), we collect all the  $a$ - $b$  transformation data along the trajectory into:

$$H_b^a = \begin{bmatrix} T_{b,1}^a \\ T_{b,2}^a \\ \vdots \\ T_{b,w}^a \end{bmatrix} \#(2)$$

With this data, the method [21] outputs a vector,  $g_{a-b}^a \in R^3$ , representing the axis between the two links and the vector,  $h_{a-b}^a \in R^3$ , representing the direction of the axis. Figure 6 illustrates the axis calibration method. Both vectors are represented in frame  $a$  which is the optical frame of the reference link. Since this frame  $a$  is in motion during the test, the vectors  $g$  and  $h$  are transformed to the common camera

frame using  $\mathbf{g}_{a-b}^c = \mathbf{T}_{a,0}^c \cdot \mathbf{g}_{a-b}^a$  and  $\mathbf{h}_{a-b}^c = \mathbf{T}_{a,0}^c \cdot \mathbf{h}_{a-b}^a$  where  $\mathbf{T}_{a,0}^c$  is the transform of link  $a$  in frame  $c$  at joint position 0.

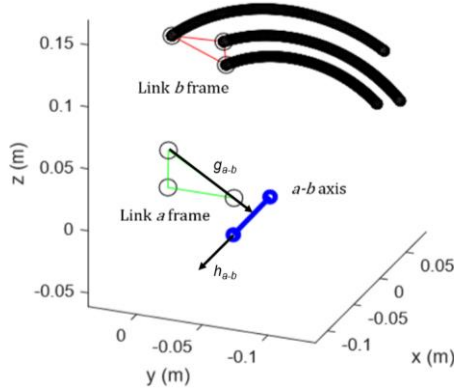


Figure 6

Representative least squares solution of the resulting axis position for link length calculation. Axis  $a$ - $b$  is found with marker data link  $b$  rotating about markers of link  $a$ .

This axis calculation is done for all  $z$  number of axis. For brevity, we denote this vector of axis locations  $\mathbf{g}^c = [g_{1-2} \ g_{2-3} \ \dots \ g_z]$  and axis directions  $\mathbf{h}^c = [h_{1-2} \ h_{2-3} \ \dots \ h_z]$  referenced in camera frame  $c$ .

Since the axis location,  $\mathbf{g}^c$ , is arbitrary on the axis, we define a plane  $m$  that is the mean of all the axis directions  $\mathbf{h}^c$ . The axis location is then projected onto plane  $m$  to get the in-plane axis locations  $\mathbf{g}^h$ . From this vector, we obtain the relative distance between each axis. The results for our axis distance calibration of the PSM and ECM, and those that are used in the provided simulation, are described in Table 6. Since it is a double four-bar linkage, using only some of the axis distances are sufficient to describe the DH kinematic model.

Table 6

PSM and ECM Motion Capture Axis Distance Results.  
Refer to Figure 3 and Figure 4 for frame notation

Frames	PSM Axis Distances [m]	ECM Axis Distances [m]
3 - 4	0.0958	0.0373
3 - 6	0.1487	0.3047
4 - $c_1$	0.1500	0.3038
6 - $c_1$	0.0961	0.0380
3 - 7	0.1842	0.3416
6 - 8	0.5152	0.3392
7 - $c_2$	0.5166	0.3409
6 - 7	0.0365	0.0374

The da Vinci systems have slight variances in kinematics due to manufacturing tolerances, link deformations, and mechanical wear and tear over time. Therefore, we provide the methods and underlying code to calibrate the kinematics of other systems [22].

### 3 Simulation Models and Environment

Robot Operating System (ROS) is a framework which uses IPC to communicate messages between several processes (nodes) using rostopics [17]. Any process only needs to subscribe/publish to a topic to communicate data to another process. ROS provides a visualization framework, Rviz, to simulate robot kinematics. ROS itself does not contain a physics engine required for a simulated environment. For this, a simulator such as Gazebo which uses Bullet physics engine [26] is used. Since it is an open source simulator for use with ROS, several sensors like camera, depth sensors, etc. are readily available to use along with the models.

In this section, the closed-loop kinematic chain models obtained in Section 2 are modeled in CAD, exported to ROS framework description formats and simulated in the visualization environment RVIZ, and dynamic simulation Gazebo.

#### 3.1 CAD Modeling

Computer Aided Design (CAD) in Solidworks is done for realistic visualization and a mass estimate of each link of the da Vinci Surgical System. The axis distance dimensions from the modified DH was used as the reference point of each link model. Other dimensions for a realistic visualization were measured. For the PSM and ECM, the RCM was used as a reference to ensure the correct location of the RCM when all links are assembled.

#### 3.2 CAD to URDF

The CAD models are exported to Universal Robot Description File (URDF) using the Solidworks to URDF exporter [23]. The URDF file format is a common XML language description of a robot to visualize link transforms and meshes in Rviz, Section 3.4. Because URDF does not support closed-loop kinematic chains, the URDF is made into a tree structure. Links that close the loop are at an end of a serial chain. The closed-loop links use the URDF mimic joint tag to have equal joint displacement as the actuated links.

### 3.3 Modifications of URDF to SDF

Simulation Description Format (SDF) is a file format that is used to describe robot kinematics and dynamics in Gazebo [24]. This format allows the description of closed-loop kinematic chains. The previously described URDF configuration is converted to the SDF format using the *gz sdf print* command which is included with Gazebo. Closed-loop kinematic chain joints that were not in the URDF are added manually in the SDF using the modified DH parameters as joint locations. Furthermore, dynamic parameters such as damping and stiffness for the joints were added.

### 3.4 Kinematic Simulation RViz

Our da Vinci Research Kit simulation in RViz is shown in Figure 1. Kinematics of the SUJ with ECM and PSMs are compiled with accurate tool-tip positions. The simulation can be accompanied by the master tool manipulator reconfigured modularly in ROS. Each joint angle is controlled with either the visual toolbar or the rostopic that is programmed through python/C++. Joint state angles and transformations of each link are available using the tf libraries of ROS. These transformations comply with the kinematics derived in early sections and those provided in the dVRK manual and hence verify the calculation of the link lengths.

### 3.5 Dynamic Simulation and Interface

A general Gazebo ROS framework is shown in Figure 7. Gazebo is spawned from a launch file and a node for Gazebo is started. Since there is little inherent support for closed-loop chains in Gazebo, we developed a control plugin that provides an interface to interact with the simulation by creating appropriate rostopics. For instance, the control plugin reads joint states of the simulation and receives topics that publish desired joint commands to Gazebo. Additional parameters required for the plugin that are user dependent (e.g., PID gains, and initial joint angles) is uploaded and taken from the ROS parameter server.

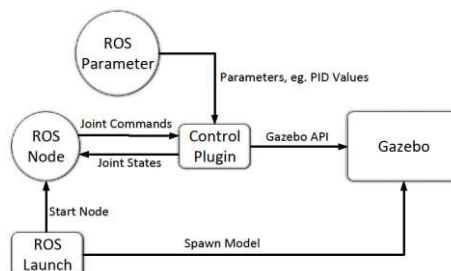


Figure 7

Flowchart depicting a high level generic simulation framework for Gazebo using ROS

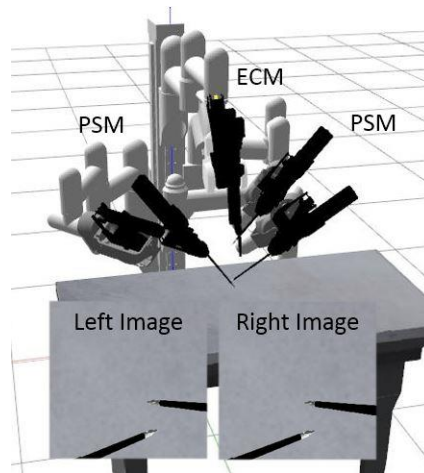


Figure 8

Simulation showing the stereo camera view of the endoscope using the stereo camera plugin in Gazebo

### 3.5.1 Dynamic Parameters

As an intermediate step for realistic simulations, the mass and inertia values are obtained from Solidworks. This ensures good dynamic parameter estimates of the hardware resulting in a stable simulation. Because these dynamics are estimates, the low-level control gains are different from the hardware. Furthermore, joint damping is kept at a minimal constant value of 0.1. The low-level PID controller gains were tuned individually for all joints for a step response.

### 3.5.2 Control Plugin

A control plugin to control the joints using ROS topics was developed. This plugin allows the user to control the joints using 3 different methods: set the joint positions directly, closed-loop control of the joint positions using a PID controller, and open loop control of the joint efforts (i.e. joint torques). Different methods can be used for different purposes. For instance, the SUJ cart does not move during a procedure and is set before a procedure begins, the setup joints can be set using the first method and it would ensure fixed joint positions during the simulation. The simulated models can be controlled in either position control mode or effort control mode based on the user's preference. More information on the specific topics and use of the plugin are provided on the Github repository: [https://github.com/WPI-AIM/dvrk\\_env](https://github.com/WPI-AIM/dvrk_env).

### 3.5.3 Sensors

Using the Gazebo simulator allows for the use of integrated sensors to observe the simulation environment. For instance, a stereo camera is necessary for the simulation of the images from the endoscopic camera. This is possible by adding

an open source sensor plugin. Figure 8 shows a stereo camera image from the DVRK endoscope using a stereo camera sensor plugin. The sensor is attached to the end of the ECM tool link and gives two images showing the tooltips of PSMs.

## 4 Model Verification

In this section, we present methods and results which verify the accuracy of the PSM and ECM simulation models. The first method obtains the RCM location using either motion capture setup for hardware or reading transformations in simulation. The simulation RCM location is then compared with the hardware RCM location. The second method verifies the dynamic simulation stability and performance.

### 4.1 Tool-tip Calibration to Obtain Remote Center of Motion

This method calculates the location of the RCM using standard pivot tool-tip calibration where the tip is actually the RCM [25]. The experimental setup places 3 optical markers on link 5, Figure 5. The manipulator is then actuated about joint and  $q_1, q_2$ . Following subsection 2.4, the optical camera system outputs the rotation  $R$  and position  $p$  of the marker frame. In Figure 5, it is obvious that the solution of the vectors  $b_{post}$  and  $b_{tip}$ , are:

$$b_{post} = Rb_{tip} + p \quad \#(3)$$

By obtaining the position,  $p$ , and orientation,  $R$ , of the marker frame that is sampled for  $n$  times while moving  $q_1$  and  $q_2$ , the matrices are expanded

$$\begin{bmatrix} R_1 & -I_1 \\ \vdots & \vdots \\ R_n & -I_n \end{bmatrix} \begin{bmatrix} b_{tip} \\ b_{post} \end{bmatrix} = \begin{bmatrix} -p_1 \\ \vdots \\ -p_n \end{bmatrix} \quad \#(4)$$

where  $I$  is the 3x3 identity matrix. There exists one vector  $b_{tip}$  pointing to the RCM location from the marker frame and another vector  $b_{post}$  pointing to the RCM location from the reference frame. A pseudoinverse of the leftmost matrix in equation 4 gives the solution to  $b_{tip}$  and  $b_{post}$ . Verifying the RCM in simulation uses the same least squares technique when obtaining the position and rotation of frame 6 in Figure 2 for PSM and Figure 3 for ECM.

### 4.2 Comparison of RCM Tracking Between Actual and Simulated Robot

Six Optitrack Motion Capture cameras and a least squares method (3) were used to identify the remote center of motion of the manipulator hardware. The experiment setup is similar to Figure 5 but with markers only on Links 5 and 2.

The manipulator was mounted to define a world frame orthogonal rotation identical to the first 2 joint axes (frame 1 and 2) rotation. Three optical markers are mounted on frame 8 to calculate the RCM and three markers on frame 3 to calculate the pitch axis (refer to Figure 5). The resulting RCM absolute position is relative to the pitch axis.

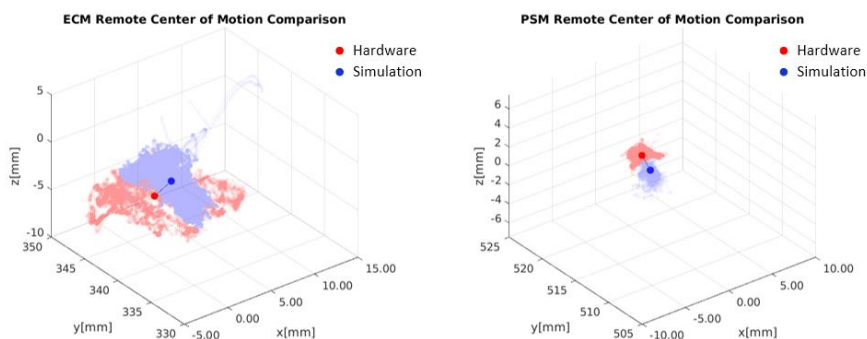


Figure 9

Estimated remote center of motions of hardware (red) and Gazebo simulation (blue). Transparent markers/cloud points show the estimated RCM location at different angles  $q_1$  and  $q_2$ .

The calculated RCM of both PSM and ECM are shown in Figure 9. The red dot is the RCM location ( $b_{post}$ ) of the hardware and the blue dot is the RCM location of the Gazebo simulation. Semi-transparent markers are RCM points calculated with  $b_{tip}$  using equation 3 at different joint angles. This is interpreted as the motion of the RCM throughout the robot workspace. The root-mean-square (RMS) error is calculated by the formula:

$$RMS = \sqrt{\sum_{i=1}^n (b_{post} - R_i b_{tip} - p_i)^2} \quad (5)$$

Table 7

Remote Center of Motion locations and RMS error for PSM/ECM Hardware and Simulation

RCM	Position [mm]			RMS Error [mm]		
	x	Y	z	x	y	z
PSM Hardware	-1.49	-516.11	2.19	0.62	0.62	0.31
PSM Simulation	0.56	-518.60	0.93	0.85	1.91	1.08
ECM Hardware	341.11	-0.08	-3.39	3.72	2.45	1.33
ECM Simulation	338.44	-0.05	-0.54	2.17	1.14	0.85

Table 7 summarizes the RCM verification results for both PSM and ECM. The absolute position error of the simulation compared to the hardware is 3.46 [mm] for PSM, and 3.91 [mm] for ECM. Errors are caused by incorrect world frame rotation setup, motion tracking inaccuracies, and joint flexibilities. The RMS

error, representing the distribution of the RCM throughout the robot workspace, is shown for both the real robot hardware and the simulation for both the PSM and ECM.

### 4.3 Simulation Performance and Joint Stability

To test the performance and stability of the Gazebo simulations, a joint trajectory tracking test was conducted. A core i7-4770K CPU @ 3.50GHz with AMD Radeon HD 8670 graphics card system running on Ubuntu 16.04 was used. The test outputs a 0.1 Hz sinusoidal trajectory with an amplitude of 1 radian (0.1m for joint 3) given to 6 joints of the PSM.

Table 8  
PSM PID Values used during trajectory tracking

Joint	P	I	d
1	70	0.1	5
2	70	0.1	5
3	400	0.01	10
4	10	0.1	1
5	10	0.1	1
6	10	0.1	1

Table 8 shows the tuned PID values for the mass and inertias given in Solidworks. The results of this test are plotted in Figure 10, where left are the commanded (blue) and resulting (orange) joint trajectories, and right are tracking errors. This shows that all joints were tracking with good stability and minimal delay.

Table 9  
Real time coefficient of different Gazebo configurations of the dVRK

Simulation	Real time coefficient
PSM	1
ECM	1
2 PSM + ECM	0.98
3 PSMs	0.99
SUJ + 3 PSM + ECM	0.51
SUJ + 3 PSM + ECM + Camera	0.47

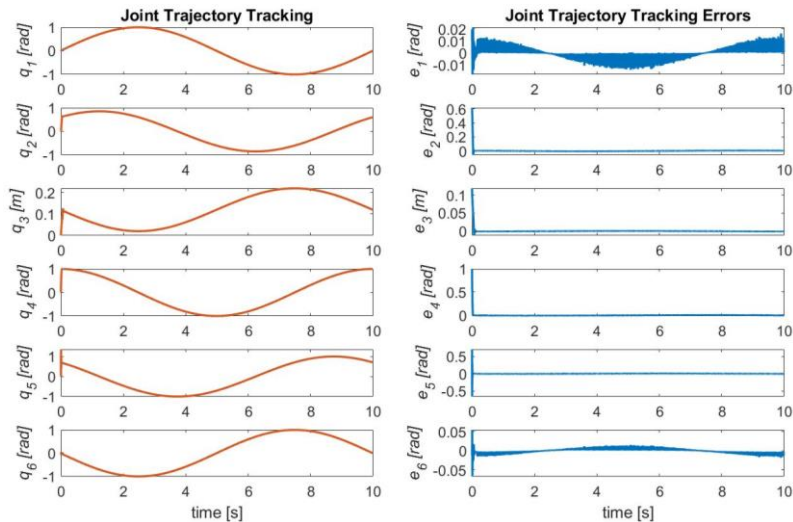


Figure 10

Joint trajectory tracking of the PSM in Gazebo Simulation. Left, commanded blue joint trajectory has similar values to orange actual joint trajectory.

During this test, the real-time coefficient is 1. This coefficient is automatically calculated and indicates the ratio between real-time and simulation time, as Gazebo can slow down simulation time as the computation cost of each iteration is increased. A test to determine the simulation load of different configurations is also conducted by measuring the real-time coefficient. The coefficient was not significantly affected by the commanded trajectory tracking but, rather, by the number of models in the simulation. Table 9 shows the results for each configuration test. The full model which included the camera plugin had a real-time coefficient of 0.47.

## Conclusions

This work provides an approach for developing closed-loop kinematic chain models, using existing serial chain models applied to the da Vinci Surgical System. An optical motion capture system was used to calibrate the link lengths of the four-bar linkage mechanism of the PSM/ECM. This procedure can also be applied to other robots with a similar parallel axis closed-loop kinematics. Due to variations in the physical configuration among da Vinci systems, this calibration method could be used to update models for another specific da Vinci System.

Furthermore, the models were used and verified for ROS based simulations in RViz and Gazebo. Verification of the remote center of motion location of the PSM and ECM manipulators showed acceptable errors as compared to the hardware RCM. Additionally, this work verifies the stability and performance of the dynamic simulation using a joint trajectory tracking test of the PSM where

every joint succeeded in stable tracking of a sinusoidal wave. Finally, a test was conducted to measure the simulation load with various model configurations. CAD Models and simulations are available at [https://github.com/WPI-AIM/dvrk\\_env](https://github.com/WPI-AIM/dvrk_env)

### **Acknowledgement**

This work has been supported by National Science Initiative NSF grant: IIS-1637759

### **References**

- [1] Satava, R. M., (2003) Robotic surgery: from past to future--A personal journey. *Surgical Clinics of North America*, 83(6), pp. 1491-1500
- [2] Bodner, J., Wykypiel, H., Wetscher, G. and Schmid, T., (2004) First experiences with the da Vinci operating robot in thoracic surgery. *European Journal of Cardio-thoracic surgery*, 25(5), pp. 844-851
- [3] Okamura, A. M., (2009) Haptic feedback in robot-assisted minimally invasive surgery. *Current opinion in urology*, 19(1), p. 102
- [4] Pandya, A., Reisner, L. A., King, B., Lucas, N., Composto, A., Klein, M. and Ellis, R. D., (2014) A review of camera viewpoint automation in robotic and laparoscopic surgery. *Robotics*, 3(3), pp. 310-329
- [5] Park, S., Howe, R. D. and Torchiana, D. F., (2001) October. Virtual fixtures for robotic cardiac surgery. In *International Conference on Medical Image Computing and Computer-Assisted Intervention* (pp. 1419-1420) Springer, Berlin, Heidelberg
- [6] Sen, S., Garg, A., Gealy, D. V., McKinley, S., Jen, Y. and Goldberg, K., (2016 May) Automating multi-throw multilateral surgical suturing with a mechanical needle guide and sequential convex optimization. In *Robotics and Automation (ICRA), 2016 IEEE International Conference on* (pp. 4178-4185) IEEE
- [7] Kazanzides, P., Chen, Z., Deguet, A., Fischer, G. S., Taylor, R. H., & DiMaio, S. P. (2014 May) An open-source research kit for the da Vinci Surgical System. In *Robotics and Automation (ICRA), 2014 " IEEE International Conference on* (pp. 6434-6439) IEEE
- [8] Chen, Z., Deguet, A., Taylor, R. H., & Kazanzides, P. (2017 April) Software Architecture of the da Vinci Research Kit. In *Robotic Computing (IRC), IEEE International Conference on* (pp. 180-187) IEEE
- [9] Khatib, O., (1987) A unified approach for motion and force control of robot manipulators: The operational space formulation. *IEEE Journal on Robotics and Automation*, 3(1), pp. 43-53

- [10] Ulrich, N. and Kumar, V., (1991 April) Passive mechanical gravity compensation for robot manipulators. In *Robotics and Automation, 1991 Proceedings, 1991 IEEE International Conference on* (pp. 1536-1541) IEEE
- [11] Fontanelli, G. A., Selvaggio, M., Ferro, M., Ficuciello, F., Vendiuelli, M. and Siciliano, B., (2018 August) A v-rep simulator for the da Vinci research kit robotic platform. In *2018 7<sup>th</sup> IEEE International Conference on Biomedical Robotics and Biomechanics (Biorob)* (pp. 1056-1061) IEEE
- [12] Perrenot, C., Perez, M., Tran, N., Jehl, J. P., Felblinger, J., Bresler, L. and Hubert, J., (2012) The virtual reality simulator dV-Trainer® is a valid assessment tool for robotic surgical skills. *Surgical endoscopy*, 26(9), pp. 2587-2593
- [13] Robotic Surgery Simulator. Available online: <http://www.simulatedsurgicals.com/ross.html> (accessed on 5 November 2018)
- [14] Moglia, A., Ferrari, V., Morelli, L., Ferrari, M., Mosca, F. and Cuschieri, A., (2016) A systematic review of virtual reality simulators for robot-assisted surgery. *European urology*, 69(6), pp. 1065-1080
- [15] Rosen, J., MacFarlane, M., Richards, C., Hannaford, B. and Sinanan, M., (1999) Surgeon-tool force/torque signatures-evaluation of surgical skills in minimally invasive surgery. *Studies in health technology and informatics*, pp. 290-296
- [16] Haidegger, T., Benyó, B., Kovács, L. and Benyó, Z., (2009) August. Force sensing and force control for surgical robots. In *7<sup>th</sup> IFAC Symposium on Modeling and Control in Biomedical Systems* (Vol. 7, No. 1, pp. 413-418)
- [17] Quigley, M., Conley, K., Gerkey, B., Faust, J., Foote, T., Leibs, J., & Ng, A. Y. (2009 May). ROS: an open-source Robot Operating System. In *ICRA workshop on open source software* (Vol. 3, No. 3.2, p. 5)
- [18] Kam, H. R., Lee, S. H., Park, T. and Kim, C. H., (2015) Rviz: a toolkit for real domain data visualization. *Telecommunication Systems*, 60(2), pp.337-345
- [19] Koenig, N. P. and Howard, A., (2004) September. Design and use paradigms for Gazebo, an open-source multi-robot simulator. In *IROS* (Vol. 4, pp. 2149-2154)
- [20] Bailey, M., Gebis, K. and Zefran, M., (2016) Simulation of closed kinematic chains in realistic environments using gazebo. In *Robot Operating System (ROS)* (pp. 567-593) Springer, Cham
- [21] Gamage, S. S. H. U. and Lasenby, J., (2002) New least squares solutions for estimating the average centre of rotation and the axis of rotation. *Journal of biomechanics*, 35(1), pp. 87-93

- [22] Nycz, C. J., Meier, T. B., Carvalho, P., Meier, G. and Fischer, G. S., (2018) Design Criteria for Hand Exoskeletons: Measurement of Forces Needed to Assist Finger Extension in Traumatic Brain Injury Patients. *IEEE Robotics and Automation Letters*, 3(4), pp. 3285-3292
- [23] SolidWorks to URDF Exporter. Available online: [http://wiki.ros.org/sw\\_urdf\\_exporter](http://wiki.ros.org/sw_urdf_exporter) (accessed on 5 November 2018)
- [24] Open Source Robotics Foundation. SDF, Describe your world. Available online: <http://sdformat.org/> (accessed on 5 November 2018)
- [25] Yaniv, Z., (2015) March. Which pivot calibration?. In *Medical Imaging 2015: Image-Guided Procedures, Robotic Interventions, and Modeling* (Vol. 9415, p. 941527) International Society for Optics and Photonics
- [26] Coumans, E., (2010) Bullet physics engine. Open Source Software: <http://bulletphysics.org>, 1, p. 3

# A Compliance Model to Improve the Accuracy of the da Vinci Research Kit (dVRK)

Grace Chryzilla<sup>1,2</sup>, Nickolas Eusman<sup>1,2</sup>, Anton Deguet<sup>1</sup>, and Peter Kazanzides<sup>1</sup>

<sup>1</sup>Department of Computer Science, Johns Hopkins University, Baltimore, MD USA, pkaz@jhu.edu

<sup>2</sup>These authors contributed equally to the work during internships at JHU

---

*Abstract:* The da Vinci surgical robot is widely used for minimally-invasive surgery. It inserts multiple articulated instruments through small incisions into the patient. The robot system contains encoders to measure joint displacements which, when combined with the kinematic model of the robot, measures the instrument position and orientation. But, the accuracy of these measurements is affected by non-kinematic errors, such as bending of the instruments due to applied loads. We develop a compliance model that relates displacement of the first two joints of the da Vinci Patient Side Manipulator (PSM) to lateral forces applied to the instrument shaft. This model enables us to compensate for these errors based on the measured joint efforts, which are derived from the measured motor currents. We perform experiments with the open-source da Vinci Research Kit (dVRK) to estimate the model parameters and to evaluate the accuracy improvement that results from application of this model. Preliminary results indicate that the model-based correction can reduce instrument position error due to externally-applied forces.

*Keywords:* da Vinci Research Kit (dVRK); compliance model; calibration

---

## 1 Introduction

The da Vinci® surgical robot [1], Fig. 1, is widely used for minimally invasive surgery. It currently relies on teleoperation by the surgeon, who sits at a master console that provides stereo video from inside the patient via a stereo endoscope inserted through one incision (port). The console also contains two Master Tool Manipulators (MTMs), which the surgeon uses to provide motion commands to the Patient Side Manipulators (PSMs) that drive robotic surgical instruments inside the patient. In the conventional scenario, a human surgeon is inside the control loop and uses his or her visual feedback to correct for positioning errors. In general, positioning errors can be due to kinematic errors, such as imprecise knowledge of the robot's kinematic parameters, and non-kinematic errors, such as friction, backlash and deformation of the robot's mechanical structure due to gravity or other externally-applied forces. This is especially true for the da Vinci instruments, which are cable-driven and have thin diameters (typically 5 mm or 8 mm).

While positioning accuracy is not crucial for conventional teleoperation, it can be

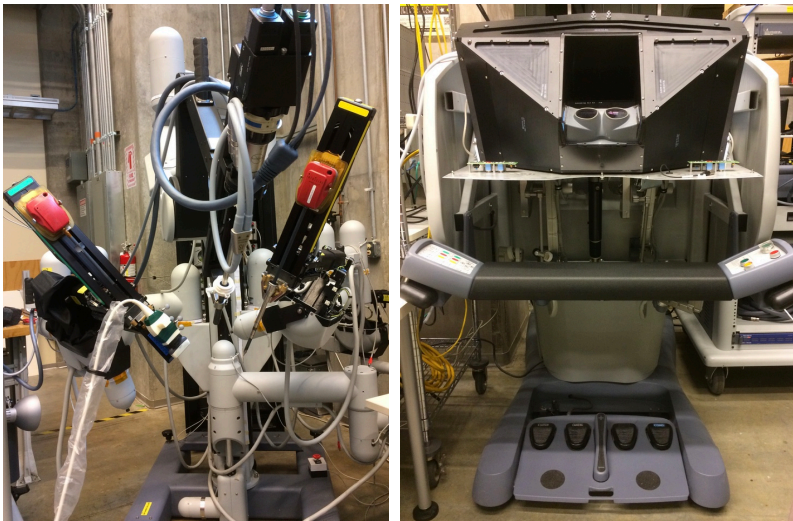


Figure 1

da Vinci Surgical Robot: patient side robot on left; master console on right.

important in other situations, such as when making measurements or when enforcing virtual fixtures. In these cases, it can be beneficial to compensate for the positioning errors. One solution is to track the surgical instrument in the endoscopic video, since direct visual observation of the tool tip is not affected by kinematic or non-kinematic errors. However, optical tracking of da Vinci instruments remains a challenging research problem (especially when optical markers are not used) and is the subject of many other efforts [2].

We therefore focus on an approach that does not require tracking of the instrument. Further, we consider only non-kinematic errors due to deformation of the instrument, which can only improve the positioning accuracy for applications that require contact with the environment. Nevertheless, there are several existing applications that could benefit from such a capability. For example, researchers at the University of British Columbia (UBC) used a da Vinci instrument to push against the prostate in order to register the da Vinci robot coordinate frame to a transrectal ultrasound (TRUS) coordinate frame [3]. In this case, deformation of the instrument will contribute to the overall registration error. Another potential scenario is 3D reconstruction of 2D ultrasound images when the 2D ultrasound probe is swept along an organ surface by a da Vinci instrument [4]. Because accuracy is important for these types of applications, the group at UBC also attached an optical marker frame to the da Vinci instrument and tracked it with the endoscope camera [5]. Improving the positioning accuracy of the da Vinci could eliminate the need for this additional tracking. Virtual fixtures provide another application scenario that could benefit from improved accuracy; for example, in cases where a guidance virtual fixture is defined by probing the anatomy [6] (there are other applications of virtual fixtures in the literature, but many do not involve contact with the environment). In another application, the da Vinci instrument was used to palpate tissue to estimate its stiffness [7], but this actually measured the stiffness of both the instrument and the tissue. In many cases, the

instrument will be much stiffer than the tissue and therefore introduce negligible error, but at some instrument orientations the error contribution may be larger.

The above application examples motivate the approach presented in this paper, which is to develop a simplified compliance model of the da Vinci PSM and surgical instrument and to use this model to reduce the error in estimation of the instrument tip position based on the encoder measurements and kinematic parameters. The research is performed with the open-source da Vinci Research Kit (dVRK) [8], which enables full access to all feedback data from the da Vinci system. In particular, this method utilizes the measured encoder feedback and the estimated joint torques, which are calculated from the measured motor currents. The dVRK also provides access to the robot controller, thereby allowing the compliance-based correction to be incorporated in the system. The contribution of this work is the identification of a model that is simple to implement, but can nevertheless improve the position accuracy of da Vinci instruments.

## 2 Compliance Model

The position and orientation of the da Vinci instrument is computed based on applying the forward kinematics to the measured joint positions,  $q$ , which are obtained from incremental encoders mounted on the actuators (motors). In general, it is necessary to distinguish between joints and actuators on the da Vinci due to coupling, especially between the four actuators that drive the instrument wrist and gripper. Our analysis, however, focuses on the first two joints of the da Vinci PSM, which are not coupled, so we do not make this distinction in the following.

The PSM contains a remote center of motion (RCM) that is designed to be located at the insertion point (port) on the patient's body. The first two joints are rotations about the RCM and the third joint is a linear translation through the RCM, as illustrated in Fig. 2-left. We consider the effect of external forces applied to the instrument, which can affect the instrument position as follows: (1) increase the difference between the commanded joint position and the measured joint position, and (2) displace the instrument due to deformation of the mechanical structure. The first effect is dependent on the control performance of the da Vinci and only affects the accuracy with which the da Vinci can be controlled. Because the encoders measure the displacement, applying the forward kinematics to the measured encoder positions will yield an instrument position that takes into account this displacement. The second effect (deformation due to mechanical compliance, Fig. 2-middle) is not measured by the encoders, however, and therefore decreases the position accuracy. Thus, our focus is to develop a model for this compliance and to use this model to predict and correct for the mechanical deformation. Although all links of the da Vinci are subject to compliance, we focus on lateral forces acting on the instrument shaft because compliance of the shaft in the two lateral directions is significantly higher than in the axial direction ( $Z_3$  in Fig. 2-left). Furthermore, we ignore compliance of the instrument wrist because we expect it to be a less significant contributor to positioning inaccuracy. Figure 2-right also shows backlash between the instrument shaft and the cannula (in the figure, the cannula is exaggerated in size to better illustrate the backlash phenomenon).

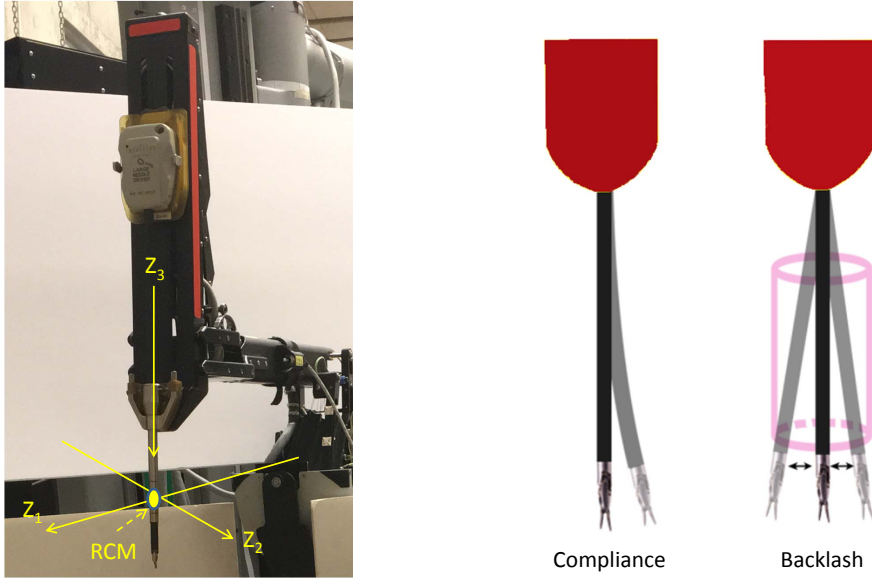


Figure 2

**Left:** PSM Kinematics, showing axes of first three joints, where joints 1 and 2 rotate about a common remote center of motion (RCM), and joint 3 translates through this RCM. **Center:** Illustration of instrument compliance. **Right:** Illustration of backlash. Note that backlash between instrument shaft and cannula is exaggerated for visual effect.

Due to the kinematic design of the da Vinci PSM, lateral forces applied to the instrument shaft align with the first two rotary joints, so we are able to develop a compliance model considering only these two joints. For analysis, we decompose the lateral force into two orthogonal forces, where one force applies a torque around the first joint and the other force applies a torque around the second joint. For each rotary joint  $q$ , we consider the following compliance model:

$$\Delta q_{def} = \delta \text{sgn}(\tau_{ext}) + K(L)\tau_{ext} \quad (1)$$

Here,  $\tau_{ext}$  is the external applied torque,  $\Delta q_{def}$  is the angular displacement, and  $\delta$  is a small angular displacement due to backlash.  $K(L)$  is an angular correction factor, relating angular displacement to applied torque, that is assumed to vary based on the length,  $L$ , from the RCM to the point at which the force is applied. These parameters are summarized in Table 1.

Equation (1) can be used to correct the measured joint angle by subtracting  $\Delta q_{def}$ , given an estimate of the external joint torque  $\tau_{ext}$  and knowledge of the parameters  $\delta$  and  $K(L)$ . Fortunately, the dVRK software provides the measured joint torque,  $\tau_{meas}$ , which is the sum of the external joint torque,  $\tau_{ext}$ , and the internal torque,  $\tau_{int}$ . In general, it is challenging to estimate the internal torque using model-based methods, such as Lagrangian dynamics, due to nonlinear effects such as friction and cable compliance. Nevertheless, some groups have achieved reasonable results

Table 1  
Nomenclature

$L$	Length, in meters, from remote center of motion (RCM) to contact point on instrument; this corresponds to the position of the third PSM joint.
$\tau_{meas}$	Measured joint torque, in Newton-meters. This is based on the measured motor current, $I_{meas}$ , multiplied by a motor torque constant, $K_\tau$ , and gear ratios.
$\tau_{ext}$	Externally applied torque, generally estimated by computing $\tau_{meas} - \tau_{int}$ .
$\tau_{int}$	Internal torque, due to dynamics and other physical effects, such as friction. Often estimated using model-based methods.
$\tau_0$	Internal torque under static conditions, typically required to counteract gravity or counter-balance forces. Used as $\tau_{int}$ in this work.
$K(L)$	Angular correction factor, which is a function of length, $L$ . Units are radians/Newton-meter.
$\delta$	Backlash of instrument shaft, primarily due to clearance between shaft and cannula, measured in radians.
$\Delta q_{def}$	Angular displacement due to link deformation, in radians.

using this approach for the dVRK [9, 10]. Alternatively, a neural network could learn the dynamics, as recently demonstrated for a different robotic surgical instrument wrist [11].

In this paper, we simplify the problem by considering the quasi-static case, where measurements are taken with the robot in a fixed position. In this case,  $\tau_{int}$  can be represented by a bias (offset) torque,  $\tau_0(q)$ , which can be calibrated in advance by rotating the joint through a range of angles. Conceptually, this is similar to considering only the gravity term of the dynamics equation, though in the case of the da Vinci PSM the bias torque is primarily due to the mechanical counterbalance. In the future, one of the dynamics-based methods cited above can be incorporated with the developed compliance model. To summarize, for the first two rotary joints, the corrected joint position  $\hat{q}$  can be computed from the measured joint position  $q$  and estimated external torque  $\tau_{ext}$  (here,  $\tau_{meas} - \tau_0$ ), greater than a defined threshold  $\tau_{min}$ , as follows:

$$\hat{q} = \begin{cases} q - \delta \operatorname{sgn}(\tau_{ext}) - K(L)\tau_{ext} & \text{if } |\tau_{ext}| > \tau_{min} \\ q & \text{otherwise} \end{cases} \quad (2)$$

In our testing, we empirically set  $\tau_{min}$  to 0.1 N-m for joint 1 and 0.2 N-m for joint 2. The nonzero values for  $\tau_{min}$  cause a discontinuity in  $\hat{q}$ , which must be further investigated if used for feedback control in the future. It is possible to set  $\tau_{min}$  to 0, but in that case the joint correction value would likely oscillate between  $\delta$  and  $-\delta$  due to measurement noise.

### 3 Experiments

We performed experiments to gather data for developing the model and then to test the application of this model to compensate for the inaccuracy due to link deformation.

We first measured the torque offset,  $\tau_0$ , by moving the first and second joints through their range of motion in 5 degree increments, while recording the measured effort. Because the position control (PID controller) was active, the measured effort with no external load corresponds to the torque offset.

We evaluated different data collection methods for estimating the instrument backlash and compliance, including use of an optical tracking system or a dial indicator to measure deflection and a force sensor or precision weights to apply the external forces/torques. Ultimately, however, we settled on a simple approach that does not require any external measurement devices. Specifically, we clamped the da Vinci instrument against a rigid beam, as shown in Fig. 3. We then performed small incremental rotations of joints 1 and 2, while recording the measured joint torque. We assume that the beam is rigid and therefore that the actual instrument tip position does not change as the instrument applies increasing forces against the clamp. The advantage of clamping the instrument, rather than moving into the beam in one direction, is that it enables estimation of both the instrument compliance and the backlash.

We developed a Python program that communicates with the PSM via a ROS [12]

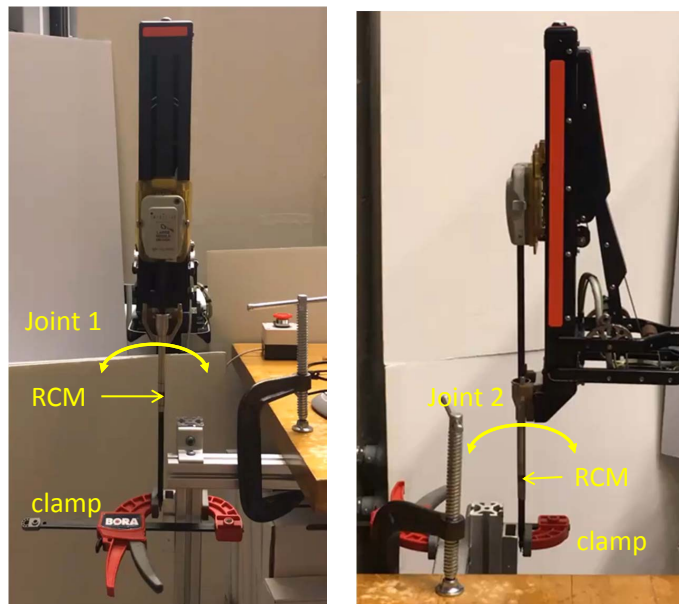


Figure 3

Data collection setup: PSM instrument is clamped against rigid beam while collecting measured joint position and torque (effort).

interface. Based on the setup in Fig. 3, the PSM's instrument was aligned with the aluminum beam and the linear joint was moved to locate the distal part of the instrument shaft at a distance of 0.09 meters (insertion depth) from the RCM point. The instrument was then clamped against the beam.

The robot was instructed to move in one direction in increments of 0.25 mm, until the absolute value of the measured effort exceeded 1.0 N-m. Then, it reversed direction and moved in 0.25 mm increments until the absolute value of the measured effort exceeded 1.0 N-m. Finally, it reversed direction again and moved back in increments of 0.25 mm until it crossed the start point. At each position, the software recorded an average of 20 measurements of the position and effort of the joint under test. This procedure was repeated at a total of 14 insertion depths, ranging from 0.09 m to 0.22 m. The above data collection was performed for the two orthogonal directions corresponding to the rotations of the first two PSM joints. The data was analyzed to estimate the angular correction factor for each orthogonal direction.

Finally, the compliance model was tested by pushing against a divot in an aluminum plate, while recording the measured joint positions and efforts. The correction model, Equation (2), was applied to the measured positions of joints 1 and 2 to obtain the corresponding corrected joint positions.

## 4 Results

Figure 4 shows the measured torque as a function of joint angle for joints 1 and 2. The data shows that the torque offset varies as a function of the joint angle (as expected), but does not vary significantly as a function of insertion depth.

Figure 5 plots the measured joint effort as a function of joint position, for one experiment in which the joint was moved while the instrument shaft was clamped to the rigid beam. Hysteresis is evident in both directions (i.e., corresponding to direction of motion for joints 1 and 2). This hysteresis is primarily due to backlash between the instrument shaft and cannula and therefore the distance between the best-fit lines provides a measurement of the backlash in each direction.

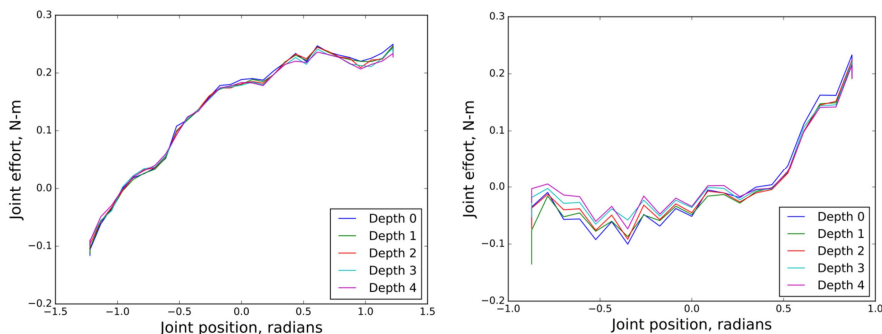


Figure 4

Measurements of torque offset as a function of joint angle for joint 1 (left) and joint 2 (right) at different instrument insertion depths.

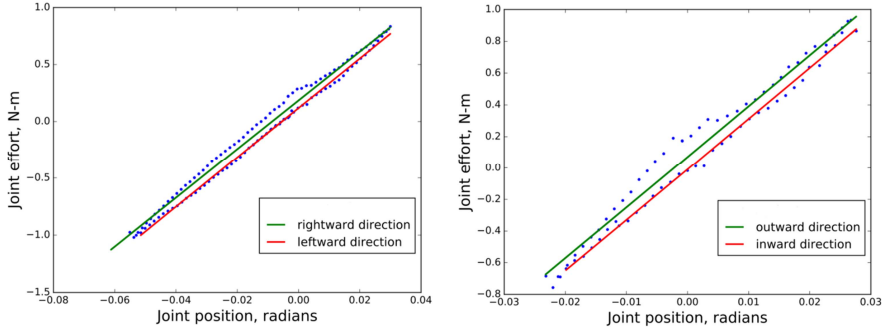


Figure 5

Measurements of joint effort as a function of joint position when instrument tip is clamped against beam for joint 1 (left) and joint 2 (right). Hysteresis (due to backlash) is evident. Plots include best-fit lines for each direction of motion.

We determine the angular correction factors  $K_1(L)$  and  $K_2(L)$  for joints 1 and 2, respectively, by computing the slopes of the lines in Fig. 5, for each instrument depth. The results are shown in Fig. 6, along with the best-fit cubic polynomials. These polynomials define the inverse of  $K_1(L)$  and  $K_2(L)$ :

$$K_1(L) = \frac{1}{639.16L^3 - 432.35L^2 + 136.32L + 3.12} \quad (3)$$

$$K_2(L) = \frac{1}{3163.17L^3 - 1969.15L^2 + 448.92L - 6.00} \quad (4)$$

Figure 6 also reveals that this parameter is not symmetric, particularly for joint 2. Since the instrument shaft is symmetric, this is most likely due to the overall mechanical structure which, for joint 2, includes a double four-bar linkage.

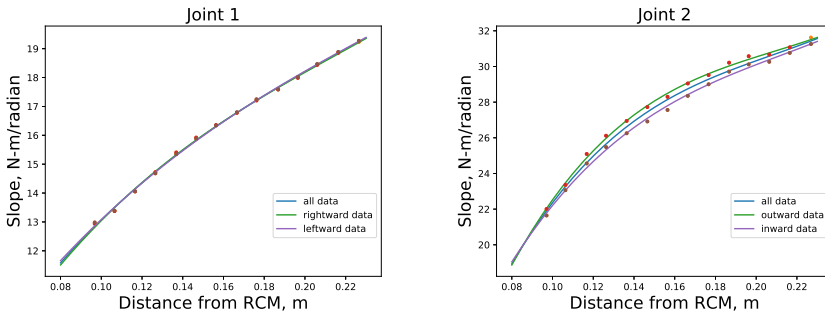


Figure 6

Inverse of angular correction factors as a function of insertion depth for directions corresponding to motion of joint 1 (left) and joint 2 (right).

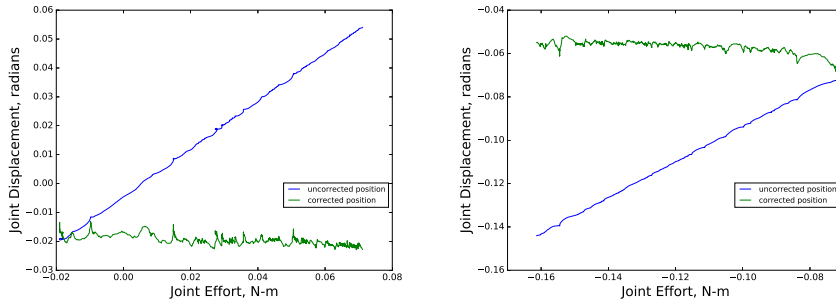


Figure 7

Uncorrected position of joint 1 compared to corrected position computed from model, while robot is pushing against divot in aluminum plate. Joint 1 is pushing in positive direction (left) or negative direction (right); in either case, true joint position should remain constant.

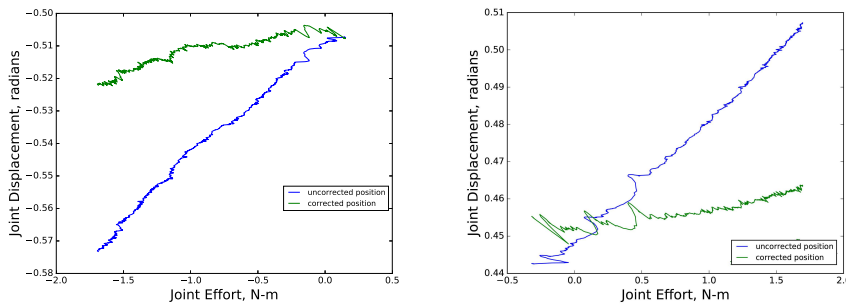


Figure 8

Uncorrected position of joint 2 compared to corrected position computed from model, while robot is pushing against divot in aluminum plate. Joint 2 is pushing in positive direction (left) or negative direction (right); in either case, true joint position should remain constant.

Finally, Figs. 7 and 8 compare the corrected and uncorrected positions of joints 1 and 2 while the robot is pushing against a divot in the aluminum plate. The plots show that the uncorrected joint positions are changing, even though the tip is not moving, due to the instrument compliance. In contrast, the corrected joint positions are nearly constant, which indicates an improvement in the accuracy of the robot.

## 5 Discussion

The da Vinci instrument position correction based on the compliance model shows promising results for increasing the accuracy of the da Vinci robot, especially when external forces are applied to the instrument. These results were obtained by focusing on one of the larger sources of error – the backlash and deformation of the instrument shaft in the lateral directions. These errors align with the first two robot joints and therefore we develop a correction model in joint space, using the measured joint torque (effort). Because the dVRK power amplifiers implement torque control, it is likely that the method would work equally well using the commanded joint torque instead of the measured joint torque.

The compliance model includes several experimentally determined parameters, including the angular correction factor  $K(L)$ , backlash  $\delta$ , and joint torque offset  $\tau_0(q)$ . The angular correction factor  $K(L)$  was determined by first fitting a line to the measured displacement and torque for each value of  $L$ . A cubic polynomial in  $L$  was then fit to the slopes of these lines, which provided the inverse of the angular correction factor for each joint. Future work should develop a mathematical model that is based on mechanical principles.

The experiments used the joint torque offset,  $\tau_0(q)$ , in lieu of the internal torque, which typically would include the effects of robot dynamics and other mechanical effects, such as friction. This simplification is valid for the static (or near static) case, where the commanded torque is primarily required to compensate for gravity or counter-balance forces. This is not an unrealistic simplification, since the da Vinci instruments are generally moved slowly and deliberately during surgical procedures. Also, in many cases, such as the da Vinci to TRUS registration previously cited [3], an accurate position measurement is only required when the instrument is not moving. Nevertheless, the implementation could be improved by incorporating estimates of the internal torque based on the dVRK dynamics [9, 10] or other methods [11].

Our results also are affected by small approximations in our methods. For example, we defined the instrument length,  $L$ , based on the measured joint position of the third axis (translation). This provides the length from the RCM point to a defined point on the instrument, which is a little offset with respect to the instrument tip (where forces would likely be applied in actual use) or with respect to the distal end of the instrument shaft (which is where we applied forces during our data collection). Thus, there will be a small discrepancy between the assumed length and the actual moment arm, which will have a minor effect on the accuracy of compensation.

Finally, our experimental results showed the ability to improve the accuracy at a single point (e.g., while pushing against a divot). We have not yet demonstrated accuracy improvement over the PSM workspace because, at present, inaccuracy of the dVRK kinematics contributes a larger source of error.

## 6 Conclusions

We developed a simple compliance model that relates lateral deflection of the da Vinci instrument shaft to angular offsets in the first two joints of the Patient Side Manipulator (PSM). Model parameters can be estimated using a simple data collection setup (a rigid beam) that does not require external measurement devices. Once the model parameters are obtained, real-time correction of instrument tip position can be achieved by applying the compliance model to the measured torques from the first two joints. While we expect some variation of model parameters between instruments, our hypothesis is that most instruments (with the same diameter) will have similar compliance models. We further expect that results will be similar between da Vinci systems, though there is likely to be some variability in the estimation of the internal torques,  $\tau_{int}$ , or the backlash,  $\delta$ .

The experiments were performed under static conditions to simplify the estimation of the internal torque, but we are investigating existing methods to estimate the internal

torque under dynamic conditions. In addition, accuracy of the PSM can be improved by calibration of the kinematic parameters.

The contribution of this work is not in the compliance model, which is straightforward, but rather in the demonstration that such a simple model can provide significant accuracy improvements. We are currently working to incorporate the data collection, parameter estimation, and real-time compensation methods into the open-source da Vinci research kit software. This will enable other researchers to replicate this work (currently, there are more than 35 dVRK systems around the world), with the added benefit of providing data to determine how the model parameters vary between different da Vinci systems and instruments.

## Acknowledgment

This work was supported by National Science Foundation (NSF) National Robotics Initiative (NRI) grant 1637789 and by JHU internal funds.

## References

- [1] G. Guthart and J. Salisbury. The Intuitive<sup>TM</sup> telesurgery system: Overview and application. In *Proc. IEEE Intl. Conf. on Robotics and Automation (ICRA)*, pages 618–621, May 2000.
- [2] D. Bouget, M. Allan, D. Stoyanov, and P. Jannin. Vision-based and marker-less surgical tool detection and tracking: a review of the literature. *Medical Image Analysis*, 35:633–654, Jan 2017.
- [3] O. Mohareri, M. Ramezani, T. K. Adebar, P. Abolmaesumi, and S. E. Salcudean. Automatic localization of the da Vinci surgical instrument tips in 3-D transrectal ultrasound. *IEEE Transactions on Biomedical Engineering*, 60(9):2663–2672, Sept. 2013.
- [4] C. Schneider, C. Nguan, R. Rohling, and S. Salcudean. Tracked “pick-up” ultrasound for robot-assisted minimally invasive surgery. *IEEE Trans. on Biomedical Engineering*, 63(2):260–268, Feb 2016.
- [5] T. K. Adebar, M. C. Yip, S. E. Salcudean, R. N. Rohling, C. Y. Nguan, and S. L. Goldenberg. Registration of 3D ultrasound through an air–tissue boundary. *IEEE Transactions on Medical Imaging*, 31(11):2133–2142, 2012.
- [6] M. Selvaggio, G. A. Fontanelli, F. Ficuciello, L. Villani, and B. Siciliano. Passive virtual fixtures adaptation in minimally invasive robotic surgery. *IEEE Robotics and Automation Letters*, 3(4):3129–3136, Oct 2018.
- [7] P. Chalasani, L. Wang, R. Yasin, N. Simaan, and R. H. Taylor. Preliminary evaluation of an online estimation method for organ geometry and tissue stiffness. *IEEE Robotics and Automation Letters*, 3(3):1816–1823, July 2018.
- [8] P. Kazanzides, Z. Chen, A. Deguet, G. S. Fischer, R. H. Taylor, and S. P. DiMaio. An open-source research kit for the da Vinci® surgical system. In *IEEE Intl. Conf. on Robotics and Automation (ICRA)*, pages 6434–6439, Hong Kong, China, June 2014.
- [9] H. Sang, J. Yun, R. Monfaredi, E. Wilson, H. Fooladi, and K. Cleary. External force estimation and implementation in robotically assisted minimally invasive

- surgery. *Intl. Journal of Medical Robotics and Computer Assisted Surgery*, 13(2), 2017.
- [10] G. A. Fontanelli, F. Ficuciello, L. Villani, and B. Siciliano. Modelling and identification of the da Vinci Research Kit robotic arms. In *IEEE/RSJ Intl. Conf. on Intelligent Robots and Systems (IROS)*, pages 1464–1469, Sept. 2017.
- [11] N. Yilmaz, M. Bazman, and U. Tumerdem. External force/torque estimation on a dexterous parallel robotic surgical instrument wrist. In *IEEE/RSJ Intl. Conf. on Intelligent Robots and Systems (IROS)*, pages 4396–4403, Oct. 2018.
- [12] M. Quigley, K. Conley, B. Gerkey, J. Faust, T. B. Foote, J. Leibs, R. Wheeler, and A. Y. Ng. ROS: an open-source Robot Operating System. In *ICRA Workshop on Open Source Software*, 2009.

# A DVRK-based Framework for Surgical Subtask Automation

Tamás D. Nagy<sup>1</sup> and Tamás Haidegger<sup>1,2</sup>

<sup>1</sup>Antal Bejczy Center for Intelligent Robotics, Óbuda University, Bécsi út 96/b, 1034, Budapest, Hungary, {tamas.daniel.nagy, tamas.haidegger}@irob.uni-obuda.hu

<sup>2</sup>Austrian Center for Medical Innovation and Technology (ACMIT), Viktor-Kaplan-Straße 2/1, 2700, Wiener Neustadt, Austria, tamas.haidegger@acmit.at

---

*Abstract:* Robotic assistance is becoming a standard in Minimally Invasive Surgery. Despite its clinical benefits and technical potential, surgeons still have to perform manually a number of monotonous and time-consuming surgical subtasks, like knot-tying or blunt dissection. Many believe that the next bold step in the advancement of robotic surgery is the automation of such subtasks. Partial automation can reduce the cognitive load on surgeons, and support them in paying more attention to the critical elements of the surgical workflow. Our aim was to develop a software framework to ease and hasten the automation of surgical subtasks. This framework was built alongside the Da Vinci Research Kit (DVRK), while it can be ported onto other robotic platforms, since it is based on the Robot Operating System (ROS). The software includes both stereo vision-based and hierarchical motion planning, with a wide palette of often used surgical gestures—such as grasping, cutting or soft tissue manipulation—as building blocks to support the high-level implementation of autonomous surgical subtask execution routines. This open-source surgical automation framework—named *irob-saf*—is available at <https://github.com/ABC-iRobotics/irob-saf>.

*Keywords:* robot-assisted minimally invasive surgery; surgical robotics; subtask automation; open-source platform

---

## 1 Introduction

In the last few decades, the headway of Minimally Invasive Surgery (MIS) had a significant influence on surgical practice. Contrary to traditional procedures performed using large incisions, MIS is executed through few-centimeter-wide ports, using so-called laparoscopic instruments, while the surgeon observes the area of operation via endoscopic camera stream. The smaller incisions required by the MIS technique have a number of benefits for both the patient and the hospital; causing less trauma and lowering the risk of complications. MIS also shortens recovery time and hospital stay. Nevertheless, this technique presents

serious cognitive and ergonomic challenges to the surgeons, like the limited range of motion, or weary positions.

The next step in the evolution of MIS was the introduction of teleoperated master-slave surgical systems. The fundamental idea of teleoperated surgery originates from space research [1]; the patient—in this case an astronaut—was to be treated by a slave device controlled by a remote surgeon, sitting at a master device on Earth. On the slave side, robot arms hold laparoscopic instruments, and copy the movement of the surgeon at the master console. To ensure visual feedback, the slave side device is equipped with an endoscopic camera, whose video stream is also sent to the master device and displayed to the surgeon.

Primarily due to the issues caused by time delay and system complexity, the idea of long distance telesurgery has not become a daily practice, and stalled in the state of research and pilots. Nevertheless, communication latency can be reduced to an insignificant level when the master and the slave devices are close to each other. Commercial Robot-Assisted Minimally Invasive Surgery (RAMIS) was born along this idea, where the master and the slave devices are in the same room. These systems are able to ease the fatigue of the surgeon, since they can operate in a comfortable, seated position, in a more ergonomic environment. Moreover, the motion of the surgeon is scalable, which means that the most delicate and fine maneuvers can be controlled by relatively large hand movements.

Undoubtedly, the most successful RAMIS device is the da Vinci Surgical System (Intuitive Surgical Inc., Sunnyvale, CA). Its 1<sup>st</sup> generation was cleared by the U. S. Food and Drug Administration in 2000, and became a commonly used device in a few years. Today, the 4<sup>th</sup> generation—da Vinci Xi—is available, while the more affordable alternative X, and the Single Port solution (SP) is also in the product portfolio of the company (Fig. 1). More than 5500 da Vinci units are installed worldwide that performed around 1 million procedures last year [1].

## 2 Da Vinci Research Kit

In the mid-2010s, the 1<sup>st</sup> generation of the robot (the da Vinci classic) was sent to retirement, since those were impractical to be serviced and supplied anymore. Nevertheless, the retired da Vincis were still functional, and could be well used in more failure-tolerant applications, like research. The development of the Da Vinci Research Kit (DVRK) was started at the Johns Hopkins University, and in a few years, an active community has gathered with more than 30 setups worldwide [2].

The DVRK consists of open-source, custom-built hardware controllers and software elements to make possible the programming of the attached da Vinci arms. The controllers of DVRK are built from two custom boards, an IEEE-1394 FPGA board and a Quad Linear Amplifier (QLA); these provide the computational power and low latency communication required for the low-level high-frequency robot control. The controller boxes are interfaced to PC using IEEE 1394a

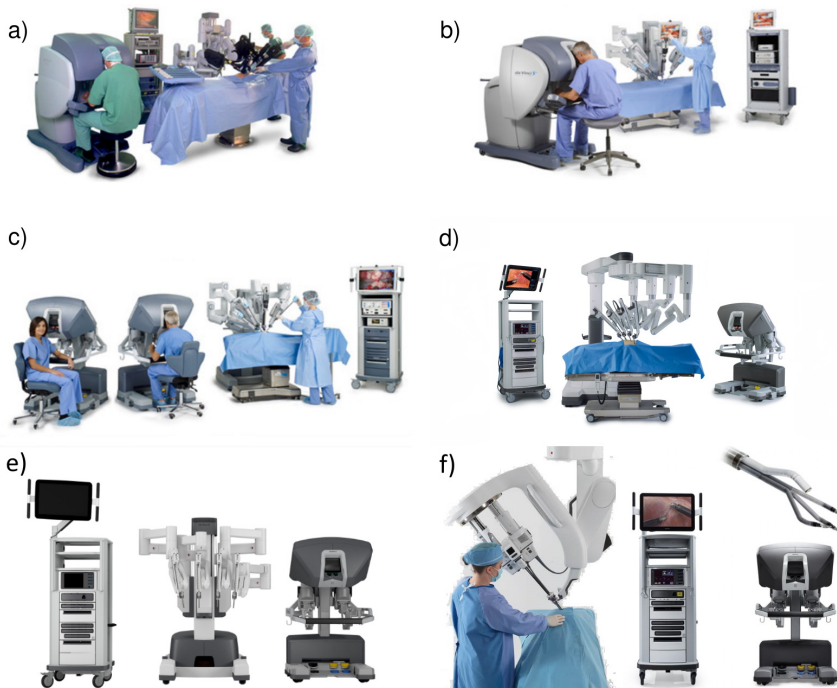


Figure 1

The 4 generations of the da Vinci Surgical System; a) da Vinci Classic, b) da Vinci S, c) da Vinci Si and d) da Vinci Xi, completed with the most recent e) X and f) SP systems.

Image credit: Intuitive Surgical Inc.

(FireWire); one of the controllers have to be connected directly to the PC, then this controller is able to manage the communication of further controllers in a daisy chain. On the PC side, the open-source *cisst* libraries [3] are for the mid-level control and FireWire communication, built by *Catkin* build system. These libraries themselves offer the functionality to the programming of the robot, however, a ROS interface was also implemented; more than half of the research institutes use the latter for the programming of the da Vinci [4].

ROS is used commonly in robotics, mainly in the field of research, and most of the research centers working with the DVRK, or the RAVEN platform [4], rely on ROS. Beyond the compatibility with the mentioned platforms, ROS is quite powerful, offering built-in solutions for a number of problems e.g., accessing sensory data, calibrating stereo-cameras, and enabling highly modular development.

### 3 Subtask Automation in Surgery

Many believe that the next step in the technical development of RAMIS is going to be partial (or conditional) automation [5]. The surgical workflow of RAS procedures often contains time-consuming and monotonous elements—so-called surgical subtasks—like suturing, knot-tying, or blunt dissection. The automation of these subtasks can reduce the fatigue and the cognitive load on the surgeon, who can hence pay more attention to the more critical parts of the intervention [6].

As the development of the technological background in the last couple of years offers a rising potential, like deep learning or mechatronics, the automation of surgical subtasks became a prevailing topic in the research of surgical robotics. A number of autonomous surgical subtasks are already implemented, or being currently developed by various research groups. A list of relevant subtasks in the research of surgical automation is compiled in Table 1.

Table 1  
List of surgical subtasks from the aspect of suitability for partial automation.

Subtask	Sensor integration	Experimental environment	Complexity	Clinical relevance	Ref.
shape cutting	stereo camera	gauze patch, FRS Dome <sup>1</sup>	medium	high	[7]
suturing	stereo camera	silicone, foam, FRS Dome	high	high	[8]
ligation	–	special phantom	medium	high	[9]
palpation	force sensor	special silicone phantom, FRS Dome	medium	medium	[10] [11]
tumor palpation and resection	force sensor	special silicone phantom, FRS Dome	high	medium	[12]
debridement	stereo camera	tiny objects	medium	high	[13] [14]
suction and debridement	–	special phantom	medium	high	[15]
bowel anastomosis	3D camera	porcine bowel	high	high	[16]

<sup>1</sup> Florida Hospital Nicholson Center, Celebration, FL

blunt dissection	stereo camera	sandwich-like silicone phantom	medium	high	[17] [18]
tissue retraction	stereo camera	silicone phantom	low	high	[19]
peg transfer	stereo camera	training phantom	medium	low	[20]

The automation of a number of subtasks are currently under active research, such as different aspects of suturing, soft tissue cutting, debridement, palpation or blunt dissection, employing techniques like learning-by-observation, motion decomposition and state machines [7–20].

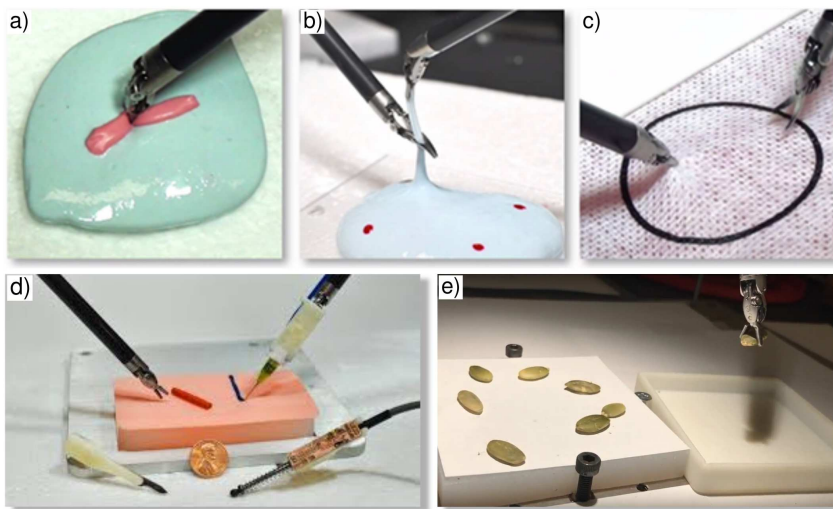


Figure 2

Recently automated surgical subtasks. a-c) Multilateral cutting, d) tumor palpation and e) resection, debridement. Image credit: [7, 12, 14].

All of the mentioned surgical subtasks are to be performed on soft tissue, in a highly deformable environment. In contrast to subtasks involving hard tissue, like bone cutting, where the target organ can be fixed and registered with the surgical device via a navigation system, soft tissue presents new challenges from the aspect of automation, as the robot has to operate in unpredictable environment. Probably the biggest challenge is the development of perception algorithms; it is not trivial how the information, needed for the execution of the current subtask can be extracted from the surrounding soft, specular environment. Despite the fact that working implementations could be found e.g., on instrument segmentation/pose estimation [21, 22] or organ segmentation and 3D reconstruction [23–25], autonomous navigation inside the patient's body still presents a

huge challenge being under intensive research. As of today, shared control is a more viable option for these clinical routines [26, 27]. Furthermore, the generation of required motion patterns and the design of control methods for the manipulation of unknown soft tissues is also problematic [28].

Our aim was to develop an open-source framework to support such development projects; to provide software packages that contains already implemented basic functionalities, eventually becoming universal building blocks in surgical subtask automation [20]. The architecture of this software package—the iRob Surgical Automation Framework, or *irob-saf*—is presented herein.

## 4 Materials and Methods

One of the fundamental tasks in the development of this surgical automation framework was the hierarchical decomposition of surgical motion patterns. The workflow of surgical interventions, as well as the motion of the surgeon, can be decomposed into elements on different levels of granularity [29–31], similar to behavior trees [32]. In the literature, there are several different definitions of some granularity levels, nevertheless, no consistent definition can be found for the whole domain. To decompose surgical motion and implement partial automation, it is necessary to define these levels as precisely as possible. For that manner, we defined the levels of granularity—according to the current state of research—as follows (Fig. 3):

1. **Operation:** The entire invasive part of the surgical procedure.
2. **Task:** Well delimited surgical activity with a given high-level target/goal to achieve.
3. **Subtask:** Circumscribed activity segments that accomplish specific minor landmarks in completing the surgical task.
4. **Surgeme:** An atomic unit of intentional surgical activity resulting in a perceivable and meaningful outcome.
5. **Motion primitive:** General elements of motion patterns, that can be directly translated into robot commands.

In most studies, the granularity level chosen for surgical automation is the level of subtasks (Table 1). The execution of those subtasks usually leads to the accomplishment of a specific milestone, which is in line with the term of partial automation. Subtasks can be further divided into surgemes, which are universal to different subtasks. Thus, from the viewpoint of automation, different subtasks can be built of a set of universal surgemes. Those thoughts lead to the assembly of a motion library (*irob-saf*), containing a set of universal surgeme implementations.

To build this motion library, a number of surgical subtasks had to be decomposed into a set of universal surgemes. For that purpose, several features and events

Level of granularity	Definition	Time span	Complexity	Example
Operation	The entire invasive part of the procedure.	20-200 min	very high	Laparoscopic cholecystectomy
Task	Well delimited surgical activity with a given high-level target/goal to achieve.	1-5 min	high	Pneumo-peritoneum → Exposing Calot's triangle → ...
Subtask	Circumscribed activity segments that accomplish specific minor landmarks in completing the surgical task.	0.1-2 min	moderate	Retraction of the gallbladder → Blunt dissection at the Cystic duct → Blunt dissection at the Cystic art. → ...
Surgeme	An atomic unit of intentional surgical activity resulting in a perceivable and meaningful outcome.	0.1-0.5 min	low	Approach the tissue ↔ Perform dissecting motion → ...
Motion primitive	General elements of motion patterns, that can be directly translated into robot commands.	1-5 sec	very low	Penetrate connective tissue → Open the dissector → Remove the dissector

Figure 3

Overview of surgical motion's granularity levels. Mapping of an example, Laparoscopic Cholecystectomy procedure onto different granularity levels [17, 20].

were defined that separates subsequent surgemes from one another. A prime one is the overall shape of motion; this distinguishes for example the cutting from free navigation. Another important feature is the presence of tissue interaction during the surgeme; the instrument can move freely in the abdomen, it can grasp a loose piece of tissue, or even manipulate a tissue layer anchored to the anatomy. If the type of tissue interaction changes during the subtask execution, it will surely mean the transition to another surgeme. The final aspect of decomposition was the instrument required to be used during the procedure, e.g., a grasping surgeme might not be performed using scissors, and a cutting might not be done using grasping tools.

## 5 The Architecture of the Framework

The ROS platform—used widely in robotics—offers solutions to build modular, reusable software on a large scale. A ROS-based architecture consists of so-called *nodes*, intercommunicating with each others over channels of three types:

- Topic: continuous data streaming
- Service: request–response type communication with blocking behavior, has benefits for e.g. requesting calculations
- Action: request–response type communication with non-blocking behavior, useful for environmental interactions.

Due to its benefits, the *irob-saf* framework was completely built on ROS, and tailored to be usable alongside the DVRK. However, due to the implemented ROS interface, the framework is easily portable to other platforms. A system, performing a surgical subtask autonomously, can be assembled from the nodes of *irob-saf* based on the principle shown in Fig. 4. Sensors and perception algorithms, directed by ROS nodes, are used for the purpose of the measurement

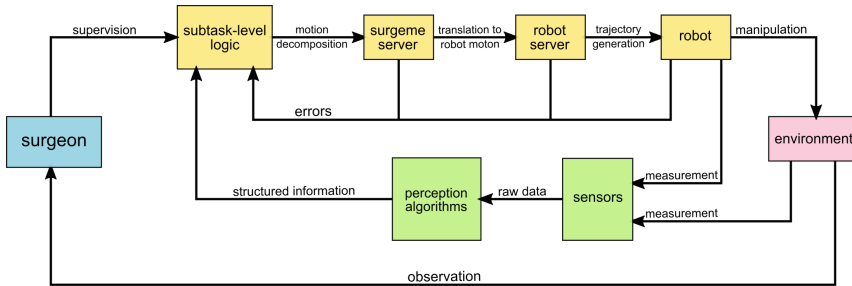


Figure 4

The control scheme of partial automation offered by the framework. Perception nodes gather information from the environment. The subtasks-level logic contains the whole workflow of the subtask, processes the incoming information, and also communicates with the surgeon. This node also sends commands to the hierarchical set of nodes, appointing the surgemes to be executed. The generated motion is executed by the robot under permanent monitoring of the surgeon.

and estimation of the properties of the environment. The information gained, including errors eventually, are all channeled into the subtask-level logic. This node is responsible for the processing of the information regarding the environment, and the commands originating from the surgeon. Additionally, the surgical workflow is coded in this node; its elements are translated into surgemes and sent to the surgeme server in the form of ROS actions. Propagating down from the surgeme server, the robot motion is generated by a hierarchical network of nodes, then sent to the robot (the ROS nodes from DVRK). Important to note, due to the principle of partial automation, the permanent monitoring of the surgeon is essential during the execution of the subtask.

Camera image is one of the most important sources of information in the automation of RAMIS. The usage of the endoscopic camera image is undoubtedly the most obvious choice, since it does not require the placement of any additional instrument into the already crowded operating room. Nevertheless, in *irob-saf*, the video stream—preferably stereo—can be provided by a wide range of cameras as long as it is interfaced with a ROS topic. Examples interfaces for USB webcams and the stereo endoscope of the da Vinci are implemented in the framework. The calibration of the cameras—either mono or stereo—is performed by the built-in, easy-to-use camera calibration tool of the ROS environment, using a checkerboard pattern [33]. Furthermore, the basic stereo image processing algorithms, like disparity map calculation or the generation of the 3D point cloud are also performed with one of the built-in libraries of ROS [34].

The algorithms usable for perception are out of scope of the current work, however, the framework offers a pre-built infrastructure to run those with the required input and output channels. These algorithms can be built using C++, Python, or even MATLAB. To ease development, the framework contains examples such as the detection of ChArUco markers [35]. It is important to note that further sensor

modalities, like force sensors, or RGB-D cameras can also be easily added to the existing infrastructure.

The arms of the da Vinci surgical robot are interfaced with the framework by high-level robot control nodes, one node per arm. These nodes are responsible for executing the trajectories generated by higher level nodes, while checking for errors originating from the robot. The trajectories are sent through ROS actions instead of topics, which are more favorable in environmental interaction scenarios. ROS actions makes it possible for the higher-level nodes to do further work during action execution, e.g., monitoring the environment, or sending actions to other nodes. Moreover, actions provide the ability to send feedback and the result of the action, or preempt the action with another, if any environmental change makes it necessary, e.g. the location of the target was changed during execution.

The framework also offers solution for hand–eye calibration; namely the coordinate systems of the arms can be registered to the camera coordinate frame, that makes possible the generation of the robot motion relative to the camera. Visual markers attached to the instruments are used to estimate the tool positions based on the stereo camera stream. The hand–eye calibration can be performed using a MATLAB script, that records tool positions in the robot coordinate frame (received from DVRK through ROS) and in the camera coordinate frame (estimated using the visual markers) simultaneously, in manually set positions. Based on the recorded positions, the optimal rigid transformation is calculated between the two coordinate systems [36–38]. The registration is then saved to a yaml file (“YAML Ain’t Markup Language”), that is loaded by the corresponding high-level robot control node, which thus able to receive position commands in the camera coordinate frame from the higher-level nodes of the system.

These high-level robot control nodes are robot-specific, but their interface to the other nodes of the framework is universal. This means that the usage of another type of robot arm requires only the implementation of the high-level robot control node itself.

The surgical motion library, mentioned in Section 4, containing the implementation of universal surgemes, can be found in the package `irob_motion` of the framework. This surgeme library offering surgemes as parameterizable ROS actions, such as: *grasp*, *cut*, *place object*, *release object*, *navigate*, *dissect* and *manipulate tissue*. The implemented surgemes are able to do the necessary safety checks, e.g., the proper instrument is used for the current surgeme. Further surgemes can be implemented based on the existing ones, and then added to the library.

The whole architecture is controlled by a subtask-level logic node. This node is subtask specific, an individual node needs to be implemented for each different surgical subtask. Here is where the information from the perception nodes is received and processed; all the errors, exceptions of the system and user (surgeon) interactions are also channeled; and the surgeme level motion commands are generated. Subtask-level logic nodes are designed to contain and perform the specific workflow of the current subtask. The framework offers skeletons and

also examples how to implement such nodes for the specific surgical subtask. At this level, behavior trees would offer a very structured representation of surgical knowledge and workflow [32], and it is planned to utilize this model in the future development of the framework.

## 6 Examples

The usage of the framework is explained through two examples on the automation of subtasks. We decided to implement subtasks that require simpler perception methods; those algorithms are out of scope of the current work. The automation of a training exercise and an actual surgical exercise is presented in the following.

### 6.1 Automating peg transfer

The first example for automation is a RAS training exercise, peg transfer. During this exercise, small tubes have to be placed from one peg to another, to enhance the visuomotor skills of the surgeon (Fig. 5). This exercise is simple enough to present how an autonomous subtask execution can be built using our framework. One and two armed solutions were implemented of the peg transfer exercise. During the one armed execution, the tubes are simply grasped and placed on another peg by one PSM arm. In the two armed version, the tube is grasped and lifted up from the peg from one PSM arm, then transferred to another PSM, that places it on the target peg.

The position of the training board was estimated by the stereo camera stream of the built-in endoscope of the da Vinci. The video stream was captured by a Deck-Link Blackmagic (Blackmagic Design Pty. Ltd., Port Melbourne, VIC) card, and forwarded to ROS using GStreamer [39]. The cameras were calibrated using the ROS built-in `camera_calibration` package. The board was marked by ArUco or ChArUco markers, that can be detected robustly by the camera, and can be used to estimate the board's position [35]. To start the nodes for computer vision, the launching of two launch files from the `irob_vision_support` package is necessary:

- `cam_blackmagic_raw.launch`: starts the node for streaming the camera image from one of the da Vinci's cameras
- `charuco_detector.launch`: for the pose estimation of the peg transfer board based on a ChArUco marker.

The nodes responsible for the generation and execution of surgical motion are operating at 4 different levels of hierarchy. The uppermost level is the level of subtasks, with nodes of the `irob_subtask_logic` package. This level is built on a single node, that contains the workflow of the subtasks, receives the pose estimation of the peg transfer board, and chooses the surges for execution. The execution of surges is requested using ROS actions, that is sent to the proper node in the lower level. The second level of hierarchy contains the im-

plementation of the universal surges. At this level, one surge server node is launched for each arm operating, receiving ROS actions from the subtask level, and sending ones to the lower, third level. This third level is responsible for the high level control of the arms, and consists of robot server nodes; one such node is responsible for the handling of one arm. These nodes accept ROS action commands for robot movements, and are also connected to the appropriate DVRK node at the fourth, lowermost level to execute the requested movements.

While the nodes of the three lower levels are universal for different subtasks, the uppermost, subtask-level logic node is unique. This node contains the workflow, basically a sequence of surges to execute, however, in case of more complex subtasks, a state machine implementation can be useful as well. The motion—both in case of one and two armed solutions—is composed of only three surges: *grasp*, *place* and *release* (Fig. 6). All surges of the framework including these three, are built of two motion primitives: spatial navigation of the instrument's endpoint, and the movement of the instrument's jaws. These motion primitives can be described well by only a few parameters, and based on the given parameters, the robot trajectories can be easily generated. These three surges are built up as follows:

- Grasp:
  1. navigate to approach position (waypoints can be added)
  2. navigate to grasp position
  3. close jaws
- Place:
  1. navigate to approach position (waypoints can be added)
  2. navigate to place position
- Release:
  1. open jaws
  2. navigate to leave position

The execution of those surges is requested by sending parameterized actions for to the surge server representing the chosen arm. The parameters of those surge action requests are calculated by the measured or estimated properties of the environment, received from the computer vision module. Such parameters can be the size of the object to grasp, the compression rate during grasping, or the approach and grasp position of the instrument endpoint.

This hierarchy can be assembled by launching the following instances, in case of two armed execution:

- `peg_transfer_dual.launch` from package `irob_subtask_logic`
- `surge_server.launch` from package `irob_motion`, in two instances, parameterized for each arms



Figure 5

The setup for the peg transfer exercise. The board is marked using a ChArUco marker for image-based pose estimation.

- `dvrk_server` from package `irob_robot`, also in two instances, parameterized for each arms
- DVRK console, with the arms to be operated

The performance of the autonomous execution was compared to humans in the case of the standard exercise, where six tubes are to be placed from the original pegs to another six pegs using two arms. The completion times of six subjects, with minimal expertise in the usage of the da Vinci system were measured after a short practice period. It turned out that the average time needed for the task was 71.4 seconds in the case of novice users, while the automatic agent's performance was 64.0 seconds. However, the speed of the execution could be further increased, at higher speed we found the accuracy of the arms position control started to decrease.

## 6.2 Automating blunt dissection

Another subtask example implemented using the framework was blunt dissection. Blunt dissection is a common subtask in MIS, usually used to separate loosely connected layers of tissue without damaging sensitive anatomical structures, like nerves or blood vessels. During this subtask, to ensure that none of those sensitive structures get damaged, no sharp instruments are used, the layers are separated by gentle opening movements of the forceps' jaws. This subtask is more relevant from the aspect of surgery, and still simple enough to be automated using simple perception algorithms. The details of this subtask automation were presented in [17].

The development and testing of this algorithm was performed using a silicone phantom consisting of two harder layers of silicone connected with a softer, destructible silicone layer. In our test environment, two calibrated web cameras

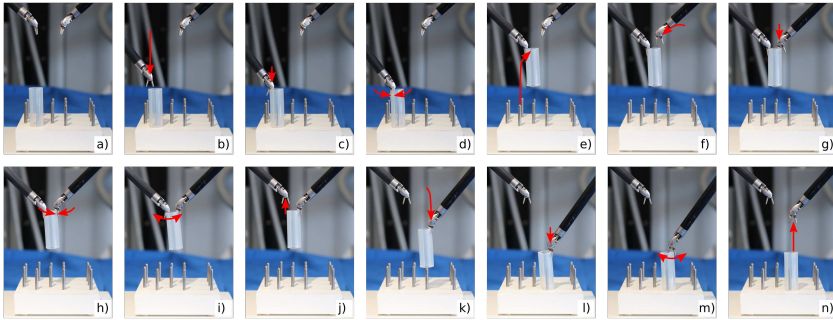


Figure 6

The workflow used in the automation of two-armed peg transfer. a) Setup before starting peg transfer. b–d) Left arm grasps the object. e) The object is lifted to the passing location. f–h) The object is grasped by the right arm. i–j) The object is released by the left arm. k–l) The object is placed on the target peg. m–n) The object is released by the right arm.

were utilized, with fixed focal length, attached onto a stable frame to provide the stereo image feed. The detection of the dissection profile relies on the depth map of the camera scene, calculated from the distance of each corresponding point pair on the rectified stereo pair.

The process presented in Fig. 7 is initiated by manually selecting a starting and an end point of the blunt dissection line. The precise dissection profile, where the dissection will be performed, is selected autonomously, by searching for the local minima of depth in the environment of the points of the manually selected dissection line (Fig. 7). The accuracy of the dissection line detection is further increased using Hampel filter to remove outliers. To ensure to progress evenly inward between the tissues, the point with the lowest depth of the dissection profile is used for the location of the next dissection movement.

As the subtask-level logic node receives the points of the dissection profile, so-called *dissect* surges are performed by the arm of the DVRK controlled da Vinci, consisting of the following primitives:

- **Dissect:**

1. navigate to the point of dissection (Fig. 8/a)
2. slowly penetrate the tissue (Fig. 8/b)
3. open the jaws to separate layers (Fig. 8/c)
4. pull out the instrument in an open position (Fig. 8/d)

The system performing blunt dissection autonomously can be assembled a similar way as the one for peg transfer. In this case, only one arm is required, and the computer vision is implemented in MATLAB. The USB stereo camera pair can be launched by `stereo_cam_usb.launch` of the `irob_vision_support` package.

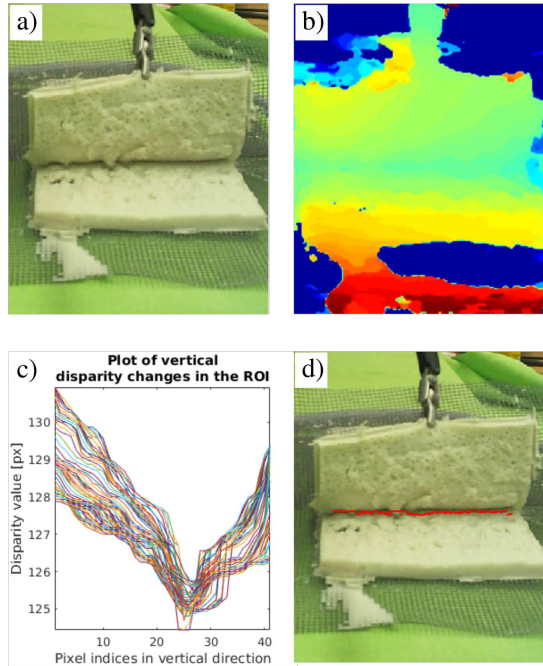


Figure 7

Method for blunt dissection automation via computer vision. a) Image of blunt dissection phantom; b) disparity map of the field of view (color represents the points' distances from the camera); c) plot of disparity changes in vertical direction; d) blunt dissection profile from the local minima of the disparity map. Image credit: [17].

The accuracy of the system was measured during 10 test cases: the average accuracy was 2.2 mm with a standard deviation of 0.5 mm in the camera views plane. In the depth axis—perpendicular to the camera plane—the 1 mm accuracy with standard deviation of 0.6 mm was measured. The overall performance of the autonomous blunt dissection algorithm was evaluated on the silicone-based custom designed phantom, by performing single dissections on 25 different locations. 21 of the 25 attempts succeeded; in 4 cases the dissection profile was missed by a maximum of 3 mm [17].

### Discussion and conclusions

An open-source, ROS-based software package was presented, which aims to ease surgical subtask automation research. This framework interfaces sensory inputs, perception algorithms and robots, and contains a surgeme-level motion library. The whole system can be controlled by a subtask-level logic ROS node, tailored to the needs of the current subtask to be automated. The iRob Surgical Automation Framework is available at <https://github.com/ABC-iRobotics/irob-saf>, and is being continuously developed and updated.

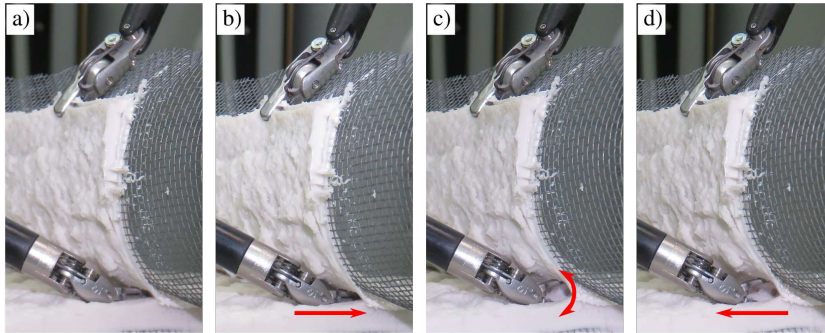


Figure 8

Motion primitives of the surgical subtask automation. a) The surgical instrument (large needle driver) moves to the dissection target; b) the robot pushes the instrument into the phantom; c) the instrument is opened; d) the robot pulls out the instrument.

Image credit: [17].

The framework can help in the implementation of further, more complex subtasks. In such development, it is straightforward to add new, necessary surges—like clipping or suturing. The implementation of new subtask can be added to the `irob_motion` package easily. Based on our experiences, the most challenging aspect in automating more complex subtasks is the perception estimation of the environment, as computer vision usually struggles with light reflections or moving, deformable and hardly recognizable tissue, even in phantom environment, or *ex vivo*.

### Acknowledgement

This work was partially supported by ACMIT (Austrian Center for Medical Innovation and Technology), which is funded within the scope of the COMET (Competence Centers for Excellent Technologies) program of the Austrian Government. Partial support of this work comes from the Hungarian State and the European Union under the EFOP-3.6.1-16-2016-00010 project. T. D. Nagy and T. Haidegger are supported through the New National Excellence Program of the Ministry of Human Capacities. T. Haidegger is a Bolyai Fellow of the Hungarian Academy of Sciences.

### References

- [1] Á. Takács, D. Á. Nagy, I. J. Rudas, and T. Haidegger. Origins of Surgical Robotics: From Space to the Operating Room. *Acta Polytechnica Hungarica*, 13(1):13–30, 2016.
- [2] P. Kazanzides, Z. Chen, A. Deguet, G. S. Fischer, R. H. Taylor, and S. P. DiMaio. An open-source research kit for the da Vinci® Surgical System. In *Proc. of the IEEE Intl. Conf. on Robotics and Automation*, pages 6434–6439, Hong Kong, 2014.

- [3] P. Kazanzides. Open Source Software Libraries for Computer Integrated Surgery. [https://cisst.org/wp-content/uploads/2016/03/YR\\_8\\_Open\\_Source\\_Software.pdf](https://cisst.org/wp-content/uploads/2016/03/YR_8_Open_Source_Software.pdf), 2005.
- [4] Z. Chen, A. Deguet, R. H. Taylor, and P. Kazanzides. Software Architecture of the Da Vinci Research Kit. In *Proc. of the IEEE Intl. Conf. on Robotic Computing (IRC)*, pages 180–187, Taichung City, Taiwan, 2017.
- [5] T. Haidegger. Autonomy for Surgical Robots: Concepts and Paradigms. *IEEE Trans. on Medical Robotics and Bionics*, 1(2):65–76, 2019.
- [6] D. Á. Nagy, I. J. Rudas, and T. Haidegger. OntoFlow, a software tool for surgical workflow recording. In *2018 IEEE 16th World Symposium on Applied Machine Intelligence and Informatics (SAMII)*, pages 119–124, Kosice, 2018.
- [7] A. Murali, S. Sen, B. Kehoe, A. Garg, S. McFarland, S. Patil, W. D. Boyd, S. Lim, P. Abbeel, and K. Goldberg. Learning by observation for surgical subtasks: Multilateral cutting of 3D viscoelastic and 2D Orthotropic Tissue Phantoms. In *Proc. of the IEEE Intl. Conf. on Robotics and Automation*, pages 1202–1209, Seattle, 2015.
- [8] S. Sen, A. Garg, D. V. Gealy, S. McKinley, Y. Jen, and K. Goldberg. Automating multi-throw multilateral surgical suturing with a mechanical needle guide and sequential convex optimization. In *Proc. of the IEEE Intl. Conf. on Robotics and Automation*, pages 4178–4185, Stockholm, 2016.
- [9] Hyosig Kang and J. T. Wen. EndoBot: A robotic assistant in minimally invasive surgeries. In *Proc. of the IEEE Intl. Conf. on Robotics and Automation (ICRA 2001)*, volume 2, pages 2031–2036, Seoul, South Korea, May 2001.
- [10] A. Garg, S. Sen, R. Kapadia, Y. Jen, S. McKinley, L. Miller, and K. Goldberg. Tumor localization using automated palpation with Gaussian Process Adaptive Sampling. In *Proc. of the 2016 IEEE Intl. Conf. on Automation Science and Engineering (CASE)*, pages 194–200, Fort Worth, 2016.
- [11] K. A. Nichols and A. M. Okamura. Autonomous robotic palpation: Machine learning techniques to identify hard inclusions in soft tissues. In *Proc. of the 2013 IEEE Intl. Conf. on Robotics and Automation*, pages 4384–4389, Karlsruhe, 2013.
- [12] S. McKinley, A. Garg, S. Sen, D. V. Gealy, J. McKinley, Y. Jen, and K. Goldberg. Autonomous Multilateral Surgical Tumor Resection with Interchangeable Instrument Mounts and Fluid Injection Device. 2016.
- [13] B. Kehoe, G. Kahn, J. Mahler, J. Kim, A. Lee, A. Lee, K. Nakagawa, S. Patil, W. D. Boyd, P. Abbeel, and K. Goldberg. Autonomous multilateral debridement with the Raven surgical robot. In *Proc. of the 2014 IEEE Intl. Conf. on Robotics and Automation (ICRA)*, pages 1432–1439, Hong Kong, 2014.
- [14] D. Seita, S. Krishnan, R. Fox, S. McKinley, J. Canny, and K. Goldberg. Fast and Reliable Autonomous Surgical Debridement with Cable-Driven Robots Using a Two-Phase Calibration Procedure. In *Proc. of the 2018 IEEE Intl. Conf. on Robotics and Automation (ICRA)*, pages 6651–6658, Brisbane, 2017.

- [15] F. Richter, R. K. Orosco, and M. C. Yip. Open-Sourced Reinforcement Learning Environments for Surgical Robotics. *arXiv preprint arXiv:1903.02090*, March 2019.
- [16] A. Shademan, R. S. Decker, J. Opfermann, S. Leonard, A. Krieger, and P. C. W. Kim. Supervised autonomous robotic soft tissue surgery. *Science Translational Medicine*, 8(337), 2016.
- [17] R. Elek, T. D. Nagy, D. Á. Nagy, T. Garamvölgyi, B. Takács, P. Galambos, J. K. Tar, I. J. Rudas, and T. Haidegger. Towards surgical subtask automation—blunt dissection. In IEEE, editor, *Proc. of the IEEE 21st Intl. Conf. on Intelligent Engineering Systems*, pages 253–258, Larnaca, 2017.
- [18] D. Á. Nagy, T. D. Nagy, R. Elek, I. J. Rudas, and T. Haidegger. Ontology-Based Surgical Subtask Automation, Automating Blunt Dissection. *Journal of Medical Robotics Research*, 3(3), 2018.
- [19] T. D. Nagy, M. Takács, I. J. Rudas, and T. Haidegger. Surgical Subtask Automation—Soft Tissue Retraction. In *Proc. of the 16th IEEE World Symposium on Applied Machine Intelligence and Informatics*, pages 55–60, Kosice, 2018.
- [20] T. D. Nagy and T. Haidegger. An Open-Source Framework for Surgical Subtask Automation. In *Proc. of the ICRA 2018 IEEE Intl. Conf. on Robotics and Automation, Workshop on Supervised Autonomy in Surgical Robotics*, Brisbane, 2018.
- [21] R. Sznitman, C. Becker, and P. Fua. Fast Part-Based Classification for Instrument Detection in Minimally Invasive Surgery. In P. Golland, N. Hata, C. Barillot, J. Hornegger, and R. Howe, editors, *Proc. of the Medical Image Computing and Computer-Assisted Intervention – MICCAI 2014*, volume 8674, pages 692–699, Cham, 2014. Springer Intl. Publishing.
- [22] M. Allan, P.-L. Chang, S. Ourselin, D. J. Hawkes, A. Sridhar, J. Kelly, and D. Stoyanov. Image Based Surgical Instrument Pose Estimation with Multi-class Labelling and Optical Flow. In N. Navab, J. Hornegger, W. M. Wells, and A. Frangi, editors, *Proc. of the Medical Image Computing and Computer-Assisted Intervention – MICCAI 2015*, volume 9349, pages 331–338, Cham, 2015. Springer Intl. Publishing.
- [23] Yuan-Fang Wang, D. R. Uecker, and Wang Yulun. Choreographed scope manoeuvring in robotically-assisted laparoscopy with active vision guidance. In *Proc. of the Third IEEE Workshop on Applications of Computer Vision. WACV'96*, pages 187–192, Sarasota, US, December 1996.
- [24] A. Krupa, J. Gangloff, C. Doignon, M. F. de Mathelin, G. Morel, J. Leroy, L. Soler, and J. Marescaux. Autonomous 3-D positioning of surgical instruments in robotized laparoscopic surgery using visual servoing. *IEEE Transactions on Robotics and Automation*, 19(5):842–853, October 2003.
- [25] D. Hutchison, T. Kanade, J. Kittler, J. M. Kleinberg, F. Mattern, J. C. Mitchell, M. Naor, O. Nierstrasz, C. Pandu Rangan, B. Steffen, M. Sudan, D. Terzopoulos, D. Tygar, M. Y. Vardi, G. Weikum, D. Stoyanov, M. V. Scanzanella, P. Pratt, and G.-Z. Yang. Real-Time Stereo Reconstruction in Robotically Assisted Minimally Invasive Surgery. In T. Jiang, N. Navab, J. P. W. Pluim, and M. A. Viergever, editors, *Proc. of the Medical Image*

- Computing and Computer-Assisted Intervention – MICCAI 2010*, volume 6361, pages 275–282, Berlin, Heidelberg, 2010. Springer Berlin Heidelberg.
- [26] J. J. Abbott, P. Marayong, and A. M. Okamura. Haptic Virtual Fixtures for Robot-Assisted Manipulation. In S. Thrun, R. Brooks, and H. Durrant-Whyte, editors, *Robotics Research*, volume 28, pages 49–64. Springer Berlin Heidelberg, Berlin, Heidelberg, 2007.
  - [27] M. Selvaggio, G. A. Fontanelli, F. Ficuciello, L. Villani, and B. Siciliano. Passive Virtual Fixtures Adaptation in Minimally Invasive Robotic Surgery. *IEEE Robotics and Automation Letters*, 3(4):3129–3136, October 2018.
  - [28] N. Abolhassani, R. Patel, and M. Moallem. Needle insertion into soft tissue: A survey. *Medical Engineering & Physics*, 29(4):413–431, 2007.
  - [29] S. S. Vedula, A. O. Malpani, L. Tao, G. Chen, Y. Gao, P. Poddar, N. Ahmidi, C. Paxton, R. Vidal, S. Khudanpur, G. D. Hager, and C. C. Chen. Analysis of the Structure of Surgical Activity for a Suturing and Knot-Tying Task. *PLOS ONE*, 11(3):e0149174, 2016.
  - [30] L. MacKenzie, J. A. Ibbotson, C. G. L. Cao, and A. J. Lomax. Hierarchical decomposition of laparoscopic surgery: A human factors approach to investigating the operating room environment. *Minimally Invasive Therapy & Allied Technologies*, 10(3):121–127, 2001.
  - [31] Y. Gao, S. S. Vedula, C. E. Reiley, N. Ahmidi, B. Varadarajan, H. C. Lin, L. Tao, L. Zappella, B. Béjar, and D. D. Yuh. JHU-ISI gesture and skill assessment working set (JIGSAWS): A surgical activity dataset for human motion modeling. In *Proc. of the MICCAI Workshop: M2CAI*, volume 3, Boston, 2014.
  - [32] B. Hannaford, R. Bly, I. Humphreys, and M. Whipple. Behavior Trees as a Representation for Medical Procedures. *arXiv:1808.08954 [cs]*, August 2018.
  - [33] ROS package for camera calibration. [http://wiki.ros.org/camera\\_calibration](http://wiki.ros.org/camera_calibration).
  - [34] ROS package for stereo image processing. [http://wiki.ros.org/stereo\\_image\\_proc](http://wiki.ros.org/stereo_image_proc).
  - [35] S. Garrido-Jurado, R. Muñoz-Salinas, F. J. Madrid-Cuevas, and M. J. Marín-Jiménez. Automatic generation and detection of highly reliable fiducial markers under occlusion. *Pattern Recognition*, 47(6):2280–2292, 2014.
  - [36] K. Strobl and G. Hirzinger. Optimal Hand-Eye Calibration. In *Proc. of the 2006 IEEE/RSJ Intl. Conf. on Intelligent Robots and Systems*, pages 4647–4653, Beijing, China, October 2006. IEEE.
  - [37] B. Bellekens, V. Spruyt, R. Berkvens, and M. Weyn. A Survey of Rigid 3D Pointcloud Registration Algorithms. pages 8–13, 2014.
  - [38] N. Ho. Optimal Rigid/Euclidean transform in 3D space. [http://ngghiaho.com/uploads/code/rigid\\_transform\\_3D.m](http://ngghiaho.com/uploads/code/rigid_transform_3D.m).
  - [39] GStreamer: Open source multimedia framework. <https://gstreamer.freedesktop.org/>.

# Portable dVRK: an augmented V-REP simulator of the da Vinci Research Kit

**Giuseppe Andrea Fontanelli<sup>1</sup>, Mario Selvaggio<sup>1</sup>, Marco Ferro<sup>2</sup>,  
Fanny Ficuciello<sup>1</sup>, Marilena Vendittelli<sup>3</sup>, and Bruno Siciliano<sup>1</sup>**

<sup>1</sup>Università degli Studi di Napoli Federico II, Dipartimento di Ingegneria Elettrica e delle Tecnologie dell'Informazione, via Claudio, 21, 80125 Napoli NA, Italy.

{giuseppeandrea.fontanelli, mario.selvaggio, fanny.ficuciello,  
bruno.siciliano}@unina.it

<sup>2</sup>Sapienza Università di Roma, Dipartimento di Ingegneria Informatica, Automatica e Gestionale, via Ariosto, 25, 00185 Roma RM, Italy.

ferro@diag.uniroma1.it

<sup>3</sup>Sapienza Università di Roma, Dipartimento di Ingegneria dell'Informazione, Elettronica e Telecomunicazioni, via Eudossiana, 18, 00184 Roma RM, Italy.

marilena.vendittelli@uniroma1.it

---

*Abstract: The da Vinci Research Kit (dVRK) is a first generation da Vinci robot repurposed as a research platform and coupled with software and controllers developed by research users. An already quite wide community is currently sharing the dVRK (32 systems in 28 sites worldwide). The access to the robotic system for training surgeons and for developing new surgical procedures, tools and new control modalities is still difficult due to the limited availability and high maintenance costs. The development of simulation tools provides a low cost, easy and safe alternative to the use of the real platform for preliminary research and training activities. The Portable dVRK, which is described in this work, is based on a V-REP simulator of the dVRK patient side and endoscopic camera manipulators which are controlled through two haptic interfaces and a 3D viewer, respectively. The V-REP simulator is augmented with a physics engine allowing to render the interaction of new developed tools with soft objects. Full integration in the ROS control architecture makes the simulator flexible and easy to be interfaced with other possible devices. Several scenes have been implemented to illustrate performance and potentials of the developed simulator.*

*Keywords: Robotic surgery simulators; Minimally invasive robotic surgery; Virtual reality*

---

## 1 Introduction

Since 2012 Intuitive Surgical has started to donate to universities and reserach institutions core components of retired first generation da Vinci robot repurposed as a

research platform. The da Vinci Research Kit (dVRK)<sup>1</sup> couples this platform with software and controllers developed at Johns Hopkins University LCSR and Worcester Polytechnic Institute AIM Lab [1]. Currently, there are more than 30 systems available in 28 sites worldwide. This quite large community (already sharing the dVRK) witnesses the relevance of this platform in surgical robotics research. By targeting this system as the elective experimental testbed research aims at augmenting the surgeon's abilities [2] and ranges from haptic-based teleoperation control [3] to sensor-based shared autonomy [4].

Despite the importance and the current wide availability of the platform, a large part of the research community in the field does not have access to it. Even when available, a wise use of this resource is desirable in order to limit costs and difficulties in replacing components. In this perspective, simulation tools help in overcoming such issues, by developing new surgical tools [5,6], integrating learning in simulation environments, and providing an easy-to-access educational tool to students.

Currently existing simulators are mainly oriented to surgeons' training [7]. The most relevant simulation systems are: *Robotic Surgery Simulator (RoSS)* [8], *Sim-Surgery Education Platform (SEP)*<sup>2</sup>, *da Vinci Trainer*<sup>3</sup>, *da Vinci Skills Simulator*<sup>4</sup>, *Robotix Mentor*<sup>5</sup> and *Chiron* [9]. Beside providing training utilities, each of these simulators allow EndoWrist manipulation, camera control, needle control and clutching, and a realistic representation of the surgical workspace. A useful guide to select the simulator that best fits the user's need is provided in [10].

Given that the above mentioned simulators are dedicated to surgeons' training they do not include a simulation model of the whole robot, i.e., Setup joints (SUJ), Patient Side Manipulators (PSMs) and Endoscopic Camera Manipulator (ECM). On the other hand, simulation models of robotics systems can be easily obtained using open-source robotic simulators. For instance, in [11] authors integrated the dVRK system in the Gazebo simulation framework to develop and test a method for computing haptic forces for tele-operated surgical robots. Integration of the training capabilities of surgical simulators with the functionalities of open-source robotic simulators would serve a large community of users both in the robotics and in the surgical domain.

In this paper, we propose a portable dVRK simulator developed in V-REP [12]. With respect to the other robotic simulator frameworks that are currently available in the research community (e.g., Gazebo, Webots, ARGoS, Marilou), V-REP offers higher flexibility and ease of use in the simulation of multi-robot systems. It is also computationally efficient in terms of CPU usage and allows object mesh manipulation and optimization [13]. The control architecture is distributed and each object/model can be individually controlled via an embedded script, a plugin, a ROS or BlueZero node, a remote API client, or a custom solution. In addition, V-

---

<sup>1</sup> <http://research.intusurg.com/dvrkwiki>

<sup>2</sup> <http://www.simsurgery.com>

<sup>3</sup> <http://www.mimicsimulation.com/products/dv-trainer/>

<sup>4</sup> [https://www.intuitivesurgical.com/products/skills\\_simulator/](https://www.intuitivesurgical.com/products/skills_simulator/)

<sup>5</sup> <https://symbionix.com/simulators/robotix-mentor/>

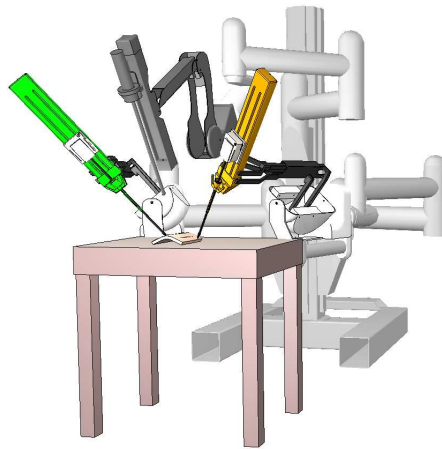


Figure 1  
The da Vinci Research Kit V-REP simulator.

REP supports C/C++, Python, Java, Lua, Matlab or Octave, and runs simulations based on the most commonly available dynamic engines, e.g., Bullet, ODE, Vortex, Newton. The presented simulator inherits such flexibility and is easily extendible. To show and highlight these properties, several scenarios are presented, where the simulator is easily interfaced with real input devices, such as the real surgeon master console, cheap haptic devices and a 3D vision system for virtual reality applications.

The developed simulator includes the kinematic models of the SUJ, PSMs, ECM and the camera sensor and it is interfaced with the ROS framework, as described in Sect. 2. Furthermore, to provide the user with a full immersion experience, a virtual reality headset is integrated together with low cost haptic interfaces as described in Sect. 3. In Sect. 4 four sample scenes, developed for manipulation of rigid dynamic objects, suturing, needle tracking and visual servoing tasks, are provided and ready for use. The potentiality of the simulator for integrating advanced instrument prototypes in a powerful and easy way is illustrated in Sect. 5. This is a very useful characteristic for design, testing and validation. Section 5.1 describes the integration of the simulator with a physics engine, Bullet Real-Time Physics Simulation<sup>6</sup>, to model soft contacts and deformable objects like tissues and organs.

## 2 V-REP Simulated Environment

The robot structure, composed of a SUJ, two PSMs and one ECM, constitutes the core of the dVRK V-REP simulator (Fig. 1) here described, together with its general performances. Starting from the CAD models available in the John Hopkins dVRK git webpage<sup>7</sup>, the robotic arms have been built by means of two types of mesh for each robot link: (i) one visual mesh with structure and texture similar to the real robot link, (ii) one simplified convex dynamic and responsible mesh used to simu-

<sup>6</sup> <https://pybullet.org/wordpress/>

<sup>7</sup> <https://github.com/jhu-dvrk>

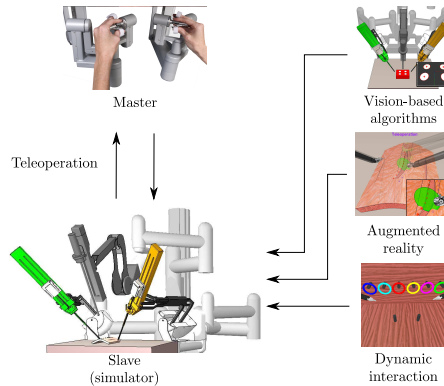


Figure 2  
Simulated environment with different application examples.

late dynamics and contacts<sup>8</sup>. The kinematic chain of each robotic arm is described in Sect. 2.2 and it is realized by linking meshes and joints in a *joint-responsible-visual* sequence. The dynamic parameters, obtained by the identification procedure performed in [14], are included for each responsible link of the two PSMs. Each PSM has been provided with standard laparoscopic instruments, such as the standard needle driver and the cadieere forceps. Two cameras have been included at the end of the endoscope to simulate the binocular vision system of the real dVRK endoscope. In order to have an acceptable simulated sampling time, while preserving a good resolution, a good trade-off is to set for the cameras half the resolution of the real endoscope, *i.e.* at  $320 \times 288$  pixels. The resulting complete robot is composed of 10178 triangles. With this settings the scene is rendered at 45 fps and the dynamics is simulated at 200 Hz with a computer powered by a Intel I7-7770HQ processor, 16 GB of ram and Nvidia GeForce 960M .

The V-REP simulator allows easily inclusion of different robots, dynamic objects, devices and sensors. These facilities allow creating advanced V-REP scenes that include control strategies, *e.g.*, visual servoing or vision-based object tracking, augmented reality and simulation of rigid objects dynamics and interaction (see Fig. 2).

## 2.1 Integration with the dVRK control software infrastructure

The V-REP simulator is designed to be fully integrable into the dVRK control infrastructure. To link our simulator to the dVRK low-level control software [1], the high-level ROS framework has been used. Therefore, the user can employ the simulator in different modalities: (i) the telemanipulated one, using the dVRK MTMs; (ii) in combination with the real robotic PSMs and ECM, to implement augmented reality simulations/algorithms; (iii) as standalone, by controlling the simulated robot using the ROS framework (*e.g.*, through C++, MATLAB and Python ROS nodes), or directly in V-REP using the embedded scripts.

The control software architecture of the dVRK is represented in Fig. 3 and is de-

<sup>8</sup> Dynamic responsible shapes influence each other during dynamic collisions and are subject to gravity and inertial forces.

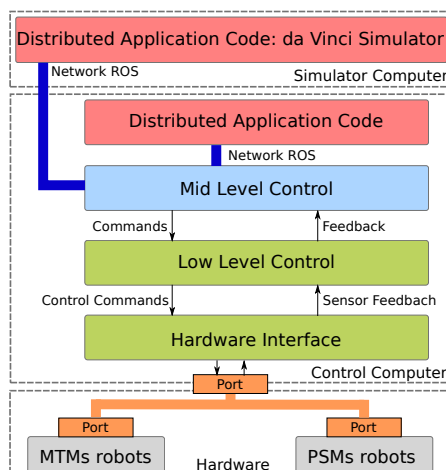


Figure 3  
Software architecture.

scribed more in details in [15]. The dVRK control architecture is composed by: (i) a hardware interface to communicate with the embedded actuator controllers through the fire-wire bus, implementing the safety checks, etc.; (ii) a low-level layer that implements all the algorithms for the inverse kinematics, master impedance control etc.; (iii) a mid-level layer that implements the ROS communication and the high level controllers. The dVRK simulator (running in a dedicate computer) and the dVRK console communicate through ROS topics. In particular, we use the *v\_repExtRosInterface* to publish the state of the simulated robot joints (PSMs, SUJ, ECM) and the gripper state for the PSMs. To control the robots joints motion from ROS, the simulator subscribes to two topics of *sensor\_msgs::joint\_state* type. Both joints and objects topics are streamed at 220Hz while cameras topics at 60 Hz<sup>9</sup>.

This architecture allows easily interfacing the simulator with the mid level control of the dVRK (to command the simulated robot through MTMs) or to other ROS-integrated input device (e.g., haptic devices).

## 2.2 Kinematic Model of the dVRK Robotic Arms

In the following, we describe the kinematics of the patient-side manipulators involved in the presented simulator (i.e., two PSMs and an ECM).

### 2.2.1 Setup Joints arm kinematics

The two PSMs and the ECM are mounted on the SUJ, that is an articulated robotic structure composed by three arms allowing the manual spatial positioning of the two PSMs and the ECM. The SUJ moving the PSMs are two 6-degrees-of-freedom (DoFs) arms (that we indicate hereafter as SUJ-PSMs) while the SUJ moving the ECM is a 4-DoFs arm (SUJ-ECM). The SUJ arms are not actuated. Nevertheless

<sup>9</sup> The simulation requires to be run in *threaded-rendering* mode, in order to decouple the rendering and the control scripts and speed up the execution.

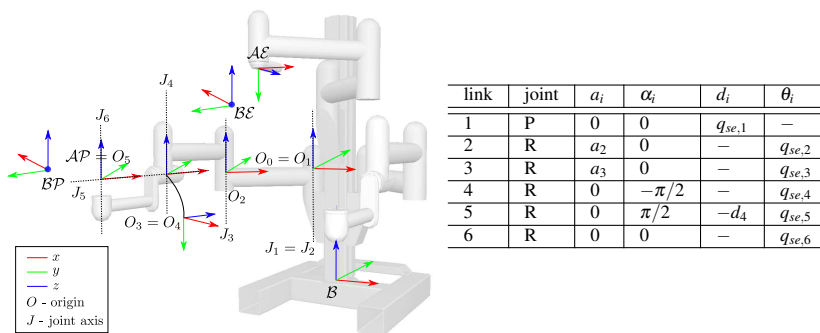


Figure 4  
SUJ kinematic description.

the angular position can be read thanks to embedded potentiometers<sup>10</sup>. The SUJ-PSMs arms generalized coordinates are given by  $q_{sp} = [q_{sp,1}, \dots, q_{sp,6}]$ . By applying the standard DH convention to the kinematic chain composed of  $\{J_1, \dots, J_6\}$  joints (Fig. 4), the homogeneous transformation matrix<sup>11</sup>  $T_{\mathcal{B}^{\mathcal{P}}}^{\mathcal{A}^{\mathcal{P}}}(q_{sp}) \in SE(3)$ , representing the pose of the SUJ-PSMs end-effector frame  $\mathcal{A}^{\mathcal{P}} : \{O_{ap}; x_{ap}, y_{ap}, z_{ap}\}$  with respect to the base frame  $\mathcal{B} : \{O_b; x_b, y_b, z_b\}$ , can be easily computed. The vector of the SUJ-ECM arm generalized coordinates is given by  $q_{se} = [q_{se,1}, \dots, q_{se,4}]$ . Therefore, the homogeneous transformation matrix  $T_{\mathcal{B}^{\mathcal{E}}}^{\mathcal{A}^{\mathcal{E}}}(q_{se}) \in SE(3)$ , that defines the pose of the SUJ-ECM end-effector frame  $\mathcal{A}^{\mathcal{E}} : \{O_{ae}; x_{ae}, y_{ae}, z_{ae}\}$  with respect to the base frame  $\mathcal{B} : \{O_b; x_b, y_b, z_b\}$ , can be computed considering only the first four rows of Table within Fig. 4. Notice that, two constant homogeneous transformation matrices  $T_{\mathcal{B}^{\mathcal{P}}}^{\mathcal{A}^{\mathcal{P}}} \in SE(3)$  and  $T_{\mathcal{B}^{\mathcal{E}}}^{\mathcal{A}^{\mathcal{E}}} \in SE(3)$  must be considered to complete the kinematics description, providing the transformation between  $\mathcal{A}^{\mathcal{P}}$  and  $\mathcal{A}^{\mathcal{E}}$  (respectively the last SUJ-PSM and SUJ-ECM frames) and the base frames  $\mathcal{B}^{\mathcal{P}}$  and  $\mathcal{B}^{\mathcal{E}}$  of the PSMs and of the ECM described in Sec. 2.2.2 and 2.2.3 (see Fig. 4).

## 2.2.2 PSM arm kinematics

The PSMs are two 7-DoFs actuated arms, where the first 6-DoFs correspond to Revolute (R) or Prismatic (P) joints, combined in a RRPRRR sequence. Each PSM arm moves a surgical instrument about a Remote Center of Motion (RCM) [14, 16]. The last DoF corresponds to the opening and closing motion of the gripper. By choosing the origin of frame  $\mathcal{B}^{\mathcal{P}}$  in the RCM point and applying the standard DH convention to the kinematic chain  $\{J_1, \dots, J_6\}$  of Fig. 5, the homogeneous transformation matrix  $T_{\mathcal{B}^{\mathcal{G}}}^{\mathcal{A}^{\mathcal{P}}}(q_p) \in SE(3)$  (where  $q_p = [q_{p,1}, \dots, q_{p,6}]$  is the vector of the PSM generalized coordinates), representing the pose of the gripper frame  $\mathcal{G} : \{O_g; x_g, y_g, z_g\}$  with respect to the base frame  $\mathcal{B}^{\mathcal{P}} : \{O_{bp}; x_{bp}, y_{bp}, z_{bp}\}$ , can be easily computed. The DH parameters are given in the table within Fig. 5, where  $a_5 = 0.0091$  m)

<sup>10</sup> <http://research.intusurg.com/dvrkwiki>

<sup>11</sup> Hereafter, we use the matrix notation  $T_b^a$ , where the superscript  $a$  denotes the frame in which vector components are expressed, the subscript  $b$  the current frame. For instance,  $T_{\mathcal{B}^{\mathcal{P}}}^{\mathcal{A}^{\mathcal{P}}}$  denotes the pose of the SUJ-PSM attach point expressed in the base frame.

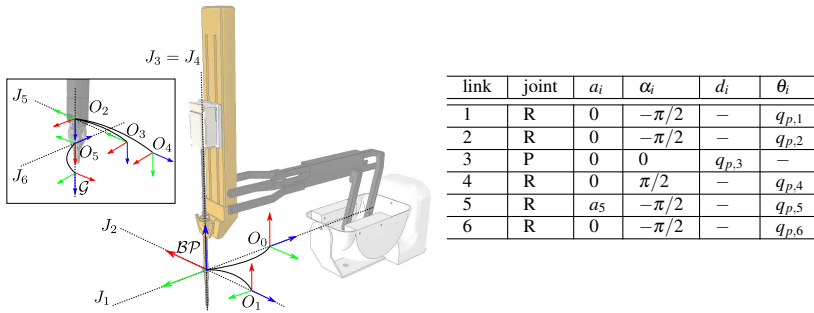


Figure 5  
PSM kinematic description.

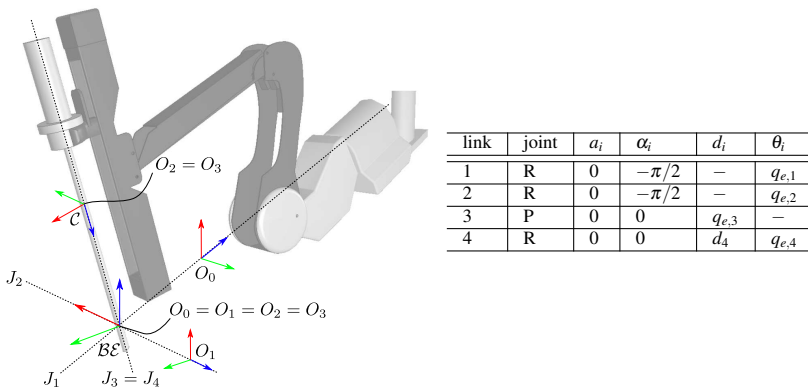


Figure 6  
ECM kinematic description.

### 2.2.3 ECM arm kinematics

The ECM is a 4-DoF actuated arm, that moves the endoscopic camera about the RCM through revolute and prismatic joints, combined in a RRPR sequence. By choosing the origin of frame  $\mathcal{CB}$  in the RCM point and applying the standard DH convention to the kinematic chain  $\{J_1, \dots, J_4\}$  of Fig. 6, the homogeneous transformation matrix  $T_{\mathcal{CB}}^{\mathcal{CB}}(q_e) \in SE(3)$  (where  $q_e = [q_{e,1}, \dots, q_{e,4}]$ ), representing the pose of the camera frame  $\mathcal{C} = \{O_c; x_c, y_c, z_c\}$  with respect to the base frame  $\mathcal{BC} = \{O_{bc}; x_{bc}, y_{bc}, z_{bc}\}$ , can be easily computed. The DH parameters are given in the table within Fig. 6 where  $d_4 = 0.007\text{m}$ .

## 3 Integration with Oculus and Geomagic devices

In the perspective of providing an effective training tool for surgeons and a learning platform for students, it is useful to consider the possibility to interface the dVRK simulator with additional physical input devices, that may not be part of the original da Vinci robot platform. Specifically, in scenarios where the physical platform is not available, there could be the necessity of *reproducing* the surgeon console hosting the pair of master tool manipulators (MTMs), along with the two vision

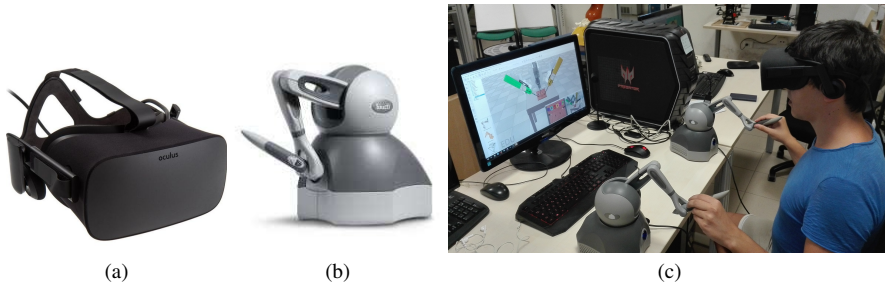


Figure 7

(a) The Head-mounted display of Oculus Rift and (b) the Geomagic Touch haptic device. The integration of the devices with the da Vinci simulator (c).

channels displaying images acquired from the ECM, employed to offer the surgeon the experience of a 3D vision.

To provide the user a fully immersive experience, the use of a virtual reality headset, such as the Oculus Rift<sup>12</sup> (see Fig. 7a), and a pair of haptic interfaces, such as the Geomagic Touch device<sup>13</sup> (see Fig. 7b), represents a non-expensive solution to reproduce the 3D vision system and the MTMs of the master console (see Fig 7c). By connecting the pair of cameras - placed at the end-effector of the ECM - with the Oculus head-mounted display (HMD) that can be freely moved in space, we can actually increase the potential of the framework and tele-operate the ECM through the movements of the user's head. On the other hand, the Geomagic Touch devices can be employed to tele-operate the PSMs of the robot and provide a feedback to the user rendering the interaction forces at the remote site. This scheme is detailed in [17] and summarized in the remainder of this section.

Implementing such functionalities is possible since Oculus and Geomagic devices come with a native SDK to develop custom applications to fully exploit the potentialities of the virtual reality headset and of the haptic interfaces, respectively. However, these SDKs make the overall system not easy to interface in Linux-based frameworks, as a full support and compatibility is granted only for Windows-based systems. Therefore, to allow this integration of devices, the overall distributed application code of the simulator is reconsidered to remove its ROS-dependent parts. Figure 8 shows the software architecture: an external application communicates with the Geomagic and Oculus devices through their corresponding libraries *OpenHaptics* and *LibOVR*, to read the state of the device and acquire specific information (e.g., tool position and velocity), or sends specific commands (e.g., rendering a given force feedback on the haptic tools). While the simulation is running, the application asks for the current joint configuration of the tele-operated PSMs end ECM, along with the current images acquired by the vision sensor objects, mounted at the end-effector of the ECM to simulate the endoscopic camera. The next two sections,

<sup>12</sup> <https://www.oculus.com/>

<sup>13</sup> <https://www.3dsystems.com/haptics-devices/touch>

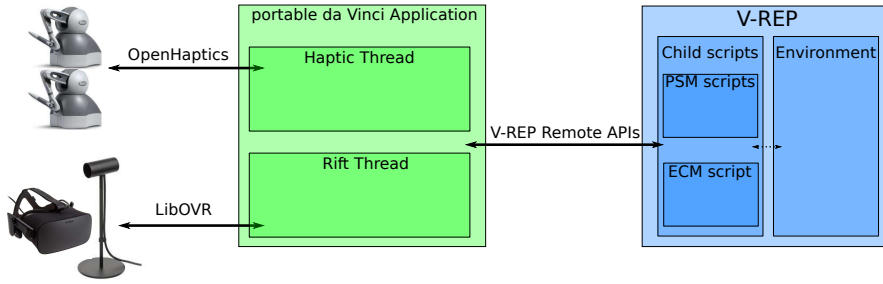


Figure 8

Modules and device communication scheme to interface Oculus Rift and Geomagic Touch devices to the simulator

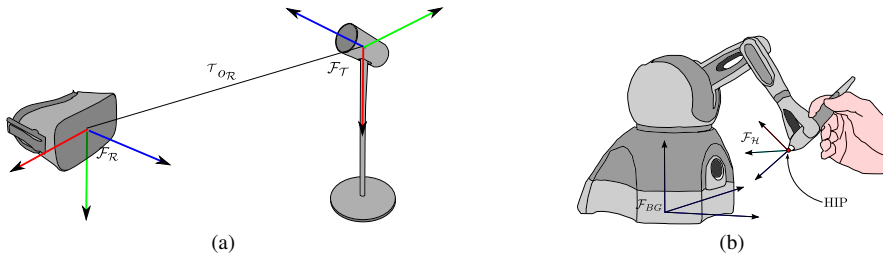


Figure 9

Reference frames of interest for (a) the Oculus Rift HMD and (b) the Geomagic Touch device, where the Haptic Interface Point (HIP) is highlighted.

provide additional details about the communication of Oculus Rift and Geomagic Touch devices with the proposed simulator.

### 3.1 Connecting the Oculus Rift device

The Oculus Rift hardware kit considers an infrared-based positional tracking system called Constellation, that provides an high-rate and accurate measurement of the HMD pose with respect to the tracker reference frame  $\mathcal{F}_{\mathcal{T}}$  (see Fig. 9a). As illustrated in Sect. 2.2.3, the ECM is a 4-DoF manipulator moving the end-effector (i.e., the endoscopic cameras) about the RCM. Therefore, it is not possible to assign an arbitrary pose to the cameras, as only 4 of the 6 space dimensions can be commanded. In this perspective, a user-enabled switching mechanism has been developed to alternatively command: (i) the orientation of the cameras, through the three revolute joints of the arm; (ii) the position along the longitudinal axis of the arm, corresponding to the z-axis of the camera frame  $\mathcal{C}$ , through the prismatic joint (as shown in Fig. 6). Specifically, by quering the Oculus SDK, we first extract the 6D velocity vector  ${}^{\mathcal{F}}v_{\mathcal{R}}$ , denoting the linear and angular velocity of the Oculus display expressed in  $\mathcal{F}_{\mathcal{T}}$ . Applying the proper rotation, we then generate the velocity vector  ${}^{\mathcal{R}}v_{\mathcal{R}}$  expressed in its own frame  $\mathcal{F}_{\mathcal{R}}$ . Finally, we extract the linear velocity component  ${}^{\mathcal{R}}v_{\mathcal{R},z}$  and the angular velocity vector  ${}^{\mathcal{R}}\omega_{\mathcal{R}}$ . To require that the ECM cameras move according to the velocities commanded by the motion of the Oculus display, we then set  ${}^{\mathcal{C}}v_{\mathcal{C},z} = {}^{\mathcal{R}}v_{\mathcal{R},z}$  and  ${}^{\mathcal{C}}\omega_{\mathcal{C}} = {}^{\mathcal{R}}\omega_{\mathcal{R}}$ . Denoting by  $J = [J_V, J_\omega]^T$

the  $6 \times 4$  Jacobian matrix of the ECM, where the linear and angular contributions  $J_V = [J_{v_x}, J_{v_y}, J_{v_z}]^T$  and  $J_\omega = [J_{\omega_x}, J_{\omega_y}, J_{\omega_z}]^T$  are highlighted, we designed a decoupled control of the position and the orientation of the ECM cameras as follows:

$$\begin{cases} \dot{q}_{1,2,4} = J_\omega^\# \mathcal{C} \omega_{\mathcal{C}} & , \text{ if orientation control enabled} \\ \dot{q}_3 = \mathcal{C} v_{\mathcal{C},z} & , \text{ if position control enabled} \end{cases} \quad (1)$$

being  $\dot{q}_{1,2,4} = [\dot{q}_1, \dot{q}_2, \dot{q}_4]^T$  the vector of the revolute joint velocities and  $\dot{q}_3$  the prismatic joint velocity, while  $J_\omega^\#$  denotes the pseudo-inverse matrix of  $J_\omega$ . We assume that the user can choose which control has to be enabled, through a keyboard input. When choosing a given control, the joint velocities involved in the unused scheme are set to 0. The values of joint velocities, computed this way, are used to directly command the joints of the ECM in the V-REP environment.

### 3.2 Connecting the Geomagic Touch devices

Each Geomagic Touch device is a 6DoF haptic interface equipped with joint encoders that measure the full 6D pose of the Haptic Interface Point (HIP) of the stylus held by the user (see Fig. 9b). The device also provides a 3-DoF force feedback, allowing the user to experience a virtual sense of touch and manipulate virtual objects or reproduce physical contacts of tele-operated objects.

The velocity vectors of the PSM end-effector (i.e., the gripper) and the HIP of the corresponding haptic device have to be kept consistent, to properly teleoperate the PSMs through the movements of the stylus. In detail, with reference to Fig. 9b and for each haptic device, we query the *OpenHaptics* library to extract the current linear and angular velocity  ${}^{\mathcal{B}\mathcal{G}}v_{\mathcal{H}}$  of the HIP, expressed in base reference frame  $\mathcal{F}^{\mathcal{B}\mathcal{G}}$ , and generate the velocity  ${}^{\mathcal{H}}v_{\mathcal{H}}$  by applying a rotation. Moreover, to require that the PSMs grippers move accordingly and be consistent with the gripper frame  $\mathcal{F}^{\mathcal{G}}$ , we set  ${}^{\mathcal{G}}v_{\mathcal{G}} = {}^{\mathcal{H}}v_{\mathcal{H}}$ .

To determine the desired joint velocity  $\dot{q}_p$  of the considered PSM, we compute the corresponding  $6 \times 6$  Jacobian matrix  $J_{\mathcal{G}}$  in the gripper frame  $\mathcal{F}^{\mathcal{G}}$ , reconstructed from the DH Tables shown in Fig. 5. Therefore, the teleoperation of the PSM through the haptic device is achieved as

$$\dot{q}_p = J_{\mathcal{G}}^{-1} {}^{\mathcal{G}}v_{\mathcal{G}}. \quad (2)$$

A typical issue in teleoperation tasks is the geometrical heterogeneity (usually referred to as *kinematic dissimilarity*) between master and slave workspaces (i.e., the haptic device and the PSM of the da Vinci system, respectively). Specifically, the Gemoagic Touch has a limited workspace, due to the short length of the links and the finite positional ranges of the joints. However, the size and the kinematic chain of the PSM is different, thus also the corresponding workspace in which the end-effector (i.e., the gripper of the PSM) moves is distinct. A common workaround that handles this discrepancy considers the use of a *clutch*-based mechanism to enable/disable the tele-operation of the slave with the master device upon explicit command of the user. This way, when the HIP of the Geomagic Touch has reached the

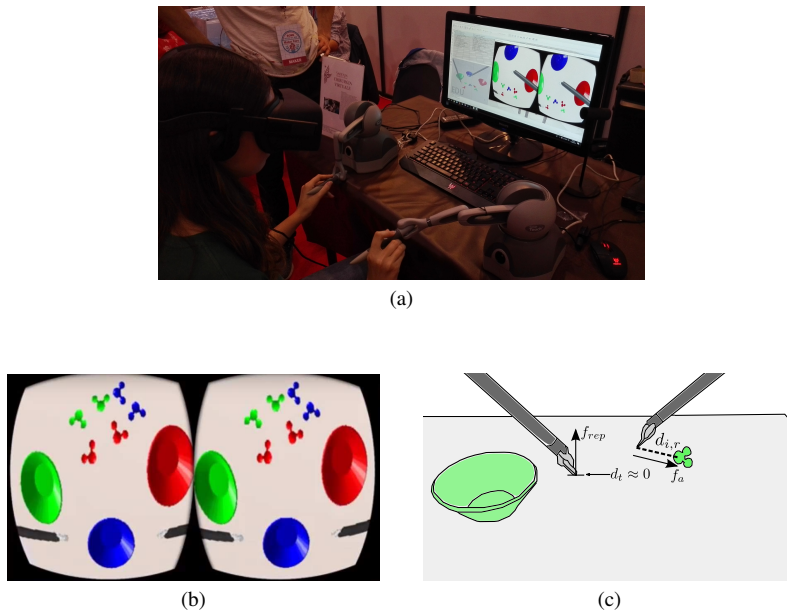


Figure 10

(a) A user interfacing with the da Vinci simulator to accomplish a training task. (b) The view seen by the user through the Oculus display. (c) A representation of the implemented repulsive force simulating the contact with the virtual table in the scene.

workspace limits of the device, the tele-operation can be disabled and the user can purposely relocate the stylus in a more favorable configuration to further move the HIP in the desired direction. This behaviour is implemented through one of the buttons mounted on the stylus of the Geomagic Touch.

Fig. 10a shows a user involved in a training task, built in the da Vinci simulator, through the use of the Oculus Rift display and the Geomagic Touch devices. The views on the two vision channels of the Oculus display is shown in Fig. 10b. The virtual scene considers a table and a set of object that can be grasped. Additional details about this training application scene are provided in Sect. 4. For demonstration purposes, we implemented a repulsive force  $f_{rep}$  on the planar surface of the table, to give the user the tactile experience of a contact of the gripper with a highly rigid object (see Fig. 10c). Future developments and improvements on the presented simulator will consider more complex dynamic interactions of the tele-operated grippers with the virtual objects in the scene. An exhaustive video showing the effectiveness of this application is available at the following link: <http://www.diag.uniroma1.it/~labrob/research/portable-DVRK.html>.

Finally, it is worth noticing that the simulation refresh rate of 220Hz, set for virtual joints and objects in the scene (see Section 2.1), is an appropriate value to render the haptic sensation of the user. In fact, human sensitivity to haptic experiences or pressure changes allows to feel regular vibrations from 200Hz to 500Hz [18] [19]. This is an operating condition satisfied by the Geomagic Touch devices, whose up-

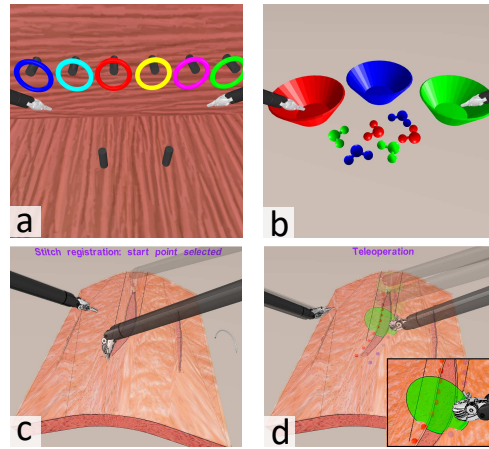


Figure 11

Training and suturing simulated environments: (a) peg on board; (b) pick and place; (c) augmented reality wound registration; (d) stitches selection and semi-autonomous execution.

date rate of the rendered forces can be set up to 1000Hz, thus providing an accurate and immediate response to the user.

## 4 Other Applications of the Simulator

Here, we introduce other potential applications of the proposed simulator:

- **Training:** the simulated robot is capable of interacting with dynamic rigid objects, thus is prone to be used for training purposes. Two example scenes are provided on this line.
- **Augmented reality:** it is possible to overlay additional information inside the simulated environment. An assisted suturing scene has been developed to show this possibility with an example of semi-autonomous task execution;
- **Vision:** the simulator can be used for advanced vision-based algorithms testing. A needle tracking and a visual servoing scene, in which the simulated vision system is exploited, are provided.

### 4.1 Training

Surgeons' training is an utmost requirement for an effective use of the daVinci system in real surgical scenarios. Most of the training time is spent in simulated environments. Simulators with embedded training modules are provided by Intuitive Surgical (see Sect. 1) for skills evaluation and enhancement. The training phase is essential to assess surgeon skills using scores information. However, engineers using the dVRK for research purposes do not have direct access to these costly simulators. To speed up development and testing of novel control strategies, engineers might need to equally train themselves on the (possibly simulated) dVRK system.

To this end, two V-REP scenes have been developed for non-surgical training tasks, namely: *pick & place*, and *peg on board*. Thanks to the high V-REP versatility, these

tasks are easily modifiable through the GUI, even from a non expert user. Fig. 11 contains some snapshots of these scenes as seen from the ECM camera.

The scenes have been realized by importing the CAD models of the setup into the simulated environment. V-REP has collision detection and response functionalities thus allowing simulating interactions and contacts among objects. Imported parts can be used to generate collidable, simplified meshes (different from the rendered ones) for fast simulation performed by the underlying dynamic engine. Moreover, it is possible to simulate simplified objects grasping by embedding a proximity sensor between the needle driver pads used to detect object proximity. We extensively tested the simulator training capabilities by connecting the simulated environment to real MTMs though the architecture presented in Sect. 2.1. Is it anyway possible to interface the simulator with other haptic devices as shown in Sect. 3.

## 4.2 Suturing

In this section, we propose an example of a suturing scene realized in our simulator. Suturing represents an important topic in minimally invasive surgery, mainly because some of the subtasks required to complete a suturing procedure can be automatized to reduce the time and improve the results for the patients. Replicating this task in simulation can help the engineer in the development of algorithms for suturing reducing his/her effort. Moreover, the use of simulators can be useful to evaluate the surgeon's skills and to give back advantageous information to the surgeon in augmented reality. The scene developed is composed by a branch-top suturing phantom that takes inspiration from commercial phantoms and a needle SH-Plus that can be easily grasped in position using the dVRK tools grippers. The grasping control needle has been developed using a proximity sensor available in the V-REP sensors list, integrated between the gripper fingers. In detail, the needle is grasped when the proximity sensors identify the needle inside the gripper fingers and the "close the gripper" action is sent to the simulator. In this scene, the position of the needle has been obtained using the *simGetObjectPosition* function but can also be obtained using visual techniques, as described in the next section. Moreover, we include in the scene some objects: (i) colored spherical *drawing objects* to highlight the insertion (blue) and extraction (red) points; (ii) a semitransparent disk with radius equal to the needle one indicating the stitch path to follow; (iii) text messages to give back to the user information about the current control state (see Fig. 11). We include all these objects directly using the V-REP GUI and custom scripts functions. Moreover, each model is controllable from ROS topic. In detail, the spatial position, color and number of all the drawing objects is controlled using a custom topic message; a *geometry\_msgs::Pose* has been used to send position and orientation of the optimal path disk; an *std\_msgs::String* has been used to control the text messages.

## 4.3 Tracking of a suturing needle

Among the common procedures executed by surgeons, suturing is particularly challenging, due to the high dexterity demanded in a typically restricted workspace. This makes the procedure tiring for the surgeon, as the performance can be affected by his conditions and fatigue. Therefore, to increase the degree of autonomy and

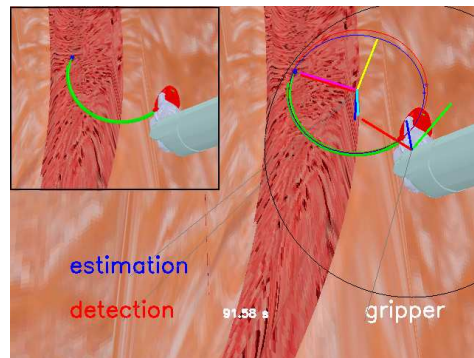


Figure 12

Simulated setup and image processing steps, with focus on the needle (top left).

accuracy in the procedure itself, developing novel robot-assisted strategies becomes necessary. In particular, the employment of a surgical manipulator eases to design specific behaviours satisfying desirable properties, e.g., minimizing the stress on the patient's tissue. This can be achieved by implementing proper control strategies, leading the needle held by the manipulator, to a reference configuration. To achieve this task, the availability of the pose of the instrument in the workspace is mandatory. Reconstructing such information is not trivial, since even when the needle is grasped, the only robot kinematics is not sufficient. Indeed, the grasping point on the needle surface is not unique, and external forces or slippages alter its relative pose with respect to the end-effector.

A possible solution to this problem considers a fusion of heterogeneous sensory data. While several methods have been proposed in literature, in the setup determined by our simulator we aim at designing a simplified vision-based needle tracking scheme, by using the visual information acquired by the cameras of the ECM and the kinematics data of the PSMs. This choice is motivated by the high-rate information of the joint encoders, and by the possibility to capture external disturbances, that can modify the pose of the needle, through camera images. The data are fused through an Extended Kalman Filter (EKF) to reconstruct the 6D needle pose [20], during the suturing procedure. The filter first builds an intermediate estimation of the pose, by reconstructing the velocity of the PSM gripper through differential kinematics, and assuming the needle rigidly linked to the end-effector, so that the pose of the needle can be reconstructed through velocity transformation. Nonetheless, the needle is not rigidly linked and external forces (e.g., interaction with tissue, slippages) can affect both position and orientation. Therefore, we process the camera images to detect the elliptical projection of the needle and extract a suitable visual measurement to correct the prediction in the update step of the filter. In particular, the ellipse detection is achieved through a simple RGB-based image segmentation, applied on a gripper-centered circular Region Of Interest (ROI), whose radius represents a projection of the spherical region of all the possible needle configurations. The set of pixels resulting from the segmentation are used to fit the corresponding ellipse on the image plane, through least-square estimation. Mathematical observations finally allow to reconstruct a measurement of the 6D pose of the needle from

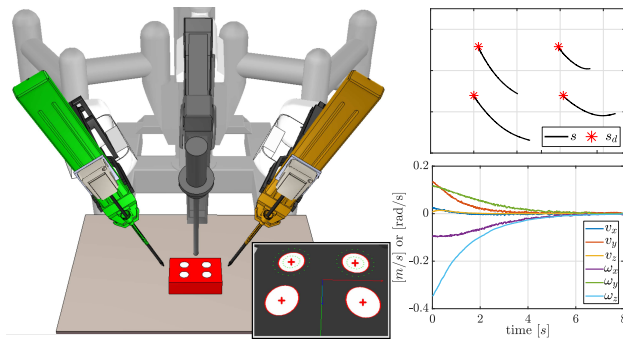


Figure 13

Visual servoing scene setup. Right-top: regulation of features on the image plane; right-bottom: 6D camera velocity converging to 0 as the desired features are approaching.

the ellipse, as explained in [21]. In the considered simulated scene (see top left view in Fig. 12), we adopted a green-colored needle along a blue tip, enforcing the vision-based pose reconstruction. The main picture in Fig. 12 shows some of the image processing entities used for the tracking: the black circle represents the ROI, the vision-based detected ellipse and the projected resulting estimation have red and blue color, respectively. The Figure also shows the corresponding reference frames

#### 4.4 Visual servoing

A visual servoing control scheme, validating the correctness of the simulated ECM, is presented. In particular, we aim at showing an Image-Based Visual Servoing (IBVS) for camera regulation, where one of the cameras of the ECM is controlled through inverse differential kinematics to regulate proper features on the image plane. For demonstrative purposes, we consider a red box with four white circles drawn on the top surface (see Fig. 13). The centroids of the circles are extracted with a blob tracker implemented in vision-based robot control software VISP [22], and used as image features to regulate. Defining a set of desired image coordinates, plots in Fig. 13 show that the circles centroids are successfully regulated through the IBVS scheme [23], where the 6D velocity of the camera is transformed to the joint velocity vector through the classical projected gradient control [24].

### 5 Integration with Advanced Instruments

The versatility of the proposed V-REP simulator allows including advanced robots and instruments in a powerful and easy way. In this section we discuss about the integration in the simulator of two novel surgical instruments we designed at the ICAROS center University of Naples Federico II. The possibility to simulate novel instruments improves the design work flow and provides the opportunity to test their performance with the help of surgeons before building them.

#### 5.0.1 The MUSHA Hand

The first instrument is our novel MUSHA hand (MH) (see Fig. 14, on the left). MH is a tree fingered under-actuated and miniaturized hand specifically designed for robotic laparoscopic surgery [25]. The hand aims at completely changing the

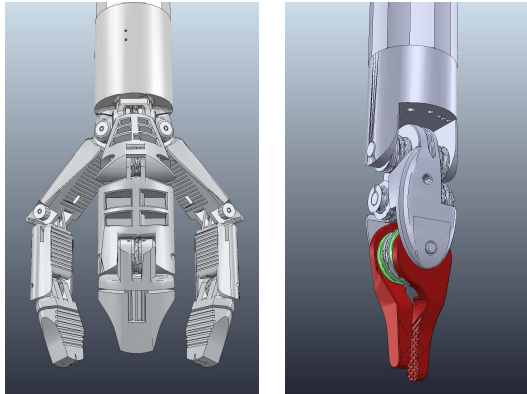


Figure 14

Advanced surgical instruments. Left: the MUSHA hand, Right: a novel needle driver with in-hand rolling capabilities.

surgical work-flow in MIRS by introducing advanced manipulation and sensing capabilities comparable to those of the human hand. The main purpose of MH is to gently interact with deformable organs to retract, manipulate and dissect them. As will be discussed in the next section, the integration of V-REP with Bullet physics engine allows evaluating the interaction between MH and a soft object.

### 5.0.2 A Novel Surgical Instrument With in-hand Rolling Capabilities

The second instrument is a new surgical needle driver that aims to reduce the surgeon mental and physical workload during difficult tasks such as suturing [5]. This instrument is provided with the ability to rotate in-hand the suturing needle to find the optimal orientation before the execution of each stitch. By adding an additional DoF to a standard needle driver tool we allow in-hand manipulation capabilities as those found in human hand during open surgery. We have integrated this advanced instrument (see Fig. 14, on the right) in the simulator for preliminary tests of the in-hand rolling capabilities as reported in [5]. In this case, the simulator has been used both for design optimization and to run a case study simulation to evaluate the percentage of cases in which this novel tool could be helpful in real suturing trajectories.

## 5.1 Integration with Other Physics Engines

In this section, we present a simulation that aims at evaluating the potential of our novel MUSHA Hand, with respect to classical tools, in selected tasks performed during adrenalectomy and colectomy procedures. The simulated tasks are organs mobilization, grasping, and measurements of critical dimensions of affected organs. Since the MH is still a prototype, not ready to be used in surgical environments, the evaluation of the conceptual design is obtained in a simulated environment by replicating qualitatively the task execution of standard laparoscopic tools in real environments. Fig. 15 presents the simulation environment. In more details, we exploit the possibility to integrate V-REP with other physics engine to extend its simulation potentialities. Bullet physics is chosen thanks to its ability to simulate

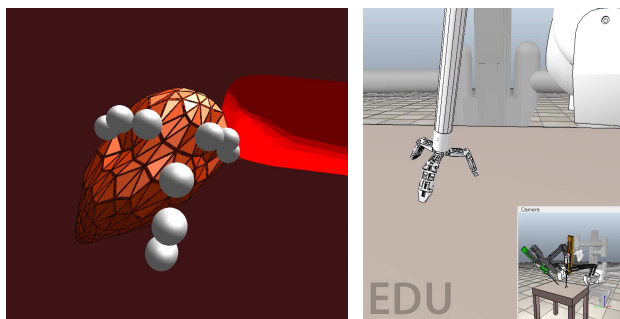


Figure 15

Simulation environment of the MH mounted on the dVRK robotic instrument. Left: Bullet physics scene containing the MH collision meshes (white spheres) and a deformable body representing the adrenal gland (orange); Right: V-REP scene of MH integrated with the dVRK robotic instrument.

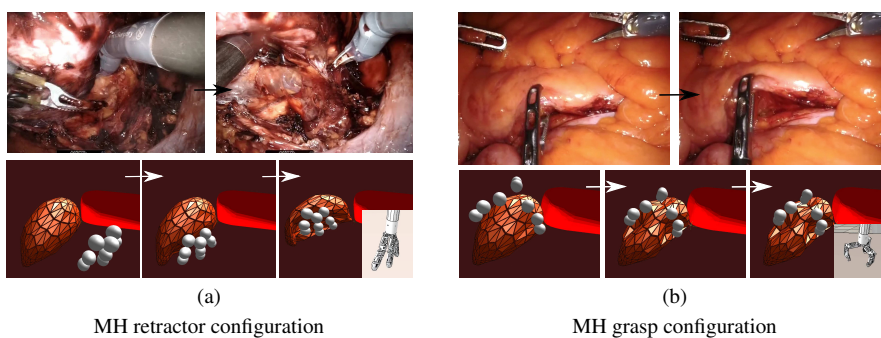


Figure 16

MH use cases: (a) retractor configuration to mobilize and lift organs during a laparoscopic adrenalectomy procedure; (b) grasp configuration to grab and pull organs during a colectomy procedure. Top: real surgical procedure, Bottom: simulated environment.

soft objects e.g. organs and tissues. The soft organ is simulated using a soft triangular mesh shape with elastic properties [26]. The organ has been anchored to the rigid scene in different points to simulate the interaction between the organ and the abdominal surfaces. The MUSHa hand collision model has been realized using three spheres for each finger simulating the hand phalanges. We have linked the bullet simulated scene to our VREP simulator through remote API functions to have at each time step the position of each hand phalanges w.r.t. the robot Remote Center of Motion (RCM). In Figs. 16a, 16b and 17, three different simulated scenes have been proposed where MH has been used in: (i) retractor configuration, to lift and mobilize organs; (ii) grasping configuration, to grab organs or tissues; (iii) caliper configuration to measure organs dimensions.

## 6 Discussion and Conclusions

In this work, a simulator of the full dVRK integrated in V-REP has been presented. The kinematics of the dVRK arms has been described and implemented in the sim-

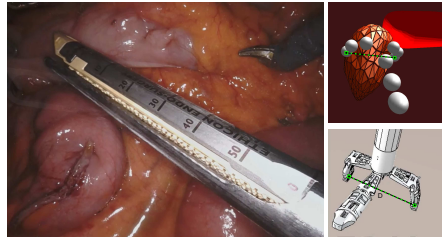


Figure 17

MH use case: caliper simulation. The hand direct kinematics can be used to estimate organs or tissues critical dimensions. Left: surgical scenario; Right top: bullet simulation; Right bottom: V-REP simulation.

ulated robot. The integration with ROS allows controlling the simulated robot using the real dVRK master device and developing advanced control strategies. A modified ROS-independent architecture also allows the integration of commercial interfaces for haptic feedback and virtual reality applications like, e.g., the Geomagic Touch and the Oculus Rift. To show the potentialities of the proposed simulator, four different scenes ready to use have been included.

Major limitations of the proposed simulator are realistic grasping of thin-shaped objects, such as the needle, and simulation of the interaction with deformable bodies. The former problem can be opportunely circumvented by disabling collisions and attaching the object rigidly to the hand. To address the second, the bullet physics engine has been connected to V-REP to simulate the interaction of tools with soft tissues and organs. A new tool for the manipulation of soft tissues is included in the simulator. As for the future, we aim to exploit bullet engine deformable body simulation capabilities recreating the deformable bodies visualization directly in V-REP.

### Acknowledgement

This project was partially supported by the POR FESR 2014-2020 National programme within BARTOLO project CUP B41C17000090007 and by the EC Seventh Framework Programme (FP7) within RoDyMan project 320992.

### References

- [1] P. Kazanzides, Z. Chen, A. Deguet, G. S. Fischer, R. H. Taylor, and S. P. DiMaio. An open-source research kit for the da vinci surgical system. *IEEE Int. Conf. on Robotics and Automation*, pages 6434–6439, May 2014.
- [2] M. Selvaggio, G. A. Fontanelli, F. Ficuciello, L. Villani, and B. Siciliano. Passive virtual fixtures adaptation in minimally invasive robotic surgery. *IEEE Robotics and Automation Letters*, pages 3129 – 3136, 2018.
- [3] M. Selvaggio, G. Notomista, F. Chen, B. Gao, F. Trapani, and D. Caldwell. Enhancing bilateral teleoperation using camera-based online virtual fixtures generation. *IEEE/RSJ Int. Conf. on Intelligent Robots and Systems*, pages 1483–1488, 2016.
- [4] J. M. Prendergast and M. E. Rentschler. Towards autonomous motion control in minimally invasive robotic surgery. *Expert Review of Medical Devices*, pages 741–748, 2016.

- [5] G. A. Fontanelli, M. Selvaggio, L. R. Buonocore, F. Ficuciello, L. Villani, and B. Siciliano. A new laparoscopic tool with in-hand rolling capabilities for needle reorientation. *IEEE Robotics and Automation Letters*, pages 2354–2361, 2018.
- [6] G. A. Fontanelli, L. R. Buonocore, F. Ficuciello, L. Villani, and B. Siciliano. A novel force sensing integrated into the trocar for minimally invasive robotic surgery. *2017 IEEE/RSJ Int. Conf. on Intelligent Robots and Systems*, pages 131–136, 2017.
- [7] A. Moglia, V. Ferrari, L. Morelli, M. Ferrari, F. Mosca, and A. Cuschieri. A Systematic Review of Virtual Reality Simulators for Robot-assisted Surgery. *European Urology*, pages 1065–1080, 2016.
- [8] A. Baheti, S. Seshadri, A. Kumar, G. Srimathveeravalli, T. Kesavadas, and K. Guru. Ross: Virtual reality robotic surgical simulator for the da vinci surgical system. *Symposium on Haptic Interfaces for Virtual Environment and Teleoperator Systems*, pages 479–480, 2008.
- [9] J. A. Sanchez-Margallo, J. P. Carrasco, L. Sanchez-Peralta, J. L. M. Cuevas, L. Gasperotti, D. Zerbato, and F. S.-M. L. Vezaro. A preliminary validation of the xron surgical simulator for robotic surgery. *Int. Conf. of the Society for Medical Innovation and Technology*, 2013.
- [10] R. Smith, M. Truong, and M. Perez. Comparative analysis of the functionality of simulators of the da vinci surgical robot. *Surgical Endoscopy*, (4):972–983, Apr 2015.
- [11] A. Munawar and G. Fischer. Towards a haptic feedback framework for multi-dof robotic laparoscopic surgery platforms. In *2016 IEEE/RSJ Int. Conf. on Intelligent Robots and Systems*, pages 1113–1118, Oct 2016.
- [12] E. Rohmer, S. P. N. Singh, and M. Freese. V-rep: A versatile and scalable robot simulation framework. In *2013 IEEE/RSJ International Conference on Intelligent Robots and Systems*, pages 1321–1326, Nov 2013.
- [13] L. Pitonakova, M. Giuliani, A. Pipe, and A. Winfield. Feature and performance comparison of the v-rep, gazebo and argos robot simulators. In M. Giuliani, T. Assaf, and M. E. Giannaccini, editors, *Towards Autonomous Robotic Systems*, pages 357–368, Cham, 2018. Springer International Publishing.
- [14] G. A. Fontanelli, F. Ficuciello, L. Villani, and B. Siciliano. Modelling and identification of the da Vinci research kit robotic arms. *IEEE/RSJ Int. Conf. on Intelligent Robots and Systems*, pages 1464–1469, 2017.
- [15] Z. Chen, A. Deguet, R. H. Taylor, and P. Kazanzides. Software architecture of the da vinci research kit. *IEEE Int. Conf. on Robotic Computing*, pages 180–187, 2017.
- [16] G. S. Guthart and J. K. Salisbury. The intuitive™ telesurgery system: overview and application. *IEEE Int. Conf. on Robotics and Automation*, pages 618–621, 2000.
- [17] M. Ferro, D. Brunori, F. Magistri, L. Saiella, M. Selvaggio, and G. A. Fontanelli. A portable da vinci simulator in virtual reality. *Third IEEE International Conference on Robotic Computing (IRC 2019)*, pages 447–448, 2019.

- [18] J. Scheibert, S. Leurent, A. Prevost, and G. Debrégeas. The role of fingerprints in the coding of tactile information probed with a biomimetic sensor. *Science*, 323(5920):1503–1506, 2009.
- [19] L. Skedung, M. Arvidsson, J. Y. Chung, C. M. Stafford, B. Berglund, and M. W. Rutland. Feeling small: exploring the tactile perception limits. *Scientific reports*, 3:2617, 2013.
- [20] M. Ferro, G. A. Fontanelli, F. Ficuciello, B. Siciliano, and M. Vendittelli. Vision-based suturing needle tracking with extended kalman filter. *Computer/Robot Assisted Surgery workshop*, 2017.
- [21] D. López de Ipiña, P. R. S. Mendonça, and A. Hopper. Trip: A low-cost vision-based location system for ubiquitous computing. *Personal and Ubiquitous Computing*, 6(3):206–219, 2002.
- [22] E. Marchand, F. Spindler, and F. Chaumette. Visp for visual servoing: a generic software platform with a wide class of robot control skills. *IEEE Robotic and Automation Magazine*, pages 40–52, 2005.
- [23] F. Chaumette and S. Hutchinson. Visual servo control, part i: Basic approaches. *IEEE Robotic and Automation Magazine*, pages 82–90, 2006.
- [24] B. Siciliano, L. Sciavicco, L. Villani, and G. Oriolo. *Robotics: Modelling, Planning and Control*. Springer-Verlag London, 2009.
- [25] M. Selvaggio, G. A. Fontanelli, V. R. MARRAZZO, U. Bracale, A. Irace, G. Breglio, L. Villani, B. Siciliano, and F. Ficuciello. The musha underactuated hand for robot-aided minimally invasive surgery. *The International Journal of Medical Robotics and Computer Assisted Surgery*, 15(3):e1981, 2019. e1981 rcs.1981.
- [26] F. Fazioli, F. Ficuciello, G. A. Fontanelli, B. Siciliano, and L. Villani. Implementation of a soft-rigid collision detection algorithm in an open-source engine for surgical realistic simulation. *IEEE Int. Conf. on Robotics and Biomimetics*, pages 2204–2208, 2016.

# Needle Navigation and Catheter Reconstruction for Breast Brachytherapy Using Open Source Software

**Thomas A Vaughan<sup>1</sup>, Harry Brastianos<sup>2</sup>, Tamas Ungi<sup>1</sup>, Andras Lasso<sup>1</sup>, Conrad Falkson<sup>2</sup>, Gabor Fichtinger<sup>1</sup>**

<sup>1</sup>School of Computing, Queen's University, 25 Union St, Kingston, Ontario, Canada, K7L 2N8; vaughan@cs.queensu.ca; ungi@queensu.ca; lasso@cs.queensu.ca; gabor@cs.queensu.ca

<sup>2</sup>Department of Oncology, Queen's University, 76 Stuart St, Kingston, Ontario, Canada, K7L 2V7; Chariloas.Brastianos@kingstonhsc.ca; Conrad.Falkson@KingstonHSC.ca

\*Authors T Vaughan and H Brastianos contributed equally to the presented work

---

*Abstract: Interstitial breast brachytherapy is a method to deliver radiation therapy directly to the site of cancer. It is a challenging procedure because of issues in localizing the seroma, needles, and catheters within the soft tissue. In this paper we present two open-source technologies based on electromagnetic tracking: a navigation system to help target needles using a tracked needle guide, and software for electromagnetic reconstruction of catheter paths. These technologies were validated phantom studies. We found that the navigation system helped a radiation oncologist to target needles more accurately than under ultrasound guidance (60 needles under each condition, 3.8 vs 3.3 mm placement error,  $p = 0.04$ ) and that reconstructed catheter paths were accurate within 0.6 mm to those determined on CT scans (144 catheters were compared to the 1.2 mm voxel size of CT scans,  $p < 0.001$ ). We conclude that these technologies accurately localize anatomy and instruments in our study.*

*Keywords: breast brachytherapy; electromagnetic reconstruction; catheter reconstruction; navigation*

---

## 1 Introduction

Interstitial breast brachytherapy is a radiation therapy procedure to prevent tumor recurrence after surgical removal of breast cancer. Radiation is delivered through catheters inserted in the breast in a pattern to optimize dose distribution. The goal of catheter placement is to insert them with uniform spacing so that radiation can cover the target volume evenly [21]. Failure to achieve adequate dose distribution can result in tissue toxicity or necrosis [25]. Although poor catheter path geometry

can be compensated for, to some extent, by dose optimization [5], the radiation oncologists goal is inserting catheters with uniform spacing throughout the tissue volume. Catheters are positioned by a guiding needle, so needle placements are the key to accurate catheter positions. Interventional radiation oncologists are challenged by several spatial factors that come into play, including the position and orientation of the seroma, the pocket of tissue left behind after tumor excision surgery. The position and orientation of catheters ideally follow a personalized insertion plan. These factors are further amplified by tissue motion and patient breathing [6].

Freehand needle insertions can be augmented by mechanical templates where needle entry, and in some cases exit, points are constrained by holes [16, 25]. A drawback with this approach is that needles can still bend in the tissue. Another drawback is that templates can be large and intrusive. Robots or other mechanical constraints have been used in other organs [14, 15] but they have similar limitations in breast catheter guidance.

Needle insertion has been guided in real-time by a variety of other technologies. One approach is to use conventional two-dimensional ultrasound [7]. The radiation oncologist uses ultrasound to locate the seroma and observe the trajectory of the needle as it is being inserted. The radiation oncologist can adjust the trajectory of the needle to some extent by manipulating the tissue or by steering the needle [6]. The drawback with ultrasound in general is variable image quality and artefacts. It has been proposed to register and fuse magnetic resonance imaging with two-dimensional ultrasound to help compensate for these issues [27] but magnetic resonance imaging is not always available. Poulin *et al.* describe an approach whereby three-dimensional ultrasound is combined with templates [17]. They apply a catheter optimization technique to create a needle insertion plan that optimizes the dose distribution and minimizes the number of needles used. To insert the needles they compared two templates: a generic clinical template where insertions were constrained to existing holes, and a patient-specific template that was custom-designed and rapid prototyped. Catheters implanted with the patient-specific template resulted in inferior dose homogeneity compared to a generic clinical template. Strassman *et al.* used an electromagnetically-tracked needle holder to guide needle insertions so that they followed a CT-based needle insertion plan [21]. They analyzed the accuracy of guidance in a generic non-anatomical foam phantom. They state that patient immobilization is necessary to use their navigation system. In their clinical experience [20] they report mean needle placement errors between 3.4 mm and 6.4 mm. Magnetic resonance imaging can be combined with specially-designed stylets to track catheters during brachytherapy insertions [2, 4, 26]. The tracked stylet was inserted into each catheter to adjust it according to position data [4]. Tissue damage from the initial placement of the catheter is a concern with this method, and the authors discuss using a set of tracked stylets so that catheters can be inserted to the correct locations on the first try in the future.

To check the placement of needles or catheters during the procedure there are imaging modalities available. Two-dimensional ultrasound and fluoroscopy are conventional methods [11]. Two-dimensional ultrasound provides a cross-sectional image of needle or catheter placement but it can be difficult to see individual needles. Three-dimensional ultrasound features many of the same limitations experienced by two-dimensional ultrasound (*e.g.* it can be difficult to interpret due in part to imaging artefacts). Fluoroscopy projects the three-dimensional needles to two dimensions and in so doing loses depth information. Fluoroscopy also exposes the patient and medical team to ionizing radiation. Electromagnetic reconstruction [1, 29] is a recent method to determine catheter placement. A position sensor is tracked as it is pulled through each catheter. The recorded positions are reconstructed into curves that represent the catheter paths (Figure 1). Electromagnetic reconstruction is an appealing alternative to medical imaging because it circumvents various modality-specific issues, *e.g.* slice thickness in CT scans, subjective interpretation in ultrasound images. It has recently been evaluated in patients [8].

Even though electromagnetic reconstruction is described and used in numerous papers there is no open-source research platform on which this technology can be readily used. Researchers who wish to use electromagnetic reconstruction must acquire individual hardware components and write custom software to do the reconstruction itself. Most authors in literature reported developing and using proprietary MATLAB (MathWorks, Natick, Massachusetts) software [3, 9, 18, 28].

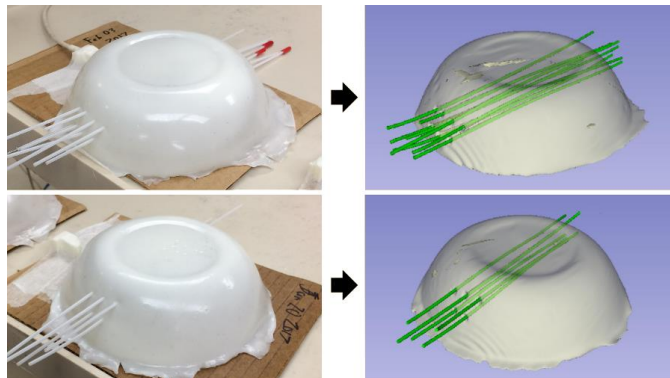


Figure 1

Electromagnetic reconstruction demonstrated on phantoms. Left, photo of the experimental setup.

Right, virtual image of catheters generated after reconstruction.

We propose two technologies implemented as open-source tools for helping radiation oncologists during brachytherapy. The first is a real-time navigation system for needle insertion in breast brachytherapy that uses a tracked needle guide. The navigation system consists of intraoperative ultrasound-based segmentation of the seroma, an electromagnetically-tracked needle guide, and a bullseye user interface for needle placement. We validate it in a phantom study benchmarking it against conventional ultrasound guidance. The second is a technology for localizing catheter paths through the breast tissue. We describe a fitting algorithm based on moving least squares polynomial fitting.

## 2 Methods

### 2.1 Open Source Environment

The PLUS Server application communicates with the spatial tracking drivers and hardware to receive spatial tracking information (positions and orientations) [12]. The server component broadcasts the spatial tracking data through the OpenIGTLink protocol to any connected clients [22]. In case of electromagnetic reconstruction, the spatial tracking data includes position data for the sensor that is pulled through each catheter, and optionally position and orientation data for a reference coordinate system. The modules and tools described in this paper were implemented in the 3D Slicer application framework ([www.slicer.org](http://www.slicer.org)) using modules from the SlicerIGT extension [24]. The PLUS Server application and 3D Slicer with its extensions are open-source software that can be used for academic or commercial purposes freely, without any restrictions. Fewer than 5,000 lines of source code describe the specific software for needle navigation and catheter reconstruction – less than 0.01% of the total number of lines of code in the open-source platform (Figure 2, VTK and 3D Slicer alone contain over three million lines of source code).

### 2.2 Navigated Needle Placement

The proposed navigated brachytherapy begins with a single brachytherapy needle being inserted through the breast and seroma under ultrasound guidance. In this paper, all brachytherapy needles were 20-gauge and featured a bevel (P/N 202-20, Best Medical, Springfield, Virginia).

An electromagnetic tracking fixture is attached to the needle in order to provide a coordinate system for the seroma. The needle can still spin within the tissue, so the seroma is tracked using a spin-invariant tracking method. The seroma shape is segmented on tracked ultrasound similar to how it is done in navigated lumpectomy [23].

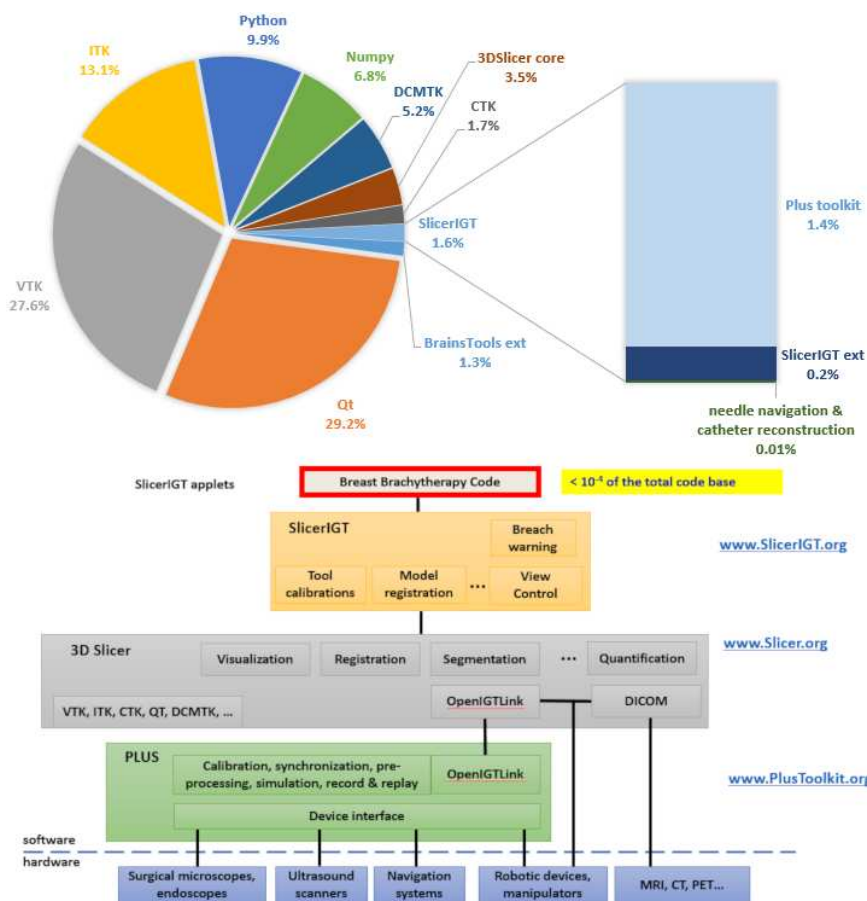


Figure 2  
Open source code re-use

A needle guide is used to track the trajectory of the brachytherapy needle. The guide is a needle sleeve that restricts needle movement along an axis relative to the sensor (Figure 3). Within the navigation system the *Guide* coordinate system indicates the position and direction of needle insertion. The guide is calibrated by clamping a needle to it and using pivot and spin methods. A chart of coordinate systems for navigated brachytherapy is provided in Figure 4.

After the first catheter guiding needle insertion, the virtual camera of the navigation view is aligned parallel to the first needle. The intention is that the user can align the guide with the navigation view so that subsequent needles are parallel to the first needle. An insertion plan is drawn on the navigation view and tracked relative to the seroma's coordinate system to help guide needles through and near to the seroma. (Figure 5). The functionality for doing this is implemented in the *Viewpoint* module from SlicerIGT [24].

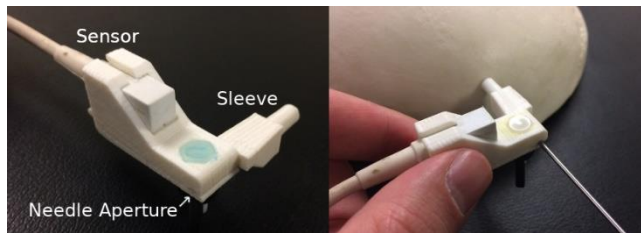


Figure 3

Guide. Left, sensor clip and needle sleeve. Right, assembled guide being used on a phantom to insert a brachytherapy needle.

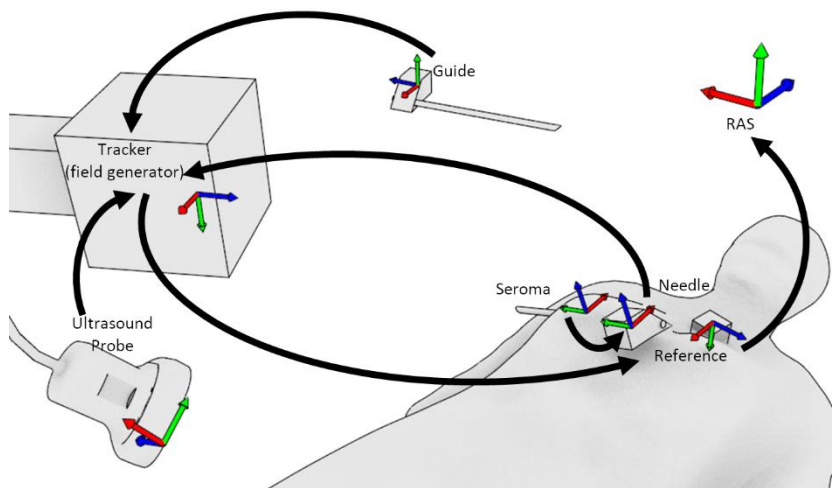


Figure 4

Coordinate systems in navigated brachytherapy

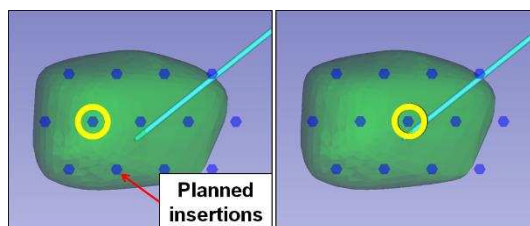


Figure 5

Left, needle insertion plan is drawn on the view according to the first needle's placement. Right, the guide is aligned with the next intended insertion (immediately to the previous needle's right).

## 2.3 Catheter Path Reconstruction

To address the lack of an open-source tool for catheter path reconstruction, an extension for 3D Slicer called *PathReconstruction* was implemented. It uses existing functionality from the *CollectPoints* and *MarkupsToModel* modules from *SlicerIGT* [24]. The extension and its dependencies can be downloaded and installed within 3D Slicer using the integrated extension manager. The flow of data is illustrated in Figure 6.

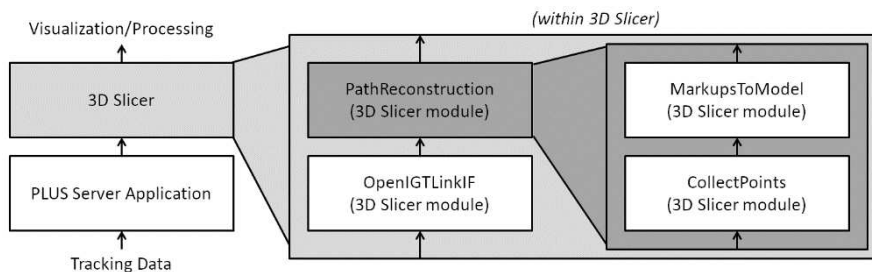


Figure 6

Flow of information in electromagnetic reconstruction

The *CollectPoints* module contains the functionality for recording a series of positions over time. The *MarkupsToModel* module contains the functionality for creating curves from point data. In this paper catheter paths are represented using polynomials fit in each of three dimensions. The overall method is similar to that of Poulin *et al.* [18]. We implemented two polynomial fitting methods and added them to the *MarkupsToModel* extension. These are global least squares fitting and moving least squares fitting.

Global least squares fitting is faster and intended to be used for previews of catheter paths. A linear solver is used to solve for the coefficients of the polynomial based on the observed coordinates and the distance along the catheter path.

$$\mathbf{Coordinates} = \mathbf{Distance} * \mathbf{Coefficients}$$

In this paper, distance was modeled by a point's position along the minimum spanning tree between the two farthest points (start and end points).

Moving least squares fitting is slower and intended for generating accurate catheter paths once all of the data has been collected. For each distance that is resampled along the polynomial, the equation needs to be solved again based on a distance weight.

$$\mathbf{Coordinates} = (\mathbf{Distance} \circ \mathbf{Weights}) * \mathbf{Coefficients}$$

Distance values that are nearer are weighed higher, while points that are farther are weighed lower. In this paper, distances were normalized between 0 and 1, and the weighing function was a Gaussian kernel with standard deviation equal to

8.33% of the length of the catheter and cut off at 99.7%. This was chosen to be similar to the 25% of data that Poulin *et al.* [18] used for fitting in their algorithm

*PathReconstruction* acts as the front-end for performing point collection (*CollectPoints*) and curve fitting (*MarkupsToModel*). All the user needs to do is specify which transform stores the position of the sensor in the catheter, then press a button to start and then to stop recording positions for each catheter. Curves are then automatically created based on the global least squares fitting method. The user has the option of finalizing all catheter shapes by applying moving least squares fitting.

## 2.4 Navigated Needle Placement Experiment

Phantom models were made of plastisol in the shape of a breast [19, 23]. The plastic was a mixture of 250 mL super-soft plastisol (part number 8228SS, MF-Manufacturing, Fort Worth, Texas), 250 mL plastisol softener (part number 4228S-1, MF-Manufacturing, Fort Worth, Texas), and two teaspoons of cellulose (product number 237132-100G, Sigma-Aldrich, St. Louis, Missouri) for ultrasound contrast. The phantoms contained palpable simulated cylindrical seromas 40 mm in length and 20 mm in diameter. The seromas were cut from a harder sheet of plastisol made from a ratio of 375 mL of regular plastic, 125 mL of plastic hardener, and one teaspoon of calcium sulfate (Sigma-Aldrich, St. Louis, Missouri) for CT contrast.

Spatial tracking and ultrasound imaging was provided by a SonixTouch GPS machine (Analogic Corporation, Peabody, Massachusetts). The tracker was pre-calibrated by the manufacturer. Two guides (Figure 3) were manufactured on a rapid prototyping machine from acrylonitrile butadiene styrene and tracked using Ascension Model 800 sensors (NDI, Waterloo, Ontario). This particular model was designed so that it could clamp onto needles for the purposes of both calibration and tracking the seroma. The guide aperture was 25.1 mm long in this experiment. One guide was for navigation, the other was used to provide a basis for tracking the seroma and the insertion plan. A tracked linear (L14-5/38 GPS) ultrasound probe (Analogic Corporation, Peabody, Massachusetts) was used to segment the seroma. The overall experiment setup is shown in Figure 7.

We measured how accurately the radiation oncologist was able to adhere to a needle insertion plan under control conditions (ultrasound guidance) versus with navigation. For both conditions, the radiation oncologist was asked to implant ten brachytherapy needles through the seroma in three planes (Figure 8). Needles were to be inserted straight with 12 mm spacing between each adjacent pair. This is the same type of pattern used in clinical practice, though the spacing between catheters ranges between 10 mm and 15 mm [30] and the number of planes can vary.

Under ultrasound guidance, the radiation oncologist began by drawing needle insertion points on the phantom using a pen and a ruler (Figure 9). Once the insertion points were drawn, the radiation oncologist inserted each needle under ultrasound guidance. The radiation oncologist referred to both the ultrasound image and to previously-inserted needles to achieve parallel insertions.

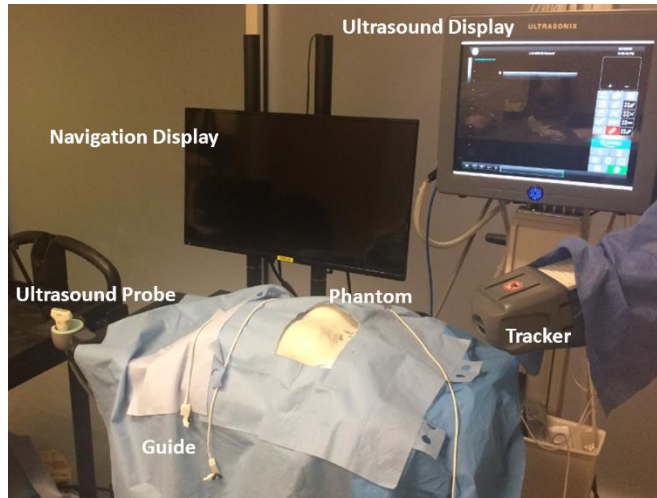


Figure 7

Experimental setup for brachytherapy navigation

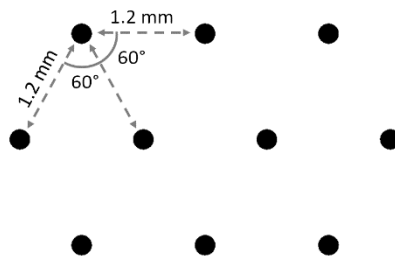


Figure 8

Intended needle insertion plan in this experiment. Needles are represented by black dots; insertion direction is perpendicular to the image.



Figure 8

Left, a radiation oncologist uses a pen and ruler to draw an insertion plan on a phantom. Right, a plan drawn on a phantom.

To measure adherence to an insertion plan, we compared inserted versus intended needle paths (analogous to catheter paths). To determine inserted paths (paths needles took through tissue) CT scans were acquired of the implanted phantoms. The needles were segmented on CT and converted to curve representations. The intended paths followed the insertion grid as described earlier. We registered paths based on a landmark registration of path endpoints then an iterative closest point registration. The main outcome measure of this experiment was the distance from each inserted path to its corresponding intended path. After registration, we sampled at 200 uniformly-spaced points the distance from one path to its corresponding planned path. We computed for each path the mean error, the minimum error, and the maximum error. The overall mean and standard deviation for each of these values are reported.

Needle retractions are an indicator of additional tissue damage, so these events were counted during each insertion procedure as a secondary outcome, along with times of performing procedure steps.

## 2.5 Electromagnetic Reconstruction Experiment

Phantoms were implanted with plastic catheters (Best Medical, Springfield, Virginia) by a radiation oncologist. Catheter paths were determined three times each as per the electromagnetic reconstruction methods described earlier. An Ascension Model 800 sensor provided a reference coordinate system, and a Model 90 sensor was used to collect sample positions within the catheters. A foot-pedal was connected to the navigation computer to allow the radiation oncologist to start and stop reconstructions. The experimental setup is shown in Figure 10.

Electromagnetic reconstruction was performed in locations where implantations occurred in patients. To measure the accuracy of electromagnetic reconstruction, we measured the distance from each reconstructed path to a corresponding ground truth path. The ground truth catheter paths were generated from segmented CT scans of the phantoms. CT scans were acquired using a Brilliance Big Bore

scanner (Philips, Amsterdam, Netherlands). We measured path error as per the method described in the previous section. The amount of time taken for catheter path reconstruction is also reported.

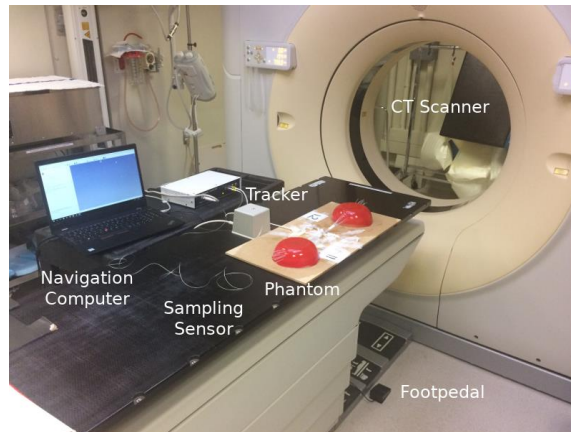


Figure 10

Experimental setup for electromagnetic reconstruction

## 3 Results

### 3.1 Navigated Needle Placement

Overall statistics for needle placement are reported in Table 1 for phantoms, and Table 2 for needles. There was a statistically significant improvement in mean error for navigation over ultrasound-guidance ( $p = 0.04$  using one-tailed Mann-Whitney U-test). There was also a statistically significant improvement in minimum error for navigation over ultrasound guidance ( $p = 0.001$  using one-tailed Mann-Whitney U-test). There was a non-significant statistical trend toward longer procedure time when using navigation versus ultrasound guidance ( $p = 0.09$ ). Testing on the other variables failed to show statistical significance or trends ( $p > 0.10$  using one-tailed Mann-Whitney U-test).

The needle placements are shown in Figure 11. Needle paths were observed to diverge as depth (in the medial direction) increased. Medial perspectives are shown to highlight the difference between inserted and intended paths.

Boxplots of mean error for each catheter are shown in Figure 12.

The amount of time taken during the different tasks are presented in Table 3.

Table 1

Overall statistics in needle insertion for six phantoms. Standard deviations indicated with  $\pm$ .

Method	Number of retractions	Time (s)
Ultrasound-guided	$1.5 \pm 1.6$	$586 \pm 206$
Navigated	$1.2 \pm 1.9$	$732 \pm 199$

Table 2

Overall statistics for sixty needle insertions for each of two methods. Standard deviations indicated with  $\pm$ .

Method	Mean error (mm)	Minimum error (mm)	Maximum error (mm)	Angle difference ( $^{\circ}$ )
Ultrasound-guided	$3.8 \pm 1.8$	$1.8 \pm 1.3$	$6.9 \pm 3.5$	$3.9 \pm 2.1$
Navigated	$3.3 \pm 1.6$	$1.1 \pm 0.9$	$6.4 \pm 3.6$	$3.8 \pm 2.2$

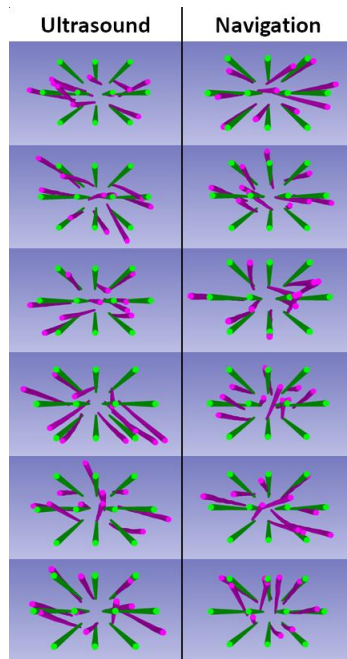


Figure 11

Medial perspective screenshots in 3D Slicer showing the locations of inserted paths (magenta) vs intended paths (green). As a reference for distances, catheters are rendered with a radius of 2 mm, ideal paths are spaced 12 mm apart, and catheters run 120 mm long.

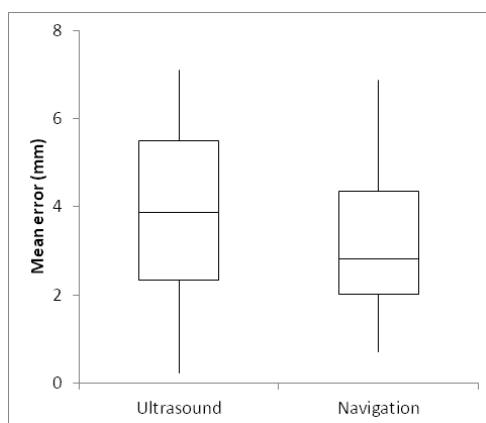


Figure 12

Boxplot of mean errors (per catheter) for ultrasound-guidance and navigation. Each column represents sixty samples.

Table 3

Time in seconds spent on each task in needle insertions for six phantoms under each method. Standard deviations indicated with  $\pm$ .

Method	First Needle	Sensor Attachment	Ultrasound Segmentation	Planning	Insertions
Ultrasound-guided	$65 \pm 7$	N/A	N/A	$129 \pm 32$	$391 \pm 178$
Navigated	$58 \pm 15$	$19 \pm 5$	$124 \pm 22$	$45 \pm 9$	$485 \pm 176$

### 3.2 Electromagnetic Reconstruction

Upon analyzing the data, we observed that one subset of reconstructions was accurate and another subset was not. The accuracy of reconstruction appeared to depend on whether the experiment was conducted in the location called "Room 1" or "Room 2". There was a statistically significant difference in the mean reconstruction error between the locations (Table 4,  $p < 0.001$  using one-tailed Mann-Whitney U-test). Results on accuracy are considered separately for these two locations. This section focuses mainly on results from "Room 2" for reasons given in the discussion.

The mean reconstruction error in Room 2 was 0.6 mm and statistically significantly lower than the voxel size of the CT scans (voxel size = 1.2 mm,  $p < 0.001$  using one-tailed sign test). Images of reconstructions from 3D Slicer are shown in Figure 13. The distribution of mean errors is shown as a boxplot in Figure 14, and the distribution of individual point errors is shown as a histogram in Figure 15. The farthest any single point on a reconstructed path was from its corresponding ground truth was 2.1 mm. There was no statistically significant

correlation between the number of sample positions and the mean error for catheters ( $p = 0.84$  using Spearman rank correlation).

In Room 1 the mean reconstruction accuracy was 2.0 mm and statistically significantly higher than the voxel size of the CT scans (voxel size = 1.2 mm,  $p < 0.001$  using one-tailed sign test).

Electromagnetic reconstruction times were recorded for each of 71 catheters three times each for a total of 213 reconstructions. The mean time per catheter was 22 seconds with a standard deviation of 10 seconds. On average 14 seconds were spent inserting the wire into the catheter, and 8 seconds were taken to pull the sensor out and collect position data.

Table 4

Accuracy of electromagnetic reconstruction in phantoms. Standard deviations indicated with  $\pm$ .

Location	Number of phantoms	Mean of mean errors (mm)	Mean of minimum errors (mm)	Mean of maximum errors (mm)
Room 1	7	$2.0 \pm 1.2$	$0.7 \pm 0.8$	$4.5 \pm 2.8$
Room 2	5	$0.6 \pm 0.2$	$0.2 \pm 0.2$	$1.1 \pm 0.3$

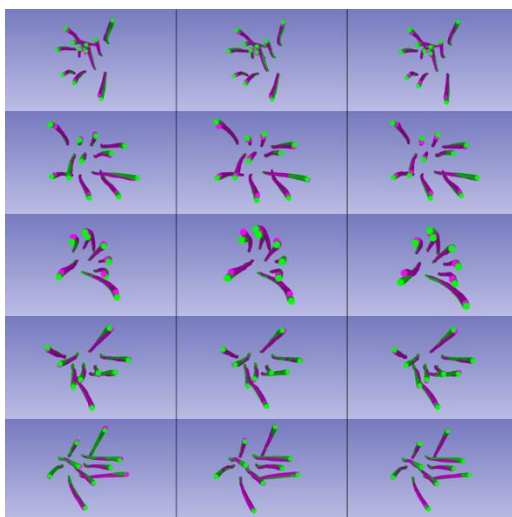


Figure 13

Medial perspective screenshots in 3D Slicer showing reconstructed paths (magenta) vs ground truth (green) for phantoms in Room 2. As a reference for distances, catheters are rendered with a radius of 2 mm.

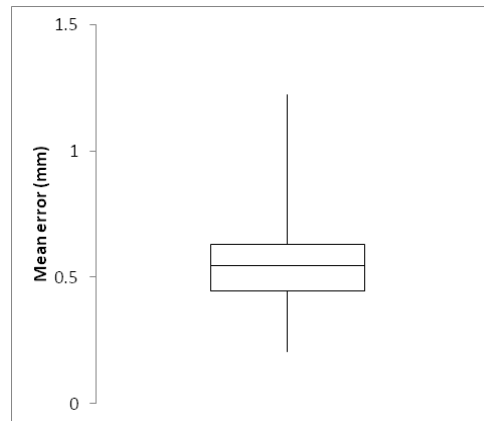


Figure 14

Boxplot of mean errors (per catheter) for electromagnetic reconstructions versus ground truth. Only data from Room 2 are shown.

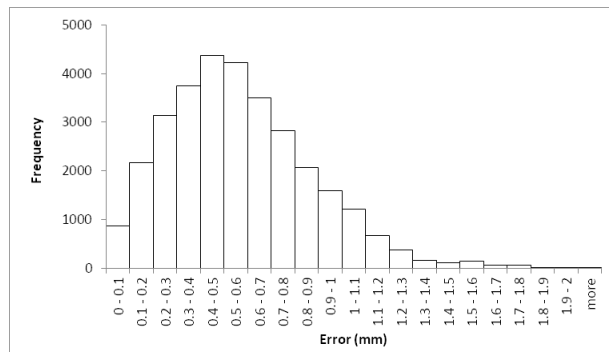


Figure 15

Histogram of individual point errors for electromagnetic reconstructions versus ground truth. Only data from Room 2 are shown.

## 4 Discussion

From the experiment in needle insertions, it appeared as though navigation helped the radiation oncologist to adhere to an insertion plan. This result does not seem to be explained by the angle of needle insertion, which was roughly equal between both experimental conditions (Table 2). Rather there appeared to be an improvement in the minimum distance between the inserted and intended paths. This could suggest that the insertion point was closer to the ideal grid. Future work will evaluate the effect of improved needle placement accuracy on dosage distribution.

There are a few limitations to the navigation method under study. Firstly, the seroma could change shape over the course of navigation due to swelling. The seroma should be checked on ultrasound periodically to ensure that the segmentation shape is still valid. Brachytherapy needles are metallic so they may interfere with the magnetic field used by the electromagnetic tracker. Prior work has found brachytherapy needles to affect positional accuracy of electromagnetic measurements by less than 0.1 mm [21]. Although the tracker is affected by magnetic field distortion, the results measure accuracy compared to a CT image which should not be affected. The needle can still bend within the tissue. It may be possible in the future to embed a sensor in the needle tip or stylet and measure such deviations from that trajectory.

There were fewer needle retractions when using navigation compared to ultrasound guidance. The small numbers make it difficult to draw conclusions regarding retractions in this experiment.

Table 3 shows how much time was spent in each task. The needle insertions took more time when using navigation, likely due to the radiation oncologist consulting both ultrasound and the navigation display. The planning step was shorter for navigation than for ultrasound guidance, likely because planning consisted of a few button clicks on a computer rather than measuring and drawing each needle insertion point on the phantom.

Electromagnetic reconstruction is now available as part of an open-source research platform. It can be downloaded and run on different operating systems, and it can be used to create reconstructions on-line (as data is being collected). The software we used to analyze the data and generate the results presented in this paper is also included as a module called *PathVerification*. This may help to enable future comparative and collaborative studies.

For the electromagnetic reconstruction experiment we split data into two groups: reconstructions that occurred in Room 1 and those that occurred in Room 2.

From electromagnetic reconstructions in Room 2 the error compared to ground truth was less than the voxel size of the CT scans. We could not generate a more precise ground truth to compare against. Accuracy was as high as can be measured given the ground truth that was available.

From electromagnetic reconstructions in Room 1 the error compared to ground truth was more than the voxel size of the CT scans.

There was a difference in accuracy of reconstructions conducted in these rooms. This was likely due to magnetic field distortion caused by the nearby CT machines similar to those seen by Maier-Hein *et al.* [13]. Although reconstructions all occurred in the same relative location on the patient table in both CT scanners, the tables themselves may have contained different components. This result emphasizes that magnetic field distortion can vary even between similar locations.

It should never be assumed that two similar locations have similar effects on magnetic field distortion.

Assuming the error was caused by magnetic field distortion, there are at least two options to improve accuracy: 1) using a tracker configuration that includes magnetic shielding (*e.g.* planar field generator [13]), and 2) characterizing and compensating for the magnetic field distortion [10] prior to electromagnetic reconstruction. These could be good directions for future investigative work.

Our experiment suggested that electromagnetic reconstruction takes around 22 seconds per catheter. This is comparable to the clinical experience of Kellermeier *et al.* who reported an average of 5 seconds for point collection and 18 seconds for transition between catheters.

### Conclusions

We have presented two technologies - a navigation system for brachytherapy needle insertion, that uses a tracked needle guide and an implementation for electromagnetic reconstruction, using an open-source research platform. In a phantom experiment, needles inserted with navigation adhered better to a grid plan, over those inserted under ultrasound-guidance only. We showed that electromagnetic reconstruction can be accurate within 1.2 mm of a CT-based, ground truth in phantoms, depending on the environment. The software for electromagnetic reconstruction is now available, as part of an open-source research platform.

### Acknowledgements

Gabor Fichtinger is supported as a Canada Research Chair in Computer-Integrated Surgery. This work was funded, in part, by NIH/NIBIB and NIH/NIGMS (via grant 1R01EB021396-01A1 - Slicer+PLUS: Point-of-Care Ultrasound) and by CANARIE's Research Software Program. Financial support was received from the Southeastern Ontario Academic Medical Association (SEAMO), Educational Innovation and Research Fund. Thomas Vaughan was funded by Ontario Graduate Scholarships, a Walter C. Sumner Memorial Fellowship, and an Alexander Graham Bell Canada Graduate Scholarship.

### References

- [1] C Bert, M Kellermeier, and K Tanderup. Electromagnetic tracking for treatment verification in interstitial brachytherapy. *Journal of Contemporary Brachytherapy*, 8(5):448-453, 2016
- [2] Y Chen, W Wang, EJ Schmidt, K-W Kwok, AN Viswanathan, R Cormack, and ZYH Tse. Design and fabrication of mr-tracked metallic stylet for gynecologic brachytherapy. *IEEE/ASME transactions on mechatronics: a joint publication of the IEEE Industrial Electronics Society and the ASME Dynamic Systems and Control Division*, 21(2):956, 2016

- 
- [3] AL Damato, AN Viswanathan, SM Don, JL Hansen, and RA Cormack. A system to use electromagnetic tracking for the quality assurance of brachytherapy catheter digitization. *Medical Physics*, 41(10):101702, 2014
- [4] J de Arcos, EJ Schmidt, W Wang, J Tokuda, K Vij, RT Seethamraju, AL Damato, CL Dumoulin, RA Cormack, and AN Viswanathan. Prospective clinical implementation of a novel magnetic resonance tracking device for real-time brachytherapy catheter positioning. *International Journal of Radiation Oncology Biology Physics*, 99(3):618-626, 2017
- [5] L de Boeck, J Beliën, and W Egyed. Dose optimization in high-dose-rate brachytherapy: a literature review of quantitative models from 1990 to 2010. *Operations Research for Health Care*, 3(2):80-90, 2014
- [6] TL de Jong, NJ van de Berg, L Tas, A Moelker, J Dankelman, and JJ van den Dobbelsteen. Needle placement errors: do we need steerable needles in interventional radiology? *Medical devices (Auckland, NZ)*, 11:259, 2018
- [7] DA DeBiose, EM Horwitz, AA Martinez, GK Edmundson, PY Chen, GS Gustafson, B Madrazo, K Wimbish, E Mele, and FA Vicini. The use of ultrasonography in the localization of the lumpectomy cavity for interstitial brachytherapy of the breast. *International Journal of Radiation Oncology Biology Physics*, 38(4):755-759, 1997
- [8] M Kellermeier, R Fietkau, V Strnad, and C Bert. Assessment of the implant geometry in fractionated interstitial HDR breast brachytherapy using an electro-magnetic tracking system. *Brachytherapy*, 17(1):94-102, 2018
- [9] M Kellermeier, J Herbolzheimer, S Kreppner, M Lotter, V Strnad, and C Bert. Electromagnetic tracking (emt) technology for improved treatment quality assurance in interstitial brachytherapy. *Journal of applied clinical medical Physics*, 18(1):211-222, 2017
- [10] VV Kindratenko. A survey of electromagnetic position tracker calibration techniques. *Virtual Reality*, 5(3):169-182, 2000
- [11] RR Kuske. Breast brachytherapy. *Hematology/Oncology Clinics*, 13(3):543-558, 1999
- [12] A Lasso, T Heffter, A Rankin, C Pinter, T Ungi, and G Fichtinger. Plus: open-source toolkit for ultrasound-guided intervention systems. *IEEE Transactions on Biomedical Engineering*, 61(10):2527-2537, 2014
- [13] L Maier-Hein, AM Franz, W Birkfellner, J Hummel, I Gergel, I Wegner, and H-P Meinzer. Standardized assessment of new electromagnetic field generators in an interventional radiology setting. *Medical Physics*, 39(6Part1):3424-3434, 2012
- [14] MA Meltsner, NJ Ferrier, and BR Thomadsen. Observations on rotating needle insertions using a brachytherapy robot. *Physics in Medicine & Biology*, 52(19):6027-6037, 2007
-

- [15] IPI Pappas, P Ryan, P Cossmann, J Kowal, B Borgeson, and M Caversaccio. Improved targeting device and computer navigation for accurate placement of brachytherapy needles. *Medical Physics*, 32(6Part1):1796-1801, 2005
- [16] A Pompeu-Robinson, M Kunz, CB Falkson, LJ Schreiner, CP Joshi, and G Fichtinger. Immobilization and catheter guidance for breast brachytherapy. *International Journal of Computer Assisted Radiology and Surgery*, 7(1):65-72, 2012
- [17] E Poulin, L Gardi, A Fenster, J Pouliot, and L Beaulieu. Towards real-time 3d ultrasound planning and personalized 3d printing for breast HDR brachytherapy treatment. *Radiotherapy and Oncology*, 114(3):335-338, 2015
- [18] E Poulin, E Racine, D Binnekamp, and L Beaulieu. Fast, automatic, and accurate catheter reconstruction in HDR brachytherapy using an electromagnetic 3d tracking system. *Medical Physics*, 42(3):1227-1232, 2015
- [19] A Samani, J Bishop, C Luginbuhl, and DB Plewes. Measuring the elastic modulus of ex vivo small tissue samples. *Physics in Medicine and Biology*, 48(14):2183-2198, 2003
- [20] G Strassmann, R Heyd, R Cabillic-Engenhardt, C Kolotas, S Walter, G Sakas, D Richter, and N Zamboglou. Accuracy of 3-d needle navigation in interstitial brachytherapy in various body regions. *Strahlentherapie und Onkologie*, 178(11):644-647, 2002
- [21] G Strassmann, C Kolotas, R Heyd, S Walter, D Baltas, T Martin, H Vogt, G Ioannidis, G Sakas, and N Zamboglou. Navigation system for interstitial brachytherapy. *Radiotherapy and Oncology*, 56(1):49-57, 2000
- [22] J Tokuda, GS Fischer, X Papademetris, Z Yaniv, L Ibanez, P Cheng, H Liu, J Blevins, J Arata, AJ Golby, T Kapur, S Pieper, EC Burdette, G Fichtinger, CM Tempany, and N Hata. Openigtlink: an open network protocol for image-guided therapy environment. *The International Journal of Medical Robotics and Computer Assisted Surgery*, 5(4):423-434, 2009
- [23] T Ungi, G Gauvin, A Lasso, CT Yeo, P Pezeshki, T Vaughan, K Carter, J Rudan, CJ Engel, and G Fichtinger. Navigated breast tumor excision using electromagnetically tracked ultrasound and surgical instruments. *IEEE Transactions on Biomedical Engineering*, 63(3):600-606, 2016
- [24] T Ungi, A Lasso, G Fichtinger. Open-source platforms for navigated image-guided interventions. *Medical Image Analysis*, 33:181-186, 2016
- [25] FA Vicini, DA Jaffray, EM Horwitz, GK Edmundson, DA DeBiose, VR Kini, and AA Martinez. Implementation of 3d-virtual brachytherapy in the management of breast cancer: a description of a new method of interstitial

- brachytherapy. *International Journal of Radiation Oncology Biology Physics*, 40(3):629-635, 1998
- [26] DE Wazer, S Kaufman, L Cuttino, T DiPetrillo, and Douglas W Arthur. Accelerated partial breast irradiation: an analysis of variables associated with late toxicity and long-term cosmetic outcome after high-dose-rate interstitial brachytherapy. *International Journal of Radiation Oncology Biology Physics*, 64(2):489-495, 2006
- [27] S Zhang, S Jiang, Z Yang, and R Liu. 2d ultrasound and 3d mr image registration of the prostate for brachytherapy surgical navigation. *Medicine*, 94(40), 2015
- [28] J Zhou, E Sebastian, V Mangona, and D Yan. Real-time catheter tracking for high-dose-rate prostate brachytherapy using an electromagnetic 3d-guidance device: A preliminary performance study. *Medical Physics*, 40(2):021716, 2013
- [29] J Zhou, L Zamdborg, and E Sebastian. Review of advanced catheter technologies in radiation oncology brachytherapy procedures. *Cancer Management and Research*, 7:199-211, 2015
- [30] RD Zwicker and R Schmidt-Ullrich. Dose uniformity in a planar interstitial implant system. *International Journal of Radiation Oncology Biology Physics*, 31(1):149-155, 1995

# Probabilistic Method to Improve the Accuracy of Computer-Integrated Surgical Systems

Tamás Haidegger<sup>1,2</sup>

<sup>1</sup> Antal Bejczy Center for Intelligent Robotics (IROB), EKIK, Óbuda University, Bécsi út 96/b, H-1034 Budapest, Hungary, [tamas.haidegger@irob.uni-obuda.hu](mailto:tamas.haidegger@irob.uni-obuda.hu)

<sup>2</sup> Austrian Center for Medical Innovation and Technology (ACMIT), Viktor-Kaplan-str. 2, A-2700 Wiener Neustadt, Austria

---

*Abstract: The technological development of the last decades resulted in the rise of entirely new paradigms in healthcare. Computer-Integrated Surgery (CIS) is providing innovative, minimally invasive solutions to heal complex injuries and diseases. It integrates robotic devices to the treatment delivery phase. By now, well over 6 million successful operations have been accomplished with various systems. In certain critical surgical procedures, where spatial accuracy is a must, physicians extensively rely on the help of CIS, and particularly on intra-operative navigation system. For these, the ways of use, including setup, registration and application accuracy metrics are provided by the manufacturers. Depending on the setup, inherent system errors can accumulate, and lead to significant deviation in position measurements. It is crucial to improve the precision of integrated setups, and to determine the overall task execution error. The stochastic approach proposed here offers an easy and straightforward solution to map and scale the error propagation. Applying pre-operative and on-site simulations, the optimal positioning of the navigation system can be achieved. This results in faster task execution and reduction of the probability of surgical errors. Surgical tracking systems have broader applications in endoscopic surgeries, and the method described in the article can be directly applied to these procedures too. It was tested in silico and on a neurosurgical prototype robot system developed at the Johns Hopkins University. The proposed features together can greatly increase the safety and reliability of all procedures where camera systems are involved, and ease the surgeon's task and potentially reduce operating time.*

*Keywords: CIS accuracy; Image-Guided Surgery; robotic surgery; error propagation*

---

## 1 Introduction

### 1.1 Computer-Integrated Surgery: an Emerging Field

*Computer-Integrated Surgery (CIS)* is the most commonly used term to cover the entire field of interventional technology, from medical image processing and augmented reality applications to automated tissue ablation [1]. A key domain within is called *Image-Guided Surgery (IGS)*, meaning the accurate correlation and mapping of the operative field to a pre-operative image or intra-operative

(e.g., ultrasound, fluoroscopy) data set of the patient, providing freehand navigation, positioning accuracy of equipment or guidance for mechatronic systems [2]. IGS has been primarily used in neurosurgery, pediatrics, orthopedics and also had a major impact in ear, nose and throat (ENT) and maxillofacial reconstruction surgery.

A cornerstone of medical imaging and robotics is registration, that means the spatial alignment of different modalities to determine the position and orientation of the patient in the operating field relative to a virtual data set of the anatomy, e.g., a pre-operative image. The registration should provide a homogeneous transformation matrix that allows the conversion of locations and control signals between different devices [3]. As of today, it is still less common to rely on intra-operative patient data, although successful implementations of magnetic resonance (MR) compatible robotic systems [4] and ultrasound guidance systems exist [5].

While currently the dominating sector is the Robot-Assisted Minimally Invasive Surgery (RAMIS), which means real-time teleoperation of the tools by the surgeon, even in this type of robots, novel features (such as visual overlay, augmented reality fusion, tool tracking) require the exact registration of the patient to the robot and the preoperative data [6]. This is also a key enabling technology towards the (partial) automation of surgery [7].

There are two common ways to perform the registration [8]. For the classical, *frame-based stereotaxis*, a stereotactic frame is mounted to the patient's head prior to the computer tomography (CT) or MR imaging and serves as an fixed coordinate system by which any point of the brain can be referenced.

A recent technique—*frameless stereotaxis*—involves a hand-held surgical probe, and it does not require the rigid head-frame. The probe may be tracked by mechanical, optical, ultrasonic or electromagnetic techniques while touching designated points with it. The transformation between the image space and the tracker coordinates can be computed through fiducial-based or anatomical landmark-based registration, relying on paired-point, surface matching (point-cloud) methods or some kind of hybrid transformation [9]. *Fiducials* are artificial markers, screws or other potential reference points. Natural anatomy features such as point landmarks, ridge curves or surfaces may also be used.

Surgical navigation systems match the two frames and provide the tool coordinates in image space, through the spatial tracking of a *Tool Rigid Body* (TRB). The patient's body must be fixed relative to the mounted reference frame (*Dynamic Reference Base*—DRB), otherwise the registration loses its validity. Intra-operative navigation is commonly achieved with a camera system that is able to track rigid bodies within its workspace. Commercially available systems are typically based on infrared stereotactic cameras and active (flashing LED) or passive (reflective paint-covered) markers.

Within all these domains, data collection at large scale became possible with the introduction of CIS systems, also as an enabler of Machine Learning methods [10]. This opened the case for a completely new field, dubbed Surgical Data

Science [11], which really enables the assessment and benchmarking of CIS systems based on surgical process models [12].

## 1.2 Motivation

Regardless of the partial success in applications, there are some concerns that prevent CIS technologies from becoming dominant in most of the medical areas. While there is a clear need for accuracy and robust operation for many procedures, the associated high expenses are less tolerated. Several projects turned out to be financial failures, as the high development and production costs can only pay back, when significant market penetration is achieved. In many countries, the state-ran healthcare system cannot support costly robot investments, forming a barrier to their deployment. Furthermore, the development of more complex IGS systems, integrating different components lead to the rise of unforeseen errors. Effective compensation for these spatial inaccuracies are necessary towards the future application of robotic technology in the Operating Room (OR). This has become an explicit requirement toward CIS systems in the new ISO/IEC standards on the basic safety and essential performance of surgical robots [13].

It is crucial to meaningfully describe a system's *application accuracy*. It may be a highly non-linear function of the intrinsic and registration accuracies of the components, therefore requiring special handling. Various error propagation techniques have been proposed in the literature—summarized and further evolved here—to determine system errors as a function of the different integrated components.

## 2 METHODS

Improvement of the safety and reliability of CIS systems can be achieved through the simulation and testing of their control architecture, generating test sequences for the entire navigation and control architecture, and assessing their accuracy [14].

IGS robot systems are based on the principle that during regular operation, the position of the surgical tool mounted on a robot can be controlled precisely, once its location is known relative to the base (reference) coordinate system. A generic robot-integrated IGS system's schematic diagram is shown in Fig. 1, where the nodes represent control frames and the lines mean homogeneous transformations connecting those. The navigation system (e.g., a camera) is able to track at least two markers; first, the position of the *Dynamic Reference Base*, (i.e., a fiducial anchored to the patient) and second, the *Tool Rigid Body*, attached to the end of the robot. The navigation system is also used to register the pre-operative image of the patient to the DRB with the help of e.g., a hand-held probe and skin-mounted fiducials. Then, the surgical plan can be mapped from pre-operative image space (IMG) to the patient's actual coordinate system in the OR (PAT), then to robot coordinates (ROB). The trackable TRB and the last joint, the *Robot*

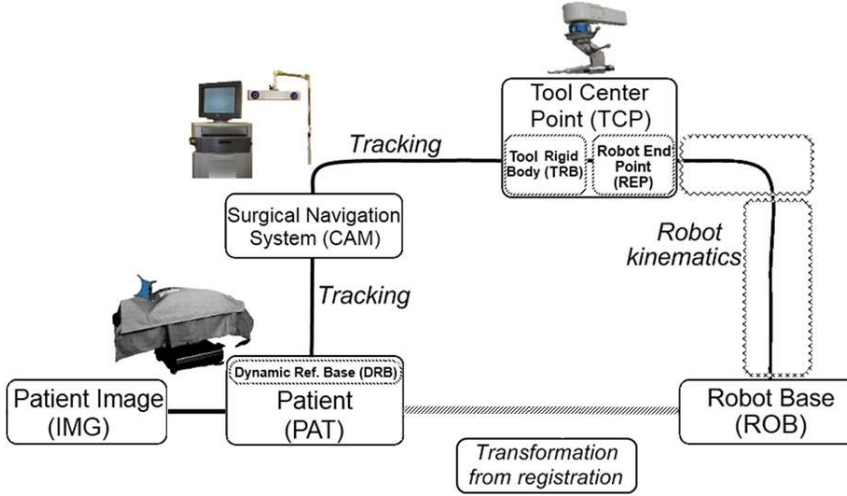


Figure 1

General control concept of IGS robot systems. The solid line represents the typical route of control, while the dashed line is the proposed closed loop approach, relying on the accurate updating of the robot-to-patient registration.

*End Point (REP)* are different, and the transformation is identified through e.g., pivot calibration. For simplicity, *Tool Center Point (TCP)* is used to denote the end of the robot. The theory of a tracking-based IGS robot was described in [15].

The control signals ( $\text{Ctrl}$ ) generated to move the robot are computed in the IMG frame based on the treatment plan, and then transformed to the Robot base frame (ROB) for execution via the Camera's coordinate frame (CAM):

$$\text{Ctrl}|_{\text{IMG}} = {}^{\text{TCP}}\mathbf{T}_{\text{ROB}} \cdot {}^{\text{CAM}}\mathbf{T}_{\text{TCP}} \cdot {}^{\text{PAT}}\mathbf{T}_{\text{CAM}} \cdot {}^{\text{IMG}}\mathbf{T}_{\text{PAT}} \cdot \text{Ctrl}|_{\text{ROB}}, \quad (1)$$

where  $\text{Ctrl}|_{\text{ROB}}$  and  $\text{Ctrl}|_{\text{IMG}}$  stand for the control signals expressed in the robot's and the image's frame, respectively. The transformation is in homogeneous coordinates and the  $\text{Ctrl}$ -s are coordinate values also given as homogeneous vectors. With most IGS systems, the  ${}^{\text{PAT}}\mathbf{T}_{\text{ROB}}$  is acquired through registration, and used as a static transformation during the procedure. In Fig. 1, it means closing the control loop (having performed another registration under static conditions):

$${}^{\text{PAT}}\mathbf{T}_{\text{ROB}} = {}^{\text{TCP}}\mathbf{T}_{\text{ROB}} \cdot {}^{\text{CAM}}\mathbf{T}_{\text{TCP}} \cdot {}^{\text{PAT}}\mathbf{T}_{\text{CAM}}. \quad (2)$$

## 2.1 Different Accuracies

It is crucial to properly document the experiments evaluating the usability of a CIS system, especially if it integrates various elements. There are three different types of accuracies (in terms of spatial errors) that can be specified with different error numbers (determined in general) according to [16]:

- intrinsic (technical) accuracy (0.1–0.6 mm),
- registration accuracy (0.2–3 mm),
- application accuracy (0.6–10 mm).

*Intrinsic accuracy* applies to certain elements, such as the robot or the navigation system. It describes the average error of the given component in operational use. Random errors (e.g., mechanical compliance, friction, loose hardware), resolution of the imaging device, inadequate control and noise can all result in low intrinsic accuracy. On the user interface side, discretized input and modeling errors may further decrease precision.

*Registration errors* are also present, as computational methods involve some kind of residual errors. In IGS, a major source of error can be the markers (different types, forms and materials), displacement of the fiducials and determination of the center of the fiducials.

*Application accuracy* refers to the overall targeting error of the integrated system while used in a clinical procedure or a mock setup. It realistically measures the task specific effectiveness of a system and is commonly used for validation. The application accuracy depends on all other sources of errors in a complex, non-linear way, therefore typically phantom, cadaver or clinical trials are required to determine it.

Further problems arise with the simple, ergonomic expression of spatial errors. Physicians may need a single number showing the precision of the system. In many applications, only the absolute distance from a desired location matters, therefore the *root mean square error* (RMSE) is given for the system:

$$E_{\text{RMS}} = \sqrt{\frac{1}{N} \sum_{i=1}^N (\mathbf{x}_i - \mathbf{x})^2}, \quad (3)$$

where  $N$  is the number of measurements,  $\mathbf{x}$  is the desired point and  $\mathbf{x}_i$  is the  $i^{\text{th}}$  measured point. RMSE incorporates both mean and standard deviation values [17]:

$$E_{\text{RMS}}^2 = E_{\text{mean}}^2 + E_{\text{STD}}^2. \quad (4)$$

The RMSE is only an unbiased representation of isotropic and independent errors in the 3D space. For other cases, the covariance matrix of the distribution should be used. Eq. (3) does not incorporate the angular errors of the system, even though any 3D registration or tracking component with a rotational error will affect the translational accuracy. This model is valid for zero-mean Gaussian distributions, and RMSE gives a single value even to multi-dimensional distributions.

Evaluating real robotic systems usually involves not only mathematical modeling and simulation, but also extensive accuracy tests. One of the difficulties in evaluating an IG robot is to acquire the ground truth—the gold standard. This is

feasible through the use of a significantly more precise device (e.g., laser scanner, accurate camera system), the use of a measurement phantom or other trusted method (providing the ground truth).

Most commonly, the medical device is guided (directed) to different positions and orientations along a precisely known set of landmarks (fiducials) or an accuracy board. The positions can also be recorded with an independent localizer.

To evaluate the different point-based tests, certain measures have been developed and used. Let us assume that there are  $N + M$  points in total used during the experiment. These can either be artificial fiducials or anatomical landmarks;  $\mathbf{p}_1, \mathbf{p}_2, \dots, \mathbf{p}_N$  points are used during the registration, and  $\mathbf{p}_1^*, \mathbf{p}_2^*, \dots, \mathbf{p}_M^*$  points are used during the procedure (and to derive the error at the target).

Specific to the intra-operative tracker and the setup, the *Fiducial Localization Error* (FLE) includes the intrinsic and extrinsic sources of error, representing the accuracy to localize a  $\mathbf{p}_i (i = 1, \dots, N)$  point; consequently the centroid of the cluster of measured points [18]. FLE can be defined as the mean value of the error of all samples:

$$E_{\text{FLE}} = \frac{1}{N_{\text{Fiducial}} M_{\text{Trial}}} \sum_{i=1}^{N_{\text{Fiducial}}} \sum_{j=1}^{M_{\text{Trial}}} \varepsilon(i, j), \quad (5)$$

where  $\varepsilon$  is the error of a single measurement at a given fiducial. One of the most precise optical trackers available on the market is the *Optotrak Certus* from NDI. It has a 0.1–0.15 mm RMSE FLE according to the specifications. Typical surgical navigation systems provide less accurate measurements, a 0.2–1 mm RMSE error.

*Fiducial Registration Error* (FRE) is the mean square distance between homologous fiducial points; the residual error of the paired-point registration between the given subset of the known and recorded fiducial coordinates ( $\mathbf{p}_i, i = 1, \dots, N$ ) during an accuracy test [19]:

$$E_{\text{FRE}} = \sqrt{\frac{1}{N} \sum_{i=1}^N \|\mathbf{T}\mathbf{p}_i - \mathbf{q}_i\|^2}, \quad (6)$$

where  $N$  is the number of fiducials used during the registration,  $\mathbf{q}_i$  is the position of the  $i^{\text{th}}$  fiducial in one space (may be the robot),  $\mathbf{p}_i$  is the same point in the other (patient space) and  $\mathbf{T}$  is the computed homogeneous transformation. FRE is connected to FLE [19] through:

$$E_{\text{FRE}}^2 = \left(1 - \frac{1}{2N}\right) E_{\text{FLE}}^2. \quad (7)$$

*Target Registration Error* (TRE) is the deviation between points ( $\mathbf{p}_i^*, i = 1, \dots, M$ ) in the reference and the other (registered) coordinate system. FLE, FRE and TRE are presented in Fig. 2. TRE is typically used for the characterization of

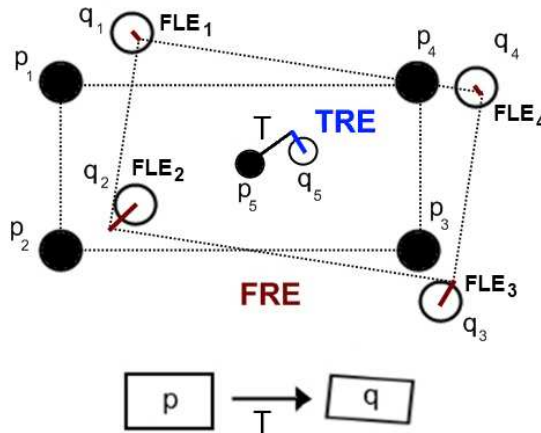


Figure 2

Definition of FRE and TRE to assess point-based registration methods. The black and white circles represent corresponding point pairs in the two different spaces. FLE is the spatial deviation between the true and the recorded position of the landmark points that the registration is built on. FRE is the residual error of the applied transformation calculated over the points used to derive the  $\mathbf{T}$  transformation. TRE is the error of mapping (a set of) independent points from the original space to the registered space [16].

schematic point-based registrations. Ideally, FRE and TRE both equal zero.

$$E_{\text{TRE}} = \sqrt{\frac{1}{M} \sum_{i=1}^M \|\mathbf{T}\mathbf{p}_i^* - \mathbf{q}_i\|^2}, \quad (8)$$

where  $M$  is the number of fiducials used to compute TRE (that are not identical to any of the points used during registration). In medical cases, TRE might be computed based on distinguished anatomical points. Mean TRE is related to mean FLE through [20]:

$$E_{\text{TRE}}^2(\mathbf{r}) \approx \frac{E_{\text{FLE}}^2}{N} \left( 1 + \frac{1}{3} \sum_{i=1}^3 \frac{d_i^2(\mathbf{r})}{f_i^2} \right), \quad (9)$$

where  $\mathbf{r}$  is the target point,  $N$  the number of fiducials,  $d_i(\cdot)$  the distance of the target from the axis  $i$  of the fiducial points and  $f_i$  is the RMSE distance of all the fiducial points from that same axis. Novel research publications show that TRE and FRE are independent for point-based registrations, therefore (9) can only be used to estimate TRE for a given fiducial configuration and a defined target position [20, 21]. The FRE in a particular case does not correlate with TRE for any arbitrary chosen configuration. Many commercially available surgical navigation systems use (incorrectly) FRE as a metric for the precision of the system, while others use proprietary algorithms to define an accuracy number to display to the surgeon.

Different research groups defined further types of errors to better describe their models or procedures [22]:

- *Image Plane Error* (IPE) is the measurement error of the camera sensor. It contains the focus, distortions and other imperfections of the lens through the extrinsic and intrinsic camera parameters,
- *Calculated Registration Error* (CRE) is the correlation of pre-operative image and intra-operative anatomical data,
- *Mean Fiducial Error* (MFE) is similar to CRE, using fiducials for registration,
- *Mean Target Error* (MTE) represents the 6 DOF error of a rigid tracking target in the centroid of the fiducials. Its value depends on the FLE of each fiducial and the spatial arrangement of the tracking target,
- *Target Positioning Error* (TPE) is the spatial mismatch between the position of the device and the surgical target that incorporates TRE plus confounders in clinical use.
- *Target Localization Error* (TLE) is the spatial mismatch between the reported position of the device versus its ideal location.
- *Total Targeting Error* (TTE) is the overall error. For the RMSE values,  $E_{TTE}^2 = E_{TRE}^2 + E_{TLE}^2$ .

More recently, iterative solutions have been developed to solve the *absolute position/orientation problem* in registration, since the need to define better accuracy metrics has gained more attention in the international research community [23, 24].

### 3 System Error Estimation Concepts

Validation and assessment of image-guided robotic systems can be cumbersome, thus significant effort has been invested into metrology and standards development by the research community. Deterministic spatial accuracy analysis of image registration and surgical robot systems was performed by many research groups [13, 25–28]. Stochastic analysis has mostly been avoided due to the fact that it is computationally demanding and can lead to extremely complex solutions.

A major challenge is to find the best homogeneous transformation that accurately registers matching point pairs in two different data sets. Different metrics, such as the FLE, FRE and TRE have been defined beforehand, and this article describes a new, stochastic approach to deal with the imperfections of an integrated system in a practical manner.

### 3.1 Accuracy Assessment of Integrated Systems

One of the typical assumptions of the benchmarking methods (based on the *central limit theorem*) is to use Gaussian distribution to model the noise of the original measurements. Focusing solely on registration error estimation, Moghari et al. [29] compares the different noise models found in literature. It is concluded that all the algorithms can be unified through the model presented in [30] that assumes inhomogeneous and anisotropic zero-mean Gaussian noise. For the modeling of navigational devices, identical, isotropic, zero-mean Gaussian noise is used most commonly [31, 32], although some measurements suggest that the noise may be different for all existing surgical navigation systems [33]. The manufacturers claim to improve on homogeneity continuously, therefore identical distribution will be assumed hereafter. First, let us review previously developed solutions for error estimation, to be able to present their limitations and shortfalls.

#### 3.1.1 Erroneous Transformation Matrix Calculation

The most generic form describing the geometric relation between point clouds for IGS has been derived in the early 1990s. In IG therapy, usually only the positional error is indicated, as the accuracy of the treatment delivery—in these applications—depends on the 3D spatial error [28]. Let us assume that we only have an erroneous  ${}^A_B\tilde{\mathbf{T}}$  approximation of the ideal  ${}^A_B\mathbf{T}$  transformation:

$${}^A_B\tilde{\mathbf{T}} = {}^A_B\mathbf{T} \cdot \Delta_B^A\mathbf{T} \quad \text{and} \quad \Delta_B^A\mathbf{T}_{\text{Rot}} \approx \mathbf{I} + \theta\mathbf{N}, \quad (10)$$

where  $\mathbf{I} + \theta\mathbf{N}$  is a first-order Taylor series approximation of a rotation expressed with an angle ( $\theta$ ) around a given axis  $\mathbf{n} = [n_x, n_y, n_z]$ ,  $\mathbf{I}$  being the identity matrix:

$${}^A_B\mathbf{T}_{\text{Rot}}(\mathbf{n}, \theta) = e^{\theta\mathbf{N}}, \quad \text{where} \quad \mathbf{N} = \begin{bmatrix} 0 & -n_z & n_y \\ n_z & 0 & -n_x \\ -n_y & n_x & 0 \end{bmatrix}. \quad (11)$$

A measured  $\tilde{x}_A$  value is the approximation of a real  $x_A$ ,

$$\tilde{\mathbf{x}}_A = \mathbf{x}_A + \Delta\mathbf{x}_A, \quad (12)$$

then the transformed value derives to be:

$$\tilde{\mathbf{x}}_B = {}^A_B\tilde{\mathbf{T}}\mathbf{x}_A = \mathbf{x}_B + \Delta\mathbf{x}_B, \quad (13)$$

with uncertainty:

$$\Delta\mathbf{x}_B = {}^A_B\mathbf{T}_{\text{Rot}}(\theta\mathbf{N}\mathbf{x}_A + \Delta\mathbf{x}_A + \Delta_B^A\mathbf{T}_{\text{Trans}}). \quad (14)$$

The disturbance effect of small rotations on small translations is neglected:

$$\Delta_B^A\mathbf{T}_{\text{Rot}} \cdot \Delta_B^A\mathbf{T}_{\text{Trans}} \approx \Delta_B^A\mathbf{T}_{\text{Trans}}. \quad (15)$$

This method analytically calculates position error accumulation; however, it may be difficult to compute and not accurate enough for certain applications (due to the Taylor series approximation).

### 3.1.2 Covariance Matrix Based Approximation

It is possible to use a computed estimate of the steady-state error covariance of a system to determine its accuracy [34]. This means that given the vector of the state variables  $\mathbf{x}_1, \mathbf{x}_2, \dots, \mathbf{x}_k$ , the error covariance can be determined for every measurement point:

$$\boldsymbol{\Sigma}_{\mathbf{x}_i} = E\{\Delta\mathbf{x}_i\Delta\mathbf{x}_i^T\} = E\{(\mathbf{x}_i - \tilde{\mathbf{x}}_i)(\mathbf{x}_i - \tilde{\mathbf{x}}_i)^T\}, \quad (16)$$

where  $\mathbf{x}_i$  and  $\tilde{\mathbf{x}}_i$  represents the true and estimated states at point  $i$ , respectively. The noise distribution of each point  $\mathbf{x}_i$  is given by the covariance matrix  $\boldsymbol{\Sigma}_{\mathbf{x}_i}$ . There are different methods to estimate  $\boldsymbol{\Sigma}_{\mathbf{x}_i}$  directly from state-space models through e.g., the closed-form solution of the discrete algebraic Riccati equation [34]. The limitation of the method is that it requires an accurate model of the system and a larger number of a priori measurements. Let us assume that  $\mathbf{x}_B = f(\mathbf{x}_A, \mathbf{t})$ , where  $\mathbf{t}$  is the representation of the position and orientation. Then a linearized solution can be given to (14):

$$\Delta\mathbf{x}_B = \left. \frac{\partial f(\mathbf{x}_A, \mathbf{t})}{\partial \mathbf{t}} \right|_{\mathbf{t}=\tilde{\mathbf{t}}} = \mathbf{J}_f \Delta\mathbf{t}, \quad (17)$$

where  $\mathbf{J}_f$  is the Jacobian matrix (first-order Taylor series approximation) of function  $f$  [35]. It is possible to acquire the least squares solution for  $\Delta\mathbf{t}$  through:

$$\Delta\mathbf{t} = (\mathbf{J}_f^T \mathbf{J}_f)^{-1} \mathbf{J}_f^T \Delta\mathbf{x}_B. \quad (18)$$

The covariance of  $\mathbf{t}$  is given by the expected value of the outer product:

$$\begin{aligned} \boldsymbol{\Sigma}_{\mathbf{t}} &= E\{\Delta\mathbf{t}\Delta\mathbf{t}^T\} \\ &= (\mathbf{J}_f^T \mathbf{J}_f)^{-1} \mathbf{J}_f^T \bar{\boldsymbol{\Sigma}}_{\mathbf{x}_B} ((\mathbf{J}_f^T \mathbf{J}_f)^{-1} \mathbf{J}_f^T)^T, \end{aligned} \quad (19)$$

where  $\bar{\boldsymbol{\Sigma}}_{\mathbf{x}_B}$  is constructed from the covariance matrices of  $\mathbf{x}_B$ .

### 3.1.3 Covariance Propagation

Instead of measuring the covariance of the system separately, it can also be calculated with backward and forward propagation through the approximation of the non-linear, affine coordinate transformations according to [36, 37]. Given (17), the covariance matrix  $\boldsymbol{\Sigma}_f$  can be determined:

$$\boldsymbol{\Sigma}_f = E\{(\mathbf{J}_f \Delta\mathbf{x}_A)(\mathbf{J}_f \Delta\mathbf{x}_A)^T\} = \mathbf{J}_f \boldsymbol{\Sigma}_{\mathbf{x}_A} \mathbf{J}_f^T, \quad (20)$$

If the covariance of  $\mathbf{x}_B$  is known, backward propagation can be used, which means employing (20) on the inverse  $f$  function:

$$\boldsymbol{\Sigma}_{f^{-1}} = \mathbf{J}_{f^{-1}} \boldsymbol{\Sigma}_{\mathbf{x}_A} \mathbf{J}_{f^{-1}}^T = (\mathbf{J}_f^T \boldsymbol{\Sigma}_{\mathbf{x}_A}^{-1} \mathbf{J}_f)^{-1}. \quad (21)$$

Pseudo-inverse methods can be applied to get the solution for overparametrized cases. With the help of (20) and (21) it is possible to compute the covariance at a Point of Interest (POI) through the known homogeneous transformations leading to the target point from the original base frame.

This form of description allows us to analytically derive the errors in different frames and representations. An example is the computation of the following errors [36]:

- deriving the 2D covariance matrix of a single camera image of a navigation system,
- propagating the error to 3D FLE error based on a camera model,
- deriving the 6D rigid body error based on the FLE,
- propagating the rigid body error to the POI to derive the 3D TRE.

The advantage of this approach is that it allows to build up the whole computation from the lowest level of errors within the imaging system (that may originate in internal camera calibration inaccuracies, imperfect lenses, inaccurate computational algorithms or image blur). However, usually very limited information is available about a navigation system at this level of details, therefore the simplified models applied may end up contributing the similar amount of distortion in the computation than empirically derived higher-level models would.

## 4 Stochastic Modeling of Complex System Noise

A serious limitation of the above described methods is that most of them do not deal with the orientation error at a target, and does not provide any information about the error distribution. Throughout the article it is assumed that errors or accuracies have Gaussian distribution, which is in some cases not valid. Originally, the concept of coordinate frame registration handled accuracy as a norm of the deviation in  $x$ ,  $y$ ,  $z$  from the target point—entirely disregarding the orientation uncertainty. In several applications, such as an IG interventional robot applying virtual spatial constraints (such as Virtual Fixtures – VF), it is critical to consider rotational errors as well. The orientation error is considered only from the point of forbidden regions, not including the required accuracy of the approach direction (i.e., the surgical technique).

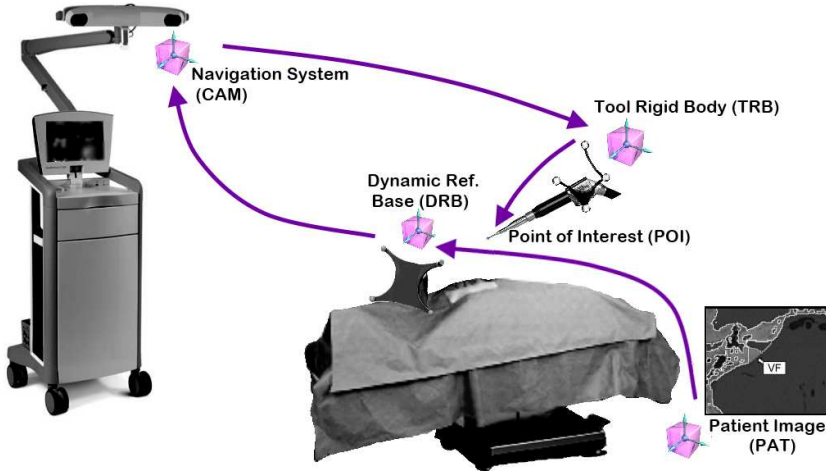


Figure 3

Basic setup of IGS procedures, showing the different coordinate frames used in control to determine the tool's position relative to the pre-operative image.

## 4.1 Theory of Complex Errors

Let us consider a system where the Point of Interest is tracked with an intra-operative navigation system (with any modality). The Dynamic Reference Base is rigidly attached to the patient, and registered to the pre-operative image through any registrational method, with a known angular and translational residual error. The markers (enabling tracking) on the tool are determining a certain coordinate frame—Tool Rigid Body—that is connected to the POI through another transformation acquired from e.g., a pivot calibration, again with known error statistics. The goal is to transform the spatial constraints (e.g., Virtual Fixture) defined in the registered pre-operative image space to the POI in real/time by the set of homogeneous transformations. Let us note that in the case of a typical robotic IGS system the POI corresponds to the Tool Center Point. Fig. 3 shows the general arrangement of the setup. VF defined in the PAT frame can be acquired in the POI frame using the following chain of homogeneous transformations:

$${}_{\text{POI}}^{\text{PAT}}\mathbf{T} = {}_{\text{POI}}^{\text{TRB}}\mathbf{T} \cdot {}_{\text{TRB}}^{\text{CAM}}\mathbf{T} \cdot {}_{\text{CAM}}^{\text{DRB}}\mathbf{T} \cdot {}_{\text{DRB}}^{\text{PAT}}\mathbf{T}. \quad (22)$$

It is typically assumed that all terms have known Gaussian distribution, therefore the probability distribution of the POI is anisotropic Gaussian with density function  $f(\cdot)$  [14]. The overall transformation can be expressed as the function of the ideal and noise terms:

$${}_{\text{POI}}^{\text{PAT}}\mathbf{T} = f(\mathbf{t}) + f(\Delta\mathbf{t}), \quad (23)$$

and it is necessary to express  $f(\Delta\mathbf{t})$  for the setup in a simple and effective way. The VF can be described with a convex hull [38], and the probability  $\mathbf{P}(\text{POI} \notin \text{VF})$  that the POI is in the forbidden region can be analytically calculated as:

$$\mathbf{P}(\text{POI} \notin \text{VF}) = \int_{\mathbf{t} \notin \text{VF}} f(\mathbf{t}) \, d\mathbf{t}. \quad (24)$$

It is possible to apply a stochastic approach through (24) to determine the location of the tooltip. This can be considered as the general extension of the approach proposed in [32]. Once we have the VF definitions transformed to the POI's coordinate system, we can derive the exact probability of the tool hitting the forbidden region. Current computational devices allow for the handling of these functions.

Similarly to  $\mathbf{P}(\text{POI} \notin \text{VF}_1)$ , let us denote by  $\mathbf{P}(\text{POI} \notin \text{VF}_2)$  the probability that the POI is deeply in the forbidden sector (beyond a given threshold). An  $\eta$  penalty function—to control the device delivering the treatment—can be built by arbitrary weighting coefficients or functions ( $\mathbf{w}$ ) tailored to the application. We can derive  $\eta$  by integrating the density function within the different VFs and scale it with  $\mathbf{w}$ . In a practical case, significant errors occurring with lower probability can be considered as:

$$\eta = w_1 \mathbf{P}(\text{POI} \notin \text{VF}_1) + w_2 \mathbf{P}(\text{POI} \notin \text{VF}_2), \quad (25)$$

where  $w_1 > w_2$ , if  $\text{VF}_1$  is more limiting than  $\text{VF}_2$ . The whole concept can be extended to incorporate more regions.

In addition, the angular distribution can also provide information about the probability that the POI is moving toward the VF. This is critical e.g., in automated bone drilling tasks. The exact calculation of the probability of the error gives a much stricter control over the motion of the tool, resulting in higher accuracy and safety.

An important feature of the proposed method is implicitly managing a previously challenging case: critical errors with low probability. With the help of differently chosen VF segments and  $\mathbf{w}$  factors, any complex constraint function can be built and applied to the IG system in real-time during the execution of the operation.

## 4.2 Deployment of the Concept

The above presented method has several advantages. It can be applied to IGS systems during the setup phase to verify the performance of the devices in the actual OR arrangement. The manufacturer should provide the generic accuracy numbers of the tracking device and the robot system or these can be acquired pre-operatively. This is especially useful in the case when pre-operatively defined control features are applied, such as Virtual Fixtures.

At the beginning of the surgical procedure, when the devices are roughly positioned around the patient, the simple reading of the actual position information can serve as the input for the simulation. The stochastic method provides the error distribution based on the Monte Carlo simulation in a very short time, and with that knowledge, the surgeon can decide to re-arrange the setup or proceed with the operation.

The algorithm can be extended to call for re-assessment if the devices are significantly relocated compared to the original location. (E.g., the camera is pulled to the opposite side of the room.) However, this seldom happens in the case of real surgeries, where the physicians typically follow a pre-defined protocol.

### 4.3 Simulation Results

Simulations were performed to verify the concept. An IG bone drilling setup has been simulated (based on Fig. 3) with the parameters of an anthropomorphic robotic arm and a typical OR setup with an optical navigation system. A simplified VF was used to protect a certain region of the patient, while the robot operates in the proximity of it. The actual parameters were chosen to mimic the NeuroMate (commercially available) robot from Renishaw (Wotton-under-Edge, UK), and the registrations were defined based on multiple dry-lab tests. The distribution of the POI's error was acquired with Monte Carlo simulation using 20,000 samples (Fig. 4 (a–h)). Numeric results were derived for test cases, where one VF was a 0.2 mm radius sphere and another was a 0.4 mm radius sphere (Fig. 5), corresponding to a very delicate operation, e.g., the acoustic nerve during a hemifacial spasm treatment via suboccipital approach, pedicle screw placement or laser osteotomy on the sternum. Results showed that the method was effective by providing the probabilities, and showed great flexibility in application. The reason for the extreme-scale anisotropy of the final distribution is the further displacement of the camera base, which is absolutely necessary in a real OR arrangement.

### 4.4 Error Modeling for Faster Surgical Execution

The main collateral advantage of the new approach is to allow for the a priori estimation of the POI's distribution. Based solely on the devices' known intrinsic accuracy parameters and the registration values (acquired before the surgical procedure) thorough error distribution estimation can be performed. Unless the OR setup changes, this simulation leads to better approximation of the surgical tool's position. With the known anisotropic Gaussian distribution, it is possible to determine which directions are more dangerous from the application point of view (where the STD is larger). The robot can be allowed to move faster towards directions with lower error distribution.

Fig. 6 shows the differences in the distribution of the POI along different axes. The ratio of the STDs along the principal axes can be tenfold, even with the original distributions being isotropic. Principal component analysis showed that two components account for 98% of the variance. This means that if the typical

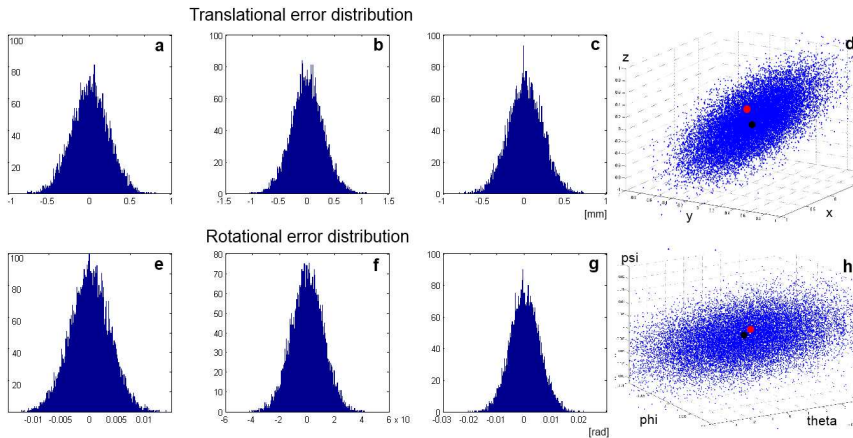


Figure 4

Distribution of the Point of Interest with a simulated IGS system. (a–c) Distribution of position (compared to the deterministic approach); [0.32, 0.28, 0.30] mm STD along  $x$ ,  $y$ ,  $z$ , respectively. (d) 3D plot of the translational error. Red dot shows the theoretical position, black dot represents the effect of the registrational errors, i.e., the position estimation according to the classical deterministic method. (e–g) [0.0023, 0.0027, 0.0051] rad STD rotation error around  $x$ ,  $y$ ,  $z$ , respectively. (h) 3D plot of the angular errors along [ $\phi$ ,  $\theta$ ,  $\psi$ ]

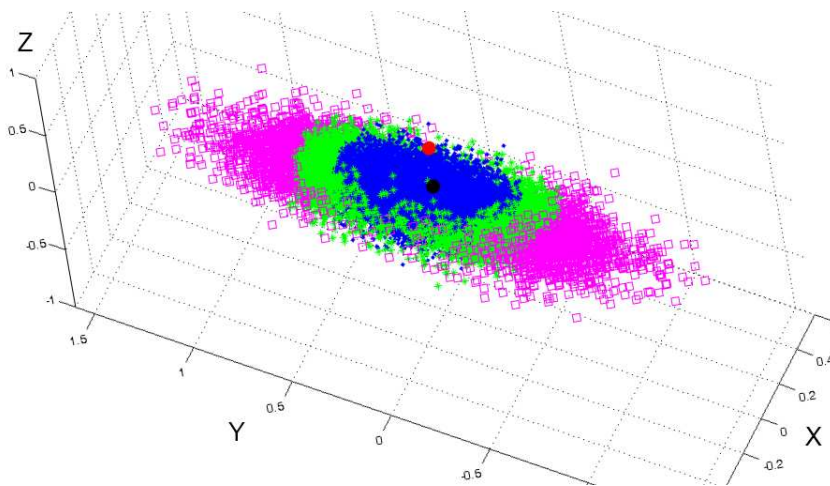


Figure 5

The POI (tooltip) transformed to the coordinate space of the patient. Green stars show where the overall RMSE error is larger than 0.2 mm and magenta squares mark the region where the error is over 0.4 mm. The exact probability of the POI being beyond the VF is 0.438 and 0.214 for the 0.2 and 0.4 mm VF, respectively. The red dot shows the theoretical position, the black dot represents the effect of the registration errors. The point-cloud is shown from an angle from where its anisotropic distribution is most apparent.

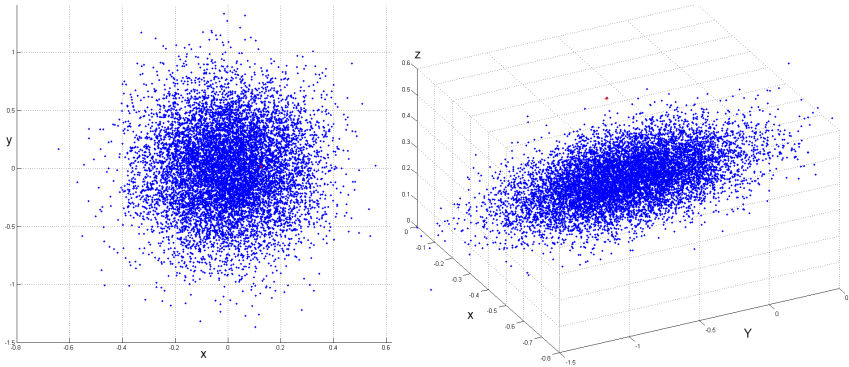


Figure 6

(a) The POI's position transformed to the coordinate space along axis  $z$ . (b) The distribution of the POI shows highly anisotropic distribution along axis  $x$ .

motion of the tool during the surgery is towards the directions with lower error distribution, the robot can speed up due to the lower error. Consequently, the optimal arrangement of the camera system can be given for each procedure, based on a pre-operative simulation and analysis.

## 5 Application to a Physical System

### 5.1 The JHU Image-Guided Neurosurgical System

A key aspect of these new techniques is to be applicable to existing systems, already deployed in ORs, or research laboratories. This requires delicate prototyping procedure and thorough testing on setups that well mimic the intended use.

We have developed the integrated surgical robotic system at the Johns Hopkins University (JHU, Baltimore, MD) to support skull base drilling. The system consists of a modified *NeuroMate* robot, a *StealthStation* (SS) surgical navigation device from Medtronic Navigation Inc. (Louisville, CO) and adequate network and control equipment (Fig. 7). The goal was to improve the safety and quality of neurosurgery while reducing the operating time. The robotized solution is only used for the removal of the bone tissue, to gain access to the anatomical region affected by a tumor or other lesions. Our technical approach was to use pre-operative imaging to identify the region of the skull base that could be safely drilled. We chose a cooperative control implementation (also called shared or compliant control), in which the surgeon applies forces to move the robot and the robot enforces the safety boundaries.

The JHU system has three major advantages. First, it offers advanced visualization features typical used in stereotactic surgery; the tool's position can be

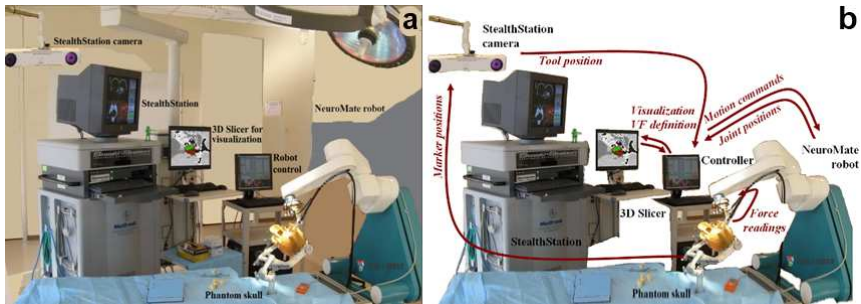


Figure 7

Hardware and software elements of the integrated neurosurgical system. (a) Physical arrangement of the devices.

(b) Major flow of information between the system components.

followed on the 3D model of the patient, acquired from pre-operative CT scans. Second, the surgical tool is mounted on the rigid robot, thereby improving its stability. The surgeons still hold the classic drill tool and directs its movement, but they can release the tool any time. Finally, the most important advantage—and the novelty of the application—is that the physician can define virtual boundaries on the CT scan prior to the operation. This is called *Virtual Fixture*, and once registered to the robot, it is strictly enforced, thus preventing the tip of the tool from going beyond the defined safe area.

## 5.2 JHU System Components

The system uses an FDA-approved *Medtronic StealthStation* for navigation. The SS is only capable of tracking two rigid bodies at a time (one reference frame—DRB and one tool—TRB), and there is an option to manually switch between different reference frames and tools.

We use three different rigid bodies in our setup (two at a time):

- a *Tool Rigid Body* is fixed on the robot's end-effector (therefore specifically we may call it *Robot Rigid Body*),
- one is connected to the patient (e.g., at a *Mayfield head clamp*).

These two rigid bodies allow us to determine the robot's position with respect to the skull. A third tool, a hand-held pointing probe is used to register the CT image coordinates (the patient anatomy) to the Patient Image.

The tool serving as the end-effector is an *Anspach eMax 2* high-speed instrument (The Anspach Effort Inc., Palm Beach Gardens, FL). The tool-holder (with reinforced bracket) is attached to the end of the NeuroMate through a force sensor, a 6 DOF sensor (JR3 Inc., Woodland, CA). The system further integrates the *3D Slicer* ([www.slicer.org](http://www.slicer.org)) software [39] for pre-operative planning and intra-operative visualization.

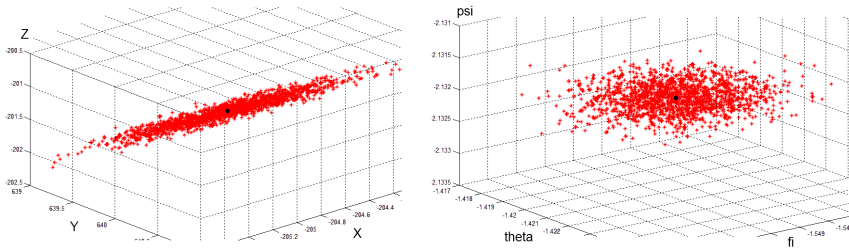


Figure 8

(a) The POI (tooltip) position transformed to the coordinate space of the patient on the real JHU setup. (b) The distribution of the rotation.

In the next step, I verified the concept on a real IG setup. The ongoing neurosurgical setup at JHU is a valid platform, complying with the standard description. While the previously presented error propagation approaches result in a moderately distorted POI distribution for a similar setup, in reality, measurements showed significant distortion of the error parameters for the actual robot tool. Fig. 8a shows the translational distribution, while Fig. 8b displays the angular distribution of the JHU system's drill. Principal component analysis showed that two components account for 99,7% of the variance in  $x$ ,  $y$ ,  $z$  directions and 98.6% of the rotations along  $x$ ,  $y$ ,  $z$  axes.

## Conclusion

Effective mapping of spatial error based on a priori information is necessary to support the operation of computer-integrated medical devices. This is also in line with the most recent patient safety requirements and surgical robot standards. Generalized error values and the experience of the medical staff determines the use of a system under different conditions. The major focus of this research was to improve the theoretical tools and practical means available for accuracy assessment of interventional image-guided systems. The classical approach to simple 3D error theory is not sophisticated enough to ensure the highest level of safety for many advanced surgical robotic systems. A new concept was proposed—stochastic approach to determine the 6 DOF error distribution of a generic surgical robotic system. The method is based on the direct handling of the error distribution function and forbidden regions defined as a Virtual Fixture, and can provide the actual distribution of errors at the tool right before the intervention begins. This allows for the optimal placement of the devices in order to reduce the overall effect of navigation and registration errors. Simulation results showed the applicability of the theory, and computations have also been performed for the JHU robot system, where the inhomogeneity of the distribution along different axes was shown to be over a hundred fold, therefore seriously limiting the performance of the system. The error propagation simulation can provide im-

portant data on the accuracy of any surgical setup that may help manufacturers giving recommendations for improved operating room setups.

## Acknowledgment

The author sincerely thanks the supporting work of Profs. Peter Kazanzides, Zoltán Benyó, Imre Rudas, József Sándor and Drs. Tian Xia, Sándor Győri. This work has been partially supported by ACMIT (Austrian Center for Medical Innovation and Technology), which is funded within the scope of the COMET (Competence Centers for Excellent Technologies) program of the Austrian Government. T. Haidegger is supported through the New National Excellence Program of the Ministry of Human Capacities. Partial support of this work comes from the Hungarian State and the European Union under the EFOP-3.6.1-16-2016-00010 project. T. Haidegger is a Bolyai Fellow of the Hungarian Academy of Sciences.

## References

- [1] A. Takács, D. Á. Nagy, I. Rudas, and T. Haidegger. Origins of surgical robotics: From space to the operating room. *Acta Polytechnica Hungarica*, 13(1):13–30, 2016.
- [2] K. H. Wong. Imaging Modalities. In *Lecture Notes in Computer Science (LNCS), Proc. of the 1<sup>st</sup> Intl. Conf. on Information Processing in Computer-Assisted Interventions (IPCAI)*, pages 241–273, Geneva, 2010.
- [3] J. Maintz and M. Viergever. A survey of medical image registration. *Medical Image Analysis*, 2(1):1–37, 1998.
- [4] Y. Chen, I. Godage, H. Su, A. Song, and H. Yu. Stereotactic systems for mri-guided neurosurgeries: A state-of-the-art review. *Annals of biomedical engineering*, pages 1–19, 2018.
- [5] C. Urban, P. Galambos, G. Györök, and T. Haidegger. Simulated medical ultrasound trainers a review of solutions and applications. *Acta Polytechnica Hungarica*, 15(7):111–133, 2018.
- [6] M. Hoeckelmann, I. J. Rudas, P. Fiorini, F. Kirchner, and T. Haidegger. Current capabilities and development potential in surgical robotics. *Intl. J. of Advanced Robotic Systems*, 12(5):61, 2015.
- [7] T. Haidegger. Autonomy for surgical robots: Concepts and paradigms. *IEEE Trans. on Medical Robotics and Bionics*, 1(2):65–76, 2019.
- [8] P. Grunert, K. Darabi, J. Espinosa, and R. Filippi. Computer-aided navigation in neurosurgery. *Neurosurgical Review*, 26(2):73–99, 2003.
- [9] P. Markelj, D. Tomaževič, B. Likar, and F. Pernuš. A review of 3d/2d registration methods for image-guided interventions. *Medical image analysis*, 16(3):642–661, 2012.

- [10] A. I. Károly, R. Fullér, and P. Galambos. Unsupervised clustering for deep learning: A tutorial survey. *Acta Polytechnica Hungarica*, 15(8):29–53, 2018.
- [11] D. Á. Nagy, I. J. Rudas, and T. Haidegger. Surgical data science, an emerging field of medicine. In *Neumann Colloquium (NC), 2017 IEEE 30th*, pages 000059–000064. IEEE, 2017.
- [12] B. Gibaud, G. Forestier, C. Feldmann, G. Ferrigno, P. Gonçalves, T. Haidegger, C. Julliard, D. Katić, H. Kenngott, L. Maier-Hein, et al. Toward a standard ontology of surgical process models. *International journal of computer assisted radiology and surgery*, 13(9):1397–1408, 2018.
- [13] T. Jacobs, J. Veneman, G. S. Virk, and T. Haidegger. The flourishing landscape of robot standardization [industrial activities]. *IEEE Robotics & Automation Magazine*, 25(1):8–15, 2018.
- [14] T. Haidegger, S. Győri, B. Benyó, and Z. Benyó. Stochastic approach to error estimation for image-guided robotic systems. In *Engineering in Medicine and Biology Society (EMBC), 2010 Annual International Conference of the IEEE*, pages 984–987. IEEE, 2010.
- [15] T. Haidegger, P. Kazanzides, B. Benyó, L. Kovács, and Z. Benyó. Surgical case identification for an image-guided interventional system. In *Proc. of the IEEE/RSJ Intl. Conf. on Intelligent Robots and Systems (IROS)*, Taipei, 2010.
- [16] T. Haidegger, P. Kazanzides, I. Rudas, B. Benyó, and Z. Benyó. The importance of accuracy measurement standards for computer-integrated interventional systems. In *EURON GEM Sig Workshop on The Role of Experiments in Robotics Research at IEEE ICRA*, pages 1–6, 2010.
- [17] D. Y. Hsu. *Spatial Error Analysis*. Wiley–IEEE, New York, NY, 1998.
- [18] C. R. Maurer, J. M. Fitzpatrick, M. Y. Wang, R. L. Galloway, R. J. Maciunas, and G. S. Allen. Registration of head volume images using implantable fiducial markers. *IEEE Trans. on Medical Imaging*, 16(4):447–462, 1997.
- [19] J. M. Fitzpatrick, J. B. West, and C. R. Maurer. Predicting Error in Rigid-Body Point-Based Registration. *IEEE Trans. on Medical Imaging*, 17(5):694–702, 1998.
- [20] J. M. Fitzpatrick. Fiducial registration error and target registration error are uncorrelated. In *Proc. of SPIE Medical Imaging*, volume 7261, pages 1–12, Orlando, FL, 2009.
- [21] A. Danilchenko and J. M. Fitzpatrick. General approach to error prediction in point registration. In *Proc. of SPIE Medical Imaging*, volume 7625–0F, pages 1–14, San Diego, CA, 2010.
- [22] T. Haidegger. *Theory and method to enhance computer-integrated surgical systems*. PhD thesis, in electrical engineering, 2011.
- [23] T. Haidegger, P. Kazanzides, I. Rudas, B. Benyó, and Z. Benyó. The Importance of Accuracy Measurement Standards for Computer-Integrated Interventional Systems. In *Proc. of the EURON GEM Sig Workshop on The Role of Experiments in Robotics Research at IEEE ICRA*, pages 19–24, Anchorage, AK, 2010.

- [24] G. Widmann, R. Stoffner, M. Sieb, and R. Bale. Target registration and target positioning errors in computer-assisted neurosurgery. *Intl. J. of Medical Robotics and Computer Assisted Surgery*, 5(4):355–365, 2009.
- [25] J. M. Fitzpatrick. The role of registration in accurate surgical guidance. *Proc. of the Institution of Mechanical Engineers, Part H: J. of Engineering in Medicine*, 224(5):607–622, 2010.
- [26] D. M. Kwartowitz, S. D. Herrell, and R. L. Galloway. Toward image-guided robotic surgery: determining intrinsic accuracy of the da Vinci robot. *Intl. J. of Computer Assisted Radiology and Surgery*, 1(3):157–165, 2006.
- [27] M. Kuhn, M. Jablonowski, P. Gieles, M. Fuchs, and H.-A. Wischmann. A Unifying Framework for Accuracy Analysis in Image-Guided Surgery. In *Proc. of the Annual Intl. Conf. of the IEEE Engineering in Medicine and Biology Society (EMBC)*, pages 238–240, Amsterdam, 1996.
- [28] R. H. Taylor and P. Kazanzides. Medical Robotics and Computer-Integrated Interventional Medicine. *Advances in Computers: Emerging Technologies*, 73:219–258, 2008.
- [29] M. H. Moghari, B. Ma, and P. Abolmaesumi. A theoretical comparison of different target registration error estimators. In *Lecture Notes in Computer Science (LNCS), Proc. of the Annual Conf. of the Medical Image Computing and Computer Assisted Intervention Society (MICCAI)*, volume 5424, pages 1032–1040, New York, NY, 2008.
- [30] M. H. Moghari and P. Abolmaesumi. A high-order solution for the distribution of target registration error in rigid-body point-based registration. In *Lecture Notes in Computer Science (LNCS), Proc. of the Annual Conf. of the Medical Image Computing and Computer Assisted Intervention Society (MICCAI)*, volume 9, pages 603–611, Kobenhavn, 2006.
- [31] W. Zylka, J. Sabczynski, and G. Schmitz. A Gaussian approach for the calculation of the accuracy of stereotactic frame systems. *J. Medical Physics*, 26(3):381–392, 1999.
- [32] A. D. Wiles, D. G. Thompsona, and D. D. Frantz. Accuracy assessment and interpretation for optical tracking systems. In *Proc. of SPIE Medical Imaging*, volume 5367, pages 421–432, San Diego, CA, 2004.
- [33] R. Khadem, C. C. Yeh, M. Sadeghi-tehrani, M. R. Bax, J. A. Johnson, J. N. Welch, E. P. Wilkinson, and R. Shahidi. Comparative tracking error analysis of five different optical tracking systems. *Computer Aided Surgery*, 5(2):98–107, 2000.
- [34] B. Allen and G. Welch. A general method for comparing the expected performance of tracking and motion capture systems. In *Proc. of the ACM Symp. on VR Software and Technology*, pages 210–220, Monterey, CA, 2005.
- [35] W. Hoff and T. Vincent. Analysis of Head Pose Accuracy in Augmented Reality. *IEEE Trans. on Visualization and Computer Graphics*, 6(4):319–334, 2000.
- [36] T. Sielhorst, M. Bauer, O. Wenisch, G. Klinker, and N. Navab. Online Estimation of the Target Registration Error for n-Ocular Optical Tracking Systems. In *Lecture Notes in Computer Science (LNCS), Proc. of the Annual*

- Conf. of the Medical Image Computing and Computer Assisted Intervention Society (MICCAI)*, volume 4792, pages 652–659, Brisbane, 2007.
- [37] M. Bauer, M. Schlegel, D. Pustka, N. Navab, and G. Klinker. Predicting and estimating the accuracy of n-ocular optical tracking systems. In *Proc. of the 5<sup>th</sup> IEEE/ACM Intl. Symp. on Mixed and Augmented Reality (ISMAR)*, pages 43–51, Santa Barbara, 2006.
- [38] T. Xia, C. Baird, G. Jallo, K. Hayes, N. Nakajima, N. Hata, and P. Kazanzides. An integrated system for planning, navigation and robotic assistance for skull base surgery. *Intl. J. of Medical Robotics and Computer Assisted Surgery*, 4(4):321–330, 2008.
- [39] S. Pieper, M. Halle, and R. Kikinis. 3D Slicer. In *IEEE Intl. Symp. on Biomedical Imaging*, pages 632–635, Arlington, VA, 2004.

# Robot-Assisted Minimally Invasive Surgical Skill Assessment—Manual and Automated Platforms

Renáta Nagyné Elek<sup>1</sup> and Tamás Haidegger<sup>1,2</sup>

<sup>1</sup> Antal Bejczy Center for Intelligent Robotics, University Research, Innovation and Service Center, Óbuda University, Bécsi út 96/b, 1034 Budapest, Hungary, renata.elek@irob.uni-obuda.hu

<sup>2</sup> Austrian Center for Medical Innovation and Technology, Viktor Kaplan-Straße 2/1, 2700 Wiener Neustadt, Austria, haidegger@irob.uni-obuda.hu

---

*Abstract:* The practice of Robot-Assisted Minimally Invasive Surgery (RAMIS) requires extensive skills from the human surgeons due to the special input device control, such as moving the surgical instruments, use of buttons, knobs, foot pedals and so. The global popularity of RAMIS created the need to objectively assess surgical skills, not just for quality assurance reasons, but for training feedback as well. Nowadays, there is still no routine surgical skill assessment happening during RAMIS training and education in the clinical practice. In this paper, a review of the manual and automated RAMIS skill assessment techniques is provided, focusing on their general applicability, robustness and clinical relevance.

*Keywords:* Robot-Assisted Minimally Invasive Surgery; surgical robotics; surgical skill training; surgical skill assessment

---

## 1 Introduction

Minimally Invasive Surgery (MIS) has shown to improve the outcome of specific types of surgeries, due to fact that the operator reaches the organs in interest through small skin incisions. This results in less pain, quicker recovery time and smaller scars on the patient. While the benefits of MIS for the patient are clear, this technique is definitely hard to master for the clinician. To perform traditional MIS, surgeons have to learn the handling of the specific surgical instruments, the manipulation of the endoscopic camera (or coordination on that with the assistance), they have to operate in ergonomically sub-optimal postures [1–4].

To answer these challenges, the concept of Robot-Assisted Minimally Invasive Surgery (RAMIS) was introduced almost four decades ago. To increase ergonomics, robotic systems typically offer a 3D vision system, and their instruments are easier to control than traditional MIS tools. Furthermore, due to the instruments' rescaled movements or special design, RAMIS can be more accurate than

traditional MIS. During the relatively short history of RAMIS, da Vinci Surgical System (Intuitive Surgical Inc., Sunnyvale, CA) emerged to be the dominating surgical robot on the market. The da Vinci is a teleoperated system, where the surgeon sits at a master console, and the patient-side robot copies the motions of the surgeon within the patient. There are more than 5500 da Vinci Surgical System in clinical practice at the moment, and around a million procedures performed in the world yearly [3, 5].

While the development of RAMIS was a bold step forward in modern medicine to help surgeons to realize MIS, it is still a complicated, evolving technique to learn. In the early years, there has been strong criticism that the da Vinci is not providing the overall benefit, claimed [6–8]. The lack of training of robotic surgeons had a great impact in this opinion. Intuitive and the whole research community developed new training platforms to answer these challenges. These have become the first authentic source of data to develop and validate skill assessment methods.

In the research of RAMIS skill assessment, da Vinci Application Programming Interface (da Vinci API, Intuitive Surgical Inc.) was the first source of surgical data, but it was read-only and not accessible widely. With the development of the da Vinci Research Kit (DVRK), the data collection from the da Vinci Surgical System became available for the researchers as well [9]. More recently, Intuitive teamed up with InTouch Health to create a safe telecommunication network for its robot fleet deployed at US hospitals [10]. They extended the cooperation under the concept of Internet of Medical Things [11]. With this collaboration Intuitive is creating the technical possibility to see and assess the performance of its robots and their users.

RAMIS can be learned by surgeons, which process is often represented by learning curves. Learning curve is a graph, where the experience is represented graphically (e.g., time to complete compared to training times). Basically, there are two main approaches of surgical robotics training: patient side and master console training. Patient side training contains the patient positioning and port placement and basic laparoscopic skills (such as creation of pneumoperitoneum, application of clips etc.). Console training involves the handling of the master arms, the camera and the pedals, and cognitive tasks as well. There are lots of console training methods for RAMIS, which can provide the required practice for the surgeon [12]:

- virtual reality simulators;
- dry lab training;
- wet lab training;
- training in the operating room with a mentor.

Each has its own advantage and disadvantage, but from the clinical applicability point of view, the most important question is how fairly do these assess surgical skills. Nowadays, there is still no objective surgical skill assessment method used in the operating room (OR) beyond board examination more experienced

surgeons may provide some feedback, but rarely quantify the skills of their colleagues.

It may be important to evaluate surgical skills for quality assurance reasons, when that becomes part of the hospital's quality management system. More commonly, only the proof of participation at theoretical and practical training is required. Arguably, objective feedback could assist trainees and practicing surgeons as well in improving their skills along the carrier. The fundamental challenge with skill assessment is that traditionally, the patient outcome used to be the only objective metric, and given the amazing variety and individual characteristic of each procedure, it has been really hard to derive distinguishing skill parameters. The subjective evaluation provided by other experts did not make it easy to compare results and metrics, therefore more generally agreed, standardized evaluation practices and training platforms had to be developed. A good example for this is the Fundamentals of Laparoscopic Surgery (FLS), a training and assessment method developed by the Society of American Gastrointestinal and Endoscopic Surgeons (SAGES) in 1997, and widely adapted: it measures the manual skills and dexterity of an MIS surgeon, and provides a comparable scoring [13]. A similar metric for RAMIS surgeons recently introduced, called Fundamentals of Robotic Surgery (FRS) [14].

In general, to understand the notions of 'skill' and 'skill assessment', let us consider the Dreyfus model [15]. The Dreyfus model refers to the evolution of the learning process, and it describes the typical features of the expertise levels at various phases (Fig. 1). For example, a novice (in general) can only follow simple instructions, but an expert can well react to previously unseen situations. In the literature, we can find other skill models, such as the classic Rasmussen model, which was created for modeling skill-, rule-, and knowledge-based performance levels [16]. An other approach for modeling skills is recently created by Azari et al., which is specifically made for surgical skills (Fig.2) [17]. RAMIS provides a unique platform to measure parameters which can help us in defining these skill levels objectively, since it makes low level motion data and spatial information available. Now, the problem is to find the proper parameters and algorithms that define the surgical skills [18].

In this paper, we review the main approaches to RAMIS skill assessment from manual to fully automated, focusing on the platforms aiming to achieve wider acceptance. Beyond the technical RAMIS skill assessment, we collect the existing approaches to non-technical RAMIS skill assessment as well. The main techniques employed are presented in every cited case, along with the estimated impact of them.

## 2 Methods

To find relevant publications in the field of manual and automated skill assessment in RAMIS, we used PubMed and Google Scholar databases. The last search performed on December in 2018. This paper is mainly focusing on automated ap-

Mental Function \ SKILL LEVEL	NOVICE	COMPETENT	PROFICIENT	EXPERT	MASTER
	Recollection	Non-situational	Situational	Situational	Situational
Recognition	Decomposed	Decomposed	Holistic	Holistic	Holistic
Decision	Analytical	Analytical	Analytical	Intuitive	Intuitive
Awareness	Monitoring	Monitoring	Monitoring	Monitoring	Absorbed

Figure 1

Dreyfus model of skill acquisition. It defines 5 expertise levels and shows the differences between their qualities [19]

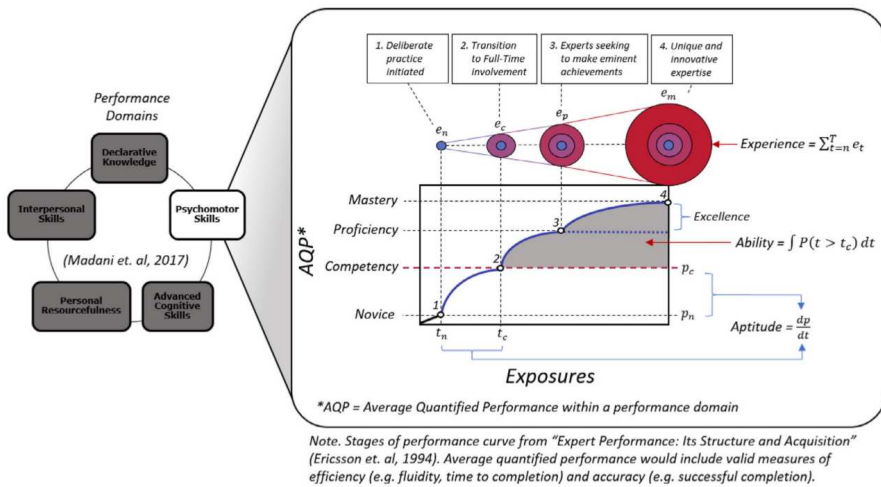


Figure 2

Quantified performance model for surgical skill performance. The model describes the terms of 'skill': experience, excellence, ability and aptitude [17]

proaches, thus training systems and manual techniques are only introduced. To find relevant publications for manual techniques, we used the keywords 'surgical robotics' and 'manual skill assessment' or 'manual skill evaluation'. From the identified publications, we chose 23 based on the relevance and citation index. In the case of virtual reality simulators, we use the keywords 'surgical robotics' and 'virtual reality' and 'training' or 'simulator'. We chose 8 publications to introduce this topic. To find publications for automated approaches and data collection, we used the keywords 'surgical robotics' and 'automated' and 'skill assessment' or 'skill evaluation', or in case of data collection 'surgical robotics' and 'data collection'. We found 47 relevant publications, and the automated techniques are summarized in Table 1. The table has the following columns:

- 'Aim': summarizes the goals of the cited paper;
- 'Input data': used type of data for the skill assessment; algorithm
- 'Data collection': sensor type, data collector device;
- 'Training task': suturing, knot-tying, etc.;
- 'Technique': used algorithms;

and the year of the publication with the reference. Finally, we introduce non-technical skill assessment techniques. For this, we used 12 relevant publications based on the keywords 'surgical robotics' and 'non-technical skill', or 'physiological symptoms' and 'stress'.

### 3 Manual assessment

In the case of manual RAMIS skill assessment, just like with traditional MIS, a team of expert surgeons in the OR (or post-operatively) evaluates the execution of the intervention based on their knowledge, the specific OR workflow and the expected outcome. This approach is easy to implement, yet very costly (in terms of human resource effort). It may be accurate averaged over multiple reviewers, but each individual assessment is quite subjective across boards, and it may be heavily distorted by personal opinions and influenced by the level of expertise of that particular domain. The types of objective manual surgical skill evaluation in the case of RAMIS are *generic*, *procedure-specific* and *error-based* [20]. The simplest approach is the error-based manual assessment, because it only requires a typical error detection during the procedures. Procedure specific techniques examine the skills what needed in specific interventions. Generic manual skill assessment is the most complex approach; it evaluate the global skills of the surgeons.

A typical approach of manual RAMIS skill assessment is not to quantify the overall skills, just to evaluate particular skills needed in specific procedures, or only measure the errors made during the execution. In many cases, procedure-specific assessment is required, where the assessment metric is created for a specific surgical procedure (such as cholecystectomy, radical prostatectomy, etc.). Prostatectomy Assessment and Competence Evaluation (PACE) scoring is created for robot-assisted radical prostatectomy skill assessment. PACE metric includes the following evaluation points [21]:

- bladder drop;
- preparation of the prostate;
- bladder neck dissection;
- dissection of the seminal vesicles;
- preparation of the neuro-vascular bundle;

- apical dissection, anastomosis.

Cystectomy Assessment and Surgical Evaluation (CASE) is for robot-assisted radical cystectomy procedures. CASE evaluates the skills based on eight main domains [22]:

- pelvic lymph node dissection;
- development of the peri-ureteral space;
- lateral pelvic space;
- anterior rectal space;
- control of the vascular pedicle;
- anterior vesical space;
- control of the dorsal venous complex;
- apical dissection.

In the case of PACE and CASE, surgical proficiency was represented in every domain on a 5-point Likert scale, where 1 means the lowest and 5 means the highest performance (the score meaning is defined in every domain, such as injuries). Beyond these two specific methods, we can find further scoring metrics for other interventions in the literature [23, 24].

For the above scoring methods refer to the execution of the procedure. In most of the cases, any damage caused reflects the skills of the surgeons retrospectively: such as blood loss, tissue damage, etc. Generic Error Rating Tool (GERT) is a framework to measure technical errors during MIS; it was specifically created for gynecologic laparoscopy [25]. The validation tests showed promising results for the usability of GERT for objective skill assessment (its correlation to OSATS was examined) [26].

Generic manual assessment techniques evaluate the skills, based on the whole procedure/training technique, considering several points of the surgery, but not considering a specific technique. Global Evaluative Assessment of Robotic Skills (GEARS) was particularly created for robotic surgery, where expert surgeons assess the operator's robotic surgical skills manually. GEARS metric involves the assessment of the followings [12]:

- depth perception (from overshooting target to accurate directions to the right plane);
- bimanual dexterity (one from hand usage to using both hands in a complementary way);
- efficiency (from inefficient efforts to fluid and efficient progression);
- force sensitivity (from injuring nearby structures to negligible injuries);
- robotic control skills (based on camera and hand positions).

The surgical experts score the performance on a five scale score system. GEARS is a well-studied metric: we can find validity tests and comparisons with GEARS in the literature [12, 27–37]. The original paper of GEARS showed results for the clinical usability (the experts' scores were significantly higher than novice surgeons' based on 29 subjects), and later publications provided construct validity as well.

There exist several modifications to the basic scoring skill assessment techniques. Takeshita et al. specified GEARS for endoluminal surgical platforms, called 'Global Evaluative Assessment of Robotic Skills in Endoscopy' (GEARS-E) [38]. GEARS-E is similar to GEARS, it measures depth perception, bimanual dexterity, efficiency, tissue handling, autonomy and endoscope control, but it was created for Master and Slave Transluminal Endoscopic Robot (MASTER) surgeries. GEARS-E is not yet widespread because it was developed in 2018, but the pilot study showed correlations to surgical expertise when using the MASTER.

Objective Structured Assessment of Technical Skills (OSATS) was originally created for evaluating traditional MIS skills along with FLS in 1997. OSATS involves the following evaluation points [39, 40]:

- respect for tissue (used forces, caused damage);
- time and motion (efficiency of time and motion);
- instrument handling (movements fluidity);
- knowledge of instruments (types and names);
- flow of operations (stops frequency);
- use of assistants (proper strategy);
- knowledge of specific procedure (familiarity of the aspect of the operation).

OSATS has an adaptation to robotic surgery: the Robotic Objective Structured Assessments of Technical Skills (R-OSATS) [41, 42]. R-OSATS metric evaluate the skills of the surgeon based on the depth perception/accuracy, force/tissue handling, dexterity and efficiency. R-OSATS was tested typically with gynecology students, it has construct validity, and in the tests, both the interrater and intrarater reliability were high [43].

## 4 Virtual Reality simulators

While Virtual Reality (VR) surgical robot simulators primarily support training, they can also be a great tool to measure surgical skills objectively in a well-defined environment, since all motions, contacts, errors, etc. can be computed in the VR environment. A typical RAMIS simulator involves a master side construction and the virtual surgical task simulation. The master side is responsible

for to study the usage of a teleoperation system (master arm handling, foot pedals, etc.), and to test the ergonomics. The simulation of the surgical task in case of a surgical robot simulator has to look life-like and be clinically relevant. During the training, the VR simulators often estimate the skills based on manual skill assessment techniques (such as OSATS), but in an automated way.

Since the da Vinci is dominating the global market, VR simulators are also focusing on da Vinci surgery. There are more than 2000 da Vinci simulators at the customer sites around the globe [44]. At the moment, there are six commercially available da Vinci surgical robot simulators: the da Vinci Skills Simulator (dVSS, Intuitive Surgical Inc.), dV-Trainer (Mimic Technologies Inc., Seattle, WA), Robotic Surgery Simulator (RoSS, Simulated Surgical Sciences LLC, Buffalo, NY), SEP Robot (SimSurgery, Norway), Robotix Mentor (3D systems (formerly Symbionix), Israel) and the Actaeon Robotic Surgery Training Console (BBZ Srl, University of Verona [45]). A novel surgical simulation program is the SimNow by da Vinci (Intuitive Surgical Inc.) [46]. SimNow involves surgical training using virtual instruments, guided and freehand procedure simulations and tracking skills and optimizing learning with management tools. In this section, the three most common types of VR simulators are reviewed: the DVSS, the dV-Trainer and the RoSS (Fig. 3).

DVSS can be attached to an actual da Vinci (da Vinci Xi, X or Si), with the main benefit that the surgeon can train on the actual robotic hardware, yet, it poses logistical problems, since while a trainee uses the simulator, the robot cannot be used for surgery. The dVSS contains the following surgical training categories [47]:

- EndoWrist manipulation;
- camera and clutching;
- energy and dissection;
- needle control;
- needle driving;
- suturing;
- additional games.

The dVSS measures the skills based on the economy of motion, time to complete, instrument collisions, master workspace range, critical errors, instruments out of view, excessive force applied, missed targets drops, misapplied energy time. The simulator costs about \$85000–585000 (the extra \$500000 is for the console) [47–52].

The dV-Trainer emulates the da Vinci master console, thus it operates separated from the actual da Vinci robot. It contains additional training exercises to the dVSS [47]:

- troubleshooting;

- Research Training Network (virtual reality exercises to match physical devices in use by the research training network);
- Maestro AR (augmented reality; exercises that allow 3D interactions).

The dV-Trainer assesses skill with a very similar metric to the dVSS. In newer dV-Trainer versions, an alternative scoring system is available, called 'Proficiency Based System', which based on expert surgeon data, and the interpretation of the data is different, furthermore the user can customize the protocol. The dV-Trainer costs about \$96000.

RoSS (as the dV-Trainer) is a stand-alone da Vinci simulator involving numerous modules:

- orientation module;
- motor skills module;
- basic surgical skills module;
- intermediate surgical skills module;
- blunt dissection and vessel dissection;
- hands-on surgical training module.

RoSS assesses the skills of the surgeon based on the camera usage, the number of left and right tool grasps, the distance while the left and right tool was out of view, the number of errors (collision or drop), the time to complete the task, the collisions of tools and tissue damage. RoSS costs about \$126000.

In the literature, most papers dealing with surgical robot simulators are focused on the curriculum and the technical layout, yet, in this paper, the skill assessment and scoring part is crucial.

## 5 Automated assessment

Surgical robotics provides a unique platform to evaluate surgical skills automatically. RAMIS automated skill assessment does not need additional sensors to examine the surgeon's movements, camera handling, focusing on the image etc., because these events/errors/movements can be recorded straight with the robotic system. Automated assessment can be a powerful tool to evaluate surgical skills due to its objectivity, furthermore it does not require human resources, however, in some cases, it can be hard to implement these.

Two main types of automated skill assessment methods can be recognizable in the literature: *global information-based* and *language model-based* skill assessment. Global information-based automated skill assessment means that the surgical skill is evaluated based on the whole procedure, based on the data of the endoscopic video, kinematic data, or other additional sensor data. The other approach is to evaluate skills on the subtask level, called language-model based



Figure 3

Virtual reality simulators for the da Vinci Surgical System [47, 53, 54]. A) da Vinci Skills Simulator, b) dV-Trainer, c) Robotic Surgery Simulator, d) Robotix Mentor, e) SEP Robot, f) Actaeon Robotic Surgery Training Console

skill assessment. Here, the first challenge is to recognize the surgical subtasks (often called 'surgemes'), then create a model for the procedure, and compare the models for skill assessment. Global skill assessment is easier to implement compared to language model-based techniques, but language models can be more accurate, and they are closer to the natural training (an expert will teach to the novice what was wrong on the subtask level, such as the way to hold the needle in a suturing task).

## 5.1 Data collection for automated assessment

The development of automated RAMIS skill assessment methods requires solutions for surgical data collection. The data - which correlates the surgical skills - can be kinematic, video or additional sensor-based (e.g. force sensor). It is not trivial to access even to training data from RAMIS platforms. The da Vinci has a read-only research API (da Vinci Application Programmer's Interface, Intuitive Surgical Inc.), but it is only accessible to a very few chosen groups. The da Vinci API provides a robust motion data set and it can stream the motion vectors, including joint angles, Cartesian position and velocity, gripper angle, joint velocity and torque data from the master side of the da Vinci, furthermore events such as instrument changes [55].

To collect kinematic and sensory data from the da Vinci for research usage, the



Figure 4

JIGSAWS surgical tasks: knot-tying, suturing and needle passing (captured from the video dataset)

da Vinci Research Kit (DVRK) is a more accessible tool. The DVRK (developed by a consortium led by Johns Hopkins University and Worcester Polytechnic Institute) is a research platform containing a set of open source software and hardware elements, providing complete read and write access to the first generation da Vinci [9]. DVRK is programmable via Robot Operating System (ROS) open source library [56]. The DVRK community is relatively small, but growing with only 35 DVRK sites [57].

While most of the da Vinci's have remote access and data storing enabled, due to legal and liability causes, clinical datasets are not available widely. In this case, annotated databases can provide input to RAMIS skill evaluation research. JHU–ISI Gesture and Skill Assessment Working Set (JIGSAWS) (developed by the LCSR lab at Hopkins and Intuitive) is an annotated database for surgical skill assessment, collected over training sessions [58]. JIGSAWS contains kinematic data (Cartesian positions, orientations, velocities, angular velocities and gripper angle of the manipulators) and stereoscopic video data captured during dry lab training (suturing, knot-tying and needle-passing). The dataset recorded on a da Vinci involving surgeons with different expertise level (based on a manual evaluation technique). Beyond the manual skill annotations, JIGSAWS also includes annotations about the gestures ('surgemes').

Another approach is to capture surgical data with an additional data collecting device. A novel approach for da Vinci data collection, the dVLogger was developed in 2018 by Intuitive Surgical Inc. The dVLogger directly captures surgeons motion data on the da Vinci Surgical System. DVLogger can be easily connected to the da Vinci's vision tower with ethernet connection, and it records the data at 50 Hz. DVLogger provides the following informations from the da Vinci [59]:

- kinematic data (such as instrument travel time, path length, velocity);
- system events (frequency of master controller clutch use, camera movements, third arm swap, energy use);
- endoscopic video data.

DVLogger can be a powerful tool in surgical skill assessment studies, due to its easy usage enables the data collection for everyone, during live surgeries as well,

however, it is a novel recording device, thus it is not well-known widely yet.

SurgTrak (created by the University of Minnesota and University of Washington) is an additional hardware and software set which can be used for the da Vinci as well [60, 61]. With SurgTrak, the endoscopic data can be captured from the DVI output of the da Vinci master side with an Epiphan DVI2USB device. The surgical instruments' position and orientation can be recorded with a 3D Guidance trakSTAR magnetic tracking system. Furthermore, grasper and wrist position is achievable with SurgTrak.

The above data collection techniques are useful for capturing kinematic and video data, but in some cases other devices/sensors are needed to evaluate surgical skills with specific algorithms. Force sensors are often used in the field of surgical skill assessment. It is possible to estimate the used forces during the training based on the motor currents, but due to the construction of the da Vinci, it can be very noisy. A more popular approach is when an additional force sensor is used, such as developed in U. Pennsylvania in [62]. In this case, accelerometers were placed on the da Vinci arms (which measured instrument vibrations), and a training board with a force sensor, which measured the forces during different types of training. They showed correlation between the measured data and the skill level.

## 5.2 Global information-based skill assessment

One approach for automated RAMIS skill assessment is to examine the whole procedure based on kinematic/video/additional sensor data. These methods are easier to implement than language model-based techniques, because they do not require the segmentation of the whole procedure (see details below). While global information-based methods are not sensitive to the performance quality of specific gestures, they can be as effective as language model-based techniques. There is an obvious correlation between the surgical skills and the kinematic data (Fig. 5), thus this is the most well-studied area in global information-based skill assessment [63–72], but we can find video, additional sensor-based [62, 73, 74], and the comparisons of several inputs [55, 75] automated techniques as well. Global information-based skill assessment is not as deeply studied as language model-based methods, in general.

For the global methods, the classification of the input data is needed. We can find a great summary of these in [68] (Fig. 6). The raw data (which can be any kind of data: endoscopic image, force, kinematic, etc – in the figure you can find a specific example for kinematic-data based assessment) have to be processed with some kind of feature extraction technique, and in some cases, dimensionality reduction is needed as well. The processed data can be classified, and the skill can be predicted based on the extracted features from the data.

In [68], we can find a motion-based automated skill assessment. Their input was the JIGSAWS dataset. They used 4 types of kinematic holistic features: sequential motion texture, discrete Fourier transform, discrete cosine transform and approximate entropy. After the feature extraction and dimensionality reduc-

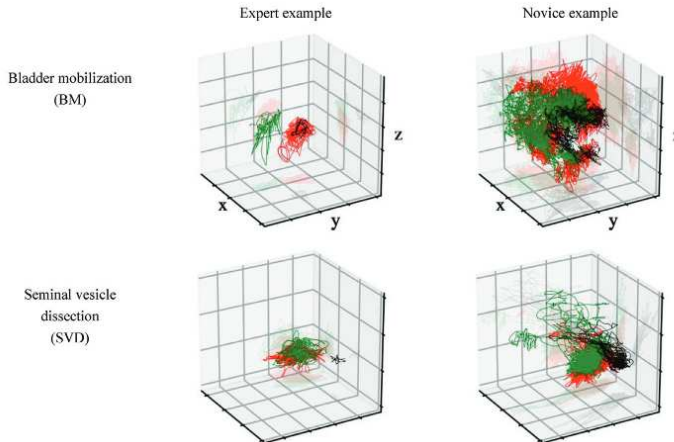


Figure 5

Robot trajectories in case of a novice and an expert surgeon during robot-assisted radical prostatectomy (red: dominant instrument, green: non-dominant instrument, black: camera) [59]



Figure 6

Flowdiagram for automated surgical skill assessment [68]

tion, they classified the data and predicted the skill score. The skill scoring was performed with a weighted holistic feature combination technique, which means that different prediction models were used to produce a final skill score. With this method a modified-OSATS score and a Global Rating Score was estimated. The results showed more accuracy than Hidden Markov Model-based solutions [68]. For more approaches, see Table 1.

### 5.3 Language model-based skill assessment

A surgical procedure model can be built with different motion granularity. A surgical procedure (such as *Laparoscopic cholecystectomy*) is built from tasks (e.g., *exposing Calot's triangle*), which is built from subtasks (e.g., *blunt dissection*), which is built from surgemes (*grasp*), which is built from dexemes (*motion primitives*) (Fig. 7). Global skill assessment methods approach the skill evaluation from the highest procedure/task level, thus not adverting the fact that surgical tasks are built from several, sometimes very different surgemes. These surgemes are not equally easy or complicated to execute, and even if a clinician believed

Level of granularity	Definition	Time span	Complexity	Example
Operation	The entire invasive part of the procedure.	20–200 min	very high	Laparoscopic cholecystectomy
Task	Well delimited surgical activity with a given high-level target/goal to achieve.	1–5 min	high	Pneumo-peritoneum → Exposing-Calot's triangle → ...
Subtask	Circumscribed activity segments that accomplish specific minor landmarks in completing the surgical task.	0.1–2 min	moderate	Retraction of the gallbladder → Blunt dissection at the Cystic duct → Blunt dissection at the Cystic art. → ...
Surge	An atomic unit of intentional surgical activity resulting in a perceivable and meaningful outcome.	0.1–0.5 min	low	Approach the tissue → Perform dissecting motion → ...
Motion primitive	General elements of motion patterns, that can be directly translated into robot commands.	1–5 sec	very low	Penetrate connective tissue → Open the dissector → Remove the dissector

Figure 7

A surgical procedure built from different levels [101]. Language model-based RAMIS skill assessment techniques typically evaluate the skills on the surge level.

to have intermediate skills based on a global skill assessment technique, he/she can be excellent/poor in just one, but very important surge and vice versa. Language model-based surgical skill assessment aims to assess surgical skills on the surge level, thus it requires three main steps: task segmentation, gesture recognition and gesture-based skill assessment. This approach has the further advantage that with the models defined, we can study the transitions between the surges, and benchmark those as well. This approach has been considered to be a cornerstone of the emerging field of Surgical Data Science (SDS) [76].

It was the Hopkins group who first proposed surge-based skill assessment [77], discrete Hidden Markov Models (HMM) were built for task and for surge level as well to assess skill. In the practice, skill evaluation was based on a model built from annotated data (known expertise level), and this model tested against the new user. To create a model for user motions, they had to identify the surges with feature extraction, dimensionality reduction and classifier representation techniques. After that, the two models were compared. To train the discrete HMMs they used vector quantization. Their method worked with 100% accuracy using task level models and known gesture segmentation, at 95% with task level models and unknown gesture segmentation, and at 100% with the surge level models in correctly identifying the skill level.

The input of language model-based skill assessment methods can be kinematic data [77–86], video data [87] or both [88–92]. In the literature, we can find surgical activity/workflow segmentation as well [93–100]. For the details of the state-of-the-art see Table 1.

## 6 Non-technical surgical skill assessment

Surgical robotic interventions can put extra cognitive load on the surgeon, especially in the case of risky, high-complexity tasks, or in emergency. Furthermore,

surgical robotic operations require teamwork, thus excellent communication and problem solving skills are needed from the surgeon (and from all of the operators as well). For all the above reasons, non-technical surgical skills are also important in case of surgical robotics, however, it is not a well-studied area. Non-technical skills involves cognitive skills (such as decision making, memory, reaction time) and social skills (such as communication skills, working ability in a team and as a leader) [20, 102].

The NASA Task Load Index (NASA-TLX) was not originally created for surgery, but has been used in this field successfully [102]. NASA-TLX is a subjective scoring tool, including questions about mental, physical and temporal demand, furthermore performance, effort and frustration [20], with the advantage to quantify subjective parameters, and making them comparable to other experiments. To conform to the needs of surgical skill assessment, Surgery Task Load Index (SURG-TLX) was derived from NASA-TLX, but this technique is not yet used for robotic surgery, just for traditional MIS [103]. SURG-TLX examines the impact of different types of stress (such as task complexity, situational stress, distractions) in case of surgeons. Non-technical Skills for Surgeons (NOTSS) was created specifically for non-technical surgical skill assessment. NOTSS metric includes the examination of situation awareness, decision making, task management, communication and teamwork, and leadership [104]. NOTSS was recently used in surgical robotics non-technical skill assessment as well [105].

The Interpersonal and Cognitive Assessment for Robotic Surgery (ICARS) was the first objective method for RAMIS non-technical skill assessment. For ICARS, 28 non-technical behaviours were identified by expert surgeons based on the Delphi method [102, 106]. In the ICARS metrics, there are four main types of non-technical skills: checklist and equipment, interpersonal, cognitive and resource skills.

Nowadays, there are not any kind of automated skill assessment method for non-technical skills. Electroencephalography (EEG) could be employed to estimate non-technical skills during RAMIS, but due to the complexity of an EEG, it is not a well-known method for surgical skill assessment [102]. There are some limited studies in this field [107]. Guru et al. used EEG signals (nine-channel EEG recording with a neuro-headset) for cognitive skill assessment during RAMIS training. They placed the sensor on the frontal, central, parietal and occipital regions. The statistical analysis showed that with cognitive metrics, there were significant differences between the groups for the basic, intermediate and expert skills based on the data of 10 surgeons.

On the other hand, there are several methods aimed at measuring physiological signals, which can refer to the stress level, however, these are not used in RAMIS widely yet. Stress directly influences the performance of a surgeon, thus the measurement of the stress level can be a tool for non-technical surgical skill assessment [108]. In the literature, we can find examples to stress-related signals of the human body: skin temperature [109, 110], temperature of the nose [111], heart rate, skin conductance, blood pressure, respiratory period [112] etc. In case of surgical performance, tremor is the most studied physiological signal, but it

did not refer to the stress level in all cases [113].

## 7 Conclusion

Surgical skill assessment is an essential component to improve the level of training, and for providing quality assurance in primary care. Robotic surgery provides a unique platform to evaluate surgical skills objectively, since it inherently collects a wide range data. Nowadays, in the clinical practice, there is no routinely employed objective skill evaluation method. In the literature of Robot-Assisted Minimally Invasive Surgery, there are two main approaches for technical skill assessment: manual and automated. There are several validated manual evaluation methods, such as GEARS and R-OSATS, which are relatively easy to implement, but require an expert panel, prone to subjective bias. Automated RAMIS skill assessment is also a heavily studied area: there are global and language model-based methods. These are harder to implement, but in the near future, these can become an extremely powerful tool to objectively evaluate surgical skills, until we see a gradual takeover of robotic execution [114]. With the help of surgical robotics, data can be easily captured with automated tools. The input can range from kinematic data produced by the motion of the surgeon (which is the most studied approach), to endoscopic video data and force signals, etc. Automated methods can predict skills score without using human resources, and permit personalized skill training. With the novel training techniques, we hypothesize significantly improved surgical performance, therefore better patient outcome in the clinical practice.

### Acknowledgment

The research was supported by the Hungarian OTKA PD 116121 grant. This work has been supported by ACMIT (Austrian Center for Medical Innovation and Technology), which is funded within the scope of the COMET (Competence Centers for Excellent Technologies) program of the Austrian Government. T. Haidegger and R. Nagyné Elek are supported through the New National Excellence Program of the Ministry of Human Capacities. T. Haidegger is a Bolyai Fellow of the Hungarian Academy of Sciences.

### References

- [1] R. M. Satava. Surgical Robotics: The Early Chronicles: A Personal Historical Perspective. *Surgical Laparoscopy Endoscopy & Percutaneous Techniques*, 12(1):6–16, 2002.
- [2] K. H. Fuchs. Minimally Invasive Surgery. *Endoscopy*, 34(2):154–159, 2002.
- [3] A. Takács, D. A. Nagy, I. Rudas, and T. Haidegger. Origins of Surgical Robotics: From Space to the Operating Room. *Acta Polytechnica Hungarica*, 13.1:13–30, 2016.

- [4] K. Cleary and C. Nguyen. State of the Art in Surgical Robotics: Clinical Applications and Technology Challenges. *Computer Aided Surgery*, 6(6):312–328, 2001.
- [5] S. Maeso, M. Reza, J. A. Mayol, J. A. Blasco, M. Guerra, E. Andradas, and M. N. Plana. Efficacy of the Da Vinci Surgical System in Abdominal Surgery Compared With That of Laparoscopy: A Systematic Review and Meta-Analysis. *Annals of Surgery*, 252(2):254–262, 2010.
- [6] A. Paczuski and S. M. Krishnan. Analyzing Product Failures and Improving Design : A Case Study in Medical Robotics, access date: 2018-12-20.
- [7] S. Tsuda, D. Oleynikov, J. Gould, D. Azagury, B. Sandler, M. Hutter, S. Ross, E. Haas, F. Brody, and R. Satava. SAGES TAVAC safety and effectiveness analysis: Da Vinci ® Surgical System (Intuitive Surgical, Sunnyvale, CA). *Surg Endosc*, 29(10):2873–2884, 2015.
- [8] H. Alemzadeh, J. Raman, N. Leveson, Z. Kalbarczyk, and R. K. Iyer. Adverse Events in Robotic Surgery: A Retrospective Study of 14 Years of FDA Data. *PLoS ONE*, 11(4):e0151470, 2016.
- [9] P. Kazanzides, Z. Chen, A. Deguet, G. S. Fischer, R. H. Taylor, and S. P. DiMaio. An open-source research kit for the da Vinci® Surgical System. pages 6434–6439. IEEE, 2014.
- [10] InTouch Health Announces Strategic Collaboration With Intuitive Surgical. <https://intouchhealth.com/strategic-collaboration-with-intuitive-surgical/>. Access date: 2018-12-20., 2016.
- [11] A. Pedersen. Intuitive Surgical Could Help Usher in a New Era for Medtech. <https://www.mddionline.com/intuitive-surgical-could-help-usher-new-era-medtech>. Access date: 2018-12-20., 2018.
- [12] A. N. Sridhar, T. P. Briggs, J. D. Kelly, and S. Nathan. Training in Robotic Surgery—an Overview. *Curr Urol Rep*, 18(8), 2017.
- [13] J. Sándor, B. Lengyel, T. Haidegger, G. Saftics, G. Papp, A. Nagy, and G. Wéber. Minimally invasive surgical technologies: Challenges in education and training. *Asian J. of Endoscopic Surgery*, 3(3):101–108, 2010.
- [14] R. Smith, V. Patel, and R. Satava. Fundamentals of robotic surgery: A course of basic robotic surgery skills based upon a 14-society consensus template of outcomes measures and curriculum development. *The international journal of medical robotics + computer assisted surgery: MRCAS*, 10(3):379–384, September 2014.
- [15] A. Peña. The Dreyfus model of clinical problem-solving skills acquisition: A critical perspective. *Med Educ Online*, 15, 2010.
- [16] J. Rasmussen. Skills, rules, and knowledge; signals, signs, and symbols, and other distinctions in human performance models. *IEEE Transactions on Systems, Man, and Cybernetics*, SMC-13(3):257–266, May 1983.
- [17] D. Azari, C. Greenberg, C. Pugh, D. Wiegmann, and R. Radwin. In Search of Characterizing Surgical Skill. *Journal of Surgical Education*, March 2019.
- [18] T. M. Kowalewski and T. S. Lendvay. Performance Assessment. In D. Stefanidis, J. R. Korndorffer Jr., and R. Sweet, editors, *Comprehensive Healthcare Simulation: Surgery and Surgical Subspecialties*, Com-

- prehensive Healthcare Simulation, pages 89–105. Springer Intl. Publishing, Cham, 2019.
- [19] J. T. O’Donovan, B. Kang, and T. Höllerer. *Competence Modeling in Twitter : Mapping Theory to Practice*. 2015.
- [20] J. Chen, N. Cheng, G. Cacciamani, P. Oh, M. Lin-Brandt, D. Remulla, I. S. Gill, and A. J. Hung. Objective assessment of robotic surgical technical skill: A systemic review (accepted manuscript). *J. Urol.*, 2018.
- [21] A. A. Hussein, K. R. Ghani, J. Peabody, R. Sarle, R. Abaza, D. Eun, J. Hu, M. Fumo, B. Lane, J. S. Montgomery, N. Hinata, D. Rooney, B. Comstock, H. K. Chan, S. S. Mane, J. L. Mohler, G. Wilding, D. Miller, K. A. Guru, and Michigan Urological Surgery Improvement Collaborative and Applied Technology Laboratory for Advanced Surgery Program. Development and Validation of an Objective Scoring Tool for Robot-Assisted Radical Prostatectomy: Prostatectomy Assessment and Competency Evaluation. *J. Urol.*, 197(5):1237–1244, 2017.
- [22] A. A. Hussein, K. J. Sexton, P. R. May, M. V. Meng, A. Hosseini, D. D. Eun, S. Daneshmand, B. H. Bochner, J. O. Peabody, R. Abaza, E. C. Skinner, R. E. Hautmann, and K. A. Guru. Development and validation of surgical training tool: Cystectomy assessment and surgical evaluation (CASE) for robot-assisted radical cystectomy for men. *Surg Endosc*, 32(11):4458–4464, 2018.
- [23] A. A. Hussein, N. Hinata, S. Dibaj, P. R. May, J. D. Kozlowski, H. Abol-Enein, R. Abaza, D. Eun, M. S. Khan, J. L. Mohler, P. Agarwal, K. Pohar, R. Sarle, R. Boris, S. S. Mane, A. Hutson, and K. A. Guru. Development, validation and clinical application of Pelvic Lymphadenectomy Assessment and Completion Evaluation: Intraoperative assessment of lymph node dissection after robot-assisted radical cystectomy for bladder cancer. *BJU International.*, 119(6):879–884, 2017.
- [24] A. A. Hussein, R. Abaza, C. Rogers, R. Boris, J. Porter, M. Allaf, K. Badani, M. Stifelman, J. Kaouk, T. Terakawa, Y. Ahmed, E. Kauffman, Q. Li, K. Guru, and D. Eun. Development and validation of an objective scoring tool for minimally invasive partial nephrectomy: Scoring for partial nephrectomy (SPaN). *J. Urol*, 199(4):e159–e160, 2018.
- [25] H. Husslein, L. Shirreff, E. M. Shore, G. G. Lefebvre, and T. P. Grantcharov. The Generic Error Rating Tool: A Novel Approach to Assessment of Performance and Surgical Education in Gynecologic Laparoscopy. *J Surg Educ*, 72(6):1259–1265, 2015 Nov-Dec.
- [26] H. Husslein, E. Bonrath, T. Grantcharov, and G. Lefebvre. Validation of the Generic Error Rating Tool (GERT) in Gynecologic Laparoscopy (Preliminary Data). *Journal of Minimally Invasive Gynecology*, 20(6):S106, 2013.
- [27] P. Ramos, J. Montez, A. Tripp, C. K. Ng, I. S. Gill, and A. J. Hung. Face, content, construct and concurrent validity of dry laboratory exercises for robotic training using a global assessment tool. *BJU International*, 113(5):836–842, 2014.

- [28] A. C. Goh, D. W. Goldfarb, J. C. Sander, B. J. Miles, and B. J. Dunkin. Global evaluative assessment of robotic skills: Validation of a clinical assessment tool to measure robotic surgical skills. *J. Urol.*, 187(1):247–252, 2012.
- [29] R. Sánchez, O. Rodríguez, J. Rosciano, L. Vegas, V. Bond, A. Rojas, and A. Sanchez-Ismayel. Robotic surgery training: Construct validity of Global Evaluative Assessment of Robotic Skills (GEARS). *J Robot Surg*, 10(3):227–231, 2016.
- [30] M. A. Aghazadeh, I. S. Jayaratna, A. J. Hung, M. M. Pan, M. M. Desai, I. S. Gill, and A. C. Goh. External validation of Global Evaluative Assessment of Robotic Skills (GEARS). *Surg Endosc*, 29(11):3261–3266, 2015.
- [31] M. Liu, S. Purohit, J. Mazanetz, W. Allen, U. S. Kreaden, and M. Curet. Assessment of Robotic Console Skills (ARCS): Construct validity of a novel global rating scale for technical skills in robotically assisted surgery. *Surg Endosc*, 32(1):526–535, 2018.
- [32] K. R. Ghani, D. C. Miller, S. Linsell, A. Brachulis, B. Lane, R. Sarle, D. Dalela, M. Menon, B. Comstock, T. S. Lendvay, J. Montie, J. O. Peabody, and Michigan Urological Surgery Improvement Collaborative. Measuring to Improve: Peer and Crowd-sourced Assessments of Technical Skill with Robot-assisted Radical Prostatectomy. *Eur. Urol.*, 69(4):547–550, 2016.
- [33] A. Guni, N. Raison, B. Challacombe, S. Khan, P. Dasgupta, and K. Ahmed. Development of a technical checklist for the assessment of suturing in robotic surgery. *Surg Endosc*, 32(11):4402–4407, 2018.
- [34] Q. Ballouhey, P. Clermidi, J. Cros, C. Grosos, C. Rosa-Arsène, C. Bahans, F. Caire, B. Longis, R. Compagnon, and L. Fourcade. Comparison of 8 and 5 mm robotic instruments in small cavities : 5 or 8 mm robotic instruments for small cavities? *Surg Endosc*, 32(2):1027–1034, 2018.
- [35] S. L. Vernez, V. Huynh, K. Osann, Z. Okhunov, J. Landman, and R. V. Clayman. C-SATS: Assessing Surgical Skills Among Urology Residency Applicants. *J. Endourol.*, 31(S1):S95–S100, 2017.
- [36] A. J. Hung, T. Botton, T. G. Clifford, S. Serang, Z. K. Nakhoda, S. H. Shah, H. Yokoi, M. Aron, and I. S. Gill. Structured learning for robotic surgery utilizing a proficiency score: A pilot study. *World J Urol*, 35(1):27–34, 2017.
- [37] A. Volpe, K. Ahmed, P. Dasgupta, V. Ficarra, G. Novara, H. van der Poel, and A. Mottrie. Pilot Validation Study of the European Association of Urology Robotic Training Curriculum. *Eur. Urol.*, 68(2):292–299, 2015.
- [38] N. Takeshita, S. J. Phee, P. W. Chiu, and K. Y. Ho. Global Evaluative Assessment of Robotic Skills in Endoscopy (GEARS-E): Objective assessment tool for master and slave transluminal endoscopic robot. *Endosc Int Open*, 6(8):E1065–E1069, 2018.
- [39] H. Niitsu, N. Hirabayashi, M. Yoshimitsu, T. Mimura, J. Taomoto, Y. Sugiyama, S. Murakami, S. Saeki, H. Mukaida, and W. Takiyama. Using the Objective Structured Assessment of Technical Skills (OSATS)

- global rating scale to evaluate the skills of surgical trainees in the operating room. *Surg Today*, 43(3):271–275, 2013.
- [40] N. Y. Siddiqui, M. L. Galloway, E. J. Geller, I. C. Green, H.-C. Hur, K. Langston, M. C. Pitter, M. E. Tarr, and M. A. Martino. Validity and reliability of the robotic Objective Structured Assessment of Technical Skills. *Obstet Gynecol*, 123(6):1193–1199, 2014.
- [41] M. R. Polin, N. Y. Siddiqui, B. A. Comstock, H. Hesham, C. Brown, T. S. Lendvay, and M. A. Martino. Crowdsourcing: A valid alternative to expert evaluation of robotic surgery skills. *Am. J. Obstet. Gynecol.*, 215(5):644.e1–644.e7, 2016.
- [42] M. E. Tarr, C. Rivard, A. E. Petzel, S. Summers, E. R. Mueller, L. M. Rickey, M. A. Denman, R. Harders, R. Durazo-Arvizu, and K. Kenton. Robotic objective structured assessment of technical skills: A randomized multicenter dry laboratory training pilot study. *Female Pelvic Med Reconstr Surg*, 20(4):228–236, 2014 Jul-Aug.
- [43] N. Y. Siddiqui, M. L. Galloway, E. J. Geller, I. C. Green, H.-C. Hur, K. Langston, M. C. Pitter, M. E. Tarr, and M. A. Martino. Validity and reliability of the robotic Objective Structured Assessment of Technical Skills. *Obstet Gynecol*, 123(6):1193–1199, 2014.
- [44] Intuitive Surgical Investor Presentation 021218 — Surgery — Cardiothoracic Surgery. <https://www.scribd.com/document/376731845/Intuitive-Surgical-Investor-Presentation-021218>. Access date: 2018-12-20.
- [45] F. Bovo, G. De Rossi, and F. Visentin. Surgical robot simulation with BBZ console. *J Vis Surg*, 3, 2017.
- [46] Intuitive — Products Services — Education Training. <https://www.intuitive.com/en/products-and-services/da-vinci/education>. Access date: 2018-12-20.
- [47] D. Julian, A. Tanaka, P. Mattingly, M. Truong, M. Perez, and R. Smith. A comparative analysis and guide to virtual reality robotic surgical simulators. *The Intl. Journal of Medical Robotics and Computer Assisted Surgery*, 14(1), 2018.
- [48] Intuitive Surgical - da Vinci Si Surgical System - Skills Simulator. [https://www.intuitivesurgical.com/products/skills\\_simulator/](https://www.intuitivesurgical.com/products/skills_simulator/). Access date: 2018-12-20.
- [49] A. Tanaka, C. Graddy, K. Simpson, M. Perez, M. Truong, and R. Smith. Robotic surgery simulation validity and usability comparative analysis. *Surg Endosc*, 30(9):3720–3729, 2016.
- [50] H. Schreuder, R. Wolswijk, R. Zweemer, M. Schijven, and R. Verheijen. Training and learning robotic surgery, time for a more structured approach: A systematic review: Training and learning robotic surgery. *BJOG: An Intl. Journal of Obstetrics & Gynaecology*, 119(2):137–149, 2012.
- [51] A. N. Sridhar, T. P. Briggs, J. D. Kelly, and S. Nathan. Training in Robotic Surgery—an Overview. *Curr Urol Rep*, 18(8), 2017.
- [52] R. Smith, M. Truong, and M. Perez. Comparative analysis of the functionality of simulators of the da Vinci surgical robot. *Surg Endosc*, 29(4):972–983, 2015.

- [53] BBZ - Medical Technologies. <http://www.bbzsrl.com/index.html>. Access date: 2018-12-20.
- [54] SEP robot trainer. <http://surgroblog.blogspot.com/2013/10/sep-robot-trainer.html>. Access date: 2018-12-20.
- [55] R. Kumar, A. Jog, B. Vagvolgyi, H. Nguyen, G. Hager, C. C. G. Chen, and D. Yuh. Objective measures for longitudinal assessment of robotic surgery training. *The Journal of Thoracic and Cardiovascular Surgery*, 143(3):528–534, 2012.
- [56] ROS.org — Powering the world’s robots. <http://www.ros.org/>. Access date: 2018-12-20.
- [57] Cisst/SAW stack for the da Vinci Research Kit. Contribute to `jhu-dvrk/sawIntuitiveResearchKit`. <https://github.com/jhu-dvrk/sawIntuitiveResearchKit>. Access date: 2018-12-20.
- [58] Y. Gao, S. S. Vedula, C. E. Reiley, N. Ahmidi, B. Varadarajan, H. C. Lin, L. Tao, L. Zappella, B. Bejar, D. D. Yuh, C. C. G. Chen, R. Vidal, S. Khudanpur, and G. D. Hager. JHU–ISI Gesture and Skill Assessment Working Set (JIGSAWS): A Surgical Activity Dataset for Human Motion Modeling. page 10.
- [59] A. J. Hung, J. Chen, A. Jarc, D. Hatcher, H. Djaladat, and I. S. Gill. Development and Validation of Objective Performance Metrics for Robot-Assisted Radical Prostatectomy: A Pilot Study. *J. Urol.*, 199(1):296–304, 2018.
- [60] K. Ruda, D. Beekman, L. W. White, T. S. Lendvay, and T. M. Kowalewski. SurgTrak — A Universal Platform for Quantitative Surgical Data Capture. *Journal of Medical Devices*, 7(3):030923–030923–2, July 2013.
- [61] SurgTrak: Affordable motion tracking & video capture for the da Vinci surgical robot - SAGES Abstract Archives. <https://www.sages.org/meetings/annual-meeting/abstracts-archive/surgtrak-affordable-motion-tracking-and-video-capture-for-the-da-vinci-surgical-robot/>.
- [62] E. D. Gomez, R. Aggarwal, W. McMahan, K. Bark, and K. J. Kuchenbecker. Objective assessment of robotic surgical skill using instrument contact vibrations. *Surg Endosc*, 30(4):1419–1431, 2016.
- [63] T. N. Judkins, D. Oleynikov, and N. Stergiou. Objective evaluation of expert and novice performance during robotic surgical training tasks. *Surg Endosc*, 23(3):590, 2009.
- [64] I. Nisky, M. H. Hsieh, and A. M. Okamura. The effect of a robot-assisted surgical system on the kinematics of user movements. *Conf Proc IEEE Eng Med Biol Soc*, 2013:6257–6260, 2013.
- [65] M. J. Fard, S. Ameri, R. B. Chinnam, A. K. Pandya, M. D. Klein, and R. D. Ellis. Machine Learning Approach for Skill Evaluation in Robotic-Assisted Surgery. *arXiv:1611.05136 [cs, stat]*, 2016.
- [66] Y. Sharon, T. S. Lendvay, and I. Nisky. Instrument Orientation-Based Metrics for Surgical Skill Evaluation in Robot-Assisted and Open Needle Driving. *arXiv:1709.09452 [cs]*, 2017.

- [67] M. J. Fard, S. Ameri, R. D. Ellis, R. B. Chinnam, A. K. Pandya, and M. D. Klein. Automated robot-assisted surgical skill evaluation: Predictive analytics approach. *The Intl. Journal of Medical Robotics and Computer Assisted Surgery*, 14(1):e1850.
- [68] A. Zia and I. Essa. Automated surgical skill assessment in RMIS training. *Int J Comput Assist Radiol Surg*, 13(5):731–739, 2018.
- [69] Z. Wang and A. M. Fey. SATR-DL: Improving Surgical Skill Assessment and Task Recognition in Robot-assisted Surgery with Deep Neural Networks. *arXiv:1806.05798 [cs]*, 2018.
- [70] Y. Sharon and I. Nisky. What Can Spatiotemporal Characteristics of Movements in RAMIS Tell Us? *Journal of Medical Robotics Research*, page 1841008, 2018.
- [71] K. Liang, Y. Xing, J. Li, S. Wang, A. Li, and J. Li. Motion control skill assessment based on kinematic analysis of robotic end-effector movements. *Int J Med Robot*, 14(1), 2018.
- [72] Z. Wang and A. Majewicz Fey. Deep learning with convolutional neural network for objective skill evaluation in robot-assisted surgery. *Int J Comput Assist Radiol Surg*, 2018.
- [73] J. D. Brown, C. E. O'Brien, S. C. Leung, K. R. Dumon, D. I. Lee, and K. J. Kuchenbecker. Using Contact Forces and Robot Arm Accelerations to Automatically Rate Surgeon Skill at Peg Transfer. *IEEE Trans Biomed Eng*, 64(9):2263–2275, 2017.
- [74] M. Ershad, R. Rege, and A. M. Fey. Meaningful Assessment of Robotic Surgical Style using the Wisdom of Crowds. *Int J Comput Assist Radiol Surg*, 13(7):1037–1048, 2018.
- [75] R. Kumar, A. Jog, A. Malpani, B. Vagvolgyi, D. Yuh, H. Nguyen, G. Hager, and C. C. Grace Chen. Assessing system operation skills in robotic surgery trainees. *Int J Med Robot*, 8(1):118–124, 2012.
- [76] L. Maier-Hein, S. Vedula, S. Speidel, N. Navab, R. Kikinis, A. Park, M. Eisenmann, H. Feussner, G. Forestier, S. Giannarou, M. Hashizume, D. Katic, H. Kennigott, M. Kranzfelder, A. Malpani, K. März, T. Neumuth, N. Padoy, C. Pugh, N. Schoch, D. Stoyanov, R. Taylor, M. Wagner, G. D. Hager, and P. Jannin. Surgical Data Science: Enabling Next-Generation Surgery. *Nature Biomedical Engineering*, 1(9):691–696, 2017.
- [77] C. E. Reiley and G. D. Hager. Task versus subtask surgical skill evaluation of robotic minimally invasive surgery. *Med Image Comput Comput Assist Interv*, 12(Pt 1):435–442, 2009.
- [78] H. C. Lin, I. Shafran, D. Yuh, and G. D. Hager. Towards automatic skill evaluation: Detection and segmentation of robot-assisted surgical motions. *Computer Aided Surgery*, 11(5):220–230, 2006.
- [79] C. E. Reiley, H. C. Lin, B. Varadarajan, B. Vagvolgyi, S. Khudanpur, D. D. Yuh, and G. D. Hager. Automatic recognition of surgical motions using statistical modeling for capturing variability. In *Studies in Health Technology and Informatics*, pages 396–401, 2008.
- [80] B. Varadarajan, C. Reiley, H. Lin, S. Khudanpur, and G. Hager. Data-Derived Models for Segmentation with Application to Surgical Assess-

- ment and Training. In *Medical Image Computing and Computer-Assisted Intervention – MICCAI 2009*, Lecture Notes in Computer Science, pages 426–434. Springer, Berlin, Heidelberg, 2009.
- [81] L. Tao, E. Elhamifar, S. Khudanpur, G. D. Hager, and R. Vidal. Sparse Hidden Markov Models for Surgical Gesture Classification and Skill Evaluation. In *Information Processing in Computer-Assisted Interventions*, Lecture Notes in Computer Science, pages 167–177. Springer, Berlin, Heidelberg, 2012.
- [82] N. Ahmidi, Y. Gao, B. Béjar, S. S. Vedula, S. Khudanpur, R. Vidal, and G. D. Hager. String motif-based description of tool motion for detecting skill and gestures in robotic surgery. *Med Image Comput Comput Assist Interv*, 16(Pt 1):26–33, 2013.
- [83] S. Sefati, N. Cowan, and R. Vidal. Learning Shared, Discriminative Dictionaries for Surgical Gesture Segmentation and Classification. In *Medical Image Computing and Computer-Assisted Intervention – MICCAI*, volume 4, 2015.
- [84] F. Despinoy, D. Bouget, G. Forestier, C. Penet, N. Zemiti, P. Poignet, and P. Jannin. Unsupervised Trajectory Segmentation for Surgical Gesture Recognition in Robotic Training. *IEEE Transactions on Biomedical Engineering*, 63(6):1280–1291, 2016.
- [85] S. Krishnan, A. Garg, S. Patil, C. Lea, G. Hager, P. Abbeel, and K. Goldberg. Transition State Clustering: Unsupervised Surgical Trajectory Segmentation for Robot Learning. In A. Bicchi and W. Burgard, editors, *Robotics Research: Volume 2*, Springer Proceedings in Advanced Robotics, pages 91–110. Springer Intl. Publishing, Cham, 2018.
- [86] G. Forestier, F. Petitjean, P. Senin, F. Despinoy, A. Huauilmé, H. I. Fawaz, J. Weber, L. Idoumghar, P.-A. Muller, and P. Jannin. Surgical motion analysis using discriminative interpretable patterns. *Artif Intell Med*, (91):3–11, 2018.
- [87] B. B. Haro, L. Zappella, and R. Vidal. Surgical gesture classification from video data. *Med Image Comput Comput Assist Interv*, 15(1):34–41, 2012.
- [88] H. C. Lin and G. Hager. User-Independent Models of Manipulation Using Video Contextual Cues. *Workshop on Modeling and Monitoring of Computer Assisted Interventions*, 2009.
- [89] L. Zappella, B. Béjar, G. Hager, and R. Vidal. Surgical gesture classification from video and kinematic data. *Medical Image Analysis*, 17(7):732–745, 2013.
- [90] A. Malpani, S. S. Vedula, C. C. G. Chen, and G. D. Hager. Pairwise Comparison-Based Objective Score for Automated Skill Assessment of Segments in a Surgical Task. In D. Stoyanov, D. L. Collins, I. Sakuma, P. Abolmaesumi, and P. Jannin, editors, *Information Processing in Computer-Assisted Interventions*, Lecture Notes in Computer Science, pages 138–147. Springer Intl. Publishing, 2014.
- [91] N. Ahmidi, L. Tao, S. Sefati, Y. Gao, C. Lea, B. B. Haro, L. Zappella, S. Khudanpur, R. Vidal, and G. D. Hager. A Dataset and Benchmarks

- for Segmentation and Recognition of Gestures in Robotic Surgery. *IEEE Transactions on Biomedical Engineering*, 64(9):2025–2041, 2017.
- [92] S. Jun, M. S. Narayanan, P. Agarwal, A. Eddib, P. Singhal, S. Garimella, and V. Krovi. Robotic Minimally Invasive Surgical skill assessment based on automated video-analysis motion studies. In *2012 4th IEEE RAS EMBS Intl. Conference on Biomedical Robotics and Biomechanics (BioRob)*, pages 25–31, 2012.
- [93] C. Lea, G. D. Hager, and R. Vidal. An Improved Model for Segmentation and Recognition of Fine-Grained Activities with Application to Surgical Training Tasks. In *2015 IEEE Winter Conference on Applications of Computer Vision*, pages 1123–1129, 2015.
- [94] Automated skill assessment for individualized training in robotic surgery — —Science of Learning. <http://scienceoflearning.jhu.edu/research/automated-skill-assessment-for-individualized-training-in-robotic-surgery>. Access date: 2018-12-20.
- [95] A. Malpani, S. S. Vedula, C. C. G. Chen, and G. D. Hager. A study of crowdsourced segment-level surgical skill assessment using pairwise rankings. *Int J CARS*, 10(9):1435–1447, 2015.
- [96] S. Krishnan, A. Garg, S. Patil, C. Lea, G. D. Hager, P. Abbeel, and K. Goldberg. Unsupervised Surgical Task Segmentation with Milestone Learning. In *Proc. Intl Symp. on Robotics Research (ISRR)*, 2015.
- [97] C. Lea, A. Reiter, R. Vidal, and G. D. Hager. Segmental Spatiotemporal CNNs for Fine-Grained Action Segmentation. In B. Leibe, J. Matas, N. Sebe, and M. Welling, editors, *Computer Vision – ECCV 2016*, Lecture Notes in Computer Science, pages 36–52. Springer Intl. Publishing, 2016.
- [98] R. DiPietro, C. Lea, A. Malpani, N. Ahmidi, S. S. Vedula, G. I. Lee, M. R. Lee, and G. D. Hager. Recognizing Surgical Activities with Recurrent Neural Networks. In S. Ourselin, L. Joskowicz, M. R. Sabuncu, G. Unal, and W. Wells, editors, *Medical Image Computing and Computer-Assisted Intervention – MICCAI 2016*, Lecture Notes in Computer Science, pages 551–558. Springer Intl. Publishing, 2016.
- [99] S. S. Vedula, A. O. Malpani, L. Tao, G. Chen, Y. Gao, P. Poddar, N. Ahmidi, C. Paxton, R. Vidal, S. Khudanpur, G. D. Hager, and C. C. G. Chen. Analysis of the Structure of Surgical Activity for a Suturing and Knot-Tying Task. *PLoS ONE*, 11(3):e0149174, 2016.
- [100] A. Zia, C. Zhang, X. Xiong, and A. M. Jarc. Temporal clustering of surgical activities in robot-assisted surgery. *Int J Comput Assist Radiol Surg*, 12(7):1171–1178, 2017.
- [101] T. D. Nagy and T. Haidegger. A DVRK-based Framework for Surgical Subtask Automation. *Acta Polytechnica Hungarica*, 14(Special Issue on Platforms for Medical Robotics Research (accepted manuscript)), 2019.
- [102] Understanding and Assessing Nontechnical Skills in Robotic Urological Surgery: A Systematic Review and Synthesis of the Validity Evidence. *Journal of Surgical Education*, 2018.
- [103] M. R. Wilson, J. M. Poolton, N. Malhotra, K. Ngo, E. Bright, and R. S. W. Masters. Development and Validation of a Surgical Workload Measure:

- The Surgery Task Load Index (SURG-TLX). *World J Surg*, 35(9):1961–1969, 2011.
- [104] S. Yule, R. Flin, N. Maran, D. Rowley, G. Youngson, and S. Paterson-Brown. Surgeons' Non-technical Skills in the Operating Room: Reliability Testing of the NOTSS Behavior Rating System. *World Journal of Surgery*, 32(4):548–556, April 2008.
- [105] N. Raison, K. Ahmed, T. Abe, O. Brunckhorst, G. Novara, N. Buffi, C. McIlhenny, H. van der Poel, M. van Hemelrijck, A. Gavazzi, and P. Dasgupta. Cognitive training for technical and non-technical skills in robotic surgery: A randomised controlled trial. *BJU International*, 122(6):1075–1081, December 2018.
- [106] N. Raison, T. Wood, O. Brunckhorst, T. Abe, T. Ross, B. Challacombe, M. S. Khan, G. Novara, N. Buffi, H. Van Der Poel, C. McIlhenny, P. Dasgupta, and K. Ahmed. Development and validation of a tool for non-technical skills evaluation in robotic surgery-the ICARS system. *Surg Endosc*, 31(12):5403–5410, 2017.
- [107] K. A. Guru, E. T. Esfahani, S. J. Raza, R. Bhat, K. Wang, Y. Hammond, G. Wilding, J. O. Peabody, and A. J. Chowriappa. Cognitive skills assessment during robot-assisted surgery: Separating the wheat from the chaff. *BJU Intl.*, 115(1):166–174, 2015.
- [108] C. M. Wetzel, R. L. Kneebone, M. Woloshynowych, D. Nestel, K. Moorthy, J. Kidd, and A. Darzi. The effects of stress on surgical performance. *The American Journal of Surgery*, 191(1):5–10, 2006.
- [109] K. A. Herborn, J. L. Graves, P. Jerem, N. P. Evans, R. Nager, D. J. McCafferty, and D. E. McKeegan. Skin temperature reveals the intensity of acute stress. *Physiol Behav*, 152(Pt A):225–230, 2015.
- [110] I. Pavlidis, P. Tsiamyrtzis, D. Shastri, A. Wesley, Y. Zhou, P. Lindner, P. Buddharaju, R. Joseph, A. Mandapati, B. Dunkin, and B. Bass. Fast by Nature - How Stress Patterns Define Human Experience and Performance in Dexterous Tasks. *Scientific Reports*, 2:305, 2012.
- [111] How the temperature of your nose shows how much strain you are under - The University of Nottingham. <https://www.nottingham.ac.uk/news/pressreleases/2018/january/how-the-temperature-of-your-nose-shows-how-much-strain-you-are-under.aspx>. Access date: 2018-12-20.
- [112] C. L. etitia Lisetti and F. Nasoz. Using Noninvasive Wearable Computers to Recognize Human Emotions from Physiological Signals. *EURASIP J. Appl. Signal Process.*, 2004:1672–1687, 2004.
- [113] G. G. Youngson. Nontechnical skills in pediatric surgery: Factors influencing operative performance. *Journal of Pediatric Surgery*, 51(2):226–230, 2016.
- [114] T. Haidegger. Autonomy for surgical robots: Concepts and paradigms. *IEEE Trans. on Medical Robotics and Bionics*, 1(2):65–76, 2019.

Table 1

Automated surgical skill assessment techniques in RAMIS. Used abbreviations: HMM: Hidden Markov Model, LDA: Linear Discriminant Analysis, GMM: Gaussian Mixture Model, PCA: Principal Component Analysis, SVM: Support Vector Machines, LDS: Linear Dynamical System, NN: Neural Network.

Aim	Input data	Data collection	Training task	Technique	Year	Ref.
kinematic data-based skill assessment	completion time, total distance traveled, speed, curvature, relative phase	da Vinci API	dry lab (bimanual carrying, needle passing, suture tying)	dependent and independent t-tests	2009	[63]
framework for skill assessment of RAMIS training	stereo instrument video, hand and instrument motion, buttons and pedal events	da Vinci API	dry lab (manipulation, suturing, transection, dissection)	PCA, SVM	2012	[55]
examine the effect of teleoperation and expertise on kinematic aspects of simple movements	position, velocity, acceleration, time, initial jerk, peak speed, peak acceleration, deceleration	magnetic pose tracker	dry lab (reach, reversal)	2-way ANOVA	2013	[64]
longitudinal study tracking robotic surgery trainees	basic kinematic data, torque data, events from pedals, buttons and arms, video data	da Vinci API	dry lab (suturing, manipulation, transection, dissection)	SVM	2013	[75]
generate an objective score for assessing skill in gestures	basic kinematic and video data	JIGSAWS	dry lab (suturing, knot tying)	SVM	2014	[90]
discriminate expert and novice surgeons based on kinematic data	completion time, path length, depth perception, speed, smoothness, curvature	da Vinci API	dry lab (suturing)	logistic regression, SVM	2016	[65]
instrument vibrations-based skill assessment	completion time, instrument vibrations, applied forces	da Vinci API	dry lab (peg transfer, needle pass, intracorporeal suturing)	stepwise regression	2016	[62]
automatic skill evaluation based on the contact force	contact forces, robot arm accelerations, time	da Vinci and Smart Task Board	peg transfer	regression and classification	2017	[73]
skill assessment based on instrument orientation	time, path length, angular displacement, rate of orientation change	da Vinci Research Kit	dry lab (needle driving)	2-way ANOVA	2017	[66]
discriminate expert and novice surgeons based on kinematic data	completion time, path length, depth perception, speed, smoothness, curvature, turning angle, tortuosity	da Vinci API	dry lab (suturing, knot-tying)	k-Nearest Neighbor, logistic regression, SVM	2018	[67]
skill score prediction	sequential motion texture, discrete Fourier transform, discrete cosine transform and approximate entropy	JIGSAWS	dry lab (suturing, knot tying, needle passing)	nearest neighbor classifier, support vector regression	2018	[68]

Aim	Input data	Data collection	Training task	Technique	Year	Ref.
objective skill level assessment based on metrics associated with stylistic behavior	basic kinematic and physiological data	limb inertial measurements unit, electromagnetic joint position tracker, EMG, GSR, IMU, cameras	da Vinci Skills Simulator tasks (ring and rail, suture sponge)	crowd sourced analysis	2018	[74]
characterization of open and teleoperated suturing movement	speed, curvature, torsion of movement trajectories	da Vinci Research Kit, JIGSAWS	dry lab (suturing)	fitting the one-sixth power law, types of ANOVA	2018	[70]
assess expertise and recognize surgical training activity	basic kinematic data	JIGSAWS	dry lab (suturing, knot-tying, needle-passing)	multi-output deep learning architecture	2018	[69]
evaluate skills based on kinematic data	time, errors, movement speed, jerkiness, trajectory redundancy, target scoring, trajectory volatility, max deviation	MicroHand S, magnetic sensor	dry lab (pick and place, ring threading)	one-way ANOVA	2018	[71]
evaluate skills based on a deep learning model	basic kinematic data	JIGSAWS	dry lab (suturing, knot tying, needle passing)	deep convolutional NN	2018	[72]
gesture classification	basic kinematic data	da Vinci API	dry lab (suturing)	local feature extraction, LDA, Bayes classifier	2006	[78]
gesture classification and recognition	basic kinematic data	da Vinci API	dry lab (suturing)	LDA, strawman GMM, 3-state HMM	2008	[79]
compare task versus subtask	basic kinematic data	da Vinci API	dry lab (suturing)	vector quantization, HMM	2009	[77]
gesture classification	basic kinematic data and video contextual cues (suture line deformations)	da Vinci API	dry lab (suturing)	HMM, high-order polynomial fitting to the extracted suturing line	2012	[88]
gesture classification and recognition	basic kinematic data	da Vinci API	dry lab (suturing)	LDA, HMM	2009	[80]
gesture classification	basic kinematic data	JIGSAWS	dry lab (suturing, knot-tying, needle passing)	sparse HMM	2012	[81]
gesture classification	video features (image intensities, image gradients, optical flow)	JIGSAWS	dry lab (suturing, needle passing, knot tying)	LDS, bag-of-features, multiple kernel learning	2012	[87]
gesture classification	basic kinematic data and video features (Space-Time Interest Points)	JIGSAWS	dry lab (suturing, needle passing, knot tying)	LDS, bag of features, multiple kernel learning	2018	[89]
gesture classification	basic kinematic data	JIGSAWS, da Vinci Surgical System	dry lab (suturing)	descriptive curve coding, common string model, SVM	2013	[82]
gesture classification	basic kinematic data	JIGSAWS	dry lab (suturing, needle passing, knot tying)	Shared Discriminative Sparse Dictionary Learning, SVM, HMM	2015	[83]

Aim	Input data	Data collection	Training task	Technique	Year	Ref.
providing individualized feedback to surgical trainees	basic kinematic data	n/a	dry lab (suturing, knot tying)	automatic identification of motifs in the tool motion signal	2015	[94]
segmentation of surgical tasks into smaller phases	basic kinematic and video data	JIGSAWS	dry lab (suturing, knot tying)	binary classifier, crowd-sourced segment ratings	2015	[95]
unsupervised segmentation of surgical tasks into smaller phases	basic kinematic (position) and video (object grasp events and surface penetration) data	da Vinci Research Kit	dry lab (pattern cutting, suturing, needle passing)	milestone learning with Dirichlet Process Mixture Models	2015	[96]
recognizing surgical activities	basic kinematic data	JIGSAWS	dry lab (suturing)	Recurrent NN	2016	[98]
gesture classification and recognition	basic kinematic data	Raven-II, Sigma 7	peg transfer	unsupervised trajectory segmentation, k-Nearest Neighbors, SVM	2016	[84]
describe differences in task flow	basic kinematic and video data	da Vinci API	dry lab (suturing, knot tying)	hierarchical semantic vocabulary	2016	[99]
gesture classification	basic kinematic and video data	JIGSAWS	dry lab (suturing, knot tying, needle passing)	HMM, Sparse HMM, Markov semi-Markov Conditional Random Field, Skip-Chain CRF, Bag of spatiotemporal Features, LDS	2017	[91]
temporal clustering of surgical activities	basic kinematic and video data	n/a	live surgery (two-handed robotic suturing, uterine horn dissection, suspensary ligament dissection, running robotic suturing, rectal artery skeletonization and clipping)	Hierarchical Aligned Cluster Analysis, Aligned Cluster Analysis, Spectral Clustering, GMM	2017	[100]
gesture classification and recognition	basic kinematic and video data	da Vinci SKILLS Simulator, SIMIMotion motion capture system	simulated tasks (peg transfer, pick and place)	Decision Tree Algorithm Model	2012	[92]
gesture classification	basic kinematic data	JIGSAWS	dry lab (suturing, needle passing)	Transition State Clustering, uses hierarchical Dirichlet Process GMM	2018	[85]
gesture classification	basic kinematic data	JIGSAWS/RAVEN-II, Sigma.7, leap motion device/dataset of micro-surgical suturing tasks captured using a dedicated robot	dry lab (suturing, needle passing, knot tying/peg transfers/micro-surgical suturing)	Symbolic Aggregate approximation, Bag of Words, vector space model	2018	[86]

Aim	Input data	Data collection	Training task	Technique	Year	Ref.
action segmentation and recognition	kinematic (end effector positions, velocity, gripper state, skip-length features) and video (distance to the closest object part from each tool, relative position of each tool to the closest object part) data	JIGSAWS	dry lab (suturing, needle passing, knot tying)	Skip-Chain Conditional Random Field, Deformable Part Model	2015	[93]
action segmentation	basic kinematic and video data	JIGSAWS	dry lab (suturing)	Segmental Spatiotemporal Convolutional NN	2016	[97]

# Safety of Surgical Robots and IEC 80601-2-77: The First International Standard for Surgical Robots

**Kiyoyuki Chinzei**

Health Research Institute  
National Institute of Advanced Industrial Science and Technology (AIST)  
1-2-1 Namiki, Tsukuba, Ibaraki 305-8564 Japan  
k.chinzei@aist.go.jp

---

*Abstract: A new standard IEC 80601-2-77 will be issued to establish safety requirements for surgical robots under regulatory control. A new term Robotically Assisted Surgical Equipment (RASE) is introduced to cover a wide variety of mechanical structures, control algorithms, human-machine interface and intended surgical procedures. This article is to introduce the key ideas of this standard, the scope, to what extent this standard will be applicable and some of the specific requirements. The future of surgical robot safety, including the emerging autonomy is also mentioned.*

*Keywords: robot safety; medical device safety; invasiveness; robotically assisted surgical equipment; autonomy*

---

## 1 Introduction

IEC (the International Electrotechnical Commission) and ISO (International Organization for Standardization) are currently preparing to publish a new safety standard for surgical robots, IEC 80601-2-77. It is expected to be issued in 2019. Since it is the first safety standard, particularly applicable to surgical robots, and it is expected to be a mandatory requirement in many nations and regions, knowing it will benefit study and development of surgical robots. This paper will provide the key ideas of this standard, the extent of the scope, and some of requirements. Though the author is appointed as the project leader of the joint working group (JWG 35) for this development, this paper does not represent the opinion of the working group, IEC or ISO. Correspondingly, this paper is written based on the draft of the standard.

## 2 Robot Safety and Safety of Medical Robots

Before discussing the standard for surgical robots, we review robot safety in Section 2.1 followed by safety of medical robots in Section 2.2.

### 2.1 Safety of (Traditional) Robots and Personal Care Robots

Here we define ‘medical robot’ as ‘robot intended to be used as a medical device’<sup>1</sup>. Safety of medical robots can be divided into two parts, robot safety and medical device safety.

Robot safety is mainly related to mechanical hazards that a moving robot can pose. Such hazards include the collision between the robot and human, or the robot and other items including the robot itself. Other typical mechanical hazards are the trapping, crushing, shearing, pinching, and/or entanglement by the robot. The real baseline is that these hazards can occur under the hazardous situations including the unintended movement, the uncontrolled trajectory/speed, which the movement goes off from the expected one. Such situations can be critical when the safeguard functions do not work as expected or the human operators who are in charge of monitoring do not react properly.

These hazards and hazardous situations can commonly happen in many types of machines at home, in factory, in commerce and transportation, etc. In particular, factory machines mostly intend to realize automation. Uninterrupted and fast movement has been pursued and hazards enlarged. Factory safety has traditionally kept hazardous machines separated from human by covering or placing such machines in the work cells.

The same principle was applied to industrial robots. ISO 10218:1992, the initial issue of the safety standard for industrial robots (current latest issue is ISO 10218-1:2011) rigorously required the separation principle. Although it was revised to allow human-robot cooperative maneuver under certain restrictions, the separation principle is still valid.

However, certain robot applications intended robots to co-work with human, including service robots, personal care robots, and medical robots. In such cases the separation principle could not maintain. ISO 13482:2014 “Safety requirements for personal care robots” was the first standard for personal care robots. This standard assumes that a robot works with a human in its vicinity or in contact with the robot. Considering the nature of personal care robots, which are usually less powerful, less bulky than industrial robots and the intended use is often not for

---

<sup>1</sup> Medical robot is defined as “**robot** intended to be used as **medical electrical equipment** or **medical electrical system**” in IEC TR 60601-4-1. **Medical electrical equipment/systems** are terms roughly correspond to ‘active medical devices and systems using electric energy.’

automation, this standard allows alternative risk mitigation measures other than the separation, such as reducing speed near human, etc.

When the discussion to develop ISO 13482 started in 2006, it was also recognized that medical robots could also apply similar risk mitigation measures. But it was concluded that medical robots should be covered by their own dedicated standards rather than the one for personal care robots, as medical robots need to address the medical device safety as well as the robot safety.

## 2.2 Safety of Medical Robots as Medical Devices

Medical robots are medical devices by definition. Medical robot safety is certainly different from the safety of other robots mainly in the following aspects.

- Patient safety: Patients are considered as lay persons - knowledge, education and training regarding the safety cannot be assumed. They are often vulnerable. In some cases, including surgery, they are anesthetized so that they cannot react to escape from hazards.
- Medical staff as contributors for safety: they are not lay persons. They can be assumed to receive training to use medical robots. This may increase the effectiveness of safety information as a risk mitigation measure. However, they are not experts of robotics and mechanical engineering.
- Invisible and insensible hazards: Some hazards, such as electric shock, toxicity of material, infection of microbe, radiation, etc., are invisible and insensible for human. When such hazards are found, they can be often already unacceptable in terms of safety. Preventing, minimizing or informing users about risks from such hazards are responsibility of manufacturers.
- Invasiveness: Surgical robots are invasive. It is a most significant difference from any other robots. Invasiveness can escalate the risk level. An adverse event that is not harmful at outside patient body can be fatal if it occurs inside patient's body.

A significant difference on the safety concerns between medical device and other products can be found in the requirements of the electric shock prevention. The medical electrical equipment standard IEC 60601-1 requires the leak current of the order of milli- to micro- ampere, whilst other safety standards set the allowance in the voltage of the order of 10 V.

### 3 Defining ‘Surgical Robots’

Before discussing the standard for surgical robots, it is necessary to clarify the boundary of surgical robots for the purpose of the standard. In Section 3.1 we discuss possible factors that can define the boundary of surgical robots. Section 3.2 describes common aspects discussed in Section 3.1.

#### 3.1 Boundary of ‘Surgical Robots’

Probably robot-assisted minimally invasive surgery (RAMIS) is the most known and typical application of surgical robots. The most famous surgical robot for RAMIS is the da Vinci Surgical System (Intuitive Surgical, Inc., Sunnyvale, CA, USA). Although there have been several revisions of the da Vinci Surgical System in its history over 20 years, all of these are the master-slave manipulators that are totally controlled by the surgeon, in other words, the operator is in the control loop [1]. The system has a limited ability to optimize the movement such as the tremor cancellation, yet it has no automated or intelligent trajectory generation and motion control.

Computer-integrated surgery (CIS) is another well studied application of surgical robots. A typical example of CIS system is ROBODOC (currently renamed as TSolution One Surgical System by THINK Surgical Inc., Fremont, CA, USA) for orthopedic surgery. CIS uses digitized information about the patient’s anatomy obtained from medical images. The trajectory is generated from the 3D information. The operator approves the trajectory then monitors the system correctly works.

Surgical robots have wide variety of mechanical structures, control algorithm, human-machine interface and intended surgical procedures [2]. JWG 35 initially investigated which types of medical devices should be covered by the standard to write, as well as what types of medical devices should be excluded. Most of the medical devices described in [2] are at the center of the definition, some are at the boundary, some are out of the boundary. Finding the boundary is not a trivial question. The meanings of terms 'surgical' and 'robot' are vague and understood differently by medical experts or stakeholders.

##### 1) Term ‘surgery’

Term surgery is differently used in different medical disciplines. A World Health Organization (WHO) document contains a working definition of surgery as “procedure conducted in the operating room involving the incision, excision, manipulation or suturing of tissue which usually requires regional or general anesthesia or profound sedation to control pain [3]”. This definition was adopted in this standard with modification. Medical procedures on the boundary of surgery can be:

- Medical treatments referred as intervention, e.g., vascular intervention

- Radiological treatments referred as radiosurgery
- Treatments by laser, ultrasound and other modes of physical energy
- Orthopedic treatments done without instruments, such as repositioning fractured bone or shoulder dislocation
- Invasive procedures not for treatment, such as biopsy
- Dental treatments by dentists
- Invasive cosmetic procedures, e.g., hair implantation [2], tattooing

## 2) Term ‘robot’

Robot is defined as “programmed actuated mechanism with a degree of autonomy, moving within its environment, to perform intended tasks”<sup>2</sup>. This definition is based on general perception about robot, that includes i) mechanisms mimicking arms, fingers, legs, or other human body parts, and/or ii) something intelligent that controls adaptive motion. The term ‘a degree of autonomy’ is not defined in ISO 8373. We will discuss this term in Section 6.

Table 1  
Modes of surgical invasiveness

Modes of invasiveness	Examples
1) Energy only administered through the surface of patient body (no incision)	- radiosurgery - focused ultrasound - shoulder relocation
2) Invasion into patient body from the surface of patient body	- open surgeries - bone fixation using screws - bone milling - laparoscopic surgery (minimally invasive surgery) - vascular intervention
3) Energy administered via the inner surface of natural orifice	- focused ultrasound via endoscope
4) Invasion into patient body via the inner surface of natural orifice	- endomucosal resection (EMR) - dental milling

## 3) Robots used in surgery are not always surgical robots

Medical devices that fall into the definition of robot certainly exist in modern surgeries; for instance, robot-shape actuated operating table [ 4 ], robotized microscope [5], etc. However, these two are usually not considered as surgical robots. These are not surgical instruments, and do not have an invasive part.

<sup>2</sup> It is a working definition by ISO TC 299 which will be adopted in the future revision of ISO 8373.

#### 4) Modes of invasiveness

Invasiveness of surgeries differ by surgeries. Table 1 shows the various modes of surgical invasiveness considering the boundary applications listed previously. The resulting 'boundary' set in this standard will be discussed in Section 4.3.

### **3.2 Common Safety Aspects of Surgical Robots**

Although possible applications of robotic technology can be broad, JWG 35 identified two common characteristics in terms of the safety.

- 1) Surgical robots are to hold and/or maneuver different types of tools attached to the end of robotic body. In robotics term, the tools are the end effectors. For surgical robots, the tools are surgical instruments. Surgical instruments can be forceps, mono- and bi-polar blade, milling drill, endoscope, laser fiber, ultrasound transducer, etc. Robotic body facilitates placement and manipulation of the surgical instruments. Surgical instruments are usually detachable for the purpose of tool exchange and sterilization.
- 2) Surgical robots are used with other medical devices. Electrical, thermal, mechanical and other functional connections between the robot and these devices, intended or unintended, can occur by collision or contact between them. Such functional connections can be sources of hazards, even though such devices individually satisfy necessary risk mitigation measures.

## **4 Structure of IEC 80601-2-77**

IEC 80601-2-77 is being developed under a joint effort of IEC and ISO, where IEC technical committee (TC) 62 is for medical electrical equipment and ISO TC 299 is for robotics. The joint working group (JWG) 35 was organized in 2015 as a liaison group of the both organizations. It will be a part of IEC 60601 safety standards series, because when a surgical robot is marketed, it is regulated as a medical electrical equipment rather than a robot in most of nations and regions. This standard is written as the differences from IEC 60601-1 general standard for safety of medical electrical equipment.

Since IEC 60601-1 refers to ISO 14971 risk management standard for medical device, the risk management process for surgical robot is also harmonized to ISO 14971.

## 4.1 Issues Covered by IEC 80601-2-77

Based on these considerations, this standard covers the following issues:

- Issues related to robot movement e.g., quality of motion control, emergency management
- Issues related to electrical and other functional connections with other objects in the patient environment, that can generate and transfer harmful energy e.g., leak current, excessive heat
- Issues related to the effect of unintended collision with other objects such as robot itself, surgical instruments, other medical devices, patient body and medical staff working nearby the robot
- Other general requirements to the robot hardware and software, e.g., structural strength, the biological safety, the usability engineering, software integrity, etc.

Surgical instruments and other medical devices usually have own safety standards to follow. Hence this standard uses these other standards to cover of the safety of these parts. For instance, endoscopic equipment is covered by IEC 60601-2-18, high frequency (HF) surgical equipment by IEC 60601-2-2, ultrasound imaging equipment by IEC 60601-2-37, etc.

## 4.2 Key Definitions

The key definitions of this standard are the following two terms. Bold types represent defined terms in this standard and IEC 60601-1.

### **Robotically assisted surgical equipment, RASE**

**Medical electrical equipment** that incorporates **PEMS**<sup>3</sup> actuated mechanism intended to facilitate the placement or manipulation of **robotic surgical instrument**

### **Robotic surgical instrument**

**Invasive device** with **applied part**, intended to be manipulated by **RASE** to perform tasks in **surgery**

A new term **RASE** was introduced. This standard intentionally avoids using the term surgical robot from a few reasons, mainly to avoid possible confusion and to emphasize that it is to assist surgeons, not to replace them by automation. The definition does not refer to specific mechanical structures, means of actuation, nor the control algorithms.

---

<sup>3</sup> programmable electrical medical system

### 4.3 Scope

The definition of robotic surgical instrument limits the scope of this standard to invasive devices. The following cases are not considered as invasive;

- Cases that energy only is administered to the patient, such as percutaneous high intensity ultrasound [6], bone fracture relocation device attached to the skin surface [7], robotic radiotherapy equipment [8].
- Cases that are not intended to touch the patient body, such as frameless stereotactic device to display the orientation of the target [9].

Therefore, robots with such devices are not in the scope of this standard. The same device can be in the scope when they are incorporated in or connected to the invasive part. For example, if a high intensity ultrasound transducer is attached to a robotic endoscope to be inserted into patient's body, or if a bone fracture relocation device is attached to the patient by invasive screws [10], they are considered as within the scope of this standard.

Table 2  
Scope applicability of robotic systems

Modes of invasiveness	Scope	Examples (mentioned in [2] otherwise indicated)
0) No robotic surgical instrument attached to actuated mechanism, or no applied part exists	No	- robotized microscope [5] <sup>a</sup> - scrub nurse robot <sup>b</sup> - NavioPFS <sup>c</sup> - ROSA, Neuromate [9] <sup>d</sup>
1) Energy only administered to surface of patient body (no incision)	No	- Cyberknife <sup>e</sup> - fracture relocation device [7] <sup>f</sup>
2) Invasion into patient body from surface of patient body	Yes	- Artas - bone fixation using screws [11] - ROBODOC, MAKO - da Vinci Surgical System - CorPath, Sensei
3) Energy administered via inner surface of natural orifice	Yes	(not realized)
4) Invasion into patient body via inner surface of natural orifice	Yes	- Neocis dental robot [4] - robotic endoscopic tools for EMR (not realized)

a: Robot without a surgical instrument.

b: Robot with a surgical instrument, lacking an applied part.

c: An applied part intelligently controlled, but lacking placement or manipulation by actuated mechanism.

- d: Robot with a surgical instrument, lacking an applied part. However, if the manufacturer wants, this standard is applicable, because the pointer tip enters the surgical field and it can accidentally hit or touch the patient.
- e: Energy only administered, covered by IEC 60601-2-68.
- f: Attached to the skin without incision.

Scope applicability of some systems in [2] and other literature are shown in Table 2, with classification based on the modes of invasiveness in Table 1.

## 5 Safety Requirements

**Essential performance** is a requirement of the performance which is necessary to achieve the safety. This standard describes the following requirements as the RASE's essential performance.

- To ensure there is no unacceptable risk if information essential to perform surgery is degraded (information integrity).
- To ensure there is no unacceptable risk if motion control of the robotic surgical instrument has performance degradation (integrity of motion control).

Figure 1 illustrates the relation of these essential performance requirements. These are considered as a loop of interaction between the surgeon and patient, where the RASE acts as the interface between them. In actual implementation, the essential performance requirements will vary by implementation. However, these are considered as common in typical RASE surgeries.

The requirement of integrity of motion control can be different by the types of robot control. As discussed in Section 2.1, mechanical hazards can occur when there is hazardous situation including:

- Unintended movement initiated
- Trajectory goes off from the expected one, or the speed is out of control
- Safeguard functions do not work or the human operators who are in charge of monitoring do not react properly.

In case of RAMIS systems, operators are responsible of continuously monitoring the movement, and the RASE is responsible to stop quickly when an operator requested.

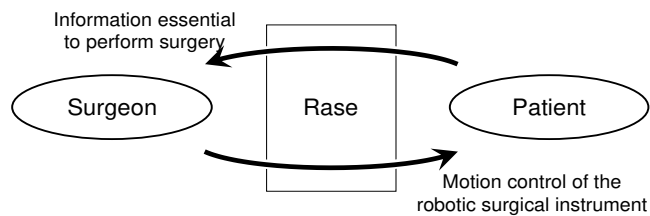


Figure 1

Example of the essential performance of RASE

Some of major particular requirements in this standard are

- Conditions to constitute the ‘continuous activation’ (the main surgeon continuously monitors the movement of the RASE and reacts to reduce the risk when a hazardous situation is expected) is extended to allow other persons (e.g., the assistant surgeon or nurses) can also take the role of monitoring and reacting. IEC 60601-1 allows the continuous activation as a risk control measure against the trapping zone hazards. However, in case of endoscopic surgery, the main surgeon needs to concentrate on watching the endoscopic view and he/she cannot watch the robot’s movement outside the patient body. Other staff can monitor and react to the hazardous situation outside the patient body.
- Interaction between surgical instruments (including those of RASE itself) shall be considered in the risk management. In particular, HF surgical equipment can be eventually hazardous by the capacitive coupling leakage and electromagnetic disturbance to the robot control system.
- Narrow size robotic surgical instruments can be allowed under certain condition. IEC 60601-1 requires keeping the minimum creepage distance and air clearances between conductive parts within several millimeters. Following this requirement can end up the size of surgical instruments impractically large for endoscopic surgery. This standard allows a risk management may relax the requirement to enable thin surgical instruments.
- If an equipment drape, the drape to cover a RASE for sterilization and other purposes, is necessary, its effects shall be considered in the risk management. Such drape may be used to maintain the sterility, including prevention of the contamination by liquid entering the sterile field. The drape should be durable against mechanical movement. Also, side effects of the drape should be considered, for example, the temperature of RASE can escalate when covered by the drape.
- Attachment of robotic surgical instruments and RASE, by means of **mechanical interface**, shall be tested so that the strength of fixation is appropriate. Design of mechanical interface is one of the critical engineering

points. Figure 2 illustrates relationship between surgical instruments and the robot body by means of mechanical interface.

This standard does not include the following requirements:

- Requirements to robotic surgical instruments that have own particular standards such as a HF surgical equipment or an endoscope
- Testing methods of mechanical performance, e.g., the accuracy and the repeatability
- Requirements specific to image guidance
- Requirements specific to RASE with some autonomy

Autonomous surgical robots, or surgical robots with artificial intelligence, are recent topics [12, 13], although we need more experience before introducing requirements in a mandatory standard.

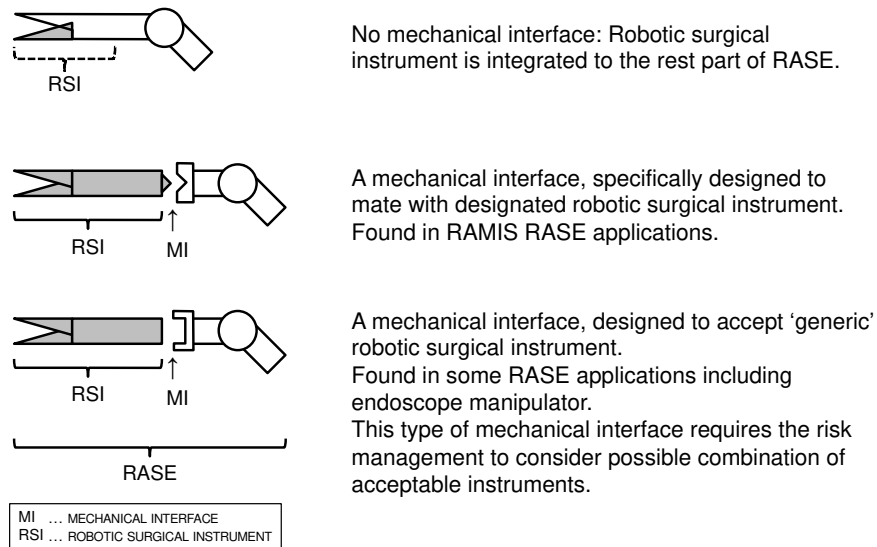


Figure 2  
Types of mechanical interface

## 6 Future of RASE – Real Surgical ‘Robot’?

RASE is not a robot if autonomy is the essential characteristics of robot. However, applications of machine learning technology to surgical procedures are under the horizon.

A technical report, which is not a mandatory document, IEC TR 60601-4-1 was published in May 2017 [16]. It is the first ISO and IEC document about autonomy of medical electrical equipment and systems. This technical report mainly provides the following:

- The definition of terms autonomy, degree of autonomy (DoA)
- Three methods of estimation of DoA
- Relationship between DoA and risk, basic safety, and essential performance;
- Usability engineering considerations for medical electrical equipment with higher DoA
- Operator's situation awareness
- Examples of DoA in medical electrical equipment, estimation of DoA, and risk assessment

The technical report does *not* provide the following:

- Risk level determined by DoA
- Conversion of DoA classified by one method to another

One of this technical report's most important message is that the degree of autonomy is not linked to the degree of the risk: the higher DoA does not necessarily mean the higher risk, and the lower DoA does not necessarily mean the lower risk. Another finding of the technical note is the fact that DoA does not introduce a new hazard, but it can introduce new sources of hazardous situation. Motivations and benefits to adopt DoA can be various; DoA may be applied to improve the usability of a medical device – but DoA can unintentionally complicate the scenarios resulting in new hazardous situations, such as *loss of operator's situation awareness*. Aviation industry already experienced fatal accidents related to the loss of situation awareness. Medical device industry can face this issue when the DoA goes high, possibly by introduction of artificial intelligence.

### **Conclusion**

A new standard IEC 80601-2-77 will be published in 2019. It is a particular standard of IEC 60601-1 series, safety standard for medical electrical equipment. Safety requirements are introduced with respect to both the robot safety and the medical device safety. The robot safety is mainly about the mechanical hazards and the medical device safety is mainly about the patient safety, invisible and insensible hazards, and the risk management of invasiveness.

The scope of this standard is also derived from these safety concerns. Invasiveness is the most significant difference of surgical robot from other robots. This paper classified several examples of surgical robot systems by the mode of invasiveness if they are within the scope or not. Conversely, the variation of surgical

instruments, the mechanical structures, the means of actuation, the control algorithms, or the intended surgical procedures are not the determinant of the scope.

Although the degree of autonomy, that characterizes robots being intelligent, and the situation awareness are not included in the current revision, these will be key concerns in this field in the future.

## References

- [1] Takács Á., Nagy D., Rudas I., Haidegger T., Origins of Surgical Robotics: From Space to the Operating Room, *Acta Polytechnica Hungarica* 13:1 13-30, 2016
- [2] Hoeckelmann M. et.al., Current Capabilities and Development Potential in Surgical Robotics, *Int J Adv Robot Syst*, 2015
- [3] World Health Organization, Safe Surgery Save Lives, *WHO/IER/PSP/2008.07*: 8, 2008
- [4] For example, <https://www.maquet.com/int/products/alphamaxx> (visited on Apr. 3, 2019)
- [5] Finke M., Schweikard A., Usability of a robotic surgical microscope, *proc BioRob 2010*: 235-240, 2010
- [6] Seo J., Koizumi N., Mitsuishi M., Sugita N., Ultrasound image based visual servoing for moving target ablation by high intensity focused ultrasound, *Int J Med Robotics Comput Assist Surg.* 2017;13:e1793
- [7] Maeda Y., Sugano N., Saito M., et al. Robot-assisted femoral fracture reduction: preliminary study in patients and healthy volunteers, *Comput Aided Surg* 13: 148-156, 2008
- [8] Hara W., Soltys S. G., Gibbs I. C., 'CyberKnife robotic radiosurgery system for tumor treatment,' *Expert Rev. Anticancer Ther.*, 7:11 1507-1515, 2007
- [9] Varma T. R. K., Eldridge P., Use of the NeuroMate stereotactic robot in a frameless mode for functional neurosurgery, *Int J Med Robot Comp*, 2: 107-113, 2006
- [10] Kim W. O., Ko S. Y., Park J. O., Park S., 6-DOF force feedback control of robot-assisted bone fracture reduction system using double F/T sensors and adjustable admittances to protect bones against damage, *Mechatronics*, 35: 136-147, 2016
- [12] Yang G.-Z. et al., Medical robotics – Regulatory, ethical, and legal considerations for increasing levels of autonomy, *Sci. Robot.* 2, eaam8638, 2017

- [13] Haidegger T., Autonomy for Surgical Robots: Concepts and Paradigms. IEEE Trans. on Medical Robotics and Bionics, Vol. 1, No. 2, pp. 1-12, 2019, DOI: 10.1109/TMRB.2019.2913282
- [16] IEC TR 60601-4-1:2017 Guidance and interpretation – Medical electrical equipment and medical electrical systems employing a degree of autonomy, 2017